Host-Guest Interactions in Microporous Aluminophosphates

Thesis submitted for the degree of Doctor of Philosophy

By

Robert Werner Dorner

2006

Davy-Faraday Research Laboratory,
The Royal Institution of Great Britain

Department of Chemistry, University College London,
University of London

ProQuest LLC
789 East Eisenhower Parkway
P.O. Box 1346
Ann Arbor, MI 48106-1346

I, Robert Werner Dorner, confirm that the work presented in this thesis is my own. Where information has been derived from other sources, I confirm that this has been indicated in the thesis.

.....
Robert Dorner

Abstract

Microporous materials have attracted considerable interest from the scientific community leading to studies to understand the mechanism involved in the crystallisation of these materials. Most preparations of these materials require a specific organic template (amine or ammonium salt), which acts as a structure directing agent (SDA). The exact behaviour of templates during crystallisation and their role in controlling selectivity to form specific microporous materials is still not completely understood. In previous work carried out at the Royal Institution of Great Britain, the most specific SDA for the synthesis of $AlPO_4$-5 (AFI), i.e. *N*-Methyldicyclohexylamine (MCHA) had been found.

In this thesis, using high-resolution powder X-ray diffraction and Rietveld analysis it was possible to locate the template within the channel system. Employing Monte Carlo docking calculations, the results obtained experimentally were corroborated. Comparing the position of the MCHA within the AFI channel system with the position of other SDAs that form the AlPO-5 topology, a relationship between a template's pKb value and its ability to form the AFI topology could be proposed. Based on the results from the location of MCHA within the framework, it was possible to synthesis a novel layered aluminophosphate material, using phenylethylamine as SDA. The material's structure was solved by single crystal diffraction.

Having located several organic molecules within the inorganic framework, experiments were conducted to test microporous aluminophosphates as hydrocarbon traps in cold start emission control. Several different substituted materials of the AFI and ATS topology were tested in dry and wet conditions. To gain further insight into the material's

ability to store toluene, the organic molecule was located through X-ray diffraction. The results were again corroborated through computational methods.

Overall the thesis has led to a better insight into organic-inorganic interactions within microporous aluminophosphates.

Table of Contents

List of Figures

Chapter 1 Introduction

Chapter 2 Experimental techniques and Analysis

Chapter 4 Synthesis and Structure Determination of a Novel Layered Aluminophosphate

Chapter 5 One Dimensional Aluminophosphates as Hydrocarbon Traps in Cold Start Emission

List of Tables

Chapter 6 Summary

Acknowledgement

I would like to take this opportunity to thank all those people who made this thesis possible and an enjoyable experience for me.

First of all I wish to express my sincere gratitude to Professor Gopinathan Sankar, who guided this work. I am also greatly indebted to Professor Richard Catlow for the opportunity to work at the grand Royal Institution of Great Britain and the support he has shown me over the period of my PhD.

I also want to thank Professor Tatsuya Okubo and Dr Elangovan at the University of Tokyo for hosting me and exposing me to a completely different and exciting culture. Thanks also go to the JSPS for accommodating this exchange and funding my stay. Furthermore, I want to thank Dr Furio Cora and Malek Deifallah for their collaborative work on the computational side of this thesis.

I am also grateful to all the research members of the institute for their support and their comradeship, especially to Andrew Pugsley for proof reading my thesis as well as being a great and reliable friend during our PhD time and all those great lunches we had with Paul Melling at Wong Keis. Further thanks go to Matt O'Brien, Andrew Beale, Manuel Sanchez-Sanchez, Olivier Leynaud and Martijn Zwijnenburg for stimulating discussions and help provided during my PhD time as well as the staff at the SRS in Daresbury, especially John Warren, Mark Roberts, Simon Teat and Steve Thompson.

Finally, I would like to express my deepest gratitude for the constant support, understanding and love that I have received from my better half Su-Jong Kim and my parents and sister during the past years.

Chapter 1

Introduction

1.1 Microporous Materials – Zeolite Introduction

Zeolites firstly came to the attention of science in 1756, when Axel Fredrick Cronsted discovered stilbite. He named the class of materials zeolites from the classical Greek words meaning 'boiling stones' as the mineral visibly lost water upon heating (1). Since the initial discovery the number of known structures has risen to over 170 frameworks.

Zeolite structures are made up of corner sharing TO_4 tetrahedra, where the T atom can be either a silicon or an aluminium atom. The sequence of these tetrahedra units are governed by Lowenstein's rule, which states that Al-O-Al bridges are forbidden (2). The arrangement of the tetrahedra leads to zeolites having open structures consisting of uniform pores and channels.

Based on these structural features the family of microporous materials has attracted a lot of attention due to its potential application in heterogeneous catalysis, ion-exchange, molecular sieving, hydrocarbon and hydrogen storage. The application of zeolites in these areas is based on them being selective and strong absorbers, selective ion-exchanges and when the cation is replaced by a proton they can act as very good solid acid catalysts.

By choosing different structure directing agents (SDAs) the cage, pore and channel size can be altered. This allows different molecules to be absorbed into the framework system (3).

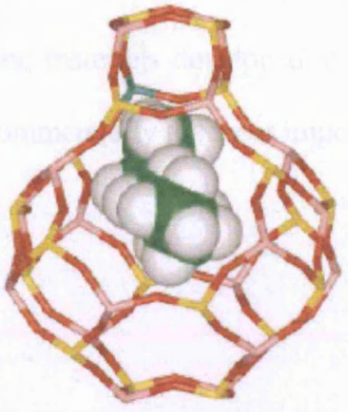

Figure 1.1: A computer generated model of an organic molecule located in a zeolite channel. The size and shape of the channel makes zeolites very specific in which organic molecule they can absorb. This shape selectivity is the basis for zeolites' ability to function as catalysts, molecular sieves and absorbers (4).

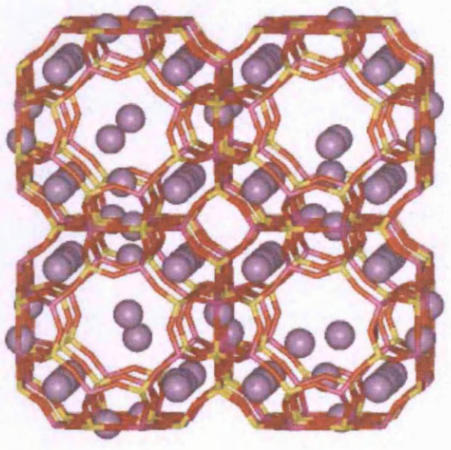

Figure 1.2: Several cations can be seen within the framework cages. These are readily ion-exchanged with other metal ions in aqueous solution. The ion-exchange capability is exploited in washing powders, where zeolites are used as water softeners. Alkali metals (Na^+ or K^+) in the zeolite get ion-exchanged with calcium and magnesium cations, which are the cause for 'hard water' (5).

Zeolites can have a Si / Al ratio ranging from 1 to being purely siliceous. Replacing an Si^{4+} within the framework with Al^{3+} creates a negative charge which can be either balanced by a proton or a metal cation such as sodium or potassium. Zeolites were first used commercially in 1954. These zeolites (Zeolite A, X and Y) were synthetic materials developed at the research laboratories of Linde and still represent commercially the most important zeolites today (6).

1.2 Aluminophosphates: Introduction and Structural Description

Microporous aluminophosphates (AlPOs) are part of the larger family of microporous materials and include a variety of different structures. Organic SDAs used in the synthesis exert a primary influence on the structure formation.

The first microporous aluminophosphate structures were synthesised in the early 1980s by a research group from the Union Carbide Corporation (7). The importance of aluminophosphates (AlPOs) exploded in the 1980s after the realisation that with the use of organic templates (amines in general) it was possible to synthesise zeolite-like microporous materials (7-9). Before that, the only AlPOs synthesised were dense frameworks, and hence were of little importance in catalysis or use as sieves. However, the knowledge gathered through zeolite synthesis turned out to be very useful. The synthesis using alkali metal cations and ammonia in the gel containing a source of aluminium ions and phosphoric acid resulted in the synthesis of a number of mineral analogues such as variscite and palmenite (10). The synthesis was later optimised by using an aqueous solution of aluminium ions and phosphoric acid plus an organic base in hydrothermal conditions (7, 9). Microporous materials are only formed in the presence of an organic amine, which acts as a structure directing agent. If no amine is used during the synthesis dense structures or hydrates ($AlPO_4.nH_20$) are formed (9).

This approach led to a whole new series of microporous materials. These materials are zeolite equivalents, made up of alternating Al and P tetrahedra co-

ordinated to one another, creating cavities and channels of various diameters and sizes (11). It has been possible to synthesis zeolite analogues as well as novel structures through this approach with pore sizes ranging from 12.1 (12) to 3.4 Å (13, 14). These materials are made up of corner-sharing TO_4 units (with T= Al or P), leading to a strict alternating sequence of aluminium and phosphorus tetrahedra. Lowenstein's rule states that in zeolitic frameworks Al-O-Al linkages are forbidden. AlPOs also follow this rule and hence Al-O-Al direct repeat sequences are avoided (6). Today the family of aluminophosphates comprises 53 structures, including 18 analogues of natural or synthetic zeolites (5).

AlPOs are assigned a number representing its framework code number, e.g. AlPO-36, and given a three letter framework code, which for AlPO-36 is ATS (**A**lPO **T**hirty-**S**ix). This concept is applied to all aluminophophates, unless it has a zeolite analogue such as AlPO-43 (GIS named after the zeolite gismondine). Another method of characterisation is based on the secondary building units (SBU – see Figure 1.3). These SBUs make up the overall framework structure. SBUs, as well as the nets and numbers of independent tetrahedral atoms for a specific structure can be found in the Atlas of Zeolite Structures (15).

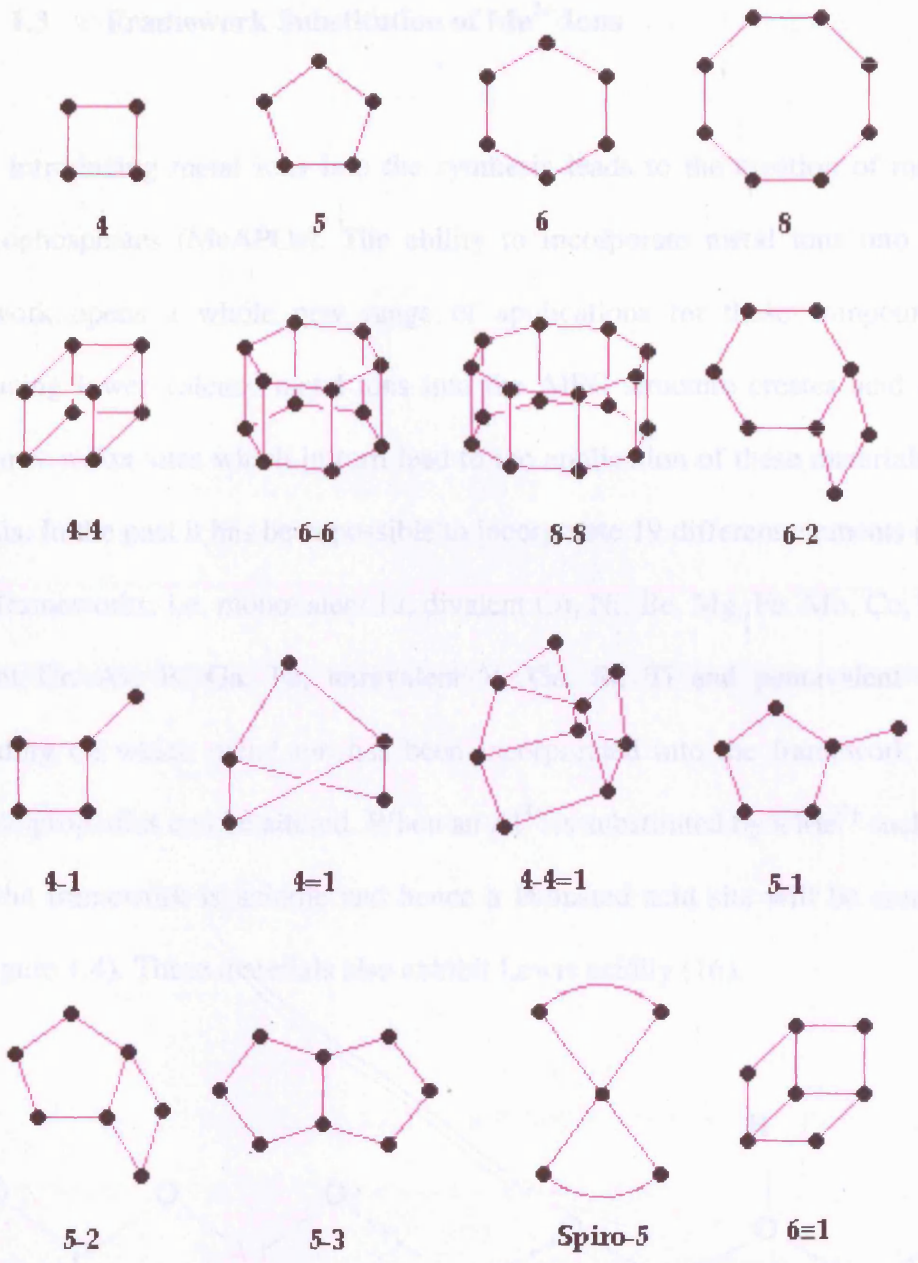

Figure 1.3: Aluminophosphate and zeolite structures can be described by certain of above mentioned secondary building units (SBUs). The points in the SBUs indicate T atoms, with the straight line between two T atoms denoting a T-O-T bond (15).

A crucial aspect of the chemistry of AlPOs is that, as they are made up of alternating tetrahedra with Al and P as their central atom, they are overall neutral but exhibit hydrophilic character.

1.3 Framework Substitution of Me^{2+} Ions

Introducing metal ions into the synthesis leads to the creation of metal aluminophosphates (MeAPOs). The ability to incorporate metal ions into the framework opens a whole new range of applications for these compounds. Introducing lower valence metal ions into the AlPO structure creates acid and sometimes redox sites which in turn lead to the application of these materials in catalysis. In the past it has been possible to incorporate 19 different elements into AlPO frameworks, i.e. monovalent Li, divalent Cu, Ni, Be, Mg, Fe, Mn, Co, Zn, trivalent Cr, As, B, Ga, Fe, tetravalent V, Ge, Si, Ti and pentavalent As. Depending on which metal ion has been incorporated into the framework the catalytic properties can be altered. When an Al^{3+} is substituted by a Me^{2+} such as Co^{2+}, the framework is anionic and hence a Brønsted acid site will be created (see Figure 1.4). These materials also exhibit Lewis acidity (16).

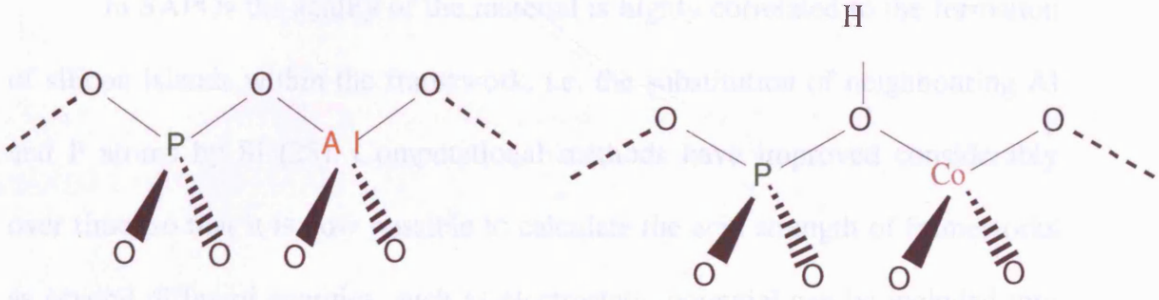

Figure 1.4: AlPO and MeAPO repeat unit – the MeAPO (CoAPO) having a Brønsted acid site due to charge compensation.

The structure directing agent (SDA), in its protonated form normally acts as a charge compensator for the incorporated heteroatom cation (17). It is only

after calcination, that the Brønsted acid sites are formed to compensate the charge on the framework. The acidic nature of these materials, in combination with their shape selectivity and redox centres makes them ideal catalysts. Brønsted acidity in addition to microporosity has also been said to be behind zeolites' ability to be used as a storage material for hydrocarbons (18).

Aluminophosphates have a wide range of applications in different acid catalysed reactions, ranging from methanol-to-olefins conversion (19-23), n-alkane hydrocracking, and complex hydrocarbon transformations. With different heteroatom substitutions, the acid strength can be altered and different frameworks generate different acid strengths, even if the same heteroatom has been substituted into the framework (24). The acidity of a material depends on several different factors, such as bond lengths and angles as well as the electrostatic potential around the acid site (25).

In SAPOs the acidity of the material is highly correlated to the formation of silicon islands within the framework, i.e. the substitution of neighbouring Al and P atoms by Si (25). Computational methods have improved considerably over time, so that it is now possible to calculate the acid strength of frameworks as several different energies, such as electrostatic potential can be included into the calculation (26). A combination of NMR and FTIR coupled with different TPD experiments have confirmed the different acidities present in different substituted frameworks or different topologies.

The incorporation of metal cations (see Figure 1.5) also introduces the possibility of redox-chemistry to aluminophosphates, if the incorporated Me^{2+} cation has the ability to change its oxidation state reversibly. Both cobalt and manganese show this property, leading to the application of materials containing these heteroatoms as redox-catalysts during the oxidation of alkanes and alkenes in the presence of air and hydrogenperoxide (19-23, 27-29).

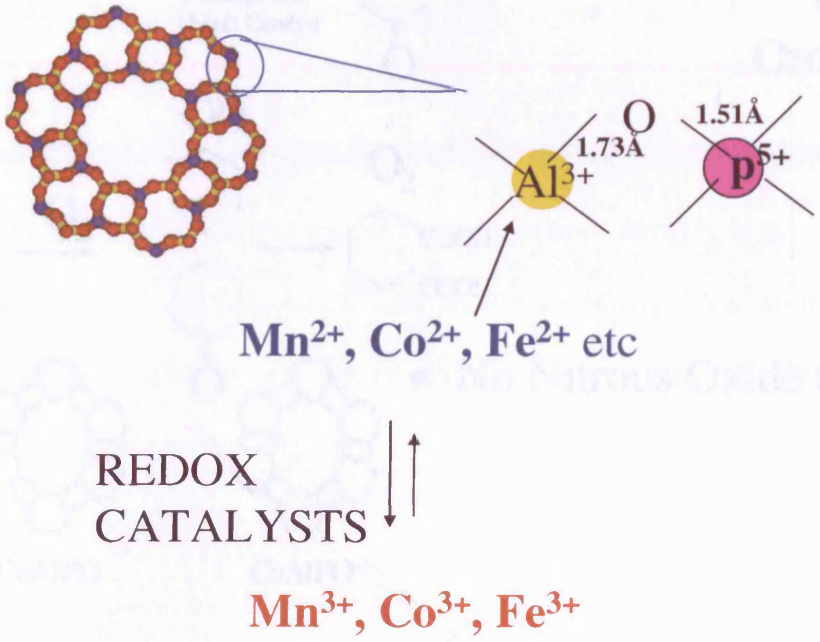

Figure 1.5: MeAPOs acting as redox-catalysts, which include heteroatoms that have the ability to reversibly change their oxidation state.

Homogenous cobalt catalysts are usually employed in the synthesis of adipic acid, which generates N_2O as side product. Nitrous oxide however leads to ozone depletion in the ozone layer, and is hence a highly undesirable side product. Work done by a research group at the Royal Institution of Great Britain in the late 1990s, employing a cobalt containing aluminophosphate (CoAPO-36) as a redox catalyst in the synthesis of adipic acid, showed that this approach did

not lead to the formation of nitrous oxide and that the catalyst could easily be recycled and re-used. MeAPOs hence provide a much more environmentally friendly synthesis route to adipic acid (30) (see Figure 1.6).

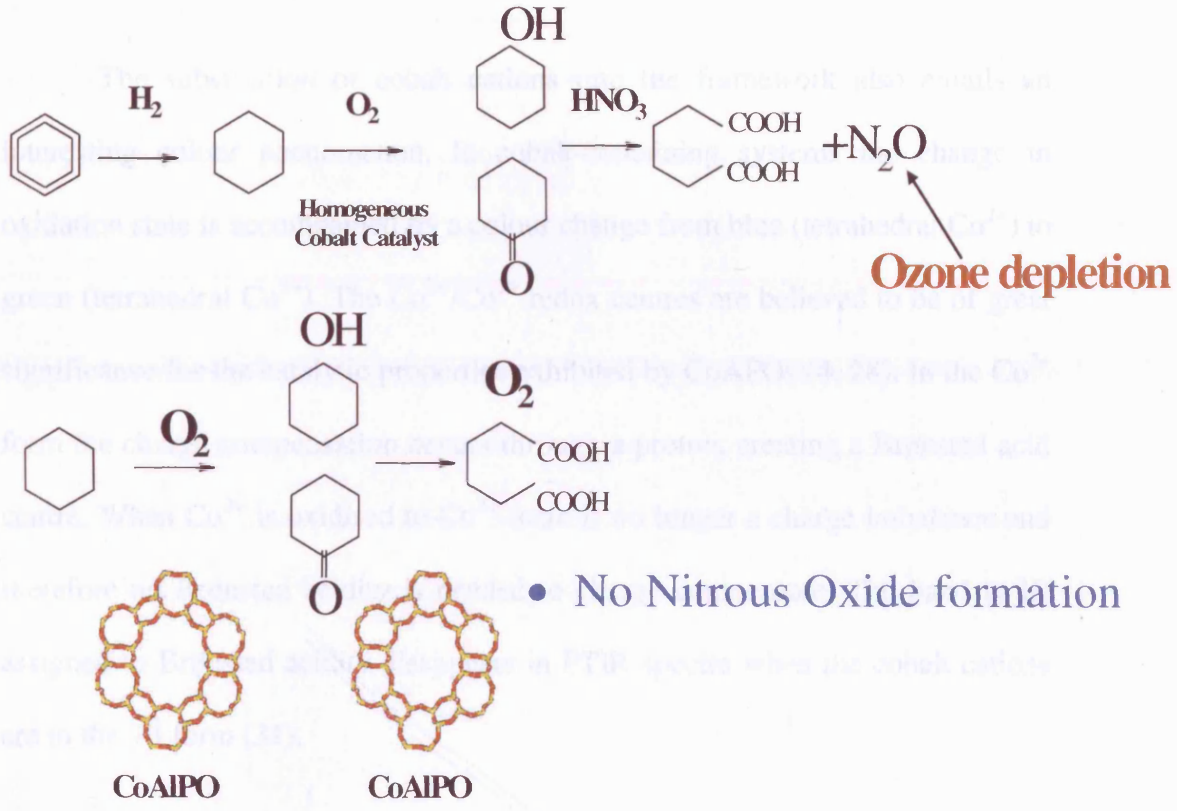

Figure 1.6: Synthesis route converting cyclohexane to adipic acid over a microporous aluminophosphate (ATS structure). This route does not lead to the formation of the ozone depleting nitrous oxide.

Redox chemistry is known to occur in many AlPO frameworks containing metal cations. There is however a significant difference between the redox chemistry of microporous materials with similar pore diameter and same amount of framework substituted heteroatoms. The ATS topology is much better

in oxidising cyclohexane to adipic acid than the AFI topology, even though both have similar pore sizes (30), which indicates that besides pore size and percentage of substituted heteroatoms there has to be another factor influencing the redox chemistry of these materials.

The substitution of cobalt cations into the framework also entails an interesting colour phenomenon. In cobalt-containing systems the change in oxidation state is accompanied by a colour change from blue (tetrahedral Co^{2+}) to green (tetrahedral Co^{3+}). The Co^{2+}/Co^{3+} redox centres are believed to be of great significance for the catalytic properties exhibited by CoAPOs (4, 28). In the Co^{2+} form the charge compensation occurs through a proton, creating a Brønsted acid centre. When Co^{2+} is oxidised to Co^{3+} there is no longer a charge imbalance and therefore no Brønsted acidity is needed to charge compensate. The band in IR assigned to Brønsted acidity disappears in FTIR spectra when the cobalt cations are in the +3 form (31).

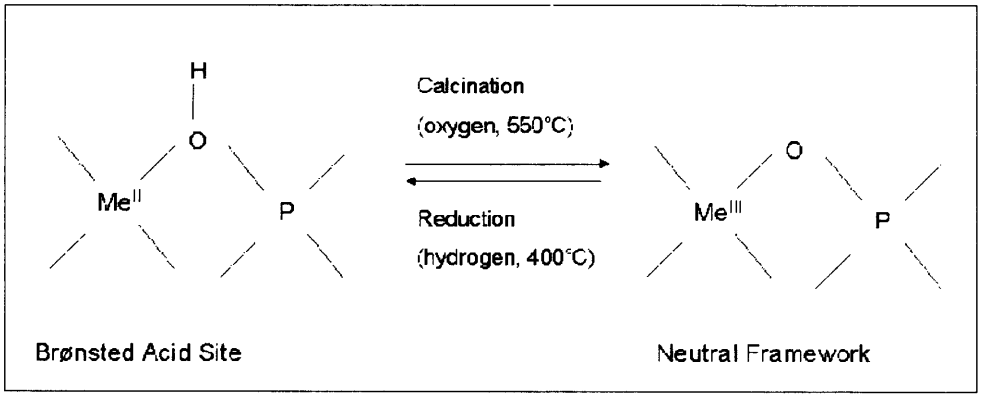

Figure 1.7: Redox properties can be introduced into aluminophosphates by incorporating certain metal cations into the framework. Calcination of the as-prepared CoAPO material leads to a neutral framework, but can be reduced back in the presence of hydrogen at 400 °C to regenerate Brønsted acid sites.

1.4 Synthesis of Microporous Aluminophosphates

Synthesis condition for microporous aluminophosphates are very sensitive and still hold many unanswered questions. It is very rare that the size of the organic base by itself will determine which aluminophosphate will be synthesised. Many amines tend to form more than one structure. Di-*N*-propylamine is probably the template with the least selectivity as it is used to synthesise AlPO-11, -31, -39, -41, -43, -46, -50 and VPI-5 (8, 9).

On the other hand, there are frameworks which can be formed by a wide range of different templates, such as AlPO-5, which can be formed by at least 25 different organic molecules. AlPO-5 and AlPO-11 are the structures which show the lowest template specificity. Both contain a one-dimensional channel, imposing the lowest stereochemical constraints on the size and shape of the template (32).

In most cases, the preparation of microporous aluminophosphates is very sensitive to synthesis conditions and often yields multi-phase samples as can be seen by the low specificity of many templates to form just one specific framework. Thus, the gel chemistry plays a very important role in forming the desired material (33). The concentration and type of metal used, as well as the template concentration have a strong effect on the formation of the product (8, 34-36). Further aspects that tend to play a role in synthesising a specific material are the source of aluminium (36-38), the synthesis duration and temperature (8, 12, 36, 39), gel aging (12, 36-38), agitation (11), and the type of solvent used

(40) as well as the concentration of the solvent (41). The final product as well as the crystallinity of the product seem to be highly correlated to the pH of the synthesis (38, 42), which tends to be in the range of 3 to 10. At lower pH, the material formed is usually of a dense nature, while at a pH higher than 10 the yield will be significantly reduced or will result in a material with low crystallinity (25).

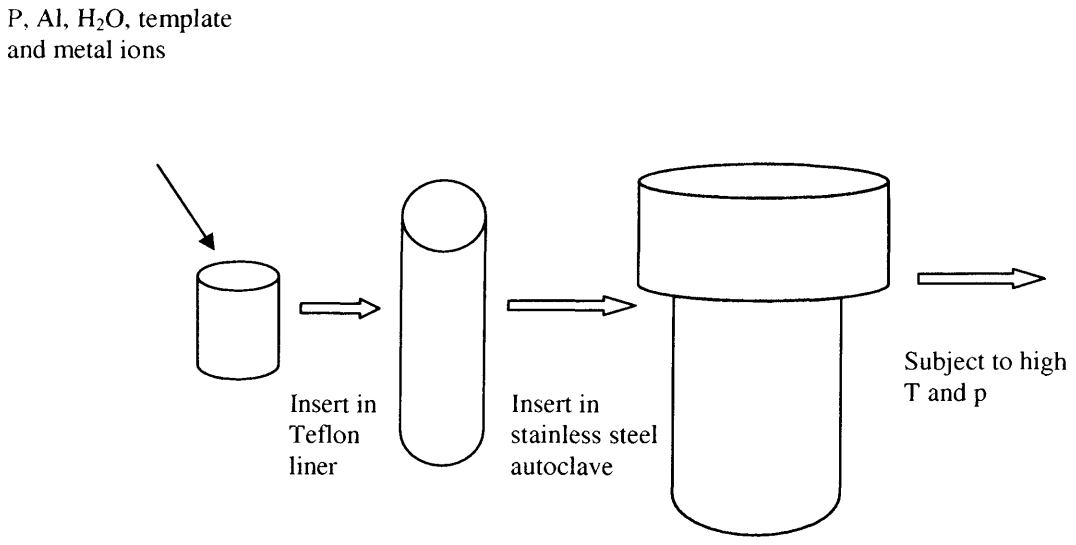

Figure 1.8: Synthesis route to produce microporous aluminophosphates.

SDAs are removed from the structure through calcination, i.e. heating the material in nitrogen and then oxygen at temperatures up to 600°C, with most microporous AlPOs remaining intact after the removal of the organic molecule. The removal is essential to make these microporous materials available for applications. The stability of the framework under industrial operating conditions is a highly important property of aluminophosphates.

Most 3-dimensional microporous materials tend to stay intact after calcination; however with higher degrees of heteroatom inclusion the framework often becomes less stable (43). In most cases only a small amount of heteroatoms (~10 wt %) are incorporated into the framework. Sometimes the inclusion of silicon, resulting in the formation of a CoAPSO can lead to a stabilisation of the framework, leaving the structure intact after calcination (44).

1.5 Objective of This Study

The overall aim of this project is to shed light onto host-guest interactions in microporous aluminophosphates.

As a result of rational studies, it was possible to find a new and specific SDA for the synthesis of $AlPO_4$-5 (AFI), i.e. *N*-methyldicyclohexylamine (MCHA) over a wide range of different pH values of the starting gel (45).

The primary step in this study was to locate the template MCHA in the AFI topology by the use of X-ray diffraction techniques in combination with theoretical approaches, i.e. employing computational methods, gaining insight into the reasons behind MCHA's high affinity to only form AlPO-5.

Based on our findings on the role MCHA plays in the synthesis of the AFI framework, it was possible to synthesise a new, layered aluminophosphate structure using a novel type of phenyl-based template. It was possible to solve the structure through single crystal X-ray diffraction and confirming the structure by high resolution powder XRD. In chapter 5, one-dimensional microporous materials are investigated in their ability to act as hydrocarbon storage materials during the cold-start period of cars. Hydrophobic materials can perform better than their hydrophilic counterparts in the presence of water. This trend is however always reversed in dry conditions. It is assumed that water binds to the active sites, resulting in a general poorer performance in wet conditions. It is hence of great interest to examine ways of improving a material's performance in

the presence of water (46). Furthermore, the exact association between framework and hydrocarbon is not completely understood. Locating the hydrocarbons through high resolution X-ray diffraction will give further insight into the interactions between framework and guest molecules.

1.6 References

1. R. M. Barrer, *Hydrothermal Chemistry of Zeolites,* Academic Press, London (1982).
2. W. Loewenstein, *American Mineralogist,* 39, 92 (1954).
3. R. Goyal, A. N. Fitch, and H. Jobic, *Journal of Physical Chemistry B, 104*, 2878 (2000).
4. J. M. Thomas, R. Raja, G. Sankar, and R. G. Bell, *Nature, 398*, 227 (1999).
5. http://www.bza.org/zeolites.html.
6. R. Szostack, *Molecular Sieves*, Blackie Academic and Professional, London, 1992.
7. S. T. Wilson, B. M. Lok, and E. M. Flaningen, *U.S. Patent No. 4,310,440* (1982).
8. S. T. Wilson, B. M. Lok, C. A. Messina, T. R. Cannan, and E. M. Flaningen, *6th International Conference of Zeolites, Butterworth, Surrey* (1994).
9. S. T. Wilson, B. M. Lok, C. A. Messina, T. R. Cannon, and E. M. Flaningen, *J. Am. Chem. Soc., 104*, 1146 (1982).
10. C. V. Cole and M. L. Jackson, *J. Phys. Chem., 3*, 282 (1950).
11. B. M. Lok, T. R. Cannan, and C. A. Messina, *Zeolites, 3*, 282 (1983).
12. M. E. Davies, C. Montes, and J. M. Garces, *ACS Symp. Ser., 398*, 291 (1989).
13. J. M. Bennett and B. K. Marcus, *Stud. Surf. Sci. Catal., 37*, 296 (1988).

14. A. Simmen, L. B. McCusker, C. Baerlocher, and W. M. Meier, *Zeolites*, *11*, 654 (1991).

15. W. M. Meier and D. H. Olson, *Atlas of Zeolite Structure Types*, Butterworth-Heinemann, 1996.

16. M. Hartmann and L. Kevan, *Chemical Reviews*, *99*, 635 (1999).

17. S. C. Popescu, S. Thomson, and R. F. Howe, *Physical Chemistry Chemical Physics*, *3*, 111 (2001).

18. S. P. Elangovan, M. Ogura, Y. Zhang, N. Chino, and T. Okubo, *Applied Catalysis B-Environmental*, *57*, 31 (2005).

19. H. Berndt, A. Martin, and Y. Zhang, *Microporous Materials*, *6*, 1 (1996).55

20. J. Chen and J. M. Thomas, *J. chem. Soc. chem. Commun.*, 603 (1994).

21. L. E. Iton, I. Choi, J. A. Desjardins, and V. A. Maroni, *Zeolites*, *9*, 535 (1989).

22. L. N. Radev and V. J. Penchev, *React. Kinet. Catal. Lett.*, *58*, 139 (1996).

23. J. M. Thomas, G. N. Greaves, G. Sankar, P. A. Wright, J. Chen, A. J. Dent, and L. Marchese, *Angew. Chem. Int. Ed. Engl.*, *33*, 1871 (1994).

24. O. B. Akolekar and S. Kaliaguine, *Journal of the Chemical Society Faraday Transactions*, *89*, 4141 (1993).

25. H. O. Pastore, S. Coluccia, and L. Marchese, *Annual Review of Materials Research*, *35*, 351 (2005).

26. I. Saadoune, C. R. A. Catlow, K. Doll, and F. Cora, *Molecular Simulation*, *30*, 607 (2004).

27. S.-S. Lin and H.-S. Weng, *Applied Catalysis A: General*, *118*, 21 (1994).

28. U. Schuchardt, D. Cardoso, R. Sercheli, R. Pereira, R. S. de Cruz, M. C. Guerreiro, D. Mandelli, E. V. Spinace, and E. L. Fires, *Applied Catalysis a-General, 211*, 1 (2001).

29. D. L. Vanoppen, D. E. De Vos, M. J. Genet, P. G. Rouxhet, and P. A. Jacobs, *Angew. Chem. Int. Ed. Engl., 34*, 560 (1995).

30. G. Sankar, R. Raja, and J. M. Thomas, *Catalysis Letters, 55*, 15 (1998).

31. L. Marchese, J. S. Chen, J. M. Thomas, S. Coluccia, and A. Zecchina, *J. Phys. Chem., 98*, 13350 (1994).

32. E. M. Flanigen, *Stud. Surf. Sci. Catal., 37*, 3 (1988).

33. R. E. Boyett, A. P. Stevens, M. G. Ford, and e. al., *Stud. Surf. Sci. Catal., 105*, 117 (1997).

34. C. U. de Navarro, F. Machado, M. Lopez, D. Maspero, and J. Perez-Pariente, *Zeolites, 15*, 157 (1995).

35. I. Girnus, E. Loffler, U. Lohse, and F. Neissendorfer, *Collect. Czech. Chem. Commun., 57*, 946 (1992).

36. S. T. Wilson, *Stud. Surf. Sci. Catal., 58*, 137 (1991).

37. S. Prasad and S. Liu, *Chem. Mater., 6*, 633 (1994).

38. X. Ren, S. Komarneni, and D. M. Roy, *Zeolites, 11*, 142 (1991).

39. Q. S. Huo, R. R. Xu, S. G. Li, Z. G. Ma, J. M. Thomas, R. H. Jones, and A. M. Chippindale, *J. Chem. Soc. Chem. Comm.*, 875 (1992).

40. W. B. Fan, R. F. Li, T. Dou, T. Tatsumi, and B. M. Weckhuysen, *Microporous and Mesoporous Materials, 84*, 116 (2005).

41. S. Ahn and H. Chon, *Microporous Materials, 8*, 113 (1997).

42. B. L. Newalkar, B. V. Kamath, R. V. Jasra, and S. G. T. Bhat, *Zeolites, 18*, 286 (1997).

43. G. Sankar, J. K. Wyles, and C. R. A. Catlow, *Topics In Catalysis*, *24*, 173 (2003).

44. P. A. Barrett, G. Sankar, C. R. A. Catlow, and J. M. Thomas, *Journal of Physics and Chemistry of Solids*, *56*, 1395 (1995).

45. M. Sanchez-Sanchez, G. Sankar, A. Simperler, R. G. Bell, C. R. A. Catlow, and J. M. Thomas, *Catalysis Letters*, *88*, 163 (2003).

46. N. R. Burke, D. L. Trimm, and R. F. Howe, *Applied Catalysis B-Environmental*, *46*, 97 (2003).

Chapter 2

Experimental Techniques and Analysis

2.1 Introduction

X-ray diffraction (XRD) is an analytical tool, which determines the long range order in a structure. Depending on the sample's crystal size, different experiments can be run. Powder samples can only be studied using powder X-ray diffraction. This technique can be used to solve new structures if it has not been possible to synthesise single crystals. However impurity peaks within the sample make structure solution from powder XRD data very difficult. Furthermore, powder X-ray diffraction is often used to gain insight into a material's unit cell parameters and symmetry through indexing. It is also used to gain insight into a sample's phase purity and crystallinity. Neutrons and electrons can also be employed for diffraction experiments; however for this study only X-ray diffraction was used.

If the synthesised material yields crystals of sufficient size and crystallinity, single crystal X-ray diffraction can be used to investigate the material's atomic structure. More information can generally be obtained from single crystal XRD in comparison to powder XRD. However, with the advances made in synchrotron technology it is possible to solve structures from microcrystals.

Computational analytical methods were used to support the experimental XRD results. Cerius2 (1) and Materials Studio (2) were used to obtain a theoretical picture of the compounds investigated.

2.2 X-Ray Techniques

2.2.1 Introduction

Visible light has its limits, as at a point its wavelength becomes too long to see small matter. X-rays, with their very short wavelengths allow one to 'see' a material's atomic structure, as the wavelengths are similar to the atomic spacings (a few Angstrom) between constituent atoms of solids which thus cause diffraction.

In 1895 Wilhelm Conrad Röntgen discovered X-rays. He used X-rays to take an image of his wife's hand. It wasn't until 1912 however, when the scattering properties of X-rays were explored by Max von Laue, taking a diffraction picture of a $CuSO_4.nH_2O$ crystal. In the same year W. L. Bragg described how materials diffract X-rays and based on that he formulated Bragg's Law, which remains the basis of crystallography up to this day. This simple mathematical formula describes the diffraction of X-rays as a function of incident X-ray angle and separation between lattice planes.

2.2.2 The Crystal Lattice

Johannes Kepler wrote perhaps the first paper on geometrical crystallography 'A New Years Gift or the Six-Cornered Snowflake', which attempted to relate the external form or shape of a crystal to its underlying structure (3). However, it was Robert Hooke who made a real breakthrough in the area of crystallography by suggesting that the different shapes of crystals occurred due to the packing of globes or spheres (4). Since the early beginnings of research into the structure of minerals and other solids we have come a long way allowing us to better understand the atomic build up of these compounds.

A good way of describing a perfectly crystalline material is a very large (effectively infinite) three-dimensional array of identical molecules (or group of atoms), giving rise to a high degree of order. The smallest, repeatable unit represents the material's unit cell. The geometry of the unit cell in real space is described by the lattice, which is an array of mathematical points defined by translation vectors, **t**.

$$\mathbf{t} = u\mathbf{a} + v\mathbf{b} + w\mathbf{c} \qquad 2.1$$

with u, v and w integers and **a**, **b** and **c** non-coplanar vectors called the unit translations. The complete lattice geometry can therefore be defined by three base vectors (5, 6).

The start of every crystal structure solution therefore includes the identification of the unit cell geometry, which is determined through the position of the diffracted

peaks. The arrangement of the atoms within the repeat unit is determined through the phases and amplitudes of the diffracted waves. The difficulty of solving crystal structures through diffraction methods is that the phase of the diffracted X-ray waves is not detected.

Crystal structures can be classified as one out of seven different crystal systems. The seven different systems are listed in ascending symmetry in Table 2.1. The lengths of the non co-linear vectors which define the unit cell are a, b and c with the angles between them α, β and γ (7).

Table 2.1: All crystal systems with the unit cell centring that can be found in each system.

Crystal System	Unit Cell	Coordinate Description
Triclinic	Primitive	$\mathbf{a} \neq \mathbf{b} \neq \mathbf{c}$ $\alpha \neq \beta \neq \gamma$
Monoclinic	Primitive	$\mathbf{a} \neq \mathbf{b} \neq \mathbf{c}$ $\alpha = \gamma = 90° \neq \beta$
	Face Centred	
Orthorhombic	Primitive	$\mathbf{a} \neq \mathbf{b} \neq \mathbf{c}$ $\alpha = \beta = \gamma = 90°$
	Base Centred	
	Body Centred	
	Face Centred	
Tetragonal	Primitive	$\mathbf{a} = \mathbf{b} \neq \mathbf{c}$ $\alpha = \beta = \gamma = 90°$
	Body Centred	
Trigonal	Primitive	$\mathbf{a} = \mathbf{b} = \mathbf{c}$ $\alpha = \beta = \gamma \neq 90°$
Hexagonal	Primitive	$\mathbf{a} = \mathbf{b} \neq \mathbf{c}$ $\alpha = \beta = 90°, \gamma = 120°$
Cubic	Primitive	$\mathbf{a} = \mathbf{b} = \mathbf{c}$ $\alpha = \beta = \gamma = 90°$
	Body Centred	
	Face Centred	

The combination of the seven crystal systems with the different possibilities of the unit cell's centring results in the 14 possible Bravais lattices for 3-dimensional systems. The possibilities for cell centering are:

Face centred	F (on all faces)	4 lattice points per unit cell
Base centred	A, B, C (on opposite faces)	2 lattice points per unit cell
Body centred	I	2 lattice points per unit cell
Primitive	P	1 lattice point per unit cell

Symmetry can be explained in terms of a crystal's repeat pattern. In a two-dimensional system there are certain repeat functions to consider. Firstly there are rotational axes. The simplest rotational unit is a monad, which is a 360° rotation, i.e. giving rise to the same symmetry as before the rotation. The first real rotational function is a diad (i.e. two-fold rotation) axis, which represents a rotation by 180°. An example of an organic molecule which contains a diad is trans-dichloroethene.

Following on from this is a triad (three-fold rotation) axis (as seen in Figure 2.2), representing a rotation by 120°, a tetrad (90°), pentad (72°), hexad (60°) and so on. However, of real importance are only all the rotational units up to the hexad with the exception of the pentad, which cannot be found in any combination of crystal symmetry functions, as no uniform pattern can be built up (see Figure 2.1) (4).

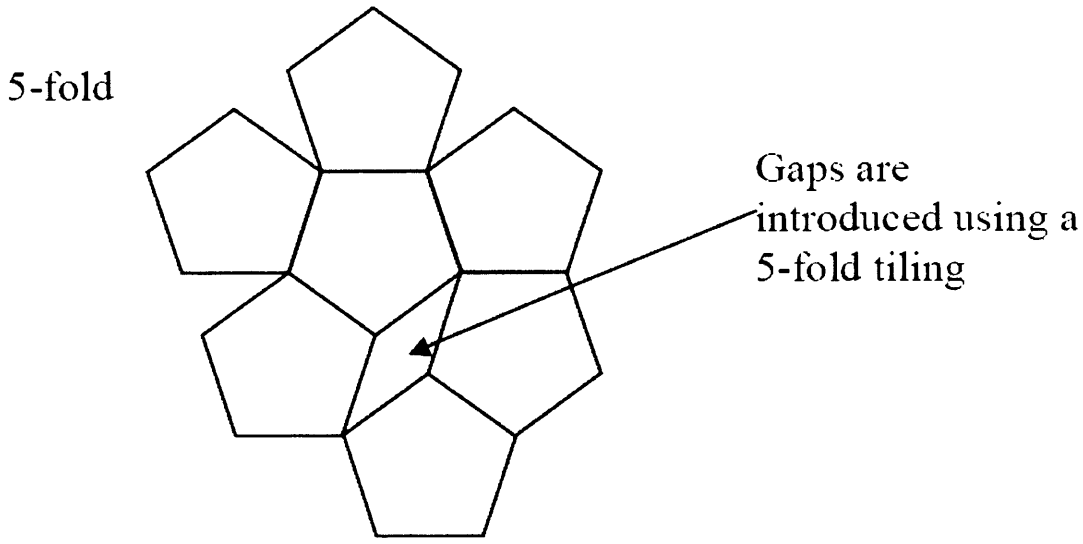

Figure 2.1: Symmetry system showing a pentad in two-dimensional space (8).

As seen in Figure 2.2 one other symmetry function in 2D Crystallography is the mirror line. This concept can be found in many other areas of chemistry such as chirality. In crystallography a mirror line is the projection of a mirror image as seen in *cis*-dichloroethene. Rotational axes and mirror lines in combination give rise to the ten two dimensional crystallographic or plane point groups. A further seven are added to these by the introduction of glide lines.

A glide line can be considered a mirror line with a shift between the reflected objects. An everyday example of glide-line symmetry, are footsteps left after walking on a sandy beach. These 17 plane groups are named using shorthand symbols. Firstly the type of lattice is highlighted by *p* or *c* (as for primitive or centred). Then the symmetry elements are presented by *m* for mirror lanes, *g* for glide lines, *4* for tetrads and so on (4).

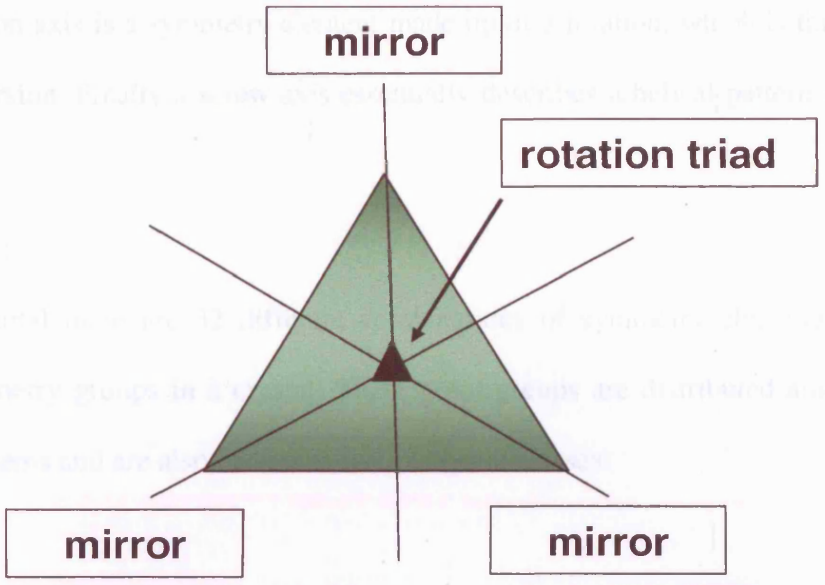

Figure 2.2: A 2-D system showing a rotational triad and three mirror planes.

However, as crystals are three-dimensional systems these concepts have to be applied to a three-dimensional environment. All the symmetry elements from the 2D environment can be taken over. However, mirror lines turn into mirror planes, glide lines into glide planes and so on. Objects can have more than one rotational axis in different directions. All these symmetry elements pass through the centre of the object, i.e. through a single point. This combination of molecular symmetry elements, i.e. those without a translational component, is called the point symmetry group for an object.

Additional kinds of symmetry arise in three dimensions, which do not occur in two dimensions. These are screw axes and inversion axes. If a crystal contains a centre of symmetry then any line passing through the centre of the crystal connects equivalent faces, atoms or molecules, i.e. all points are inverted through a centre of symmetry (9).

An inversion axis is a symmetry element made up of a rotation, which is then followed by an inversion. Finally a screw axis essentially describes a helical pattern of atoms or molecules.

In total there are 32 different combinations of symmetry elements giving 32 point symmetry groups in a crystal. These point groups are distributed amongst the 7 crystal systems and are also known as the 32 crystal classes.

If the 14 Bravais lattices and 32 point groups are combined and all the translational symmetry elements of glide planes and screw axes are considered, then there are 230 different possible combinations. These 230 space groups describe all the possible different spatial arrangements of symmetry in crystals in 3D space. Again, shorthand symbols are used to describe the unit cell and the symmetry functions present within it. As can be expected there are several more shorthand symbols for 3D than 2D systems.

Mirror planes are still abbreviated with *m*, while glide planes according to the axis they lay along are denoted with *a, b, c* or *n* for diagonal glides. A '/' indicates that the symmetry element lies perpendicular to the previously mentioned symmetry function. Rotational axes are indicated by the n-fold axis number, i.e. a triad would be described by a 3. A screw axis is denoted by a number with another number in subscript according to the nature of the screw axis, i.e. 2_1 standing for a two-fold screw axis while a bar symbol stands for a rotational inversion. When written out, the first letter always

indicates the lattice type. The subsequent letters and numbers are the symmetry operators (8).

Laue introduced the concept of interference (10). He proposed that X-ray waves remaining in phase when reflected from the lattice planes interfere constructively, giving rise to strong signals or 'peaks' in a diffraction pattern (see Figure 2.3). The same principle applies when X-rays are reflected by planes incoherently, leading to destructive interference and hence weak or non-existent peaks (11).

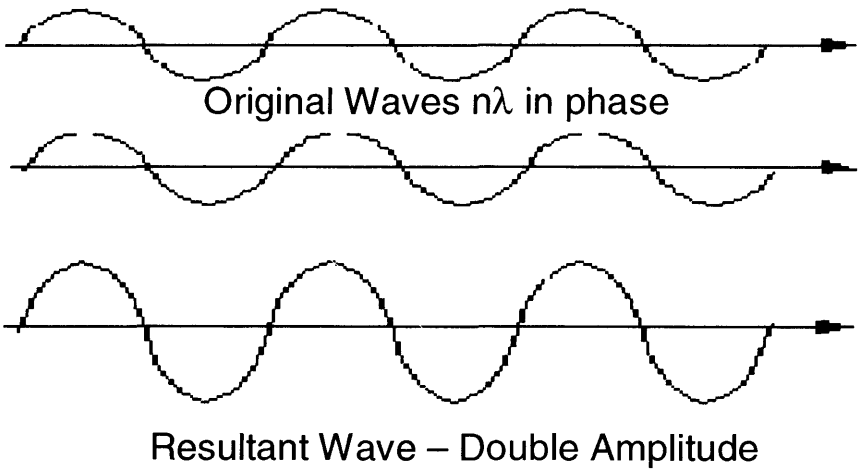

Figure 2.3: Reflected waves are in the same phase, leading to constructive interference and hence a stronger signal.

The peaks in a diffraction pattern are identified according to the planes with which they are associated. The orientation of the plane relative to the co-ordination system of the unit cell is defined by its Miller indices with the values *hkl*. The *hkl*

indices of any such plane can be determined by the examination of the plane which lies nearest to the origin without passing through it. Its intercepts on the three unit cell axes a, b and c will be a/*h*, b/*k* and c/*l*. Analysis of the patterns of weak and strong reflections within the families of *h k l* reflections allows the identification of the type of lattice centring and symmetry operations present in the crystal (5). This allows the identification of the material's space group (or sometimes a small number of possible space groups).

2.2.3 The Reciprocal Lattice

To gain meaningful information from interference patterns obtained through a diffraction experiment, the data must be analysed in terms of the crystal structure's properties. The reciprocal lattice is an important concept in this process. The reciprocal lattice is related to the real space lattice by the following set of equations:

$$\mathbf{a^*} = \vec{b} \times \vec{c} \; / \, V_c; \qquad \mathbf{b^*} = \vec{c} \times \vec{a} \; / \, V_c; \qquad \mathbf{c^*} = \vec{a} \times \vec{b} \; / \, V_c \qquad 2.2$$

Where V_c is the Volume of the unit cell:

$$V_c = \vec{a} \, . \, (\vec{b} \times \vec{c}) \qquad 2.3$$

The reciprocal lattice vector $\mathbf{d}^* = h\mathbf{a}^* + k\mathbf{b}^* + l\mathbf{c}^*$ is perpendicular to the direct lattice planes with Miller indices (*hkl*). The magnitude of this vector is the reciprocal of the shortest distance between these Miller (*hkl*) planes:

$$|\mathbf{d}^*| = 1 / d_{hkl} \qquad 2.4$$

2.2.4 X-Ray Diffraction Data Collection

X-ray diffraction follows Bragg's Law, which is based on the crystal structure concept (outlined earlier). Each crystalline solid produces a diffraction pattern, which is unique for the sample's lattice parameters and space group, and is hence used for its identification. Laboratory X-rays are typically produced by accelerating a focussed beam of electrons at a piece of metal, which in most cases would be copper (Cu) (see Figure 2.4).

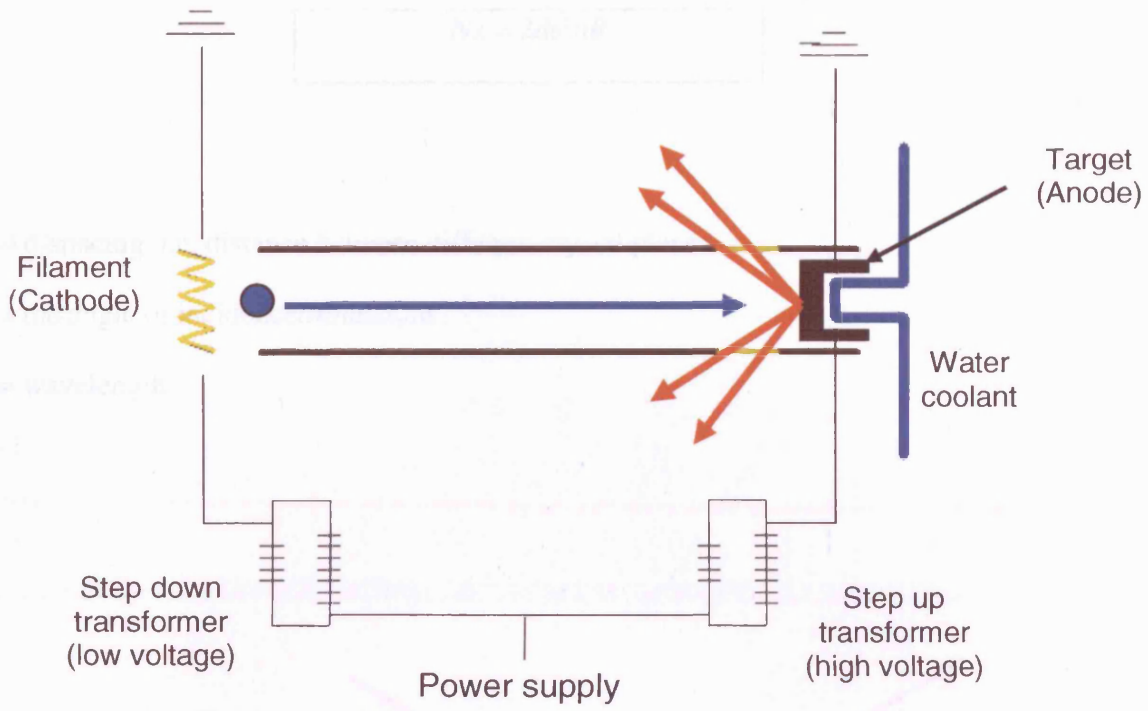

Figure 2.4: X-ray generation in laboratory equipment by accelerating an electron into the target anode.

The 1s (K-shell) electrons of the metal target are knocked out of the orbital by the incident high-energy electrons, ionising the atom. Consequently an outer orbital electron (2p or 3p) drops down to occupy the empty 1s level and the energy released in this transition is given out as X-rays (12). The reason why crystals diffract X-rays is due to the fact that the spacing within a crystal is similar to that of the X-rays' wavelength. The electron cloud, which surrounds the atoms' nucleus, scatters the X-rays randomly, the latter undergo constructive interference. W.L. Bragg proposed that the diffraction of X-rays could be explained in terms of reflection from crystal planes, which extend throughout the crystal, and thus he formulated Bragg's law (13):

$$N\lambda = 2d\sin\theta \qquad 2.5$$

d = d-spacing, i.e. distance between different crystal planes

θ = the angle of incidence/reflections

λ = wavelength

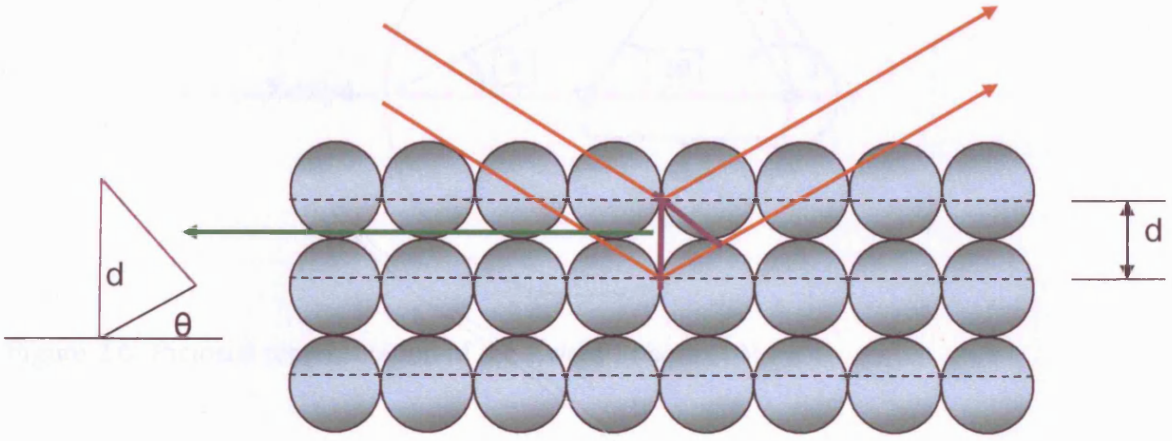

Figure 2.5: X-rays deflected from crystal planes.

In the laboratory experiments conducted, a fixed wavelength was used. As the d-spacings are constant for a certain structure the angle θ was varied.

Besides using the reciprocal lattice to describe the lattice planes of a crystal, it can also be used to describe a practical experiment in the form of the Ewald construction.

In the Ewald construction the sample is taken as the centre of a sphere with the radius $1/\lambda$ (λ = wavelength of the incident radiation). The origin of the reciprocal lattice lies on the transmitted beam, at the edge of the Ewald sphere. The diffraction condition set out in Bragg's Law, is met if one or more reciprocal lattice points intercept the sphere. This is illustrated for 2 dimensions in Figure 2.6.

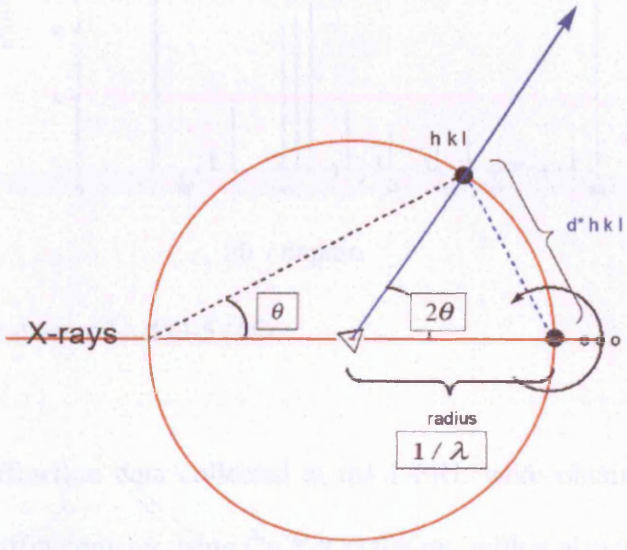

Figure 2.6: Pictorial representation of the Ewald Sphere (14).

In an X-ray experiment, the X-rays are emitted from the source and are limited by the divergence slit. Whenever the Bragg conditions are met for a set of certain crystal planes, the beam is reflected. The diffracted ray's direction is given by the Ewald sphere construction. If this reflected beam is directed at the detector a diffraction line will be recorded (15). A powder's reciprocal lattice can be generated from a single crystal's reciprocal lattice. A powder pattern is made up of several different single crystal

diffraction points, which overlap due to the random orientation of the crystallites within the powder sample. This leads to a pattern such as the one shown below.

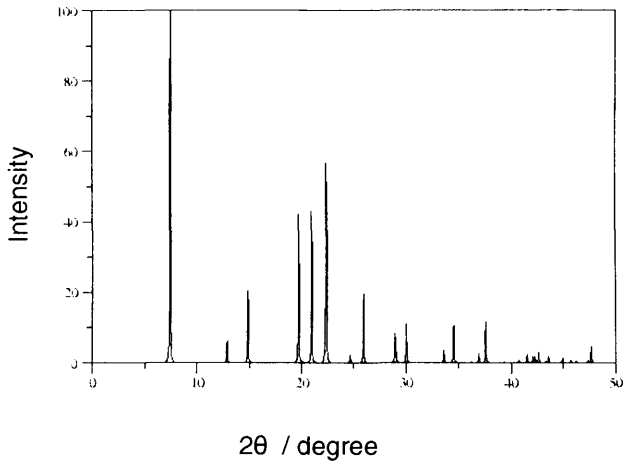

Figure 2.7: XRD-pattern of AlPO-5 (16).

Powder diffraction data collected at the DFRL were obtained from a Siemens D500, D8 or D4 diffractometer using Cu Kα radiation, with a wavelength of $\lambda = 1.5418$ Å.

Before starting the data collection however, there are vital issues that need to be considered. Firstly the most suitable radiation has to be chosen. Depending on the nature of the sample this could be conventional X-rays, synchrotron X-rays or neutrons. The next step is to select the right wavelength according to the adsorption edge of the scattering atoms. Another important aspect concerns the divergence slits. Often the divergence slits selected are too wide, which leads to the beam hitting the sample holder at low angles. This causes peak broadening, which often means it is not possible to refine the data correctly. The nature of the sample also plays a role with regard to its

absorption ability. If the sample is a heavy absorber of X-rays it is useful to mix the sample with a light element material such as diamond powder or glass beads. Finally and probably most obviously, a useful 2θ range has to be chosen to give the maximum useful data.

Other useful aspects to keep in mind, are:

1 More time should be spent on obtaining data at high 2θ values, as intensities are lower but more peaks are observed. Furthermore, the Lorentzian factor has a greater influence at higher 2θ.

2 To reduce the influence of preferred orientation of crystallites, i.e. strong *h k l* dependence, a rotating, horizontally mounted capillary should be used as sample holder for data collection. However when choosing a capillary it is necessary to ensure that the μR value is not too large, where μ is the capillary's linear absorption coefficient and R is the diameter of the capillary cylinder (17).

3 A rotating capillary mitigates the effect of different sized crystallites being present in the powder. Crystallites larger then 1 - 5 μm can lead to peaks with incorrect relative intensities (17).

2.2.5 Synchrotron Radiation (SR)

The availability since the early 1980s of synchrotron radiation (SR) has greatly enhanced the scope of diffraction studies enabling the study of materials that cannot be investigated under standard laboratory techniques (18). In particular, structure solution and refinement from powder samples and microcrystalline diffraction using SR has been exploited extensively (19).

SR is white radiation, produced by accelerating a beam of high energy electron bunches, by a magnetic field through an arc. These electrons in the storage ring are arranged in a series of bunches as seen in Figure 2.8.

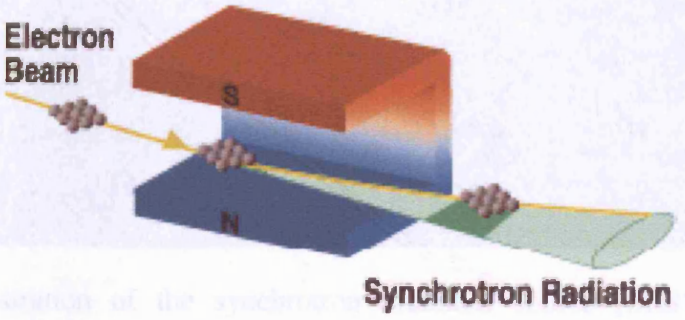

Figure 2.8: Electron bunches accelerated around the synchrotron ring (20).

At the SRS in Daresbury a linear accelerator or LINAC accelerates the electrons before they get injected into a storage ring. A booster synchrotron as seen in Figure 2.8, which can be found at the SRS in Daresbury, is able to accelerate the electrons up to 2 GeV in energy. Once these particles have reached this energy they get transferred to a large storage ring where they are constrained to or hit by several powerful bending

magnets. The orbiting electrons however lose energy. Radio-frequency energy produced by a 'Klystron' is used to continuously replenish the beam. The beam however still decays in a few hours, which results in the beam being 'dumped' and a new beam injected from the LINAC.

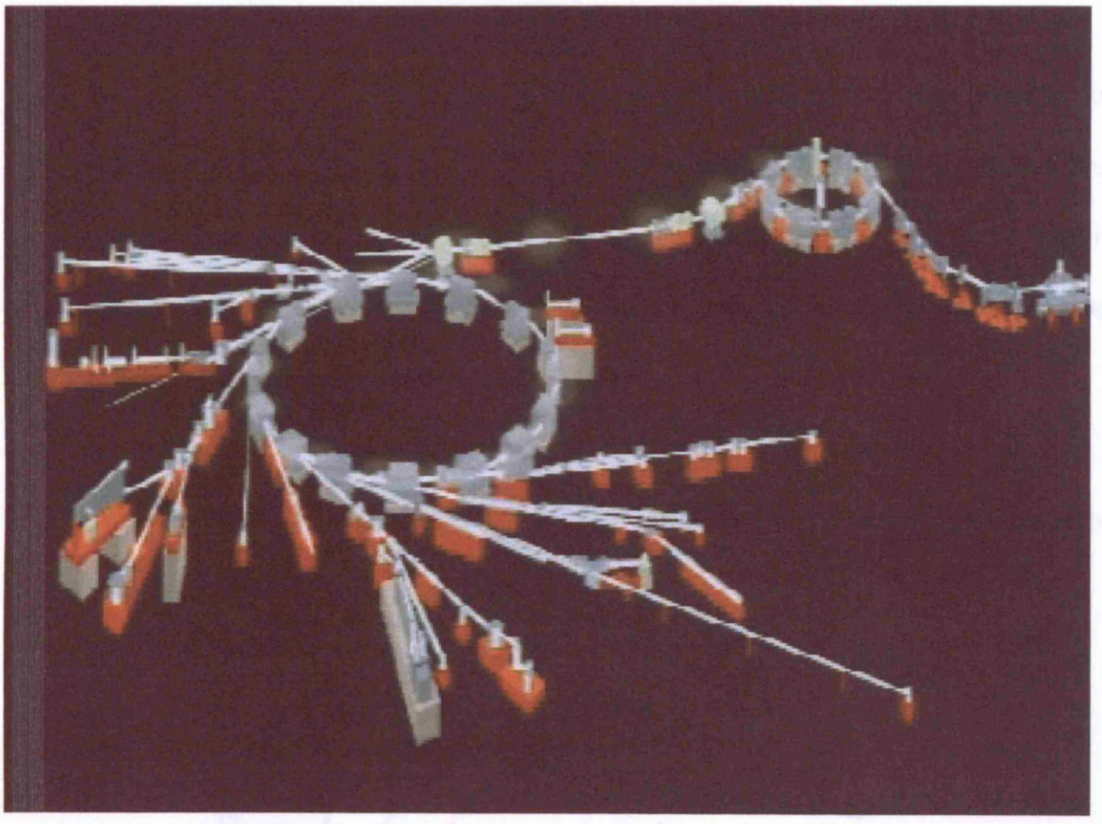

Figure 2.9: Illustration of the synchrotron radiation source (SRS) lay-out at the Daresbury Laboratories (21).

In the SRS at Daresbury, it is possible to change the electromagnetic radiation to shorter wavelengths by using multipole wigglers. These wigglers change the electron beam's radius of curvature, which leads to the emission of high flux, shorter wavelength X-rays.

Synchrotron radiation has several advantages (19):

1. It is possible to obtain a 10^6 times higher intensity in comparison to the laboratory technique, allowing a far superior signal to noise ratio.

2. As the beam neither converges nor diverges (high collimation), it is possible to obtain extremely sharp, narrow Bragg peaks with good line shape. Furthermore, due to the superior signal to noise ratio, the obtained resolution is of better quality and leads to fewer overlaps of peaks. This allows a far more precise structural analysis of compounds.

3. Wigglers allow the use of a variety of different wavelengths and record data with greater intensities (see Figure 2.10).

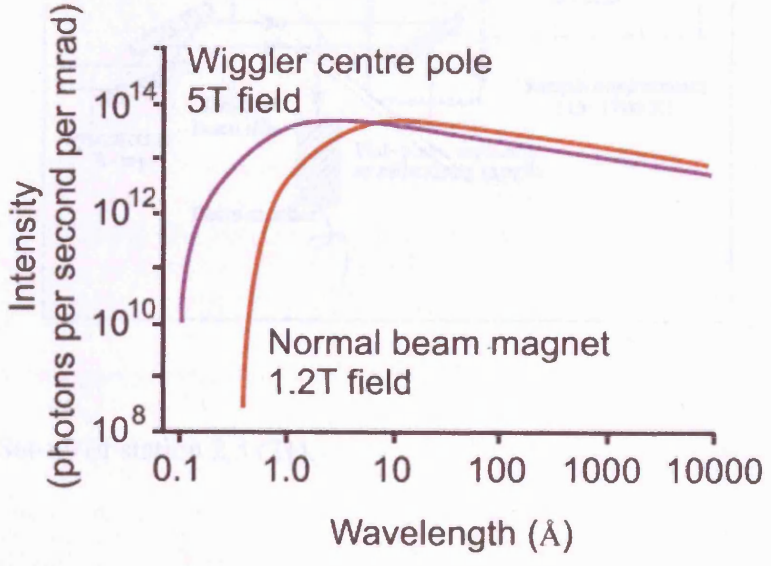

Figure 2.10: Comparison of wiggler (purple) and dipole magnet (red) wavelength spectra (22).

The XRD data collected at Daresbury were obtained using station 2.3 and 9.1, which are monochromatic stations situated on a dipole source with a two circle diffractometer. These stations' primary use is for high-resolution angular dispersive powder diffraction measurements. Figure 2.11 shows the theoretical set up of station 2.3.

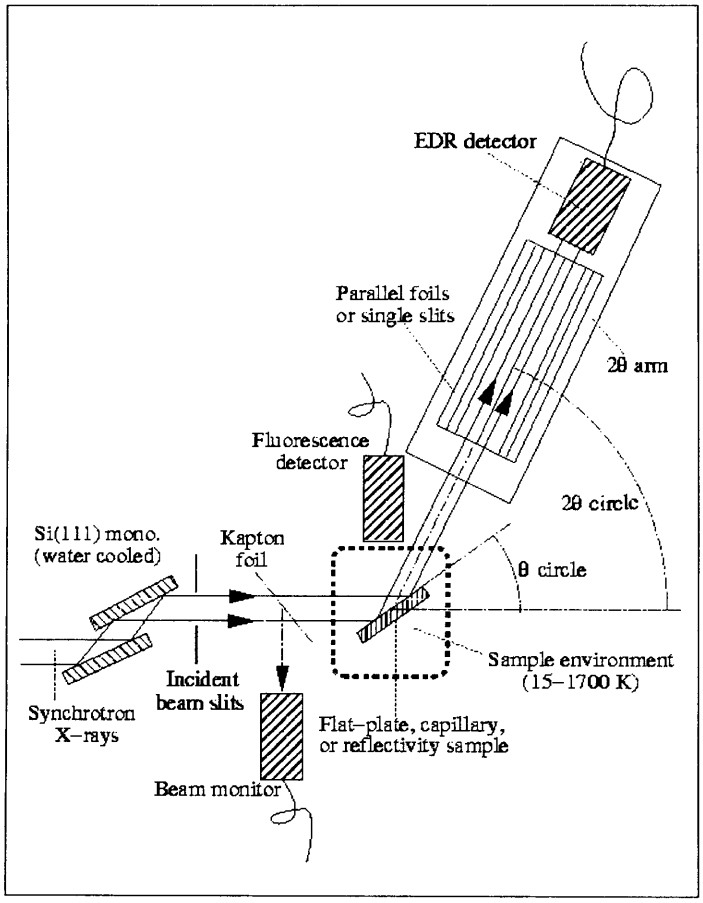

Figure 2.11: Set-up of station 2.3 (21).

2.2.6 Powder X-Ray Diffraction

Powder X-ray diffraction is amongst the most widely used analytical technique in solid-state chemistry due the fact that the data provided by this method can give insight into many properties of the compound observed and many materials are only available as powders. Firstly, and probably the most obvious application of XRD is to find out information regarding the sample's identity. The XRD pattern can be used to determine the investigated compound's identity by matching the data set obtained with XRD patterns of already known structures.

Furthermore, XRD patterns are used to obtain information regarding phase purity of the prepared sample. XRD patterns are available for known compounds. However, if unexpected peaks show up in the pattern, it can be concluded that the phase may not be pure.

Finally, based on the intensity and shape of the peaks observed we can obtain information regarding the sample's crystallinity and particle size. The following rule can generally be applied: the higher the relative intensity, the more crystalline the sample (same material and same experimental conditions). A better measure for the sample's crystallinity is the peak shape; the sharper the shape of the peak (i.e. not a broad hump), the more crystalline the sample.

Laboratory X-ray diffractometers are generally not used to solve novel structures from powder data, as the X-rays generated are less brilliant than SR and not collimated.

This means the peaks of the XRD pattern have a lower resolution and are less defined. The availability of synchrotron radiation allows the use of monochromators leading to the generation of patterns with higher resolution and better-defined peaks, which are favoured for structure solution. Furthermore, besides using these data solely to solve framework structures, powder diffraction has also been used to provide information on the location of organic templates, used in the synthesis of compounds from the aluminophosphate family (23-25), organic sorbates (26) and metal ions (27-30) by employing the Rietveld refinement method (17, 31).

2.2.7 Rietveld Refinement

Above is described how the XRD raw data are obtained. However, to get any meaningful information from the raw data, Rietveld analysis is needed. Rietveld analysis has its origin in neutron diffraction and was developed due to the problem of severe peak overlap at high angle. In 1969, with the introduction of more powerful computers it was possible to not only refine the structure but also profile parameters (31). In the Rietveld method the crystal structure is refined by fitting the entire profile of the diffraction pattern to a calculated profile. There is no intermediate step of extracting structure factors. The Rietveld technique allows obtaining 3-dimensional information from a one-dimensional data set. It is a matching technique, where a structural model is fitted to the whole of a diffraction pattern.

The quality of the refinement is determined by the closeness of fit of bond angles, distances and thermal parameters between the experimental and calculated datasets. The researcher must use his chemical knowledge to ensure proposed structures are plausible. A function made up of the observed and the calculated intensity at each step in the diffraction is minimised using a least squares refinement (32, 33).

$$S = \Sigma w_i \left| y_{io} - y_{ic} \right|^2 \qquad 2.6$$

- w_i is a weighting function given by $(w_i)^{-1} = \sigma^2_i = \sigma^2_{ip} + \sigma^2_{ib}$.
- σ^2_{ip} is the standard deviation associated with the peak generally based on counting statistics.
- σ^2_{ib} is the standard deviation associated with the background y_{ib}.
- y_{io} is the observed / experimental intensity.
- y_{ic} is the calculated intensity and depends on the structure factor calculated from the structural model. The calculated intensity is further modified by corrections to the zero point, which is a correction to the shift in peak positions caused by detector faults, sample position errors, background parameters as well as different geometrical functions adjusting the shape of the Bragg peaks.

The full expression for the calculated intensity y_{ic} is:

$$y_{ic} = s \Sigma m_k L_k \left| F_k \right|^2 G(\Delta 2\theta_{ik}) + y_{ib} \qquad 2.7$$

- **s** is the scale factor to place the calculated data on the same scale as the experimental data.
- $\mathbf{m_k}$ Is the multiplicity factor which deals with the possibility that there is more than one plane contributing to the intensity of a reflection.
- $\mathbf{L_k}$ is the Lorentz-polarisation correction accounting for the fact that a set of lattice planes *hkl* is in different positions over time as well as for the polarisation of the X-ray beam.
- $\mathbf{F_k}$ is the calculated structure factor.
- **G** corresponds to the function representing the peak shapes.
- $\mathbf{\Delta 2\theta_{ik}}$ is the zero-point corrected peak position.
- $\mathbf{y_{ib}}$ describes the background function (32).

There are several different means to establish the quality of the Rietveld refinement. The R-factor often provides a good indication of how close to a match the refinement has got. However, the importance of chemical intuition regarding sensible results cannot be overstated. One should pay close attention to the bond lengths and angles, the visual difference between calculated and experimental pattern, as well as the visualisation of the obtained information.

Table 2.2 shows all the Rietveld agreement factors, which are important in establishing the refinement's quality.

Table 2.2: Rietveld agreement factors (31).

Name	*Definition*
Profile	$R_p = \Sigma \mid y_i(obs) - y_i(calc) \mid / (\Sigma y_i(obs))$
Weighted Profile	$wR_p = [\Sigma w_i (y_i(obs) - y_i(calc))^2 / (\Sigma w_i y_i(obs)^2)]^{1/2}$
Bragg	$R_B = \Sigma \mid I_{hkl}(obs) - I_{hkl}(calc) \mid / (\Sigma I_{hkl}(obs))$
Expected	$R_{exp} = [(N - P)^* / (\Sigma w_i y_i(obs)^2)]^{1/2}$
Goodness of fit	$\chi^2 = [\Sigma w_i (y_i(obs) - y_i(calc))^2 / (N-P)]^{1/2} = R_{wp} / R_{exp}$

* N = number of observations; P = number of parameter.

Before the XRD data can be fed into the Rietveld analysis they have to be converted into a Rietveld refinement software readable file. After this conversion, the general approach to Rietveld is to start with a non-structural model (i.e. atom co-ordinate unspecific model) only refining the cell parameters, the zero error and the peak shapes. This process is called the LeBail refinement. If a good fit is obtained, i.e. a χ^2 of around 1, it can be assumed that the refinement will yield a sensible result based on the cell's symmetry and parameters.

Once the LeBail refinement has been completed, the refinement gets transferred to a Rietveld refinement. At first it is important to set the background manually, to allow a good fit between the calculated and the experimental data. Generally, manually subtracted backgrounds yield a better result than refinements using arbitrary polynomial functions. After having adjusted the background, the scale factor is adjusted to get both data sets (experimental and calculated) onto the same scale. Having entered the expected dimensions of the sample's unit cell and refined the cell parameters, the refinement

should show a reasonably good fit. Before moving on to the peak shape factors, the zero-factor has to be refined. The peak shapes observed are influenced by both the sample (e.g. domain size, stress/strain, defects) and the instrument (e.g. radiation source, geometry and slit-size) and are dependent on the 2θ value. The Pseudo-Voigt function is the function most widely used to analyse peak shapes for SR X-rays. This function is a linear combination of Lorentzian and Gaussian components, with ηL / $(1-\eta)G$ ratio, where η is a Pseudo-Voigt mixing parameter.

The advantage of the Pseudo-Voigt function is that it allows the use of Lorentzian and Gaussian components to be used in a sensible mix to give a good peak fit. With synchrotron radiation, the Pseudo-Voigt function is primarily governed by the Lorentzian factors, i.e. mainly dominated by sample effects (17). The final step of the refinement is to determine the thermal factors (for X-ray data only isotropic refinement is usually possible).

Following a complete refinement, the wRp value is expected to be lower than 10% for simple structures and around 10% for more complex structures. It is often useful to use bond and angle restraints before starting the refinement to ensure the model obtained makes chemical sense. In Figure 2.12, the dependency between different functions and the calculated and experimental data-set are shown.

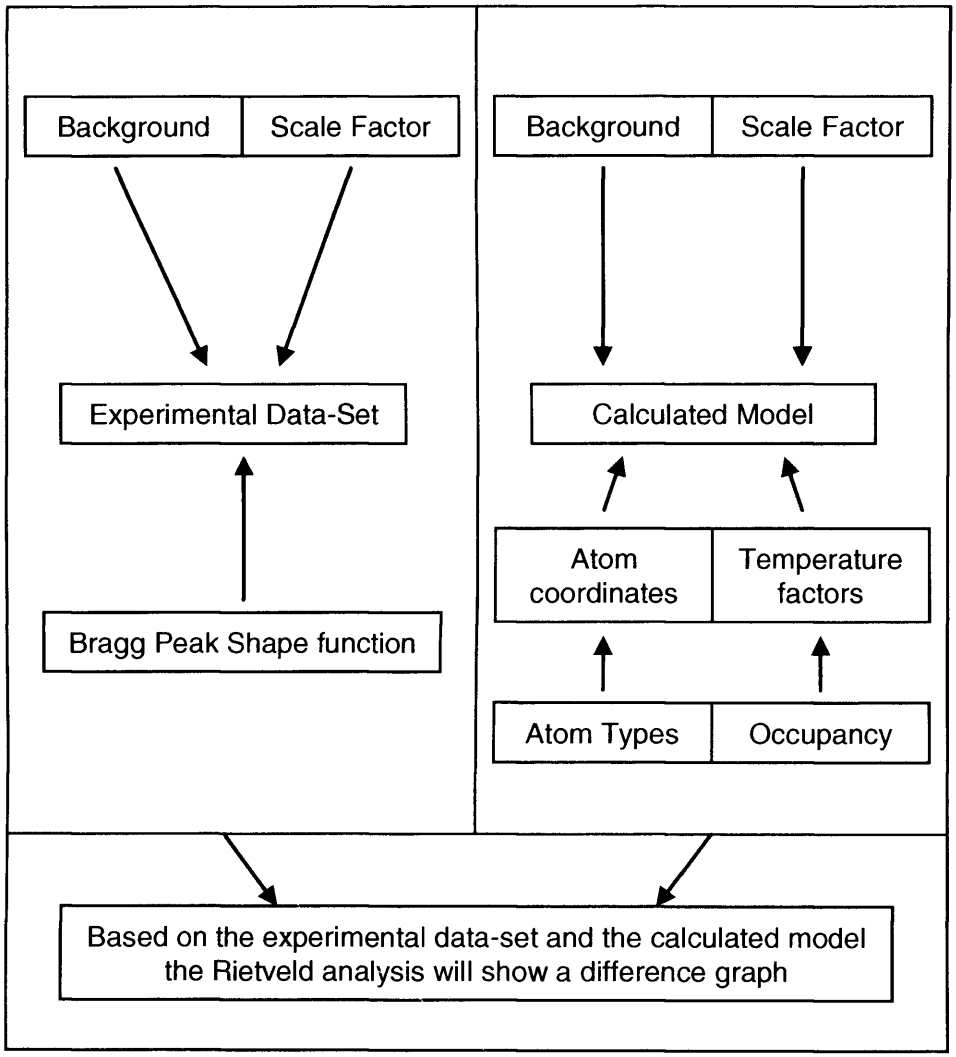

Figure 2.12: Input information needed for a Rietveld refinement.

Rietveld analysis also allows the location of absorbed species within frameworks, or in the example of aluminophophates, the location of the organic template, which was needed to synthesise the particular structure. Using the Difference Fourier Map in the Rietveld refinement extra electron density can be located, which arises from atoms or molecules which have not been detected so far.

The equation

$$\rho(x, y, z) = 1/V \, \Sigma_h \Sigma_k \Sigma_l \| F_o | - | F_c \| e^{-2\pi i(hx+ky+lz-\alpha calc)} \qquad 2.8$$

where:

- $\rho(x, y, z)$ is the electron density
- F_o is the observed structure factor and
- F_c is the calculated structure factor.

realises the differences between the calculated model and the experimental data-set. The location of extra electron density indicates the position of absorbents and structure directing templates within the channel system of microporous materials (17).

2.2.8 Single Crystal Diffraction

Single crystal diffraction data allows the construction of the 3-D reciprocal lattice structure from a 2-D data set. Powder diffraction experiments yield 1-D data sets and are normally of lesser quality due to high background noise. With single crystals, single reflections are collected rather than an assembly of overlapping patterns as is the case in powder diffraction. This makes structure solutions much easier from single crystal data. The only drawback is the need to synthesise crystals of sufficient size and crystallinity. The facilities of station 9.8 at the Daresbury SRS however allow the collection of data on crystals with a size of only 10 μm (34-36).

A typical single crystal diffraction experiment would include selecting an appropriately sized single crystal and mounting it on the diffractometer. The crystal will then be hit by X-rays, which will be diffracted by the crystal lattice in real space. The diffracted X-rays hit the detector with the data getting converted into reciprocal space. This dataset will then be used for the calculations and the results obtained are Fourier transformed back to real space, giving rise to the actual crystal structure.

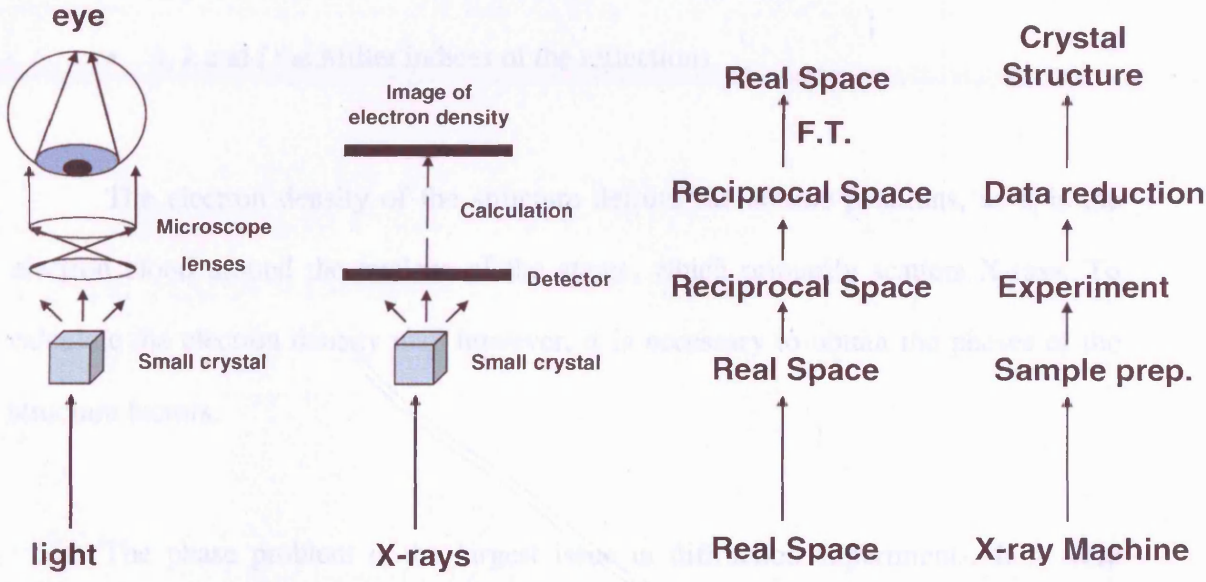

Figure 2.13: Single crystal diffraction structure solution approach.

The first step in analysing the data recorded is to convert the intensity of all reflections (I_{hkl}) into structure factors (F_{hkl}). The equations used for this conversion shows that the intensity of the reflections is proportional to the square of the structure factor (11, 37, 38).

$$I_{hkl} \alpha F^2_{hkl} \qquad 2.9$$

$$F = \sum_{j=1}^{N} f_j \exp[2\pi i(hx_j + ky_j + lz_j)] \qquad 2.10$$

With:

- f_i the scattering or form factor for each atom, describing the amplitude of the scattered wave (with the scattering efficiency of atom j).
- x, y and z the fractional co-ordinates of each atom.
- h, k and l the Miller indices of the reflections.

The electron density of the structure defines the atomic positions, as it is the electron cloud around the nucleus of the atoms, which primarily scatters X-rays. To calculate the electron density map however, it is necessary to obtain the phases of the structure factors.

The phase problem is the largest issue in diffraction experiments. If it were possible to measure the phase angle directly, then the Fourier transform of the diffraction pattern would result in the material's structure. As the electron density cannot be calculated directly, the phase angle has to be calculated by other methods.

The phases can be estimated via the Patterson (39) or direct methods (40). If the unit cell contains strongly scattering atoms (i.e. atoms with a high atomic number) the Patterson method will yield good results. Patterson-method peaks correspond to vectors

between pairs of atoms which show where atoms lie relative to each other, rather than where they lie relative to the unit cell origin.

If, however, all the atoms in the unit cell have similar scattering powers, direct methods are the preferred approach and will probably lead to a satisfactory structure solution. Direct methods refer to the determination of electron density, atomic coordinates or phases by mathematical means from a single set of measured X-ray intensities. Direct methods are probabilistic in nature. All the solved structures from this project used direct methods, as all the atoms in the unit cell were of similar mass.

When solving the structure of an unknown material, prior knowledge of the structural chemistry is essential, as it will benefit the refinement process. In the case of aluminophosphates it is known that they have an ordered framework comprising P, Al and O atoms.

Once a sensible model for the structure is reached and all structure factors (F_{hkl}) have been obtained, it is refined with the use of difference Fourier syntheses, giving rise to the atomic co-ordinates representing the structure. The electron density of the atoms at any particular co-ordinate is given by:

$$\rho(xyz) = \frac{1}{V}\sum_{hkl} |F(hkl)|.\exp[i\varphi(hkl)].\exp[-2\pi i(hx - ky - lz)] \qquad 2.11$$

Refinements were carried out using least-squares fitting procedures aimed at minimising the R-factors wR_2 and R_1. R-factors give the difference between the observed and the calculated structure factors and hence are a measure of the quality of a model. For complex, inorganic structures, such as aluminophosphates an R-factor of 0.08 is normally acceptable.

The equations defining the R-factors are given in equations 2.12 and 2.13. All of the structure solutions and refinements in this work were carried out using the WinGX (41) and Crystals (42) suites of programmes.

$$wR_2 = [\Sigma\, w_{hkl} (F^2_{obs,hkl} - F^2_{calc,hkl})^2 / (\Sigma\, w_{hkl} (F^2_{obs,hkl}{}^2)]^{1/2} \qquad 2.12$$

$$R_1 = \Sigma \left| |F_o| - |F_c| \right| / \Sigma\, |F_o| \qquad 2.13$$

Single crystal data for this work were collected at the microcrystalline diffraction facility on station 9.8 at the Daresbury SRS at a wavelength of 0.6869 Å. This station was chosen to analyse the crystals as they were of insufficient size to be run on a laboratory instrument. Crystal sizes were typically about 50 x 50 x 30 μm. The crystal was mounted on a glass fibre using Fomblin polyether and mounted on the diffractometer and put into a cryostream. Cooling the crystal ensures minimal thermal motion of the atoms within the structure and thus enables a better refinement. Additionally, cooling leads to freezing of the polyether, fixing the crystal to the goniometer. Usually, a hemisphere of data was collected for data reduction.

Station 9.8 is a high flux, tuneable, monochromatic, single crystal diffraction station employing a D8 diffractometer and utilising a Bruker-Nonius APEXII CCD area detector. A range of X-ray wavelengths between 1.45 Å and 0.30 Å can be achieved with variable temperature data collections ranging from 85 to 600 K. The monochromator employed was a Silicon (111) crystal with an asymmetric cut of 2.01° being cooled by GaInSn alloy. The monochromator is mounted on a Huber rotatory table and can be positioned to a precision of 0.001°. An Oxford cryostream was used to cool the crystal. The set-up of station 9.8 can be seen in Figure 2.14.

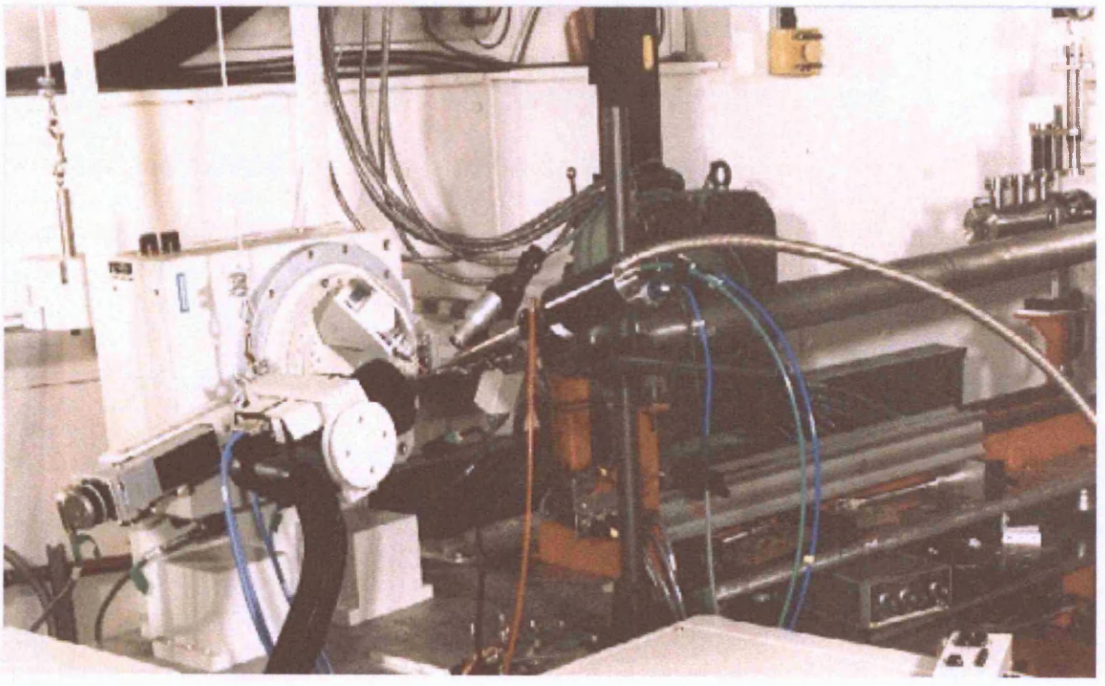

Figure 2.14: Station 9.8 at the Daresbury SRS, showing the whole transition tube, diffractometer and cryostream.

In a typical data collection the primary step includes the collection of an orientation matrix of the sample to give the orientation of the crystal with respect to the

beam. It also provides unit cell dimensions, allows checking if the crystal is twinned, and ensures that the crystal diffracts enough to produce data which will be of high enough quality to extract the crystal structure from.

2.3 Other Experimental Tools

X-ray diffraction experiments were the primary tools to analyse the materials studied. Nuclear magnetic resonance spectroscopy, thermo-gravimetric analysis (TGA), scanning electron microscopy (SEM) studies and chemical analysis were performed to complement the results obtained through X-ray experiments.

2.3.1 Nuclear Magnetic Resonance Spectroscopy

Nuclear magnetic resonance spectroscopy takes advantage of the magnetic properties of atomic nuclei. Only nuclei that have a spin quantum number, $I > 0$ exhibit the NMR phenomenon. Under the influence of an external magnetic field a nucleus, which has magnetic properties, aligns itself with the external field.

Peaks produced in a solid-state NMR spectrum are very broad, which arises from the chemical shift anisotropy. In a powder sample the absorption of all possible orientations of the nuclei with respect to the external magnetic field will be observed simultaneously, giving a characteristic broad absorption or 'anisotropy' pattern. Averaging the isotropic value may narrow the broad peaks, which is carried out by spinning the sample at an angle of $54^{o}44'$, the so-called magic angle (13).

Decoupled solid-state magnetic angle spinning (MAS) NMR was acquired for ^{27}Al to gain further insight into the co-ordination chemistry of the aluminium. ^{27}Al MAS NMR spectra were recorded on a Bruker MSL-300 spectrometer at 78.2 MHz. All

measurements were carried out at room temperature, with $Al(H_2O)_6^{3+}$ being used as external standard.

2.3.2 Thermo-Gravimetric Analysis

Thermo-gravimetric analysis (TGA) and differential thermal analysis (DTA) were performed on a PU 4K (Rigaku) equipped with a quadrupole mass spectrometer (MS, Anelva M-QA200TS). The thermo-gravimetric analysis was performed under an argon / oxygen (9:1) atmosphere with a heating rate of 5 K / min between 22°C and 800°C.

2.3.3 Scanning Electron Microscopy Studies

The phase purity and the morphology of different crystal structures were studied by scanning electron microscopy employing a Jeol JSM-630 IF.

2.3.4 Chemical Analysis: Energy Dispersive Analysis of X-rays (EDAX)

The chemical composition of samples was studied using an EDAX Philips XL 30 ESEM (Environmental Scanning Electron Microscope). The EDAX studies were conducted to confirm the elemental ratio of the novel material synthesised obtained through the single crystal diffraction experiments by measuring the fluorescence emitted by different elements.

2.4 Computational Techniques

2.4.1 Introduction

Together with the experimental studies of AlPO materials, complementary computational methods were employed. In particular, Monte Carlo docking calculations were used to locate SDAs in microporous aluminophosphate frameworks employing the Accelrys Cerius2 software suite (1) and molecular dynamics calculations to gain insight into the motional behaviour of organic molecules within AlPOs using Accelrys' Materials Studio (2).

2.4.2 Monte Carlo Calculations

A Monte Carlo simulation normally generates configurations of a system through random sampling by using the Boltzmann weighted acceptance procedure. The potential energy of each configuration in the system is calculated, accepting some and rejecting others based on their energetic difference and the temperature through the use of the Boltzman factor.

Monte Carlo simulations are performed under various ensembles, most commonly taking a constant number of particles, temperature and volume (NVT), which is known as the canonical ensemble.

Monte Carlo simulations normally calculate energies using a forcefield or an interatomic potential which expresses all the energies present in a system by calculating the energy of the lattice and the molecules present in the system.

Focefields:

- **Parameters describing various contributions to the total energy:**

  $E_{total} = E_{stretch} + E_{bend} + E_{torsion} + E_{non\text{-}bond}$

- **Bond-stretch term,** $E_{stretch} = k\,(r - r_o)^2$,

  where k = spring constant in Hooke's Law

- **Three Body Term,** $E_{bend} = k\,(\theta - \theta_o)^2$

- **Torsion Terms,** $E_{torsion} = V_n\,(1 + s \cos n\omega)$

- **Non bonded interactions,** $E_{non\text{-}bond}$

  - **Van der Waals:** $E_{vdW} = A / r^{12} - B / r^6$

- **Coulombic:** $E_c = q1*q2 / r$,

  where q = charge of atom

Figure 2.15: Forcefield energies (43).

The calculations were run employing the forcefield cvff_300_1.01. The size of the super-cell was 2 x 2 x 2 unit cells with a cut-off of 8 Å using 100,000 steps.

2.4.3 Molecular Dynamics Calculations

Molecular dynamics calculations (MD) supply information on the trajectories of a molecule as it moves around depending on temperature and time based on Newton's laws of motion. MD calculations were employed to gain insight into the motional behaviour of different organic molecules within microporous frameworks. The interaction between framework and organic species were calculated employing a forcefield as outlined earlier. The forcefield used for these calculations was again the zeolite specific forcefield cvff_300_1.01. The MD calculations were run with the NVT ensemble employing a time step of 0.001ps and running for 100,000 steps, with the size of the super-cell being 2 x 2 x 2 unit cells. The organic molecule was energy minimised before the molecular dynamics calculations were run.

2.5 References

1. Accelrys, *Cerius2*.
2. Accelrys, *Materials Studio 3.1*.
3. J. Kepler, *'The Six-Cornered Snowflake'*, Clarendon Press, Oxford University Press, 1966.
4. C. Hammond, *'The Basics of Crystallography and Diffraction'*, Oxford University Press, 1997.
5. *The Ninth BCA/CCG Intensive Teaching School in X-Ray Structure Analysis-Course Notes*, 2005.
6. G. Burns and A. M. Glazer, *'Space Groups for Solid State Scientists'*, Vol. Second edition, Academic Press Inc., 1990.
7. *'International Tables for Crystallography', Volume A*, D. Reidel Publishing Company, 1984.
8. C. Hammond, *'An Introduction to Crystallography'*, Oxford University Press, 1972.
9. L. Smart and E. Moore, *'Solid State Chemistry'*, Chapman & Hall, 1992.
10. S. F. A. Kettle, *'Physical Inorganic Chemistry - A Coordination Chemistry Approach'*, Oxford University Press, 1998.
11. W. Clegg, A. J. Blake, R. O. Gould, and P. Main, *'Crystal Structure Analysis Principles and Practice'*,, Oxford University Press, 2001.
12. C. K. Lee, A. M. Coats, and A. R. West, *Powder Diffraction, 12*, 245 (1997).
13. A. K. Cheetham and P. Day, *'Solid State Chemistry: Techniques'*, Vol. Oxford University Press, 1987.

14. http://www.luc.edu/faculty/spavko1/X-ray/pdf/ewald.pdf#search=%22ewald%20sphere%22.

15. C. Hammond, *'The Basics of Crystallography and Diffraction'*, Oxford University Press, 2001.

16. W. M. Meier and D. H. Olson, *Atlas of Zeolite Structure Types*, Butterworth-Heinemann, 1996.

17. L. B. McCusker, R. B. Von Dreele, D. E. Cox, D. Louer, and P. Scardi, *Journal of Applied Crystallography*, *32*, 36 (1999).

18. A. N. Fitch, *Nuclear Instruments and Methods in Physics Research Section B: Beam Interactions with Materials and Atoms*, *97*, 63 (1995).

19. G. Sankar, J. M. Thomas, and C. R. A. Catlow, *Topics in Catalysis*, *10*, 255 (2000).

20. http://www.synchrotron.vic.gov.au.

21. http://www.srs.ac.uk/srs/.

22. http://pd.cryst.bbk.ac.uk/pd/index03.htm.

23. H. V. Koningsveld, H. V. Bekkum, and J. C. Jansen, *ACTA Crystallographica*, *B43*, 127 (1987).

24. A. Simmen, L. B. McCusker, C. Baerlocher, and W. M. Meier, *Zeolites*, *11*, 654 (1991).

25. B. H. Toby, N. Khosrovani, C. D. Dartt, M. E. Davis, and J. B. Parise, *Microporous and Mesoporous Materials*, *39*, 77 (2000).

26. Z. A. Kaszkur, R. H. Jones, J. W. Couves, D. Waller, C. R. A. Catlow, and J. M. Thomas, *Journal of Physics and Chemistry of Solids*, *52*, 1219 (1991).

27. E. Dooryhee, G. N. Graeves, A. T. Steel, R. P. Townsend, S. W. Carr, J. M. Thomas, and C. R. A. Catlow, *Faraday Discussions*, *89*, 119 (1990).

28. A. R. George, C. R. A. Catlow, and J. M. Thomas, *Catalysis Letter*, *8*, 193 (1991).

29. C. Lamberti, C. Prestipino, S. Bordiga, A. N. Fitch, and G. L. Marra, *Nuclear Instruments & Methods in Physics Research Section B-Beam Interactions with Materials and Atoms*, *200*, 155 (2003).

30. R. Millini, G. Perego, D. Berti, W. O. Parker, A. Carati, and G. Bellussi, *Microporous and Mesoporous Materials*, *35-6*, 387 (2000).

31. H. M. Rietveld, *Journal of Applied Crystallography*, *2*, 65 (1968).

32. R. A. Joung, *'The Rietveld Method'*, Oxford Science Publications, 1993.

33. A. Larson and R. B. Von Dreele, *Los Alamos Report No. LA-UR-86-748* (1986).

34. R. J. Cernik, W. Clegg, C. R. A. Catlow, G. Bushnell-Wye, J. V. Flaherty, G. N. Greaves, I. Burrows, D. J. Taylor, S. J. Teat, and M. Hamichi, *Journal of Synchrotron Radiation*, *4*, 279 (1997).

35. M. M. Harding and B. M. Kariuki, *Acta Cryst*, *C50*, 852 (1994).

36. G. Muncaster, G. Sankar, C. R. A. Catlow, J. M. Thomas, R. G. Bell, P. A. Wright, S. Coles, S. J. Teat, W. Clegg, and W. Reeve, *Chemistry of Materials*, *11*, 158 (1999).

37. G. H. Stout and L. H. Jensen, *'X-Ray Structure Determination - A Practical Guide'*, Macmillan, 1968.

38. A. R. West, *'Solid State Chemistry and its Applications'*, Wiley, New York, 1984.

39. G. M. Sheldrick, Z. Dauter, K. S. Wilson, H. Hope, and L. C. Sieker, *Acta Cryst, D49*, 18 (1993).

40. G. M. Sheldrick, *Acta Cryst, A46*, 467 (1990).

41. L. J. Farrugia, *Journal of Appied Crystallography, 32*, 837 (1999).

42. D. J. Watkin, C. K. Prout, and P. M. Lilley, Chemical Crystallography Laboratory, University of Oxford, Oxford.

43. N. A. Ramsahye, *http://www.ri.ac.uk/dfrl/N.Ramsahye*.

Chapter 3

Location of Organic Structure Directing Agents within the One-Dimensional Aluminophosphate Topology AlPO-5

3.1 Summary

It has been shown in the past, that the molecule methyldicyclohexylamine (MCHA) is the most specific structure directing agent (SDA) for the formation of the AlPO-5 topology. It would be of great importance to establish the reasons behind this molecule's ability to form only one specific framework, as the role of templating agents in the formation of microporous aluminophosphates still holds many questions.

Combining different experimental as well as computational methods it was possible to locate the template within the framework and gain insight into the template's behaviour within the AlPO-5 structure. Comparing the results obtained from the MCHA synthesised samples with other AlPO-5 samples templated with different organic amines it was possible to deduce the reasons for MCHA's high specificity in forming the AlPO-5 structure.

3.2 Introduction

Within the one-dimensional channel $AlPO_4$-structures, AlPO-5 (International Zeolite Association structure code AFI - made up of 12, 6 and 4 member rings) can be synthesised using several different structure directing agents (SDAs) such as triethylamine (TEA) (1), tripropylamine (TPA) (2), ethyldicyclohexylamine (ECHA) or tetrapropylammonium hydroxide (3) and is the most readily formed framework in the aluminophosphate family. As discussed in chapter 1, the AlPO-5 topology is very interesting as a large percentage of heteroatoms (*ca.* 10%) can be incorporated into the framework, giving rise to redox chemistry and Brønsted acidity, which allows such materials to be used in catalysis (4, 5). Furthermore, AFI shows a high thermal stability during catalysis and does not collapse upon calcination, showing complete integrity (6-8). As AlPO-5 falls into the large pore aluminophosphate category, it can be used in a wide variety of catalytic reactions as it can process both small and large size organic molecules (9, 10).

However, most SDAs only form AFI under very specific conditions or as a side-product. Methyldicyclohexylamine (MCHA) on the other hand, forms phase pure AFI under several different conditions and allows the incorporation of several different heteroatoms such as Zn, Co, Mg, Cr, Fe or Mn into the framework (11). It is therefore of general interest to establish the position of the template within the channel framework, which may shed light on the reasons behind MCHA's high specificity in the formation of the AFI topology and give further insight into the role templates play during the synthesis of microporous aluminophosphates (11).

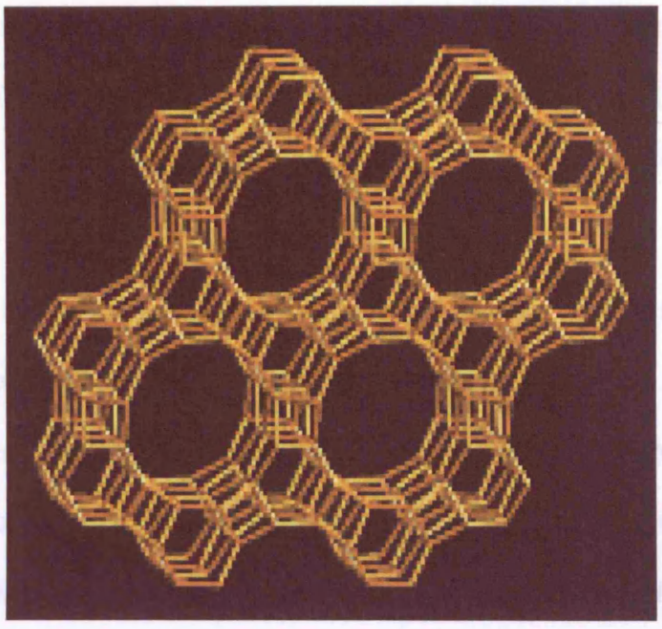

Figure 3.1: AlPO-5 (AFI) topology with 4, 6 and 12 member rings and a pore diameter of 7.3 Å for the 12 member ring (12).

There are many different approaches, which can lead to the location of the template molecule within the parent framework. In some cases, single crystal diffraction has led to pin-pointing the positioning of the SDA (2, 3, 13-16). However single crystals of sufficient size and crystallinity are often not easily obtained in hydrothermal synthesis. When a material can only be synthesised yielding a powder, high resolution synchrotron powder XRD (HRXRD) can be employed to locate extra-framework species (17). Neutron diffraction is another useful experimental tool (18) when trying to locate the SDA molecules. Neutrons, unlike X-rays interact with the nucleus of the atom and not the electron cloud surrounding the atom. This allows the refinement of hydrogen atoms, something that usually cannot be achieved with X-rays. However, as hydrogen has extensive incoherent scattering, giving rise to a high background, it is often

necessary to replace all the hydrogen by deuterium atoms. This can bear a problem in some MeAPO materials when trying to replace the OH-acid sites with OD-groups, as the presence of water can lead to structural collapse (19).

Combined X-ray diffraction and theoretical calculations were hence chosen to gain a better insight into the MCHA's location and interaction within the AFI topology. Furthermore, different SDAs were re-absorbed into calcined CoAPO-5 samples, mimicking computational docking calculations in an experimental setting, to gain further insight into framework-template interactions. The overall aim of this study was to obtain a thorough picture of the template-framework interactions within microporous aluminophosphates, helping us to synthesis novel aluminophosphates.

3.3 Experimental Details

3.3.1 Synthesis of AlPO-5

CoAPO-5 was synthesized by adding cobalt acetate tetrahydrate after the addition of aluminium hydroxide to an aqueous solution of phosphoric acid. After rigorous stirring for *ca.* 10 minutes the gel attains homogeneity and the organic template, methyldicyclohexylamine (MCHA) or triethylamine (TEA), was added to form the final gel. The gel compositions for the two materials were:

0.1 Co : 0.9 Al : 1.0 P : 0.8 MCHA : 30 H_2O and

0.1 Co : 0.9 Al : 1.0 P : 0.8 TEA : 30 H_2O

respectively.

The gel composition for the pure AlPO-5 synthesis was 1.0 Al : 1.0 P : 0.8 SDA : 30 H_2O, with the SDAs being MCHA and ECHA.

After stirring the gel for *ca.* 1 hour, it was transferred to a Teflon lined autoclave with a volume of 200 ml, which was heated in a pre-heated oven at 423 K for *ca.* 16 hours (11).

3.3.2 Absorption of Organic Molecules

The CoAPO-5 samples obtained hydrothermally were calcined in air at 535°C, with a ramp-rate of 5 K / min and subsequently keeping the furnace at this temperature

for 16 hours. The CoAPO-5 sample changed from a blue colour to a green colour (believed to be due to some Co^{2+} centres being oxidised to Co^{3+}(20)). The material was placed in a glass tube, fitted with a frit and heated in a flow of hydrogen to reduce the cobalt back to a +2 oxidation state (8). See Figure 3.2 for the experimental set-up.

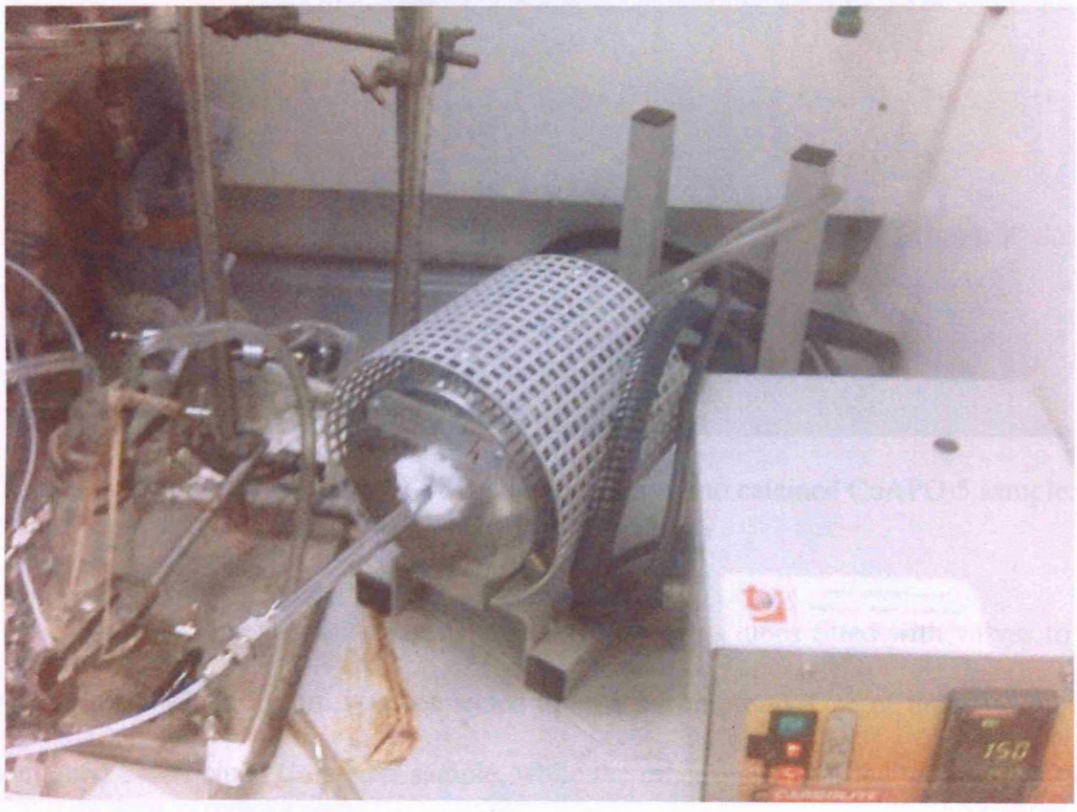

Figure 3.2: Experimental set-up for reduction of cobalt containing AlPO in hydrogen after calcination.

Having collected the material after treating it with hydrogen at elevated temperatures, three different SDAs (MCHA, ECHA and TEA) were re-absorbed in vacuum into the calcined samples (see experimental set-up in Figure 3.3).

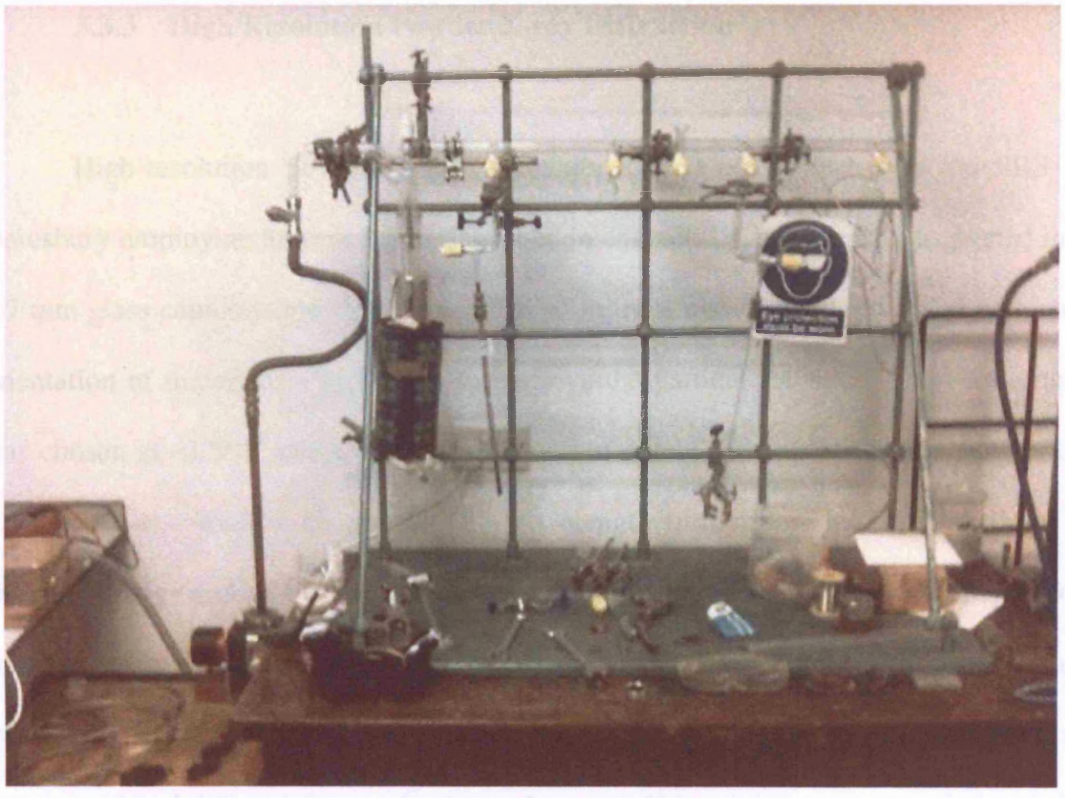

Figure 3.3: Experimental set-up for SDA re-absorption into calcined CoAPO-5 sample.

The experiment was set-up by attaching two glass tubes fitted with valves to a vacuum line, which in turn was connected to a diffusion pump. One of the glass tubes contained the calcined CoAPO-5 sample, while the other one was filled with one of the SDAs (MCHA, ECHA or TEA), which was to be absorbed into the microporous material. The system was put under vacuum of 6 x 10^{-6} mbar. Subsequently the valve between vacuum line and vacuum pump was closed. After opening the valve separating the SDA from the vacuum, the system was filled with organic vapour, due to the vacuum causing a lowering in the SDA's boiling point. After having left the CoAPO-5 exposed to the organic vapour for 90 minutes, the samples were collected and sealed in glass capillaries with a 0.7 mm diameter.

3.3.3 High Resolution Powder X-ray Diffraction

High-resolution powder X-ray diffraction data were collected at the SRS in Daresbury employing Station 2.3 as described in chapter 2. The sample was placed in a 0.7 mm glass capillary and data were recorded in transmission mode to avoid preferred orientation of the crystals as well as to improve the particle statistics. The wavelength was chosen at ~1.3 Å which is the wavelength to obtain the maximum flux for station 2.3 as was described in chapter 2. This wavelength furthermore avoids both the Co-absorption edge and an increased absorption from the capillary which would have been encountered at a longer wavelength. Data were collected from 4 – 75° 2θ with a step increment of 0.01° and with the time for each step of 2 seconds. 2 sets of patterns between 4° and 40° and 5 sets of patterns between 40° and 75° were recorded and the data summed. At high angles there is a higher peak density and hence a lower degree of separation, which means that more data sets were recorded between 40° and 75° 2θ to gather a higher quality overall XRD pattern.

3.3.4 Single Crystal X-ray Diffraction

Single crystal data were recorded on Station 9.8 at the SRS in Daresbury. The crystal was mounted on a glass fibre using Fomblin polyether to keep the crystal fixed during data collection. Station 9.8 is a high flux, tuneable, monochromatic, single crystal diffraction station employing a D8 diffractometer and utilising a Bruker-Nonius APEXII CCD area detector and a silicon (111) monochromator. A whole hemisphere of data was collected with a 10s / frame step size and a 0.1° step increment.

3.4 Results

After extracting the solids by the conventional filtering and drying procedures, they were checked for phase purity by X-ray diffraction technique employing a Siemens D4 system (see Figure 3.4).

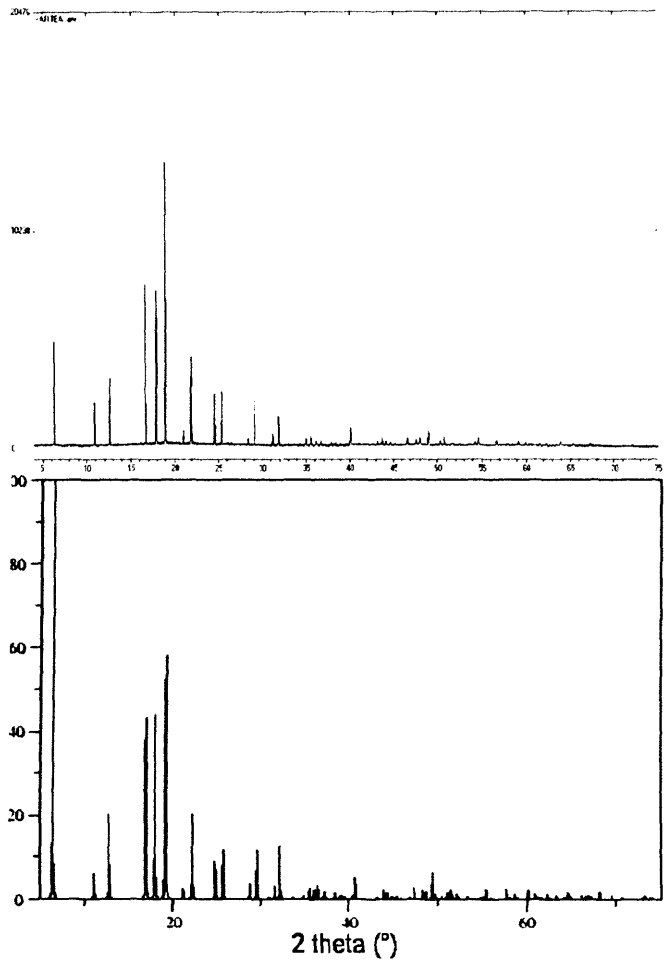

Figure 3.4: X-Ray diffraction pattern of CoAPO-5 (top) and pattern as shown in the Atlas of Zeolite Structure Types (bottom) (21).

Subsequently, SEM images were obtained of the samples using a Jeol JSM-630 IF scanning microscope showing a phase pure sample, with all the crystallites having the same morphology (see Figure 3.5). The scale and the current at which the image was taken are given on the image itself.

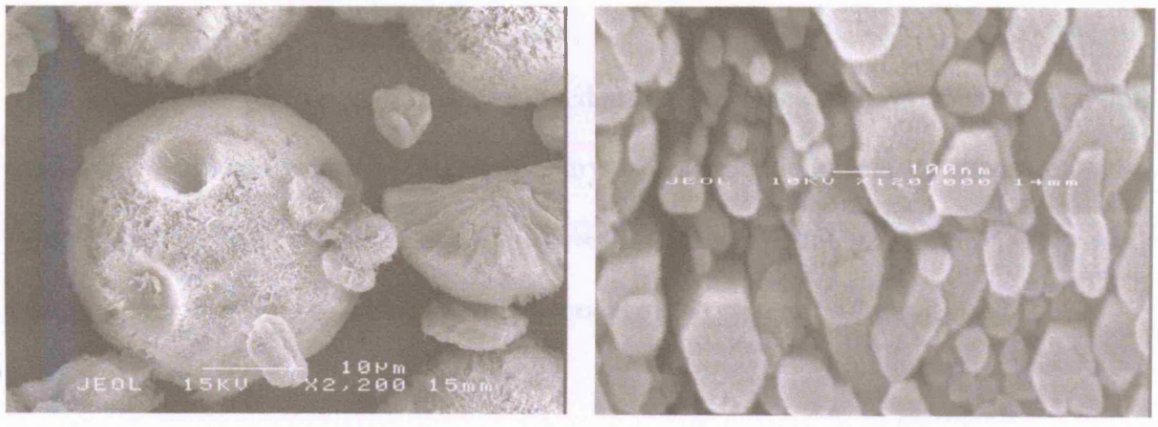

Figure 3.5: SEM image of CoAPO-5 sample, showing that the material crystallizes in hexagonal needles that agglomerate into spheres.

3.4.1 Template Location in the AlPO-5 Topology

3.4.1.1 X-Ray Diffraction Studies

3.4.1.1.1 CoAPO-5 Synthesised With MCHA

The phase pure sample was first examined using the single crystal X-ray diffraction technique employing station 9.8 at Daresbury as described in chapter 2. However as the single crystals were of inferior quality (R_{int} = 0.4322) and possibly twinned, the recorded data could not be used to gain an accurate model of the system.

Thus, high resolution X-ray powder diffraction (3, 14, 22-25) was employed to gain information on the template's position within the AlPO-5 framework. Computational methods, which have been used on previous systems to locate organic molecules (26-30) were used subsequently to gain further insight into the configuration of the template within the AFI channel system.

The data collected at the SRS in Daresbury were examined by Rietveld methodology as described in chapter 2 using the GSAS EXPGUI software (31, 32). The space group *P 6 c c*, as reported by Chao *et al.* (33) was chosen to analyse the pattern. Firstly, the data were analysed employing only the high angle part of the pattern (38° – 75° 2θ), fitting the known framework atoms only as the organic SDA has little effect on this part of the pattern (34). Manual background subtraction was employed as a better fit can be obtained with this method. Bond constraints were used, setting P-O bonds at 1.50

Å and Al-O bonds at 1.74 Å with a 5% deviation allowed, ensuring sensible bond lengths after refinement. A pseudo-Voigt function was used to fit the peak shape, as in general it tends to yield a good fit to the data collected when employing synchrotron radiation. Having obtained a good fit at high angle (see inset in Figure 3.6), the whole data range was examined. The match between calculated and experimental data was extremely poor at low angle (see Figure 3.6), which is expected, as the template molecules had not been included in the model yet and this region is affected most by the template molecule. The refinement yielded an overall poor fit at this point with wRp = 20.7% and Rp = 13.9%.

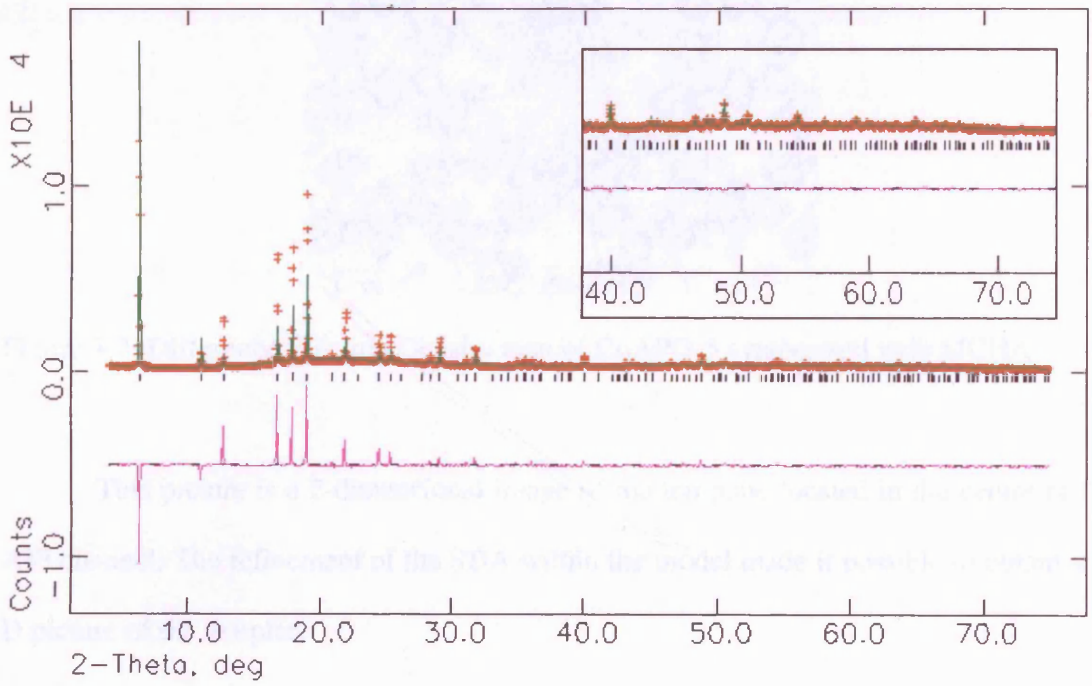

Figure 3.6: Experimental (red), simulated (green), and difference (pink) profiles for the powder XRD pattern of CoAPO-5 synthesised with MCHA before template location (wRp = 20.7% and Rp = 13.9%) recorded at 1.298 Å. The inset is showing the high angle data with a good fit as the template mainly exerts an influence on the Bragg peaks at low angle.

After having fitted the data at high angle, the difference electron density Fourier (DELF) map was obtained. Extra high electron density could be located from the DELF map, which is seen centred in the middle of the channel with six spheres positioned around the central high electron density medium (see Figure 3.7).

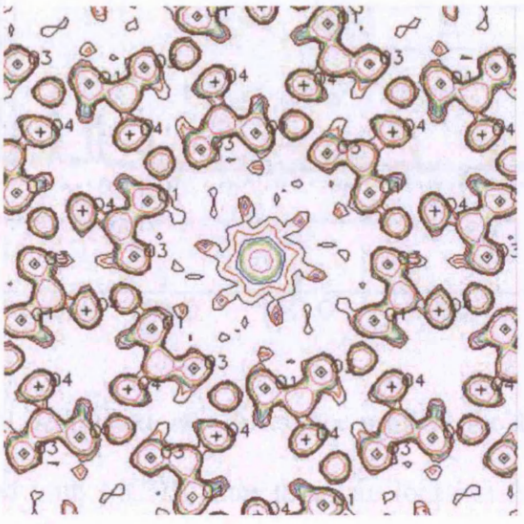

Figure 3.7: Difference Electron Density map of CoAPO-5 synthesised with MCHA.

This picture is a 2-dimensional image of the template located in the centre of the AFI channel. The refinement of the SDA within the model made it possible to obtain a 3-D picture of the template.

Before continuing the refinement the scale factor was fixed and only further refined once the model had become more complete. Having added the template atoms to the GSAS refinement, the fit between the calculated and the experimental patterns improved drastically, leading to an improvement of wRp value from 20.72% to 5.50% (see Figure 3.8).

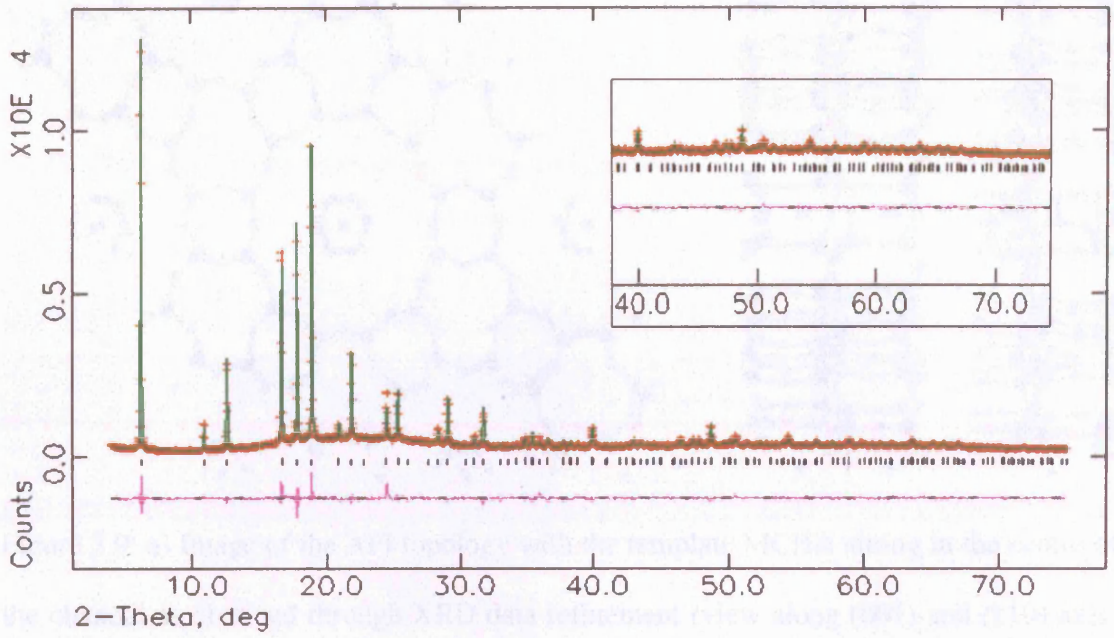

Figure 3.8: Experimental, simulated, and difference profiles for the powder XRD pattern of CoAPO-5 synthesised with MCHA after template location (wRp = 5.5% and Rp = 4.2%) recorded at 1.298 Å.

Once the fractional co-ordinates were deduced from the Rietveld analysis, the results were visualised by using the PowderCell 2.4 software (35) (see Figure 3.9).

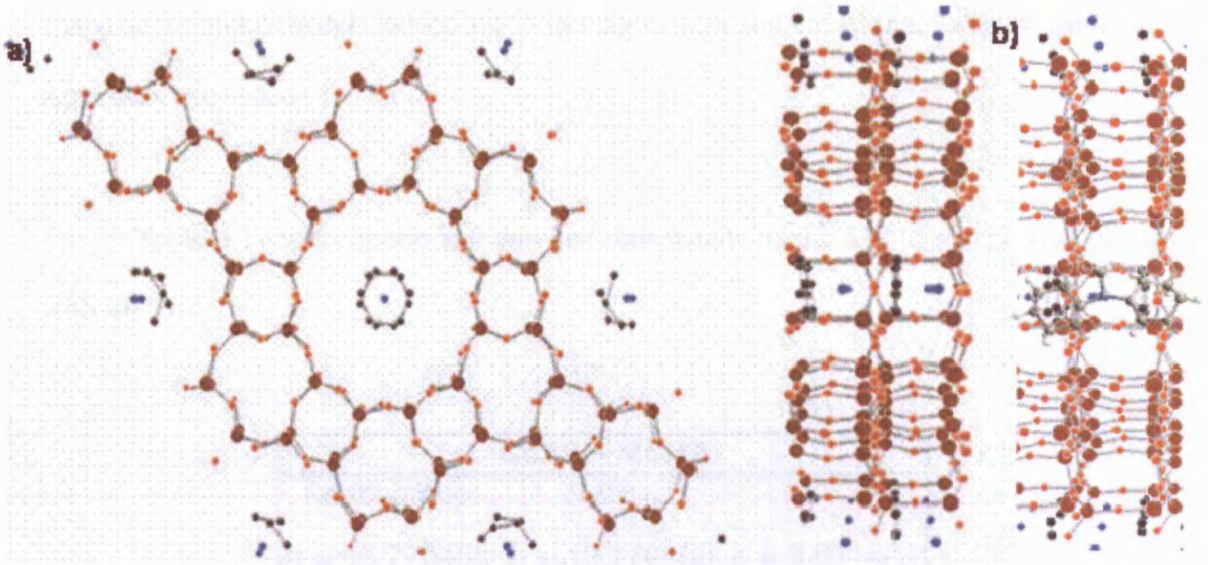

Figure 3.9: a) Image of the AFI topology with the template MCHA sitting in the centre of the channel as obtained through XRD data refinement (view along (001) and (110) axis) and b) with MCHA in its actual configuration superimposed.

It can be seen that the conformation of the SDA is not in the expected arrangement, i.e. the cyclohexane rings are neither in the boat nor in the chair conformation. Instead they are in a rigid planar formation, resembling a benzene ring, which can be explained by the fact that the MCHA molecule is sitting in several different positions within the channel system. The unit-cell parameters and symmetry can be seen in Table 3.1. Tables 3.2 and 3.3 show a list of selected bond lengths and angles; Table 3.4 gives the atom co-ordinates, thermal displacement factors and occupancy obtained through the Rietveld refinement with the estimated standard deviations (e.s.d.s) given in brackets. The e.s.d.s are calculated assuming that the counting statistics are the only source of error. Systematic errors (e.g. arising from an inadequate background, peak-

shape or structural model), which are in fact significant sources of inaccuracies, cannot be accurately estimated.

Table 3.1: Space group and unit cell dimensions of the AFI topology synthesised with MCHA.

CoAFI - MCHA		
Spacegroup:	*P 6 c c*	
a = 13.7704(2)	*b* = 13.7704(2)	*c* = 8.3714(1)
α = 90°	*β* = 90°	*γ* = 120°

Table 3.2: Selected bond lengths obtained from the Rietveld refinement of the AFI system synthesised with MCHA[1].

CoAFI MCHA	
Vector	Length
P1_O1	1.5179(5)
P1_O2	1.4680(6)
P1_O3	1.5422(5)
P1_O4	1.5071(5)
Al2_O1	1.7491(7)
Al2_O2	1.7351(7)
Al2_O3	1.7949(7)
Al2_O4	1.7673(7)
C1_C1	1.3744(11)

[1] All bond restraints in all Rietveld refinements performed in this thesis have a weighting of 1.0.

Table 3.3: Selected bond angles obtained from the Rietveld refinement of the AFI system synthesised with MCHA[2].

CoAFI MCHA	
Angle	**Degrees**
O1_P1_O2	95.456(4)
O1_P1_O3	96.952(5)
O1_P1_O4	124.734(5)
O2_P1_O3	99.929(4)
O2_P1_O4	104.177(5)
O3_P1_O4	129.619(5)
O1_Al2_O2	103.004(5)
O1_Al2_O3	106.492(6)
O1_Al2_O4	121.044(6)
O2_Al2_O3	93.704(5)
O2_Al2_O4	102.908(6)
O3_Al2_O4	123.442(6)
C1_C1_C1	120.000
P1_O1_AL1	145.258(5)

Table 3.4: Atom co-ordinates, thermal displacement factors and occupancy obtained from the Rietveld refinement of the AFI system synthesised with MCHA.

CoAFI - MCHA					
Atom Type	***x***	***y***	***z***	***U(iso)***	***Occup***
P1	0.4401(6)	0.3238(5)	0.0663(7)	0.0157(6)	1.000
Al2	0.4648(4)	0.3415(5)	0.4438(8)	0.0103(5)	0.900
Co1	0.4648(4)	0.3415(5)	0.4438(8)	0.0103(5)	0.100
O1	0.4156(3)	0.2160(6)	-0.0171(6)	0.0190(5)	1.000
O2	0.4666(5)	0.3471(7)	0.2367(5)	0.0167(6)	1.000
O3	0.3616(4)	0.3461(5)	-0.0396(6)	0.0120(4)	1.000
O4	0.5549(3)	0.3972(5)	-0.0044(5)	0.021(5)	1.000
C1	0.0520(11)	0.9372(11)	0.3763(12)	0.058(10)	1.000
N1	0.0000	0.0000	0.1280(11)	0.061(11)	0.217(9)

[2] No restraints were applied to the bond angles for any of the systems.

3.4.1.2 Pure AlPO-5 synthesised with MCHA and ECHA

MCHA was also located in the pure AlPO-5 employing high resolution powder diffraction. The template was found in the identical position as that found within the CoAPO version (see Figure 3.10).

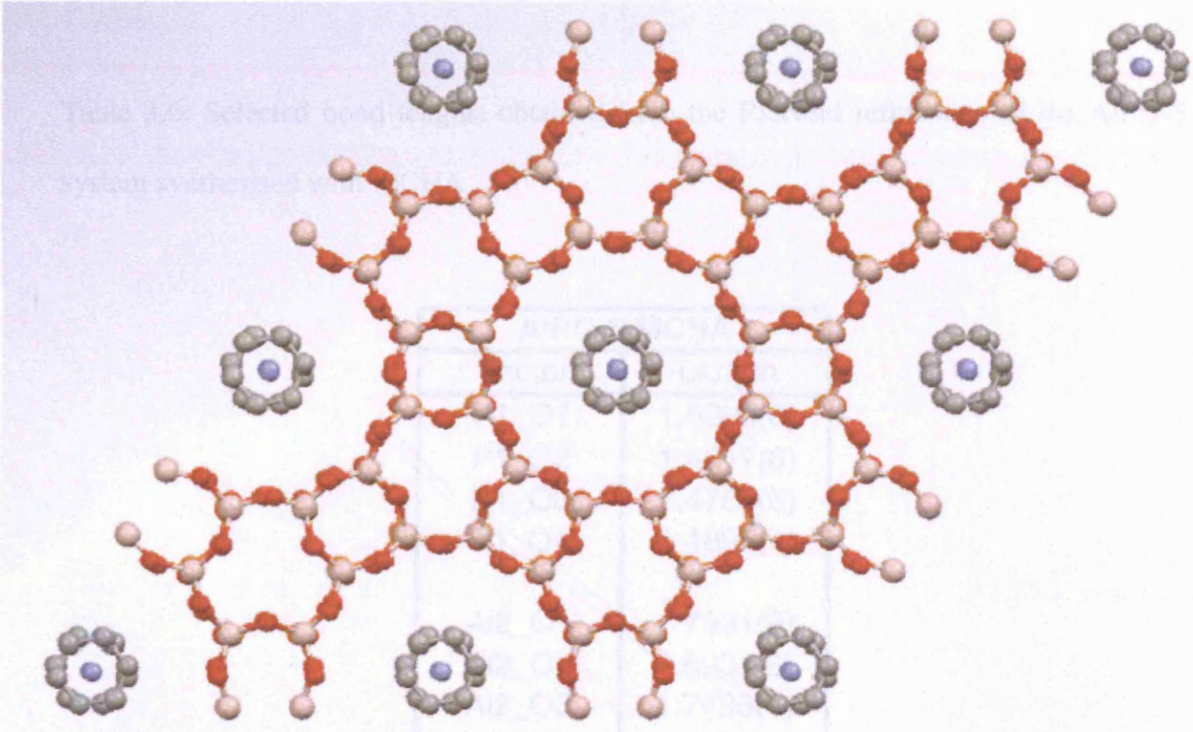

Figure 3.10: Image of the pure AlPO-5 framework with the template MCHA (C1 grey and N1 blue) sitting in the centre of the channel obtained through the refined XRD data (view along (001) axis).

The space group, unit cell dimensions, bond lengths and bond angles as well as the atomic parameters are give in Tables 3.5 to 3.8.

Table 3.5: Space group and unit cell dimensions of the AlPO-5 topology synthesised with MCHA.

AlPO-5 MCHA		
Spacegroup:	*P 6 c c*	
a = 13.7030(2)	b = 13.7030(2)	c = 8.4045(1)
α = 90°	β = 90°	γ = 120°

Table 3.6: Selected bond lengths obtained from the Rietveld refinement of the AlPO-5 system synthesised with MCHA.

AlPO-5 MCHA	
Vector	Length
P1_O1	1.5390(6)
P1_O2	1.4617(6)
P1_O3	1.4754(6)
P1_O4	1.4895(4)
Al2_O1	1.7961(8)
Al2_O2	1.6931(6)
Al2_O3	1.7493(7)
Al2_O4	1.7135(7)
C1_C1	1.3974(12)

Table 3.7: Selected bond angles obtained from the Rietveld refinement of the AlPO-5 system synthesised with MCHA.

AlPO-5 MCHA	
Angle	**Degrees**
O1_P1_O2	96.968(6)
O1_P1_O3	95.882(5)
O1_P1_O4	113.082(7)
O2_P1_O3	105.898(6)
O2_P1_O4	114.081(5)
O3_P1_O4	125.902(6)
O1_Al2_O2	106.695(8)
O1_Al2_O3	110.678(6)
O1_Al2_O4	99.141(6)
O2_Al2_O3	103.185(5)
O2_Al2_O4	128.155(7)
O3_Al2_O4	108.526(6)
C1_C1_C1	120.000
P1_O1_Al2	149.344(6)

Table 3.8: Atom co-ordinates, thermal displacement factors and occupancy obtained from the Rietveld refinement of the AlPO-5 system synthesised with MCHA.

AlPO-5 MCHA					
Atom Type	***x***	***y***	***z***	***U(iso)***	***Occup***
P1	0.4622(4)	0.3451(4)	0.0591(4)	0.0376(6)	1.000
Al2	0.4540(4)	0.3332(4)	0.4266(6)	0.0271(5)	0.900
O1	0.4216(4)	0.2239(5)	0.0026(4)	0.0280(5)	1.000
O2	0.4342(5)	0.3185(6)	0.2272(6)	0.0272(6)	1.000
O3	0.3678(4)	0.3534(7)	-0.0194(5)	0.0285(5)	1.000
O4	0.5842(4)	0.4232(7)	0.0028(4)	0.0303(6)	1.000
C1	-0.020(10)	0.8897(11)	0.1060(11)	0.0981(10)	1.000
N1	0.0000	0.0000	0.3315(13)	0.0864(11)	0.290(9)

ECHA has been reported in the past to form the ATS framework under a specific set of conditions (36). To form this structure, heteroatoms (such as Zn, Co, Mg etc.) have to be present in the synthesis gel and there must be a low water concentration, as otherwise the AFI topology is formed. By locating ECHA in the AFI topology through HRXRD, insight should be gained as to whether the SDA's size is the main driving force behind ECHA's ability to form the ATS structure. The SDA was located in the framework by applying the identical approach to that taken to locate MCHA within the AFI topology. After again only fitting the framework atoms to the data, a wRp value of 26.4% and Rp of 16.7% was obtained. At low angle there is once more a very poor fit of the data (see Figure 3.11).

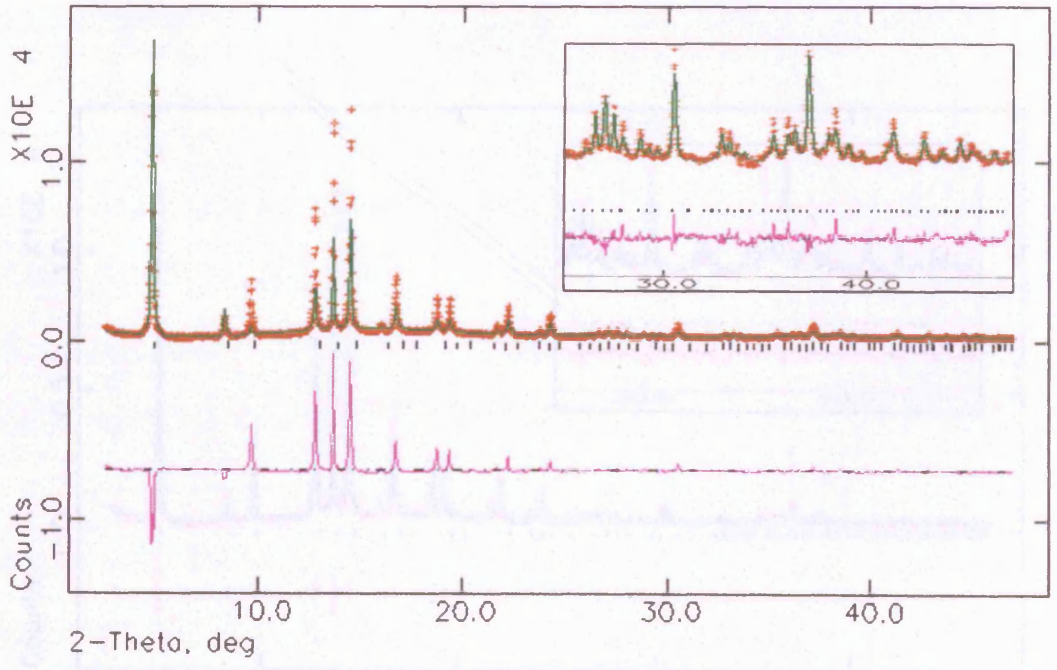

Figure 3.11: Experimental, simulated, and difference profiles for the powder XRD pattern of AlPO-5 synthesised with ECHA before template location (wRp = 26.4% and Rp = 16.7%) recorded at 1.006 Å.

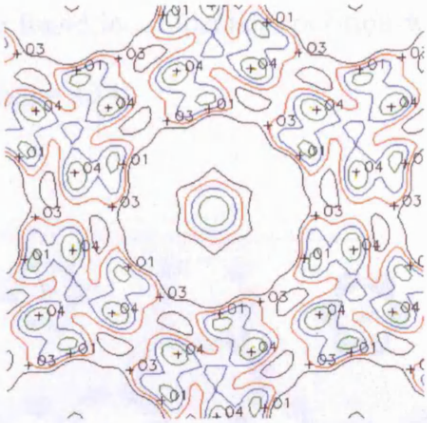

Figure 3.12: Difference Electron Density map of AlPO-5 synthesised with ECHA.

Having located the organic molecules' atoms through the DELF map (see Figure 3.12) and having entered them into the refinement, the data showed a much better fit and led to a reduction in R-values with wRp = 7.6% and Rp = 5.9% (see Figure 3.13).

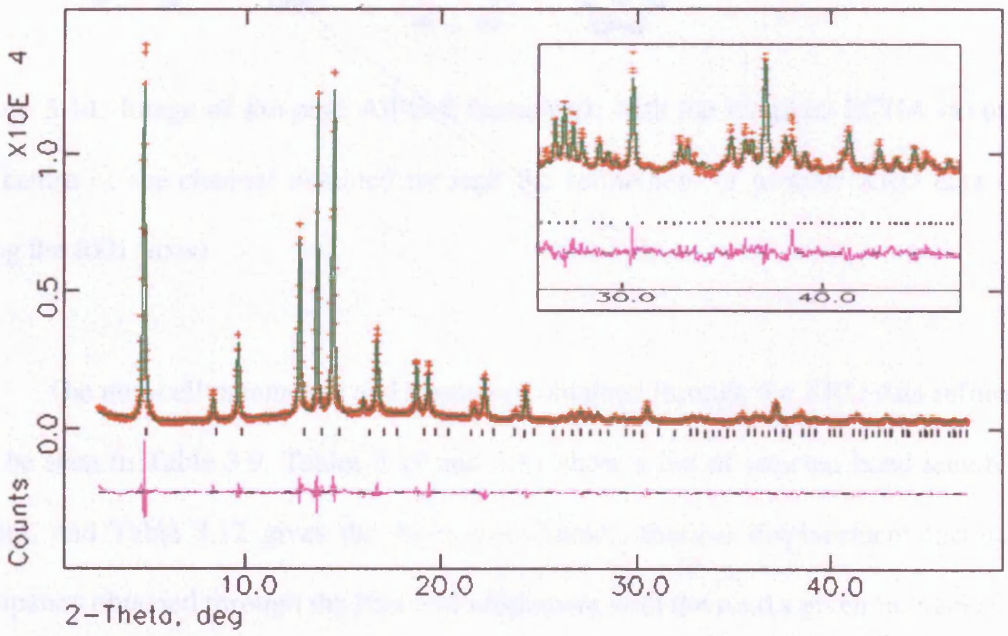

Figure 3.13: Results from Rietveld refinement of XRD pattern obtained from AlPO-5 synthesised with ECHA after template location (wRp = 7.6% and Rp = 5.9%).

ECHA is seen to be found in an identical position within the channel system of AlPO-5 as MCHA is (see Figure 3.14).

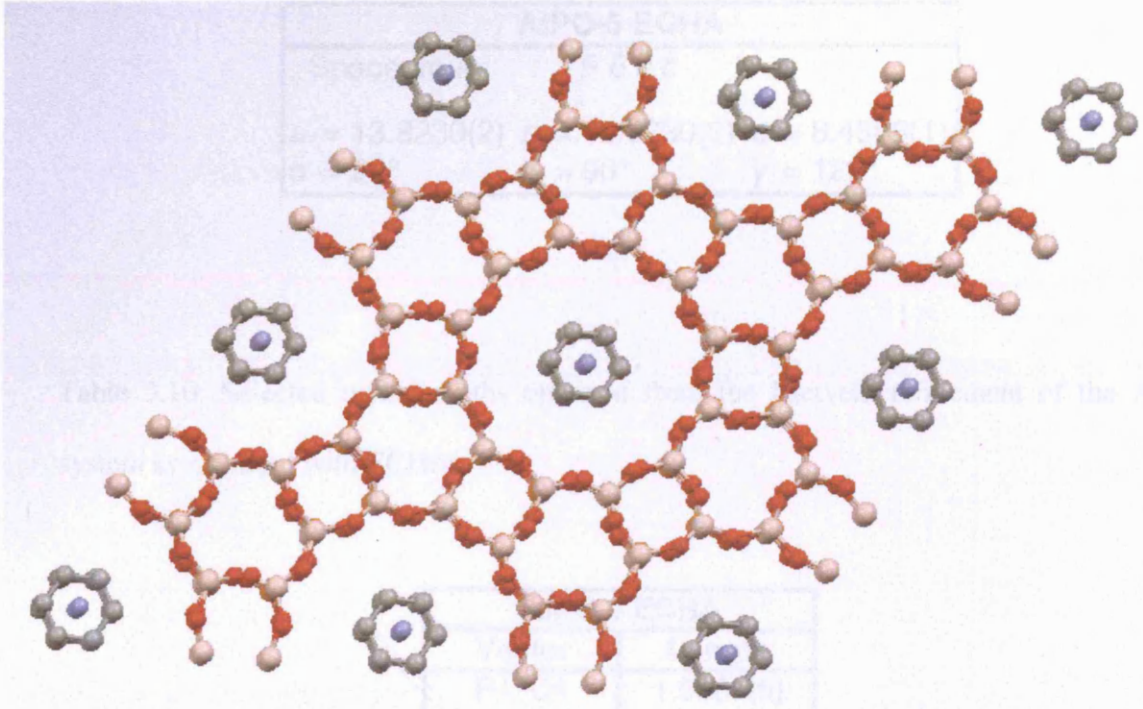

Figure 3.14: Image of the pure AlPO-5 framework with the template ECHA occupying the centre of the channel obtained through the refinement of powder XRD data (view along the (001) axis).

The unit-cell parameters and symmetry obtained through the XRD data refinement can be seen in Table 3.9. Tables 3.10 and 3.11 show a list of selected bond lengths and angles, and Table 3.12 gives the atom co-ordinates, thermal displacement factors and occupancy obtained through the Rietveld refinement with the e.s.d.s given in brackets.

Table 3.9: Space group and unit cell dimensions of the AFI topology synthesised with ECHA.

AlPO-5 ECHA		
Spacegroup:	*P 6 c c*	
a = 13.8230(2)	*b* = 13.8230(2)	*c* = 8.4588(1)
α = 90°	*β* = 90°	*γ* = 120°

Table 3.10: Selected bond lengths obtained from the Rietveld refinement of the AFI system synthesised with ECHA.

AlPO-5 ECHA	
Vector	**Length**
P1_O1	1.5301(6)
P1_O2	1.4777(5)
P1_O3	1.4907(5)
P1_O4	1.4800(6)
Al2_O1	1.7924(6)
Al2_O2	1.7098(6)
Al2_O3	1.7853(6)
Al2_O4	1.7119(5)
C1_C1	1.4999(16)

Table 3.11: Selected bond angles obtained from the Rietveld refinement of the AFI system synthesised with ECHA.

AlPO-5 ECHA	
Angle	**Degrees**
O1_P1_O2	97.353(8)
O1_P1_O3	96.741(7)
O1_P1_O4	113.566(7)
O2_P1_O3	105.957(8)
O2_P1_O4	114.507(6)
O3_P1_O4	124.241(6)
O1_Al2_O2	107.873(7)
O1_Al2_O3	110.361(6)
O1_Al2_O4	101.792(8)
O2_Al2_O3	103.143(7)
O2_Al2_O4	124.068(5)
O3_Al2_O4	109.384(7)
C1_C1_C1	120.000
P1_O1_Al2	148.562(6)

Table 3.12: Atom co-ordinates, thermal displacement factors and occupancy obtained from the Rietveld refinement of the AFI system synthesised with ECHA.

AlPO-5 ECHA					
Atom Type	***x***	***y***	***z***	***U(iso)***	***Occup***
P1	0.4622(5)	0.3434(7)	0.0568(4)	0.0376(6)	1.000
Al2	0.4545(4)	0.3324(6)	0.4277(6)	0.0271(6)	0.900
O1	0.4216(5)	0.2232(5)	0.0043(6)	0.0286(7)	1.000
O2	0.4376(4)	0.3203(5)	0.2270(5)	0.0581(5)	1.000
O3	0.3672(4)	0.3522(5)	-0.0109(4)	0.0882(7)	1.000
O4	0.5812(3)	0.4214(6)	0.0198(5)	0.0911(6)	1.000
C1	-0.0099(10)	0.8869(12)	0.1178(10)	0.0528(11)	1.000
N1	0.0000	0.0000	0.4764(12)	0.0148(13)	0.3998(11)

3.4.1.3 CoAPO-5 Synthesised With TEA

CoAPO-5 crystals of sufficient size (25 x 12.5 x 12.5 μm) and crystallinity (hexagonal needles) were obtained from the synthesis using TEA as template, to acquire single crystal data on Station 9.8 at the SRS in Daresbury (see Figure 3.15) at a wavelength of 0.6869 Å at 120 K. One crystal was selected and mounted on a glass fibre using Fomblin polyether to keep the crystal fixed during data collection.

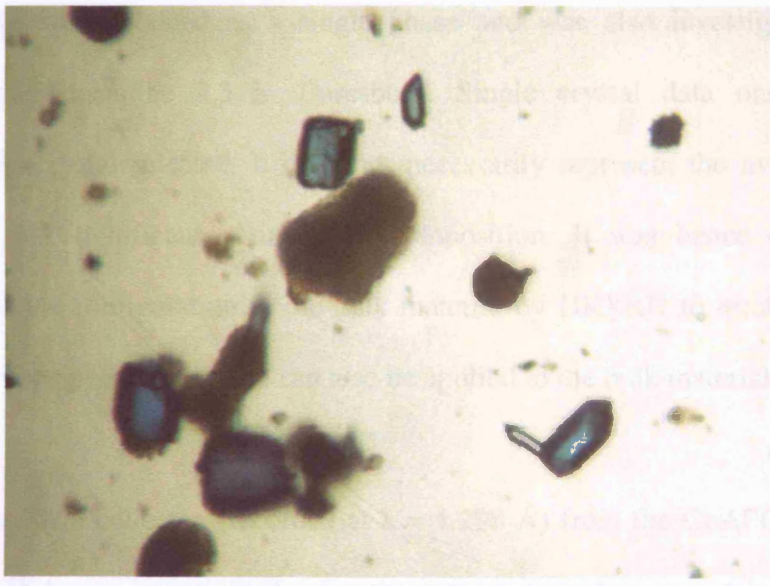

Figure 3.15: CoAPO-5 crystals synthesised with TEA with an average size of 25 x 12.5 x 12.5 μm.

After an initial short data-set collection, to ensure that the data obtained from the crystal were of sufficient quality and could be indexed, a whole hemisphere of data was collected, with a 10 s / frame step-size. After harvesting spots from different frames the unit cell dimensions and space group were assigned on the basis of systematic absences

and intensity statistics, leading to a satisfactory refinement. The structure was solved using the single crystal refinement software Crystals (37). SHELXS (38) was used to locate the framework atoms employing direct methods, with the remaining SDA atoms located through the difference electron density map. The final refinement of the structure was performed on the data having $I > 2\sigma(I)$ and included anisotropic thermal parameters for all non-hydrogen atoms. The refinement yielded good R-values, with R = 7.8% and Rw = 5.7% and no problems were flagged.

The sample was obtained as a single phase and was also investigated using HRXRD employing beamline 2.3 in Daresbury. Single crystal data only provide information on the crystal selected. It does not necessarily represent the average bulk material if there are significant variables in composition. It was hence decided to investigate the SDA's configuration in the bulk material by HRXRD to establish if the model obtained from single crystal data can also be applied to the bulk material.

The powder data collected (recorded at λ = 1.298 Å) from the CoAPO-5 sample synthesised with TEA was investigated using the same approach as was taken with the CoAPO-5 sample synthesised with MCHA. Having fitted the framework atoms only wRp = 23.1% and Rp = 16.2%, giving rise to a very poor fit at low angle but showed a good fit at high angle (see Figure 3.16).

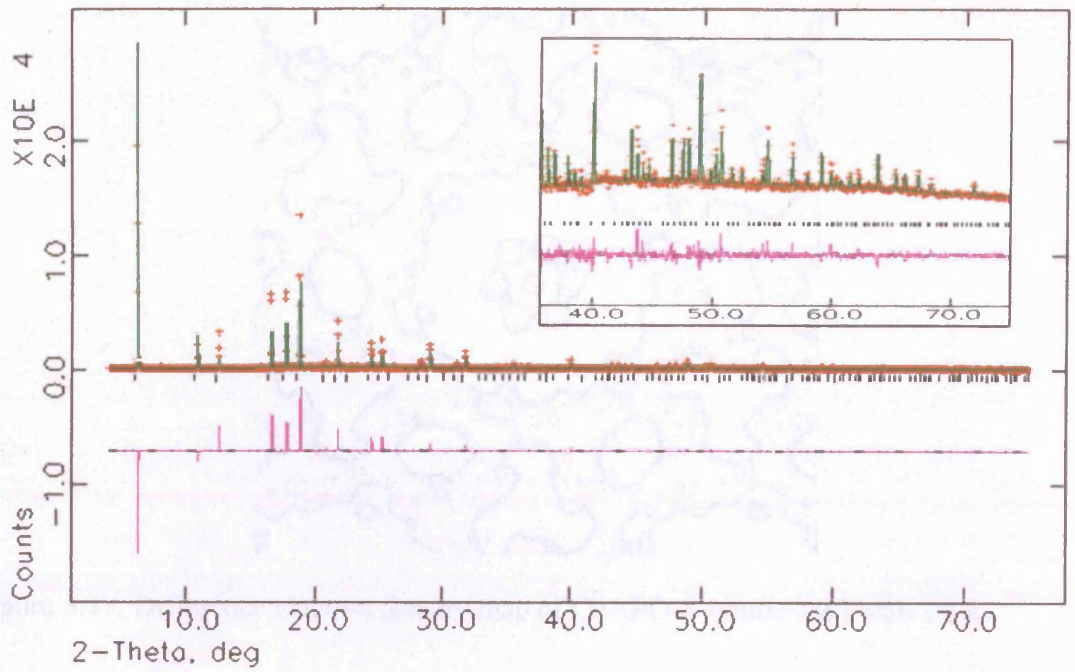

Figure 3.16: Powder pattern of CoAPO-5 synthesised with TEA before template location.

The DELF map (see Figure 3.17) was then employed to locate the missing SDA-atoms. The map shows a clear arrangement of a central peak surrounded by six spheres and another set of six spheres further away closer to the framework.

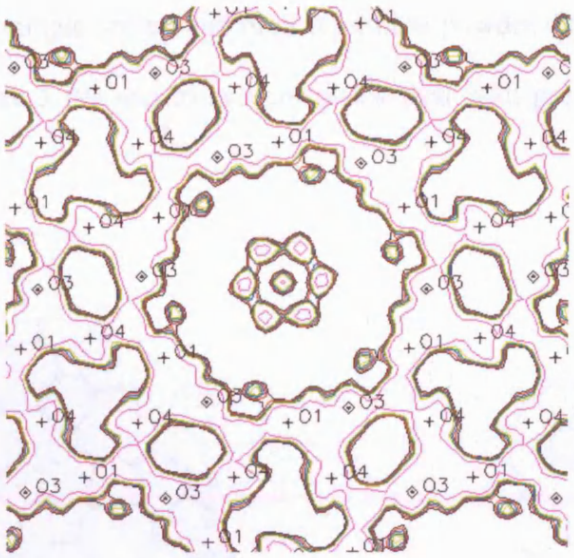

Figure 3.17: Difference electron density map of CoAPO-5 synthesised with TEA.

Having fitted the atoms from the organic molecule, the fit improved considerably at low angle, giving rise to wRp = 8.7% and Rp = 7.0%.

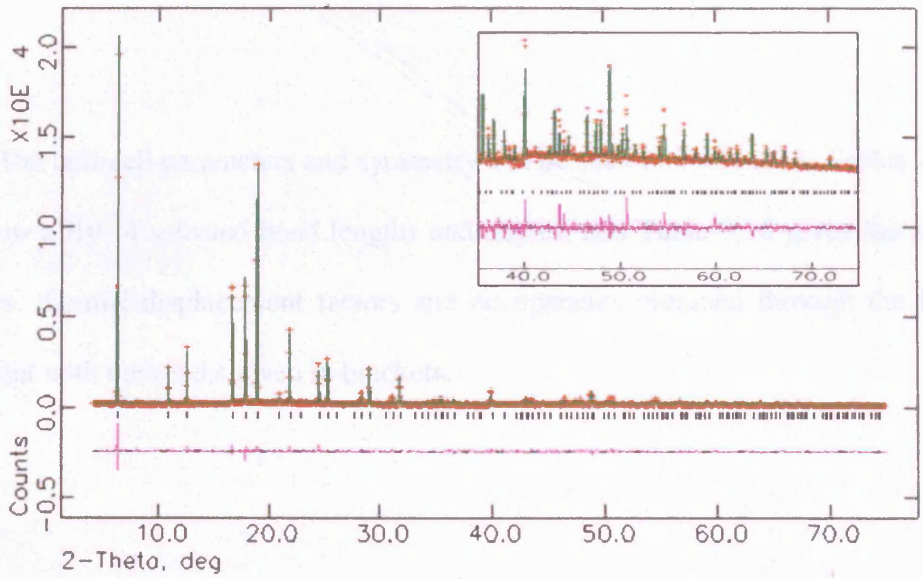

Figure 3.18: Powder pattern of CoAPO-5 synthesised with TEA after template location (wRp = 8.7% and Rp = 7.0%).

Both data-sets (single crystal and high resolution powder diffraction data) yielded identical results (Figure 3.19a and b) and correlates well with previous reported results (39).

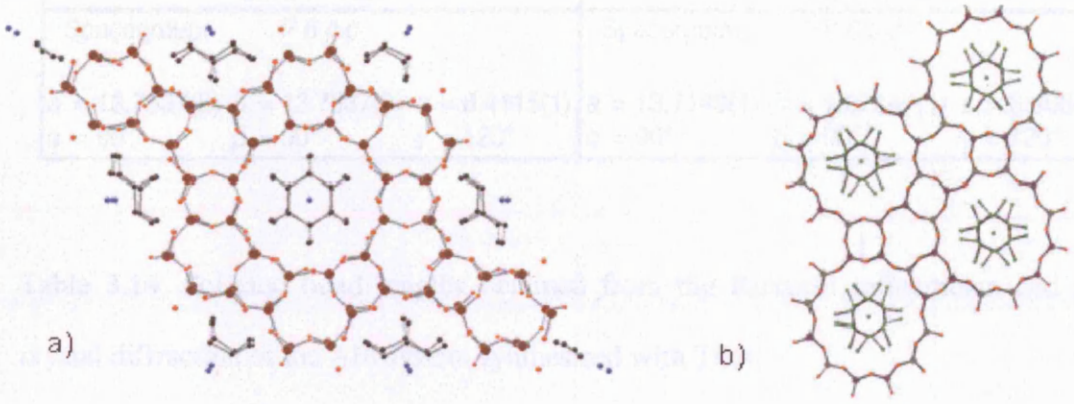

Figure 3.19: Refined CoAPO-5 structure synthesised with TEA obtained from (a) XRD data (wRp = 8.7% and Rp = 7.0%) and (b) single crystal data (R-factor = 7.8% and Rw = 5.7%).

The unit-cell parameters and symmetry can be seen in Table 3.13. Tables 3.14 and 3.15 show a list of selected bond lengths and angles, and Table 3.16 gives the atom co-ordinates, thermal displacement factors and occupancies obtained through the Rietveld refinement with the e.s.d.s given in brackets.

Table 3.13: Space group and unit cell dimensions of AFI topology synthesised with TEA[3].

Powder XRD			Single Crystal		
CoAFI - TEA			CoAFI - TEA		
Spacegroup:	*P 6 c c*		Spacegroup:	*P 6 c c*	
a = 13.7537(2)	*b* = 13.7537(2)	*c* = 8.4115(1)	*a* = 13.7149(1)	*b* = 13.7149(1)	*c* = 8.3684(1)
α = 90°	β = 90°	γ = 120°	α = 90°	β = 90°	γ = 120°

Table 3.14: Selected bond lengths obtained from the Rietveld refinements and single crystal diffraction of the AFI system synthesised with TEA.

Powder XRD		Single Crystal	
CoAFI TEA		CoAFI TEA	
Vector	Length	Vector	Length
P1_O1	1.5177(7)	P1_O1	1.4979(3)
P1_O2	1.4563(5)	P1_O2	1.4467(2)
P1_O3	1.5100(4)	P1_O3	1.5444(1)
P1_O4	1.5005(5)	P1_O4	1.4684(2)
Al2_O1	1.7626(8)	Al2_O1	1.8092(3)
Al2_O2	1.6741(5)	Al2_O2	1.6876(2)
Al2_O3	1.7450(6)	Al2_O3	1.7950(2)
Al2_O4	1.7227(6)	Al2_O4	1.7163(2)
C1_C1	1.7535(12)	C1_C1	1.6600(5)
C1_C2	1.4486(11)	C1_C2	1.6985(6)

3 The difference between the cell parameters between the two different systems can be explained by the fact that the powder data was obtained at room temperature, while the single crystal data was recorded at 120K.

Table 3.15: Selected bond angles obtained from the Rietveld refinements of the AFI system synthesised with TEA[4].

Powder XRD		Single Crystal	
CoAFI TEA		CoAFI TEA	
Angle	**Degrees**	**Angle**	**Degrees**
O1_P1_O2	109.899(6)	O1_P1_O2	108.1159(2)
O1_P1_O3	96.594(6)	O1_P1_O3	93.0205(2)
O1_P1_O4	112.064(8)	O1_P1_O4	109.0710(2)
O2_P1_O3	103.618(7)	O2_P1_O3	106.1079(3)
O2_P1_O4	110.008(7)	O2_P1_O4	108.2953(2)
O3_P1_O4	123.499(6)	O3_P1_O4	130.2701(2)
O1_Al2_O2	104.681(5)	O1_Al2_O2	104.6034(1)
O1_Al2_O3	112.458(8)	O1_Al2_O3	113.1140(2)
O1_Al2_O4	103.860(6)	O1_Al2_O4	103.8283(2)
O2_Al2_O3	104.436(7)	O2_Al2_O3	104.6034(3)
O2_Al2_O4	124.900(5)	O2_Al2_O4	121.3335(2)
O3_Al2_O4	106.599(7)	O3_Al2_O4	108.7743(2)
C1_C1_C1	120.000	C1_C1_C1	120.000
C1_C1_C2	125.005(11)	C1_C1_C2	136.275 (6)
P1_O1_Al2	149.377(7)	P2_O1_Al2	144.501(3)

[4] The deviating bond angles are due to the three fold disorder of the oxygen atoms. This also leads to shorter than expected organic – inorganic bond lengths of around 3Å (40).

Table 3.16: Atom co-ordinates, thermal displacement factors and occupancy obtained from the Rietveld refinement and single crystal diffraction of the AFI system synthesised with TEA.

CoAFI - TEA					
Powder XRD					
Atom Type	***x***	***y***	***z***	***U(iso)***	***Occup***
P1	0.4599(5)	0.3405(7)	0.0591(4)	0.0565(5)	1.000
Al2	0.4541(5)	0.3320(6)	0.4275(4)	0.0333(7)	0.900
Co1	0.4541(5)	0.3320(6)	0.4275(4)	0.0333(7)	0.100
O1	0.4233(6)	0.2274(7)	-0.0175(4)	0.0552(8)	1.000
O2	0.4393(8)	0.3265(6)	0.2296(6)	0.0884(6)	1.000
O3	0.3643(6)	0.3539(6)	-0.0034(5)	0.0657(6)	1.000
O4	0.5812(6)	0.4232(7)	0.0277(5)	0.0728(5)	1.000
C1	-0.0775(10)	0.8529(10)	0.1483(10)	0.0545(12)	0.841(9)
N1	0.0000	0.0000	0.4838(12)	0.0530(10)	0.718(11)
C2	0.1248(12)	0.2614(11)	0.2049(10)	0.10815(9)	0.091(10)

Single Crystal					
Atom Type	***x***	***y***	***z***	***U(iso)***	***Occup***
P1	0.4571(3)	0.3452(2)	0.0601(4)	0.0601(3)	1.000
Al2	0.4503(3)	0.3319(3)	0.4308(3)	0.04308(3)	0.900
Co1	0.4503(3)	0.3319(3)	0.4308(3)	0.04308(3)	0.100
O1	0.4218(3)	0.2289(3)	-0.0182(2)	0.05309(3)	1.000
O2	0.4379(3)	0.3310(3)	0.2317(2)	0.09202(3)	1.000
O3	0.3603(3)	0.3498(3)	-0.0030(3)	0.06498(3)	1.000
O4	0.5798(3)	0.4201(3)	0.0293(3)	0.05788(2)	1.000
C1	1.0191(6)	0.8903(6)	0.4606(5)	0.09542(5)	0.787(5)
N1	0.0000	0.0000	0.4633(6)	0.05813(4)	0.697(6)
C2	1.2022(7)	1.0496(8)	0.4309(6)	0.10428(7)	0.153(8)

3.4.2 Computational Studies on Host-Guest Interactions

Having established the position of MCHA within the framework from experimental data, it was decided to evaluate those findings by computational methods and gain further insight into the template's position within the framework. Several different Monte Carlo calculations using the Cerius2 software (41) were run employing the forcefield cvff_300_1.01. The size of the super-cell was 2 x 2 x 2 unit cells with a cut-off of 8 Å. In all cases, the low energy sites for the template were in the centre of the channel system, giving a close match with the experimental results deduced from XRD data. The template occupies several different positions within the AlPO-5 channel with no pronounced preference for one specific position. The 20 energetically most favourable positions of the template within the framework were chosen and superimposed on one another (see Figure 3.20).

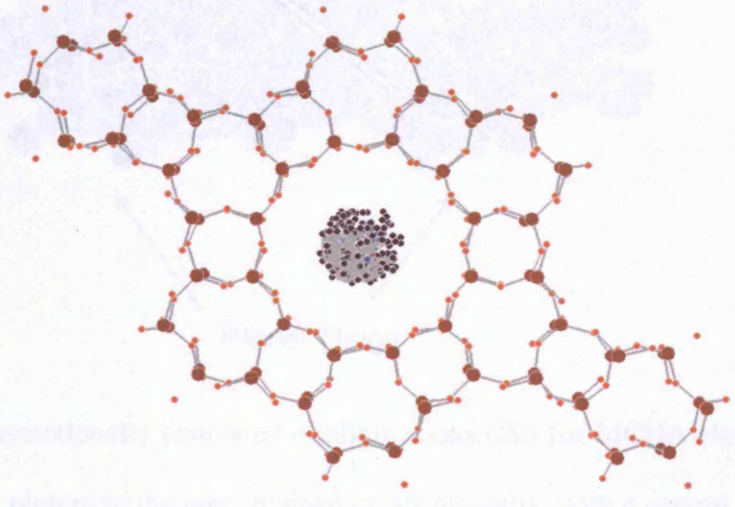

Figure 3.20: Picture arising from 20 energetically favourable conformations of MCHA that were obtained through Monte Carlo docking calculations.

The results of the computational study extend and complement those obtained from experiment. As a consequence of the framework's space group, MCHA seems to align in the centre of the channel, giving rise to a hexagonal shape. Figure 3.21 shows that the nitrogen atom (blue sphere) is located more or less in the middle of the atomic distribution. This central nitrogen atom is surrounded by carbon atoms. When taking an average of these arrangements a picture very close to that obtained experimentally can be detected, i.e. the template can be found in a sequence of planar rings with nitrogen atoms in the centre of the channel between these rings (see Figure 3.21).

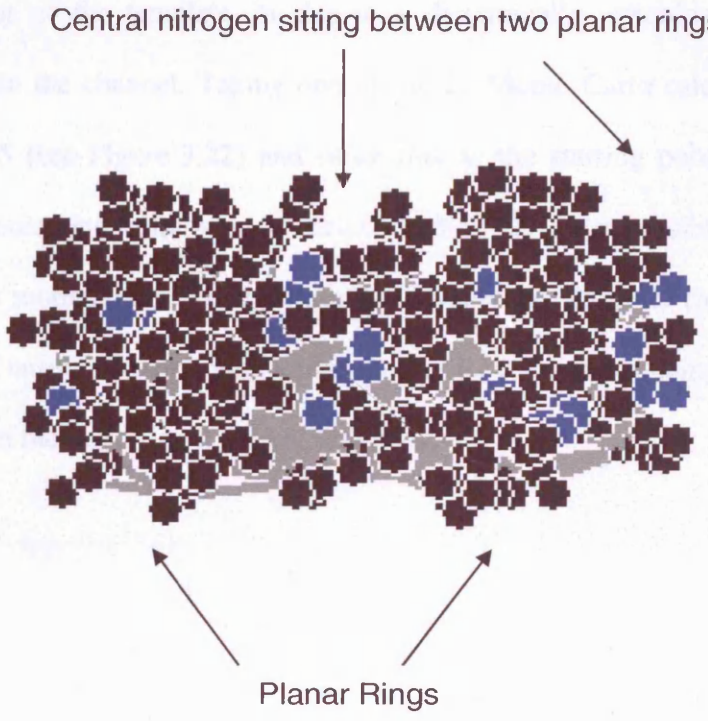

Figure 3.21: Computationally generated configurations (20) for MCHA along (010) axis, showing a similar picture to the one obtained experimentally, with a central nitrogen atom sitting between two planar rings.

When examining the computational model it is clear, that due to the fact that the observed template (MCHA) is an average of many different possible arrangements and one cannot distinguish between the carbon from the cyclohexane groups and the carbon from the methyl-group. However, the overall appearance of the template molecule is the same experimentally and computationally, i.e. the carbon ring giving rise to a hexagonal shape.

These results from XRD data and Monte Carlo calculations however cannot determine whether the arrangement of the template within the channel is due to different static positions of the template, or due to a dynamically, spinning movement of the template within the channel. Taking one of the 20 Monte Carlo calculations of MCHA within AlPO-5 (see Figure 3.22) and using this as the starting point to run Molecular Dynamics calculations, employing Materials Studio (42) it was possible to get insight into the template's motional behaviour within the framework. The MD calculations were run with the NVT ensemble employing a time step of 0.001ps and running for 100,000 steps, with the size of the box being 2 x 2 x 2 unit cells.

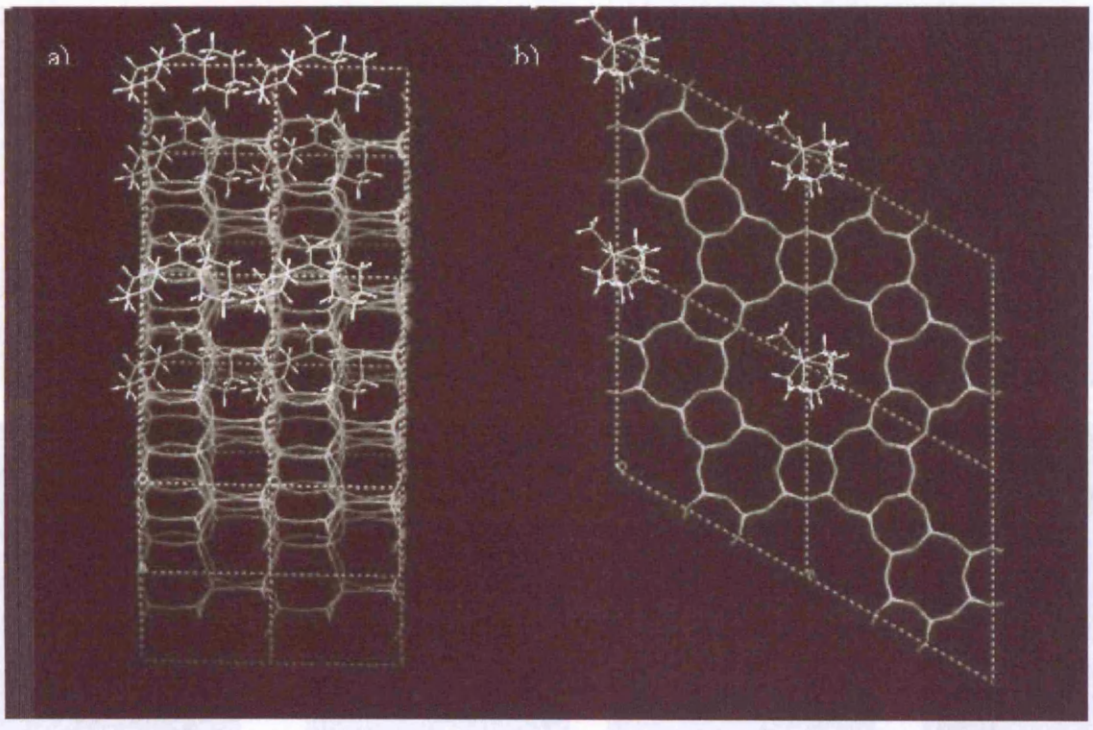

Figure 3.22: One of the 20 energetically most favourable conformations of the MCHA obtained from the Monte Carlo docking calculations, which was used as the starting point for the Molecular Dynamics calculations:

a) along (010) axis,

b) along (001) axis.

Rather than spinning around, the template sits in one fixed position. Calculations run at 50 K and at 298 K (see Figure 3.23) yielded almost identical results, highlighting that the template's disorder is static rather than caused by the SDA's motion within the channel.

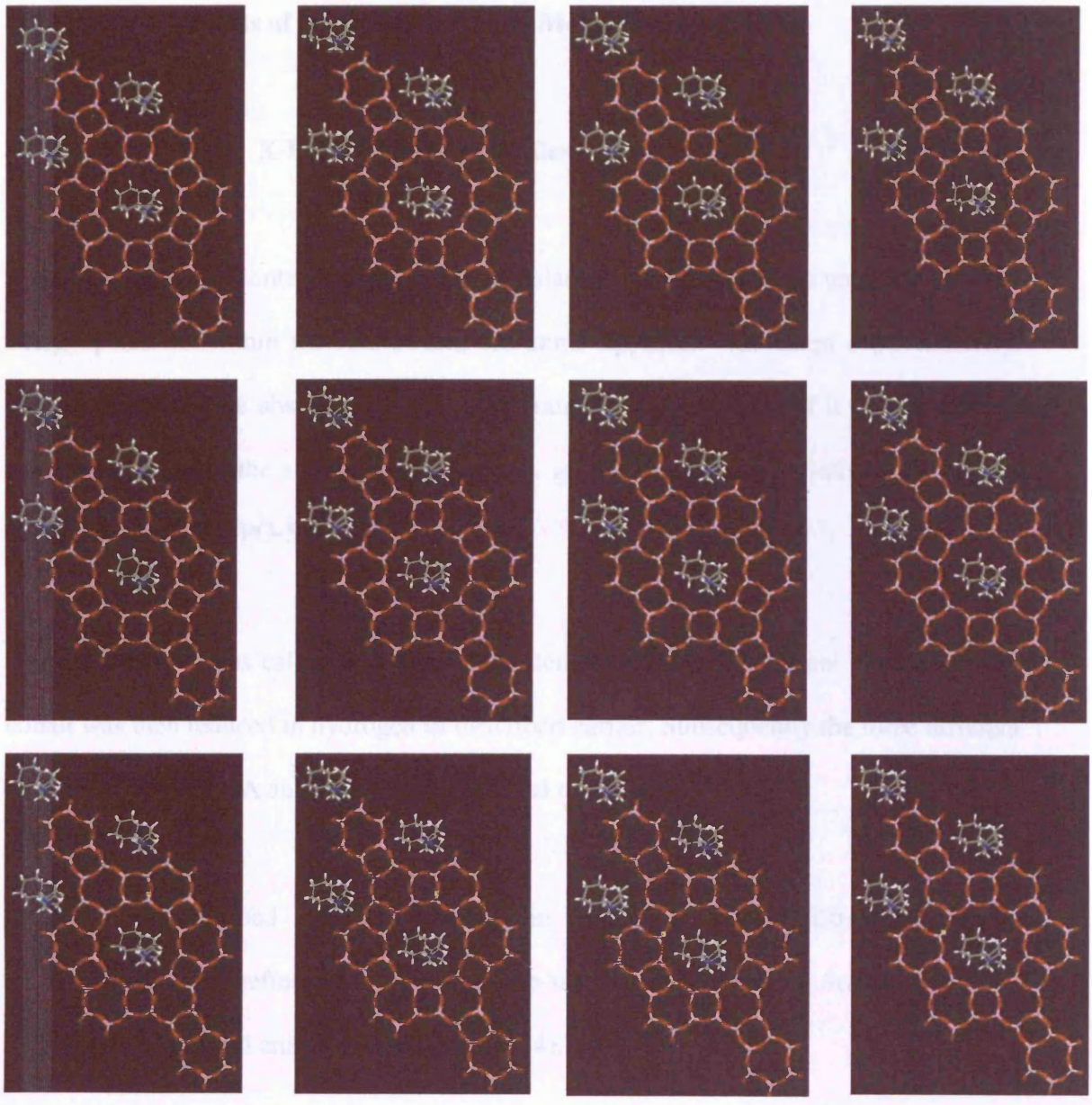

Figure 3.23: Twelve frames taken from the Molecular Dynamics calculations recorded at 298 K, highlighting that the molecule is static in the channel system rather then rotating.

3.5 Results of Absorbing Organic Molecules into AlPO-5

3.5.1 X-Ray Diffraction Studies

Having run Monte Carlo Docking calculations to determine the template's lowest energy positions within the framework, the same approach was taken experimentally. Different SDAs were absorbed into the AFI framework to establish if it would take the same position as in the as-synthesised sample, giving further insight into the host-guest interactions in the AlPO-5 system.

CoAPO-5 was calcined to remove the template from the channel system and the cobalt was then reduced in hydrogen as described earlier. Subsequently the three different SDAs (MCHA, ECHA and TEA) were absorbed in vacuum.

The re-absorbed templates were again located by X-ray diffraction analysis employing Rietveld refinement and using data that were recorded on Station 2.3 at the SRS in Daresbury and analysed (see Figure 3.24).

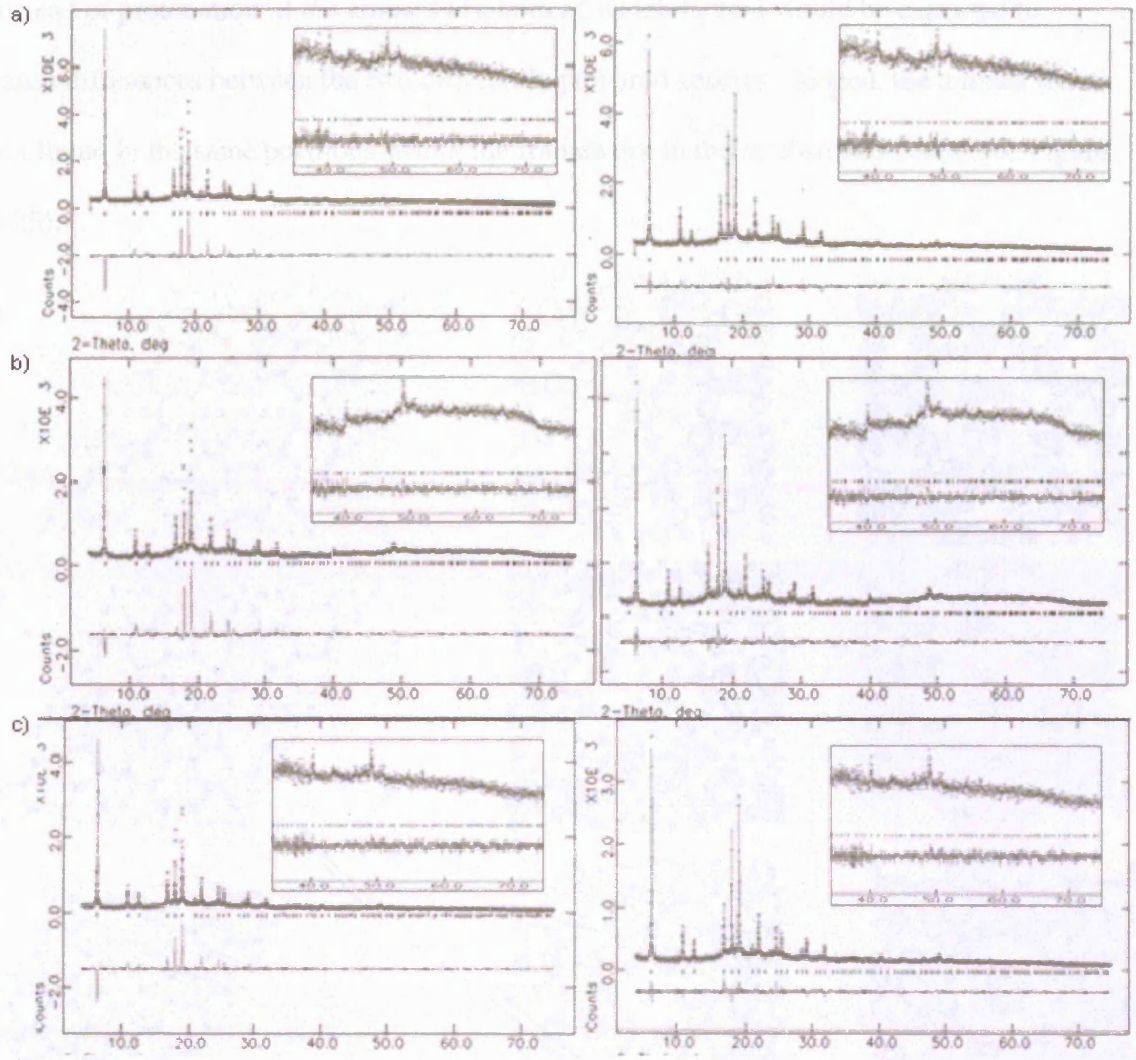

Figure 3.24: HRXRD pattern of CoAPO-5 before and after SDA location (recorded at 1.301 Å) with:

a) MCHA re-absorbed into the channel system (final wRp = 8.3% and Rp = 6.4%),

b) ECHA re-absorbed into the channel system (final wRp = 7.8% and Rp = 5.9%),

c) TEA re-absorbed into the channel system (final wRp = 9.6% and Rp = 7.5%).

Differences between the as-synthesised materials and the re-absorbed cases include the lack of water present in the re-absorbed cases and the formation of Brønsted acid sites

instead of protonation of the amine (43), both of which factors would be expected to cause differences between the two differently prepared species. Indeed, the amines were not found in the same positions within the framework in the re-absorbed cases (see Figure 3.25).

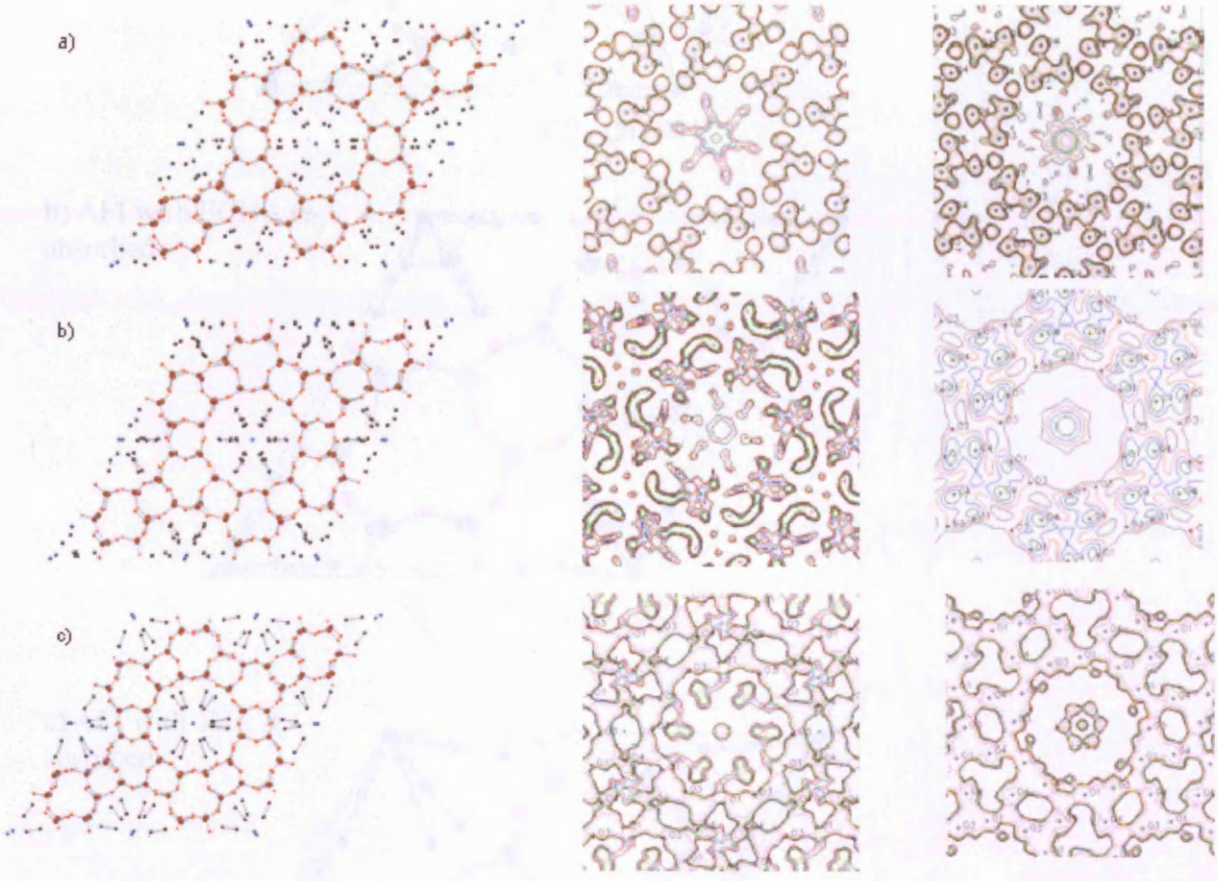

Figure 3.25: Structures of the MeAPO-5 framework with the different, absorbed SDAs (left), located through the difference electron density maps (middle) from high resolution XRD data. The corresponding as-synthesised samples' DELF maps are pictured for comparison on the right:

a) CoAFI with MCHA re-absorbed,

b) CoAFI with TEA re-absorbed,

c) CoAFI with ECHA re-absorbed.

a) AFI with MCHA re-absorbed

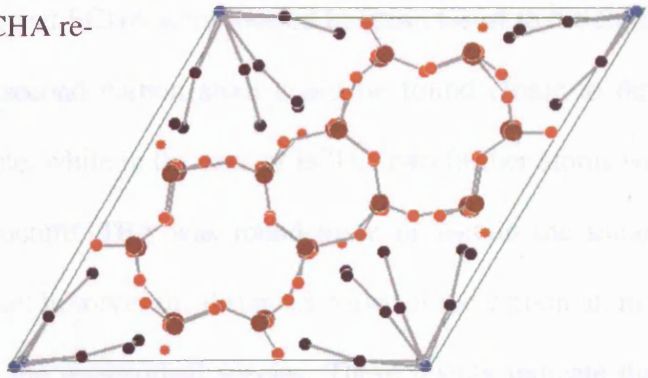

b) AFI with ECHA re-absorbed

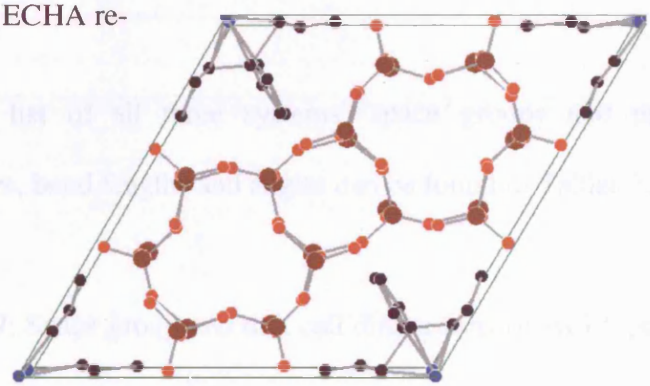

c) AFI with TEA re-absorbed

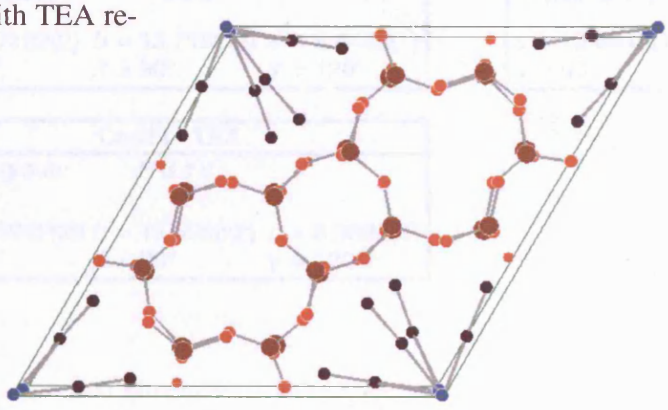

Figure 3.26: Unit cell of the AFI systems with the different SDAs re-absorbed. The organic atoms are labelled for ease of identification.

MCHA and ECHA were located in sites closest to the framework wall. In the case of MCHA, a second carbon atom could be found closer to the framework in the re-absorbed sample, while in the case of ECHA two further atoms were located closer to the framework structure. TEA was found more or less in the same position as in the as-synthesised case; however the distances between the carbon atoms increased from the as-synthesised to the re-absorbed species. These results indicate that the templates have a wider spread in the channel when re-absorbed.

A list of all three systems' space groups and unit cell dimensions, atom coordinates, bond lengths and angles can be found in Tables 3.17-20.

Table 3.17: Space group and unit cell dimensions of AFI topologies with different SDAs absorbed.

CoAFI - MCHA		
Spacegroup:	*P 6 c c*	
a = 13.7182(2)	*b* = 13.7182(2)	*c* = 8.4142(1)
α = 90°	*β* = 90°	*γ* = 120°

CoAFI - ECHA		
Spacegroup:	*P 6 c c*	
a = 13.6948(1)	*b* = 13.6948(1)	*c* = 8.3722(1)
α = 90°	*β* = 90°	*γ* = 120°

CoAFI - TEA		
Spacegroup:	*P 6 c c*	
a = 13.6962(29	*b* = 13.6962(2)	*c* = 8.3893(2)
α = 90°	*β* = 90°	*γ* = 120°

Table 3.18: Atom co-ordinates, thermal displacement factors and occupancy obtained from the Rietveld refinements of the AFI systems with different SDAs re-absorbed.

a)

CoAFI - MCHA					
Atom Type	***x***	***y***	***z***	***U(iso)***	***Occup***
P1	0.4588(3)	0.3421280(4)	0.0584990(4)	0.02208(6)	1.000
Al2	0.4538(4)	0.3310(6)	0.4263(5)	0.02512(5)	0.900
Co1	0.4538(4)	0.3310(6)	0.4263(5)	0.02512(5)	0.100
O1	0.4248(6)	0.2387(7)	0.0059(7)	0.02289(7)	1.000
O2	0.4434(8)	0.3219(8)	0.2096(7)	0.02345(7)	1.000
O3	0.3732(7)	0.3412(6)	-0.0021(6)	0.01925(6)	1.000
O4	0.5816(2)	0.4129(4)	0.0278(3)	0.01870(7)	1.000
C1	0.0217(13)	0.8502(13)	0.1527(12)	0.0417(12)	0.852(10)
N1	0.0000	0.0000	0.4193(12)	0.05(10)	0.290(10)
C2	0.2912(12)	0.2727(12)	0.3304(13)	0.13288(12)	0.496(9)

b)

CoAFI - ECHA					
Atom Type	***x***	***y***	***z***	***U(iso)***	***Occup***
P1	0.4594440(5)	0.3395630(4)	0.0570040(6)	0.0238(7)	1.000
Al2	0.4593310(5)	0.3382570(5)	0.428666(5)	0.0246(6)	0.900
Co1	0.4593310(5)	0.3382570(5)	0.428666(5)	0.0246(6)	0.100
O1	0.4210020(4)	0.2165650(5)	0.0355900(6)	0.0258(7)	1.000
O2	0.4394110(6)	0.3136600(7)	0.2278660(6)	0.0280(7)	1.000
O3	0.3716210(5)	0.3552150(6)	0.0070190(6)	0.0189(5)	1.000
O4	0.5758100(5)	0.4103460(6)	0.0085910(5)	0.0195(4)	1.000
N1	0.0000	0.0000	0.1446000(2)	0.0358(9)	0.235(11)
C1	0.1206160(12)	0.1250100(12)	0.3787500(12)	0.0793(12)	0.355(13)
C2	0.2616720(12)	-0.0051270(12)	0.2019490(12)	0.0869(12)	0.373(12)
C3	-0.169975(12)	-0.178276(11)	-0.160524(10)	0.0893(12)	0.684(12)

c)

CoAFI - TEA					
Atom Type	***x***	***y***	***z***	***U(iso)***	***Occup***
P1	0.4644490(4)	0.3404410(3)	0.0594200(6)	0.0268(6)	1.000
Al2	0.4525570(5)	0.3290920(6)	0.4293470(6)	0.0227(7)	0.900
Co1	0.4525570(5)	0.3290920(6)	0.4293470(6)	0.0227(7)	0.100
O1	0.4209810(8)	0.2232200(7)	0.0021000(6)	0.0218(7)	1.000
O2	0.4450390(7)	0.3453250(5)	0.2257250(4)	0.0187(6)	1.000
O3	0.3747250(6)	0.3585140(6)	-0.0098690(4)	0.0167(8)	1.000
O4	0.5827940(6)	0.4186640(6)	0.0261160(6)	0.0185(7)	1.000
C1	0.1577700(13)	0.1441700(12)	0.1781600(11)	0.0694(13)	0.867(14)
N1	0.0000	0.0000	-0.860032(10)	0.0192(11)	0.396(10)
C2	0.2954080(10)	0.2529020(11)	0.200978(11)	0.1396(11)	0.436(10)

Table 3.19: Selected bond lengths obtained from the Rietveld refinements of the AFI systems with MCHA, ECHA and TEA re-absorbed [1].

CoAFI MCHA		CoAFI ECHA		CoAFI TEA	
Vector	Length	Vector	Length	Vector	Length
P1_O1	1.5022(2)	P1_O1	1.5033(8)	P1_O1	1.4857(6)
P1_O2	1.4936(3)	P1_O2	1.4663(7)	P1_O2	1.4881(5)
P1_O3	1.4833(5)	P1_O3	1.3876(6)	P1_O3	1.4878(6)
P1_O4	1.4874(3)	P1_O4	1.4487(7)	P1_O4	1.4548(7)
Al2_O1	1.7227(7)	Al2_O1	1.7637(8)	Al2_O1	1.7370(7)
Al2_O2	1.7636(8)	Al2_O2	1.7395(8)	Al2_O2	1.7323(7)
Al2_O3	1.7829(6)	Al2_O3	1.7831(8)	Al2_O3	1.7649(8)
Al2_O4	1.7918(9)	Al2_O4	1.7381(7)	Al2_O4	1.7601(7)
C1_C1	2.2193(10)	C1_C1	1.6827(9)	N1_C1	2.0986(10)
C1_C2	2.1532(6)	C1_C2	2.1077(9)	C1_C1	2.0740(10)
				C1_C2	2.2220(7)

Table 3.20: Bond angles obtained from the Rietveld refinements of the AFI systems with MCHA, ECHA and TEA re-absorbed.

CoAFI MCHA		CoAFI ECHA		CoAFI TEA	
Angle	Degrees	Angle	Degrees	Angle	Degrees
O1_P1_O2	99.499(6)	O1_P1_O2	95.810(5)	O1_P1_O2	112.545(6)
O1_P1_O3	91.483(6)	O1_P1_O3	106.986(5)	O1_P1_O3	97.776(7)
O1_P1_O4	108.501(5)	O1_P1_O4	111.602(6)	O1_P1_O4	115.502(5)
O2_P1_O3	109.923(6)	O2_P1_O3	105.059(6)	O2_P1_O3	100.680(5)
O2_P1_O4	108.655(6)	O2_P1_O4	116.422(5)	O2_P1_O4	108.546(6)
O3_P1_O4	125.412(4)	O3_P1_O4	124.104(5)	O3_P1_O4	120.747(5)
O1_Al2_O2	107.735(6)	O1_Al2_O2	109.869(7)	O1_Al2_O2	118.646(7)
O1_Al2_O3	113.636(7)	O1_Al2_O3	101.687(7)	O1_Al2_O3	114.664(5)
O1_Al2_O4	97.887(6)	O1_Al2_O4	99.953(7)	O1_Al2_O4	101.143(6)
O2_Al2_O3	105.993(7)	O2_Al2_O3	109.603(6)	O2_Al2_O3	97.974(6)
O2_Al2_O4	125.072(6)	O2_Al2_O4	121.995(7)	O2_Al2_O4	118.055(6)
O3_Al2_O4	109.620(6)	O3_Al2_O4	111.412(5)	O3_Al2_O4	106.410(7)
P1_O1_AL2	152.038(6)	P1_O1_AL2	143.599(6)	P1_O1_Al1	147.231(6)

[1] The C-O bond distances (roughly 3Å) are feasible if the atom is not considered as an actual atom but as a picture of electron density, giving rise to an average over the oxygen atom.

3.5.2 Thermo-Gravimetric Analysis (TGA)

TGA experiments were undertaken on the as-synthesised and the re-absorbed species to gain further insight into the host-guest interactions. The TGA experiments were run with a Mass Spectrometer coupled to the TGA equipment in order to distinguish between the different desorbing species. In the as-synthesised sample, there are two different desorption peaks arising from water (between 79 and 108°C and between 178°C and 278°C) (see Figure 3.27).

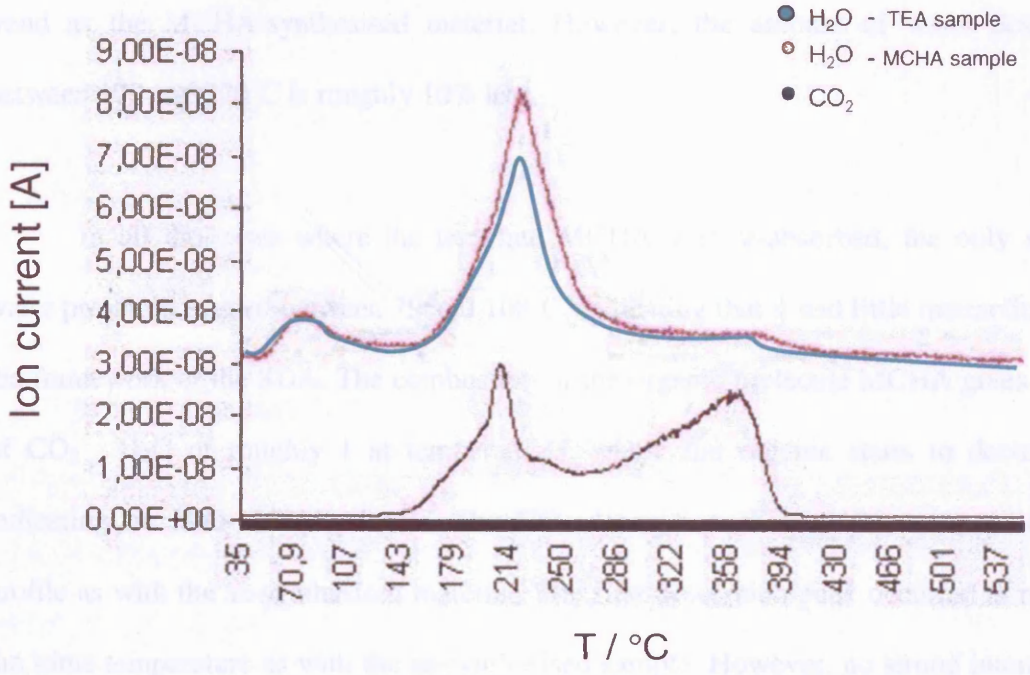

Figure 3.27: Results from the TGA study of CoAPO-5 (as-synthesised with MCHA and TEA) showing a clear correlation between SDA decomposition (CO_2) and H_2O desorption (with the ion current being molecules desorbing).

The first desorption peak of water between 79 and 108°C can be explained by the presence of water, which is loosely bound to the framework's surface or in the channel system. The second peak can be attributed to water, which is bonded to the SDA. Once the SDA starts to decompose (around 143°C) further water molecules are released, indicating the presence of SDA-water clusters. Even as the combustion of the SDA yields CO_2, NO_2 and H_20 as reaction products ($4\ C_{13}H_{26}N\ (MCHA\text{-}H^+) + 65\ O_2 \rightarrow 26\ CO_2 + 26\ O_2 + 26\ H_2O$), the TGA results still indicate an excess of ~1.5 H_20 molecules per MCHA, as calculated from the areas underneath the mass spectroscopy peaks as shown in Figure 3.27. The TGA results from the CoAPO-5 sample synthesised with TEA showed the same trend as the MCHA-synthesised material. However, the amount of water desorbing between 170 and 270°C is roughly 10% less.

In all the cases where the template MCHA was re-absorbed, the only surplus water present desorbed between 79 and 108°C, indicating that it had little interaction with the framework or the SDA. The combustion of the organic molecule MCHA gives a ratio of CO_2 : H_2O of roughly 1 at temperatures, where the organic starts to decompose, indicating no H_2O-MCHA cluster. The CO_2 desorption showed the same desorption profile as with the as-synthesised material. The first desorption peak occurred at roughly the same temperature as with the as-synthesised sample. However, no strong interactions between water and template molecules occurred in these cases (see Figure 3.28).

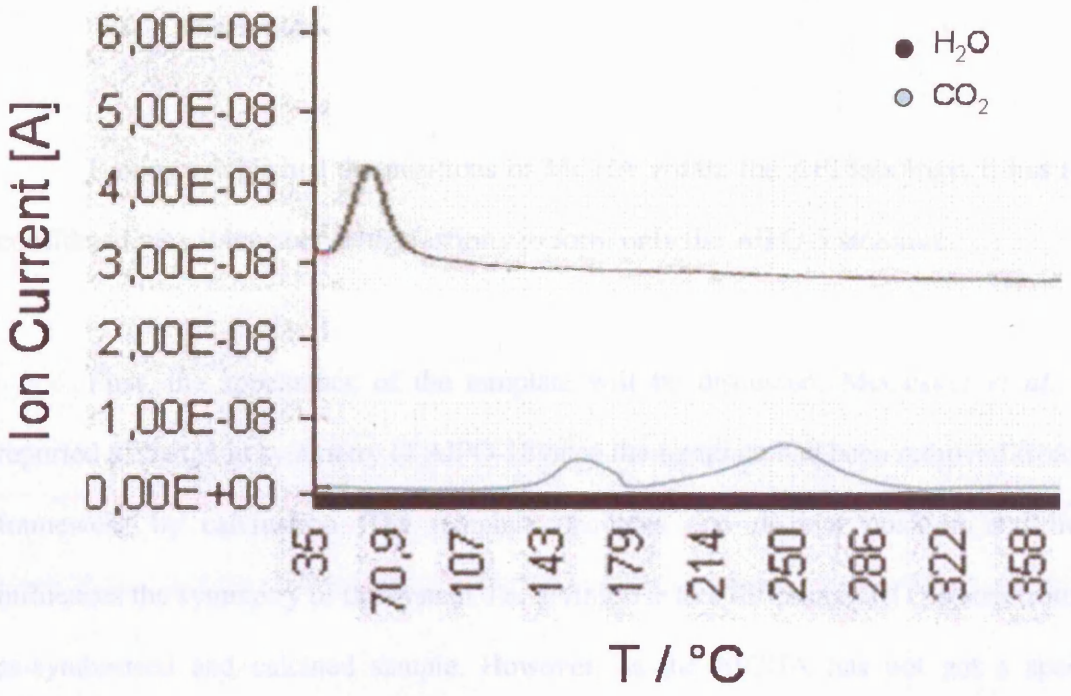

Figure 3.28: Results from the TGA study of CoAPO-5 with the template (MCHA) re-absorbed, showing that the only water present in the sample is water which is loosely bound to the framework.

Results from the TGA experiments show clearly that the template in the as-synthesised sample forms strong interactions with water, which is present during the synthesis, leading to SDA-H_2O clusters. In the re-absorbed species, the template does not interact with water and no template-H_2O clusters are formed.

The CO_2 desorption profile in the as-synthesised material, giving rise to two different peaks has been reported before. These peaks have been attributed to the presence of heteroatom centres, acting as sorption centres and thus blocking the template from leaving the channel system (44).

3.6 Discussion

Having established the positions of MCHA within the AFI topology, it has to be considered why it has such a high affinity to form only the AlPO-5 structure.

First, the appearance of the template will be discussed. McCusker *et al.* (25) reported a change in symmetry of AlPO-18 once the template had been removed from the framework by calcination. The template occupies one distinct position and hence influences the symmetry of the system, i.e. giving rise to a different XRD pattern from the as-synthesised and calcined sample. However, as the MCHA has not got a specific position within the AFI channel system but occupies several different sites, an overall average of all positions is recorded giving rise to a rigid, flat, benzene-like six-member ring.

It also has to be noted, that the C-C bond length within the template is not the length of a standard sp^3 hybridised carbon-carbon bond but is much shorter at ~1.40 Å than the expected 1.54 Å, which can be explained by the fact that the observed image is not an actual depiction of an individual SDA, but an average picture of several different disordered positions of the template within the CoAPO-5 framework channels. The same explanation applies to the carbon-nitrogen bond, which at 2.31 Å is longer than the standard value of 1.47 Å. The computational studies confirmed that the appearance of the SDA within the AFI channel arises due to static disorder of the organic molecule.

Another interesting point is that while the C-C bonds in the MCHA system are 1.4 Å, they are 1.5 Å in the ECHA system. The difference in C-C bond distances can be explained by the increased bulk of ECHA compared to MCHA, which is emphasised by the change in *a* and *b* unit cell parameters of the two different AFI systems. The aluminophosphate synthesised with ECHA has the largest *a* and *b* cell lengths, followed by MCHA and then TEA (see Tables 3.1, 3.9 and 3.13). After calcination, the cell volumes are all identical (see Table 3. 17) and are smaller than in the as-synthesised material, indicating that the size of the SDA plays a role in the structure direction of aluminophosphates.

However, ECHA is located in a position that is very similar to that of MCHA within the AlPO-5 channel system, i.e. located in the centre of the channel. Based on this result, it can be concluded, that ECHA's ability to form the ATS structure, when heteroatoms are present in the synthesis gel is not purely based on its size. If the SDA's size was the only driving force in structure directing AlPOs, one would expect to see ECHA forming the ATS topology even as a pure AlPO.

Comparing the position of TEA with MCHA in the as-synthesised samples, one can see that TEA is located far closer to the framework, indicating a stronger interaction with the MeAPO's framework. This trend is reversed in the re-absorbed cases.

To gain further insight into the underlying reasons for these trends, one has to look at the properties of amines. In tertiary amines hydration is not restricted by steric

hindrance; instead it is aided by the inductive effect of larger side-groups on the nitrogen, which gives rise to an increase in solvation according to following sequence:

tributylamine > *tripropylamine* > *trimethylamine* (45)

The inductive effect of the alkyl-group on the base increases with increasing alkyl chain length and hence leads to an increase in basicity. A marked strengthening of basicity is accompanied by increased hydration of the protonated amine (45).

The two cyclohexane rings and the methyl-group in MCHA can be considered to have a higher inductive effect (13 C atoms attached to N) than the three ethyl-groups in TEA (6 C atoms attached to N). Another factor, which is highly influential in the solvation of the nitrogen, is the flexibility of the substituents attached to it (46). The less flexible the substituents, the more available the lone-electron pair is for protonation. The cyclohexane rings as well as the methane group attached to the nitrogen in MCHA are far more rigid than the ethyl-groups in TEA. Based on the inductive effect and hardness of the substituents, it can be concluded that MCHA has a much lower pKb value than TEA, and hence is more basic (47).

A higher basicity leads to the lone-electron pair in a tertiary amine being protonated more easily, which in turn results in a higher hydration of the cation and thus in a lesser interaction between template and framework.

TGA results from the samples clearly indicate that the SDA has very strong interactions with H_2O. The protonated form of MCHA interacts strongly with the oxygen of water and thus forms template-H_2O clusters, which leads to the MCHA not interacting strongly with the framework's oxygen and thus the template occupies the centre of the channel system. TEA on the other hand has not been fully hydrated which results in the interaction between the charge carried by the protonated nitrogen and the framework oxygen (43). TEA can hence be seen occupying sites closer to the framework than MCHA or ECHA, which is a direct result of TEA's lower solvation energy (based on its substituents' lower inductive effect). MCHA on the other hand has only very little interaction with the framework, which makes it an ideal template for AlPO-5, as it is the framework, which forms most readily. Another template which forms highly crystalline AlPO-5 samples is tripropylamine (2), which again has a high basicity due to the high inductive effect of the substituents. MCHA however can be considered to have a higher basicity as its substituents on the basic centre are more rigid then the relatively flexible propyl-groups.

When the SDAs are re-absorbed, they follow the same principle. As there is no water present to shield the charge of the nitrogen's free electron pair, the SDAs have a stronger interaction with the CoAPO-5's Brønsted acid sites (48) (or possibly Lewis acid sites). In the cases of MCHA and ECHA this can be seen to a greater degree, as instead of located centrally in the channel system, the SDAs have very strong interactions with the framework and are located close to the channel walls. As after calcination, MeAPO-5 forms Brønsted acid sites to charge compensate the metal substitution (43, 48, 49) the electronegative nitrogen in MCHA and ECHA interacts with the acid site and can thus

locate close to the framework. TEA also has a stronger interaction with the framework when it is re-absorbed, represented by the longer C-C distances, indicating a wider spread in the channel system. However, as TEA is less shielded in the as-synthesised form in comparison to MCHA, there is a much smaller difference in the SDA's position within the channel system in the two cases (re-absorbed and as-synthesised).

The introduction of a divalent metal ion leads to a charged framework. Based on this fact, one would not expect the TEA to be close to the framework in the pure AlPO-5 form. Indeed, Ikeda *et al.* have shown that TEA occupies the centre of the channel when no metal-ions are substituted into the framework (50), giving rise to a picture which resembles that of the CoAPO-5 MCHA system (see Figure 3.29).

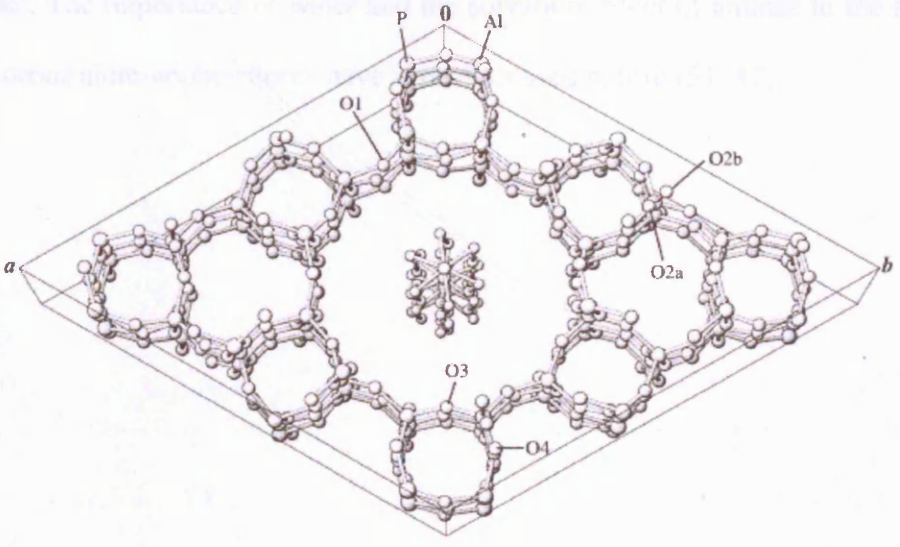

Figure 3.29: AlPO-5 synthesised using TEA as SDA. The template can be seen sitting in the centre of the channel system (50).

Furthermore, ECHA only forms the ATS topology under very specific conditions. Only when the synthesis gel contains metal ions and a low concentration of water does this SDA form the ATS topology. As the organic molecule is hydrated to a lesser extent it will have a stronger interaction with the framework when substituted metal ions introduce a charge to the framework. Due to the bulkiness of the template the formation of the ATS structure is favoured over the formation of the AFI topology. However, if a high concentration of water is used in the synthesis gel (synthesis conditions: 0.9 Al : 1.0 P : 0.1 Co : 0.8 ECHA : 30 H_2O) the AlPO-5 topology gets formed.

This evidence again underlines the fact that the hydration and pKb value of the template plays an essential role in the synthesis of microporous aluminophosphate materials. The importance of water and the solvation effect of amines in the synthesis of microporous aluminophosphates have been discussed before (51, 52).

3.7 Conclusion

XRD results locating MCHA in CoAPO-5 in the as-synthesised and the re-absorbed species show clear differences. In the as-synthesised form, little interaction between the template and the framework occurs, leading to the template occupying the centre of the channel system. In the re-absorbed cases the template is closer to the AlPO channel walls, indicating a stronger interaction with the framework. Results from the TGA experiments show clearly that MCHA in the as-synthesised sample forms strong interactions with water, which is present during synthesis, leading to MCHA-H_2O clusters. In the re-absorbed species, the template does not interact with water and no template-H_2O clusters are formed. It can be concluded that MCHA is a good template for the formation of AFI, as it has only little interaction with the framework after hydration and the AFI topology is the most readily formed topology. In combination with the results obtained from other AFI samples synthesised with different SDAs it can be concluded that the amine's pKb value and the associated attributes, i.e. different levels of hydration play an essential role in the synthesis of this topology.

Amines with increasing pKb value (and hence lower hydration) tend to form more complex structures, which can be attributed to their stronger interactions with the framework or framework-intermediates. In amines the alkyl substituents act as electron donating groups leading to a higher polarisation of the lone electron pair on the nitrogen (46). It can thus be generalized that tertiary amines have a lower pKb value than the corresponding primary amines (tributylamine = 3.11 compared to butylamine = 3.57)

(45). Primary amines and diamines tend to form a wide spectrum of different 3-dimensional microporous and layered materials (53-57).

It can be concluded that the SDA's pKb value plays a pivotal role in the synthesis of microporous aluminophosphates. Other factors, such as shape and size of the template have also shown to be of significance in the formation of one-dimensional microporous aluminophosphates.

3.8 References

1. Y. Liu, R. L. Withers, and L. Noren, *Solid State Sciences*, *5*, 427 (2003).
2. O. Weiss, G. Ihlein, and F. Schuth, *Microporous and Mesoporous Materials*, *35-6*, 617 (2000).
3. C. J. P. Bennett J.M., Flanigen E.M., Pluth, J.J., Smith J.V., *ACS Sym. Ser.*, *218*, 109 (1983).
4. S. R. A. Arends I., Wallau M., Schuchardt U., *Angewandte Chemie-International Edition in English*, *36*, 1144 (1997).
5. M. Hartmann and L. Kevan, *Chemical Reviews*, *99*, 635 (1999).
6. G. Sankar, R. Raja, and J. M. Thomas, *Catalysis Letters*, *55*, 15 (1998).
7. S. T. Wilson and E. M. Flanigen, *Acs Symposium Series*, *398*, 329 (1989).
8. P. A. Barrett, G. Sankar, C. R. A. Catlow, and J. M. Thomas, *Journal of Physical Chemistry*, *100*, 8977 (1996).
9. T. Blasco, P. Concepcion, J. M. L. Nieto, and A. Martinez-Arias, *Collection of Czechoslovak Chemical Communications*, *63*, 1869 (1998).
10. S. K. Saha, H. Maekawa, S. B. Waghmode, S. A. R. Mulla, K. Komura, Y. Kubota, Y. Sugi, and S. J. Cho, *Materials Transactions*, *46*, 2659 (2005).
11. M. Sanchez-Sanchez, G. Sankar, A. Simperler, R. G. Bell, C. R. A. Catlow, and J. M. Thomas, *Catalysis Letters*, *88*, 163 (2003).
12. W. M. Meier and D. H. Olson, *Atlas of Zeolite Structure Types*, Butterworth-Heinemann, Stoneham, 1996.
13. P. A. Barrett, G. Sankar, R. Stephenson, C. R. A. Catlow, J. M. Thomas, R. H. Jones, and S. J. Teat, *Solid State Sciences*, *8*, 337 (2006).

14. S. Qiu, W. Pang, H. Kessler, and J.-L. Guth, *Zeolites*, *9*, 440 (1989).

15. G. Sankar, J. K. Wyles, and C. R. A. Catlow, *Topics In Catalysis*, *24*, 173 (2003).

16. P. A. Barrett, R. H. Jones, J. M. Thomas, G. Sankar, I. J. Shannon, and C. R. A. Catlow, *Chemical Communications*, 2001 (1996).

17. J. L. Jorda, L. B. McCusker, C. Baerlocher, C. M. Morais, J. Rocha, C. Fernandez, C. Borges, J. P. Lourenco, M. F. Ribeiro, and Z. Gabelica, *Microporous and Mesoporous Materials*, *65*, 43 (2003).

18. J. P. Coulomb, C. Martin, Y. Grillet, and N. Tosipellenq, *Studies in Surface Science and Catalysis*, *84*, 445 (1994).

19. I. Saadoune, C. R. A. Catlow, K. Doll, and F. Cora, *Molecular Simulation*, *30*, 607 (2004).

20. A. M. Beale, G. Sankar, C. R. A. Catlow, P. A. Anderson, and T. L. Green, *Phys. Chem. Chem. Phys.*, *7*, 1856 (2005).

21. http://www.bza.org/zeolites.html.

22. A. Meden, L. B. McCusker, C. Baerlocher, N. Rajic, and V. Kaucic, *Microporous and Mesoporous Materials*, *47*, 269 (2001).

23. J. L. Paillaud, P. Caullet, L. Schreyeck, and B. Marler, *Microporous and Mesoporous Materials*, *42*, 177 (2001).

24. V. Ramaswamy, L. B. McCusker, and C. Baerlocher, *Microporous and Mesoporous Materials*, *31*, 1 (1999).

25. A. Simmen, L. B. McCusker, C. Baerlocher, and W. M. Meier, *Zeolites*, *11*, 654 (1991).

26. L. Gomez-Hortiguela, F. Cora, C. R. A. Catlow, and J. Perez-Pariente, *Journal of the American Chemical Society*, *126*, 12097 (2004).

27. K. D. Schmitt and G. J. Kennedy, *Zeolites*, *14*, 635 (1994).

28. A. P. Stevens, A. H. Gorman, C. M. Freeman, and P. A. Cox, *Journal of the Chemical Society - Faraday Transactions*, *92*, 2065 (1996).

29. P. A. Cox, J. L. Casci, and A. Stevens, *Faraday Discussions*, *106*, 473 (1997).

30. D. W. Lewis, D. J. Willock, and C. R. A. Catlow, *Nature*, *382*, 604 (1996).

31. A. C. Larson and R. B. Von Dreele, *Los Alamos National Laboratory Report LAUR 86-748* (2000).

32. B. H. Toby, *Journal of Applied Crystallography*, *34*, 210 (2001).

33. K.-J. Chao, S.-P. Sheu, and H.-S. Sheu, *Journal of the Chemical Society - Faraday Transactions*, *88*, 2949 (1992).

34. L. B. McCusker, R. B. Von Dreele, D. E. Cox, D. Louer, and P. Scardi, *Journal of Applied Crystallography*, *32*, 36 (1999).

35. W. Kraus and G. Nolze, *PowderCell 2.4*.

36. M. Sanchez-Sanchez and G. Sankar, *Studies in the Surface Science and Catalysis*, *154 Part A-C*, 1021 (2004).

37. D. J. Watkin, C. K. Prout, and P. M. Lilley, Chemical Crystallography Laboratory, University of Oxford, Oxford.

38. W. T. Robinson and G. M. Sheldrick, *Crystallographic Computing 4. Techniques and New Technologies.* , Oxford Univ. Press, Oxford, 1988.

39. S. F. Radaev, W. Joswig, and W. H. Baur, *Journal of Materials Chemistry*, *6*, 1413 (1996).

40. J. M. Bennett, J. P. Cohen, E. M. Flaningen, J. J. Pluth, and J. V. Smith, *ACS Sym. Series*, *218*, 109 (1983).

41. Accelrys, *Cerius2*.

42. Accelrys, *Materials Studio 3.1.*

43. S. C. Popescu, S. Thomson, and R. F. Howe, *Physical Chemistry Chemical Physics*, *3*, 111 (2001).

44. J. Kornatowski, G. Finger, and D. Schultze, *Journal Of Physical Chemistry A* (2002).

45. H. J. Hall, *Journal of American Chemical Society 79*, 5697 (1957).

46. B. Safi, K. Choho, F. De Proft, and P. Geerlings, *Chemical Physics Letters*, *300*, 85 (1999).

47. R. T. Sanderson, *Chemical Bonds and Bond Energy*, Academic Press, New York, 1976.

48. S. P. Elangovan, C. Kannan, B. Arabindoo, and V. Murugesan, *Applied Catalysis A General*, A (1998).

49. G. Lischke, B. Parlitz, U. Lohse, E. Schreier, and R. Fricke, *Applied Catalysis a-General*, *166*, 351 (1998).

50. T. Ikeda, K. Miyazawa, F. Izumi, Q. Huang, and A. Santoro, *Journal of Physics and Chemistry of Solids*, *60*, 1531 (1999).

51. Z. Q. Liu, W. G. Xu, G. D. Yang, and R. R. Xu, *Microporous and Mesoporous Materials*, *22*, 33 (1998).

52. M. A. Camblor, L. A. Villaescusa, and M. J. Diaz-Cabanas, *Topics in Catalysis*, *9*, 59 (1999).

53. K. Maeda, A. Tuel, S. Caldarelli, and C. Baerlocher, *Microporous and Mesoporous Materials*, *39*, 465 (2000).

54. C. Marichal, J. M. Chezeau, M. Roux, J. Patarin, J. L. Jorda, L. B. McCusker, C. Baerlocher, and P. Pattison, *Microporous and Mesoporous Materials*, *90*, 5 (2006).

55. A. Tuel, V. Gramlich, and C. Baerlocher, *Microporous and Mesoporous Materials*, *47*, 217 (2001).

56. N. N. Tusar, N. Z. Logar, I. Arcon, F. Thibault-Starzyk, and V. Kaucic, *Croatica Chemica Acta*, *74*, 837 (2001).

57. B. Wei, G. S. Zhu, J. H. Yu, S. L. Qiu, F. S. Xiao, and O. Terasaki, *Chemistry of Materials*, *11*, 3417 (1999).

Chapter 4

Synthesis and Structure Determination of a Novel Layered Aluminophosphate

4.1 Summary

Phenyl-based templates have not been explored in depth in the synthesis of aluminophosphates. Aniline, the most readily available phenyl-based amine, has a high pKb value and hence does not mix easily with the gel. This leads to the formation of AlPO-C, a structure which forms not needing a template present at all. The reason for aniline's low solubility in the gel is the fact that the lone-electron pair on aniline's nitrogen helps to stabilise the delocalised π-electrons of the phenyl-ring and is hence not available for hydration. Introducing inductive alkyl-groups leads to a reduction in the molecule's pKb value and thus a better solubility in the gel mixture. Phenylethylamine was hence chosen as a template for the synthesis, leading to a novel layered aluminophosphate material rather than a 3-dimensional aluminophosphate as expected.

The structure was solved from single crystal X-ray diffraction data and was confirmed by high resolution powder diffraction data. The as-synthesised layered material, with composition $[AlPO_4(OH)](NH_3C_2H_4C_6H_5)]$, crystallises in the monoclinic space group *C 2/c* with a = 39.06(10) Å, b = 5.31(13) Å, c = 9.67(2) Å and $\alpha = 90°$, $\beta = 94.6(4)°$, $\gamma = 90°$. In the aluminophosphate layers, the six-coordinated aluminium polyhedra form extended chains that are cross-linked

by phosphate groups. These inorganic layers are held together through hydrogen bonding to the protonated, organic templates involving the terminal oxygen atoms of the phosphate groups and the nitrogen of the phenylethylamine. Two template molecules can be found between the inorganic layers, held together purely by van-der-Waals and Coulombic forces with the structure remaining stable up to *ca.* 300°C.

Furthermore, the same structure could be synthesised using benzylamine as a template. Other phenyl- and benzyl-based SDAs that were used to produce aluminophosphate materials were *N*-methylaniline and phenylpropylamine. These SDAs did not however yield crystals of sufficient size for single crystal analysis and solving the structure purely by powder XRD methods proved cumbersome due to small impurity phases in the sample.

4.2 Introduction

Since the work by Wilson *et al.* in the early 1980's there has been a large increase in the number of known framework topologies of aluminophosphates (1, 2) many with interesting catalytic and absorption properties (3) as described in chapter 1. The aluminophosphate family now includes structures composed of 1D chains, 2D lamellar-layers and 3D open-framework structures. It is still not clearly understood how certain organic molecules act as structure directing agents (SDAs). Some organic molecules can form layered as well as microporous, open framework structures. 1,4-diaminobutane for example can form a 2D layered structure (4) as well as a 3D aluminophosphate structure (5).

Layered materials also exhibit rich aluminium chemistry. The aluminium can be found in a four (6, 7), five (8, 9) and six co-ordination (9-11) within different layered materials. Unlike most microporous aluminophosphates, several layered aluminophosphate materials exhibit Al-O-Al bonds (9-13). In this part of the work the synthesis and crystal structure of a layered two-dimensional aluminophosphate, $[AlPO_4(OH)\ (NH_3C_2H_4C_6H_5)]$, obtained using phenylethylamine as the organic structure directing agent is described.

Based on the knowledge obtained from the framework–SDA interactions in the AFI topology mentioned previously, SDAs with a pKb value of around 4 were targeted. It was hence possible to synthesise a layered material with a class of amines (phenyl- and benzyl based) that has not been explored in depth so far. Similar layered structures have been reported in literature before (11, 14) and can

be found in nature as the mineral tancoite with octahedral aluminophosphate chains (15) (see Figure 4.1).

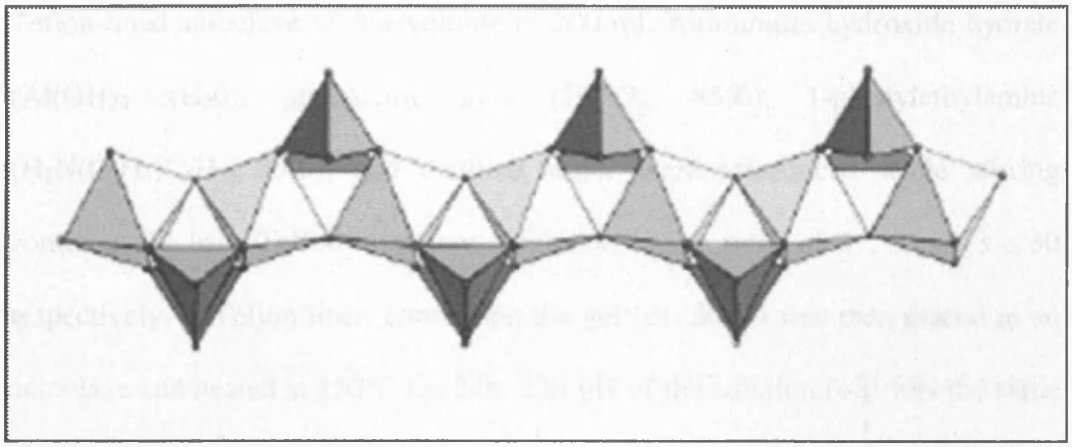

Figure 4.1: Structure of the tancoite-chains represented in polyhedra (15).

Layered aluminophosphate materials are usually synthesised by using diaminoalkanes or aminoalkanes, with the diamine generally doubly protonated to compensate for the negative charge of the anionic aluminophosphate layers (6). To our knowledge, only known aluminophosphate structures have been synthesised using phenyl-based SDAs (16). The focus has been on alkane based amines as aromatic amines (e.g. aniline) do not tend to mix easily with the gel during synthesis. The aim of this project was to explore the use of aromatic amines as templates.

4.3 Synthesis

The synthesis of the layered material was carried out hydrothermally in a Teflon-lined autoclave with a volume of 200 ml. Aluminium hydroxide hydrate ($Al(OH)_3$ xH_20), phosphoric acid (H_3PO_4, 85%), 1-phenylethylamine ($H_2N(C_2H_4)C_6H_5$, 99%), and distilled water were introduced while stirring continuously in a Teflon container, with the molar ratio of 1 : 1 : 1.3 : 30 respectively. A Teflon liner, containing the gel (ca. 50ml) was then placed in an autoclave and heated at 150°C for 24h. The pH of the solution (+8) was the same at the beginning and at the end of the reaction. The material was also synthesised in the presence of 10% zinc as well as cobalt acetate tetrahydrate in combination with a reduction in the molar ratio of the aluminium species to 0.9. Several different synthesis conditions were investigated to observe the SDA's ability to form further structures. A list of all conditions can be seen in Table 4.1:

Table 4.1: Synthesis conditions using phenylethylamine as template (temp).

No.	Gel mixture	T [1)]	Duration	Phase
1	1.0 Al : 1.0 P : 0.8 temp : 30 H_2O	150° C	24 h	LM [2)]
2	1.0 Al : 1.0 P : 1.3 temp : 30 H_2O	150° C	24 h	LM
3	0.9 Al : 0.1 Co : 1.0 P : 0.8 temp : 30 H_2O	150° C	24 h	LM
4	0.9 Al : 0.1 Co : 1.0 P : 1.3 temp : 30 H_2O	150° C	24 h	LM
5	0.9 Al : 0.1 Co : 1.0 P : 1.3 temp : 30 H_2O	190° C	24 h	LM+AFI [3)]
6	0.9 Al : 0.1 Zn : 1.0 P : 1.3 temp : 30 H_2O	150° C	24 h	LM
7	0.7 Al : 0.3 Co : 1.0 P : 1.3 temp : 30 H_2O	150° C	24 h	LM
8	0.5 Al : 0.5 Co : 1.0 P : 1.3 temp : 30 H_2O	150° C	24 h	LM
9	0.9 Al : 0.1 Co : 1.0 P : 2.0 temp : 30 H_2O	150° C	24 h	LM
10	0.9 Al : 0.1 Co : 1.0 P : 1.3 temp : 50 H_2O	150° C	24 h	LM
11	0.9 Al : 0.1 Co : 1.0 P : 1.3 temp : 5 H_2O	150° C	24 h	LM
12	0.9 Al : 0.1 Co : 1.0 P : 1.3 temp : 30 H_2O	150° C	120 h	LM

[1)] T = Temperature; [2)] LM = Layered Material; [3)] AFI = AlPO-5 topology

Under most conditions phenylethylamine forms the layered material. Only when the synthesis gel is placed at elevated temperatures, AlPO-5 is formed as an impurity (see Figure 4.2).

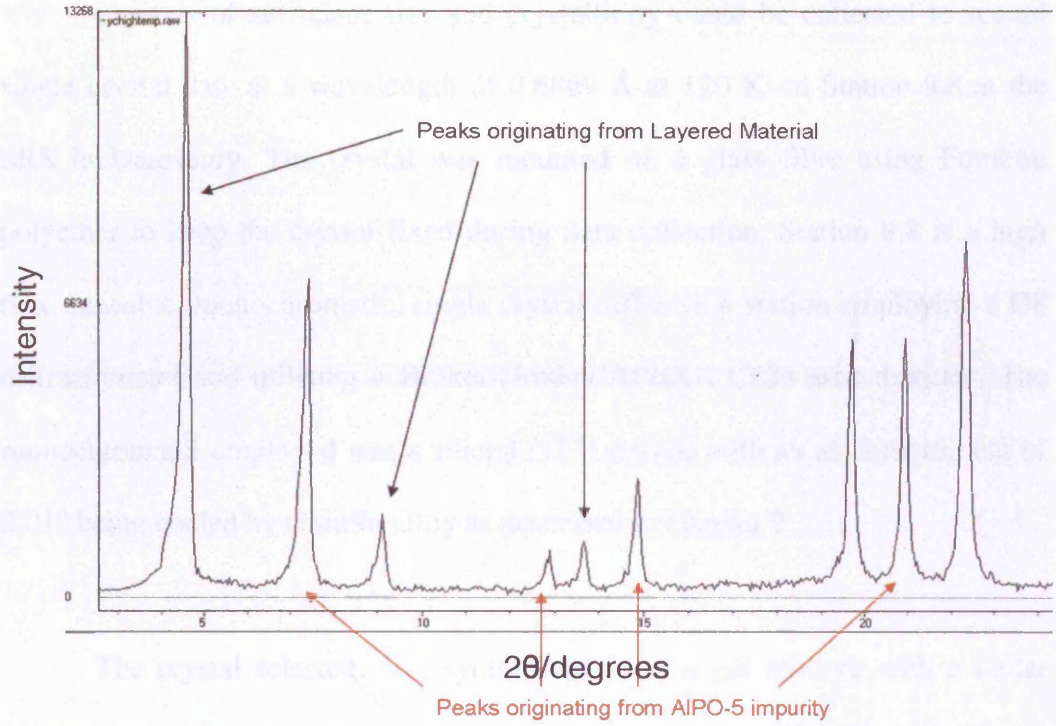

Figure 4.2: XRD pattern of the sample obtained from synthesis No.5, showing the AlPO-5 impurity in the data.

It can be hence concluded, that phenylethylamine has a high affinity to form the layered structure, but seems also to be able to form the AFI topology under specific conditions.

4.4 Structure Solution

4.4.1 Single Crystal X-Ray Diffraction Study

Crystals of sufficient size and crystallinity could be collected to record single crystal data at a wavelength of 0.6869 Å at 120 K on Station 9.8 at the SRS in Daresbury. The crystal was mounted on a glass fibre using Fomblin polyether to keep the crystal fixed during data collection. Station 9.8 is a high flux, tuneable, monochromatic, single crystal diffraction station employing a D8 diffractometer and utilising a Bruker-Nonius APEXII CCD area detector. The monochromator employed was a silicon (111) crystal with an asymmetric cut of 2.01° being cooled by GaInSn alloy as described in chapter 2.

The crystal selected, was synthesised from a gel mixture with a molar ratio of 1.0 P : 0.9 Al : 0.1 Co : 1.3 phenylethylamine : 30 H_2O. The crystal was carefully examined under a polarised optical microscope, where it appeared bright against a dark background. Upon rotation into different orientations however it turned dark. The crystal showed optical extinction, and it could hence be assumed that the crystal was single as supposed to being a multiple of different crystals attached to one-another. Initially a run with the shutters closed was recorded for background subtraction. The crystal had a size of 50 : 50 : 30 μm (see Figure 4.3).

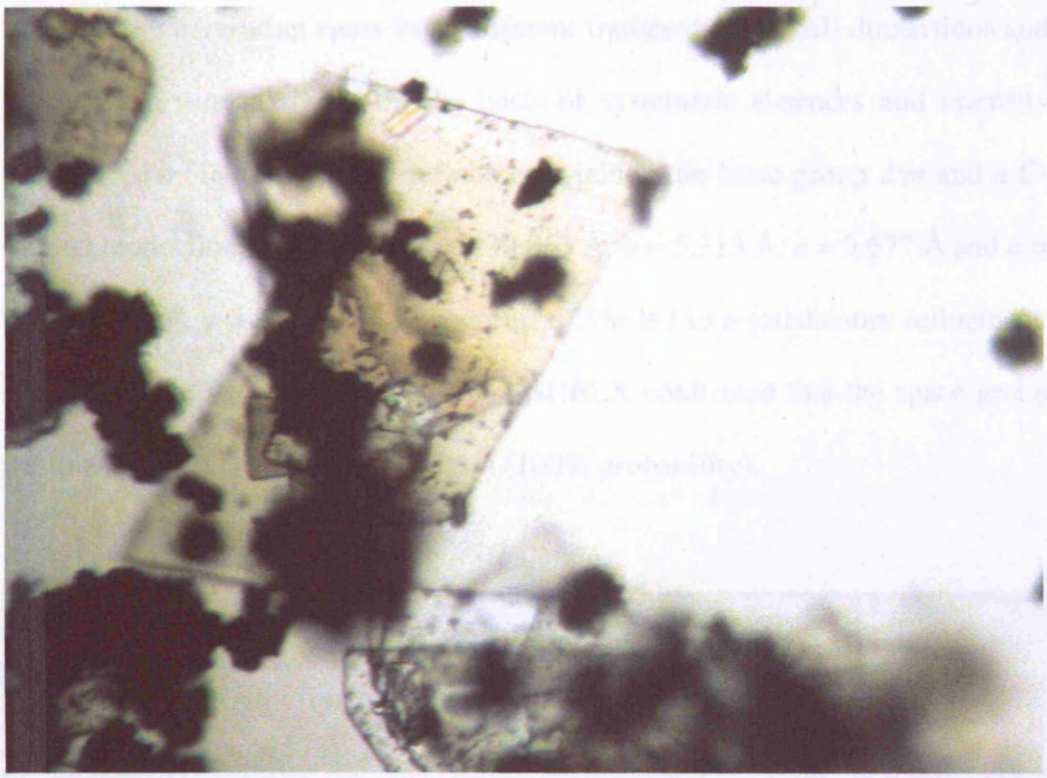

Figure 4.3: Layered material crystal with a size of 50 : 50 : 30 μm, selected for single crystal XRD data collection.

An initial short data collection was recorded ensuring the crystal was of sufficient quality, allowing the data collected to be indexed and to obtain an orientation matrix for the crystal. The ability to index the initial pattern gave encouragement that it would be possible to process a full dataset and hence, a whole hemisphere of data was collected, with a 10s / frame step size. Coverage of a hemisphere of reciprocal space was achieved by 0.1° frame increments, with a 2θ collection range of 2.04 to 31.11° (Index range $-53 < h < 53$, $-8 < k < 8$, $-15 < l < 15$) . 3045 reflections were collected and merged to yield 1723 unique reflections.

After harvesting spots from different frames the unit cell dimensions and space group were assigned on the basis of systematic absences and intensity statistics (see Figure 4.4). The refinement yielded the Laue group *2/m* and a C-centred monoclinic unit cell with $a = 39.063$ Å, $b = 5.313$ Å, $c = 9.677$ Å and $\alpha = 90°$, $\beta = 94.6°$, $\gamma = 90°$. The space group *C 2/m* led to a satisfactory refinement. After complete structure determination, SHELX confirmed that the space group was the appropriate one for the system (100% probability).

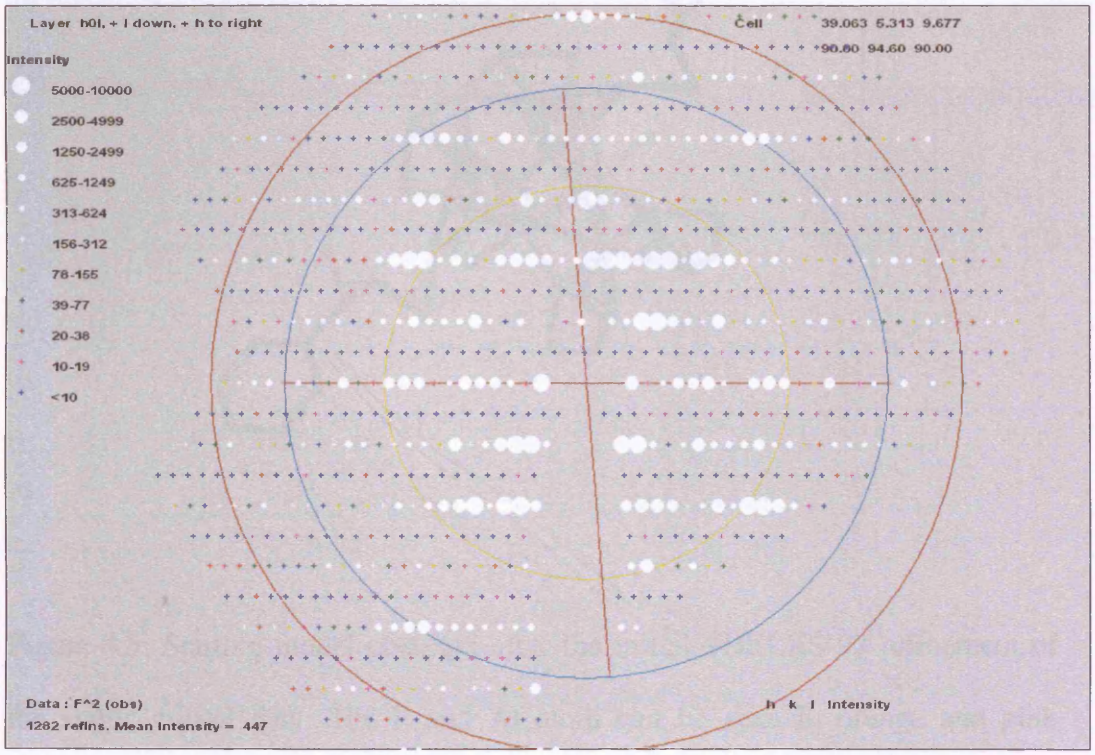

Figure 4.4: Single crystal pattern obtained from X-ray diffraction experiment (intensity measures of peaks are shown in the legend).

The structure was solved using a combination of single crystal software suits WinGX (17) and Crystals (18). SHELXS-97 (19) was used to locate the framework atoms as well as the organic molecules employing direct methods and knowledge of the system to be refined, i.e. atom types present in the structure. It

was assumed that an $AlPO_4$-structure had been synthesised and hence a starting model was selected with following atomic ratio: 1 Al : 1 P : 4 O : 1 N : 8 C. This yielded a reasonable starting model (see Figure 4.5), finding the Al and P atom within the structure.

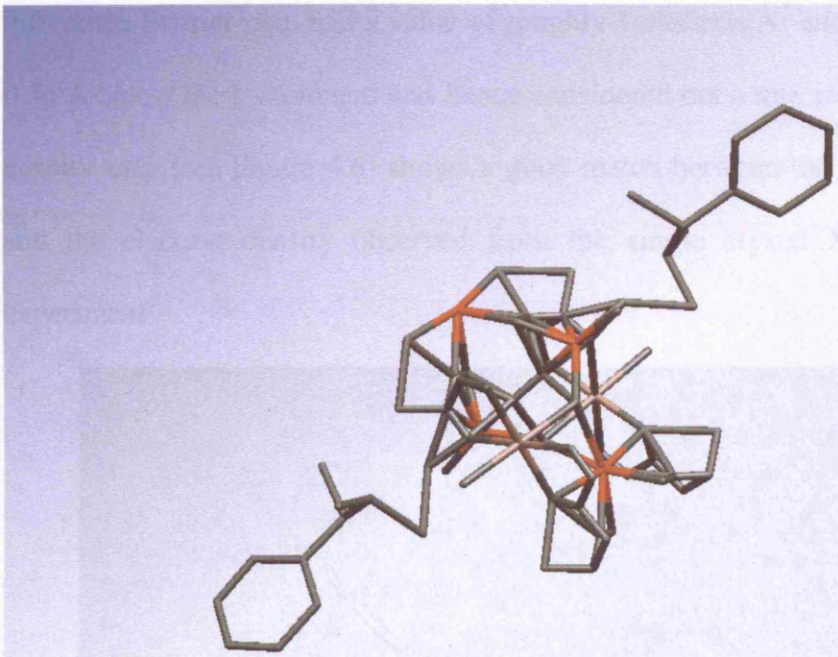

Figure 4.5: Starting model obtained after the initial SHELXS-97 refinement of the single crystal data. The P and Al atom can be seen in orange and pink respectively, while the Q-peaks are in grey.

Phenylethylamine was easily detected within the structure through the Q-peaks obtained from the refinement (see Q-peaks in Figure 4.5). The missing oxygen atoms were detected from the remaining Q-peaks by examining their intensities and bond distances from the already located Al and P atoms.

The phenyl H-atoms' positions were calculated based on stereo-chemical considerations. The final refinement of the structure was performed on the data having $I > 2\sigma(I)$ and included anisotropic thermal parameters for all non-hydrogen atoms. A satisfactory refinement of the data was obtained with the final agreement factors being $R_1 = 0.0639$ and $wR_2 = 0.073$. The highest peak in the difference Fourier map had a value of roughly 1 electron/Å^3 and was placed just 0.56 Å below the P-atom and was hence considered not a true atom. The electron density map (see Figure 4.6) shows a good match between the refined structure and the electron density observed from the single crystal X-ray diffraction experiment.

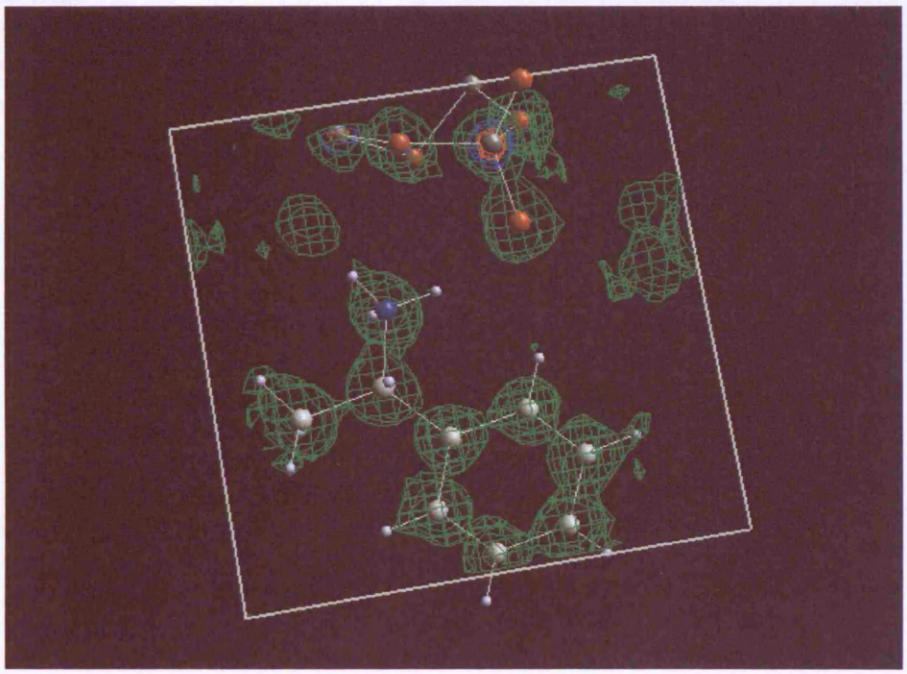

Figure 4.6: Refined structure of layered material (asymmetric unit) with the electron density obtained from the single crystal X-ray diffraction experiment.

A summary of the single crystal X-ray experiment is given in Table 4.2. Final positional and equivalent isotropic thermal parameters are listed in Table 4.3, while selected bond distances and angles appear in Table 4.4.

Table 4.2: Crystallographic data and structure refinement for the layered material.

Identification	Layered material
Empirical Formula	$[AlPO_4(OH)](NH_3C_2H_4C_6H_5)$
Formula Weight	261 g mol^{-1}
Temperature (K)	120
Wavelength (Å)	0.68690
Crystal System, Space Group	Monoclinic, *C 2/c*
Unit Cell Dimensions	a = 39.06(10) Å
	b = 5.31(13) Å
	c = 9.67(2) Å
	$\alpha = 90°$
	$\beta = 94.6(4)°$
	$\gamma = 90°$
Volume	2002 $Å^3$
F(000)	594.0
Crystal Size	0.05 x 0.05 x 0.03 mm
Independent Reflections ($I > 0$)	3337
No. obs. Data [$I > 2\sigma(I)$]	2388
Final R indices	$R_1 = 0.0639$
	$wR_2 = 0.073$

Table 4.3: Atomic coordinates and equivalent isotropic displacement parameters for the layered material.

Atom	*x*	*y*	*z*	$U(eq)Å^2$
P1	0.04550(4)	0.2022(3)	0.26295(11)	0.01704
Al1	0.00000	-0.3168(4)	0.25000	0.01837
Al2	0.00000	0.00000	0.00000	0.01684
O1	0.02704(10)	-0.0177(7)	0.3379(3)	0.00086
O2	0.03500(9)	0.1897(7)	0.1050(3)	0.01858
O3	0.03282(10)	0.4544(7)	0.3178(3)	0.01982
O4	0.08348(10)	0.1779(8)	0.2936(3)	0.02439
O5	0.01925(10)	-0.2802(7)	0.0835(3)	0.01953
H12	0.023906	-0.431250	0.047812	0.04972
N1	0.09246(13)	-0.2652(10)	0.4398(4)	0.02869
H1A	0.08906	-0.40020	0.38142	0.04303
H1B	0.09458	-0.12358	0.38782	0.04303
H1C	0.07401	-0.24902	0.49068	0.04303
C1	0.12075(18)	-0.5594(13)	0.6024(6)	0.03589
H1D	0.09802	-0.57128	0.63831	0.05383
H1E	0.13845	-0.57295	0.68122	0.05383
H1F	0.12383	-0.69318	0.53673	0.05383
C2	0.12429(15)	-0.3042(12)	0.5321(5)	0.02611
H2	0.12482	-0.17165	0.60652	0.03134
C3	0.15654(15)	-0.2745(12)	0.4566(5)	0.02720
C4	0.18367(17)	-0.4415(13)	0.4784(6)	0.03372
H4	0.18183	-0.58155	0.53847	0.04047
C5	0.21374(18)	-0.4067(15)	0.4135(8)	0.04364
H5	0.23240	-0.52023	0.43151	0.05236
C6	0.21706(18)	-0.2047(16)	0.3246(8)	0.0438
H6	0.23735	-0.18446	0.27853	0.05266
C7	0.19034(17)	-0.0350(13)	0.3025(6)	0.03538
H7	0.19239	0.10353	0.24010	0.04245
C8	0.16031(16)	-0.0685(12)	0.3678(6)	0.02873
H8	0.14201	0.04921	0.35343	0.03448

Table 4.4: Selected bond lengths (in Å) and angles (in degree).

P1 – O4	1.495(4)
P1 – O3	1.538(4)
P1 – O2	1.552(3)
P1 – O1	1.579(4)
Al1 – O5	1.842(3)
Al1 – O3	1.848(4)
Al1 – O1	2.054(4)
Al2 – O5	1.827(4)
Al2 – O2	1.922(4)
Al2 – O1	1.963(3)
C2 – N1	1.486(7)
C1 – C2	1.528(9)
C2 – C3	1.515(8)
C3 – C4	1.385(9)
C4 – C5	1.388(9)
C5 – C6	1.388(11)
C6 – C7	1.383(10)
C7 – C8	1.388(9)
C3 – C8	1.406(8)
O4 – P1 – O3	110.4(2)
O4 – P1 – O2	111.8(2)
O3 – P1 – O2	108.1(2)
O1 – P1 – O4	109.1(2)
O1 – P1 – O3	108.35(19)
O1 – P1 – O2	109.1(2)
O5 – Al1 – O5	167.9(3)
O5 – Al1 – O3	93.41(16)
O3 – Al1 – O3	97.8(2)
O1 – Al1 – O5	92.75(16)
O1 – Al1 – O3	167.06(17)
O1 – Al1 – O1	78.7(2)
O5 – Al2 – O2	93.25(16)
O2 – Al2 – O2	179.99(4)
O1 – Al2 – O5	99.43(15)
O1 – Al2 – O2	90.48(14)
O1 – Al2 – O1	179.99(4)
C1 - C2 - N1	106.9(5)
C1 - C2 - C3	114.6(5)
N1 - C2 - C3	112.5(4)
C2 - C3 - C4	121.0(6)
C2 - C3 - C8	120.5(5)
C4 - C3 - C8	118.4(6)
C3 - C4 - C5	120.7(6)
C4 - C5 - C6	120.5(7)
C5 - C6 - C7	119.5(6)
C6 - C7 - C8	120.1(6)
Al1 -. O1 - Al2	94.37(16)
Al1-. O1 - P1	128.28(18)

4.4.2 Scanning Electron Microscope Study

The morphology of the sample was characterized by scanning electron microscopy employing a Jeol JSM-630 IF scanning microscope. The material's physical appearance was obtained in a plate-like layered structure (see Figure 4.7), representing the layers, found within the unit cell.

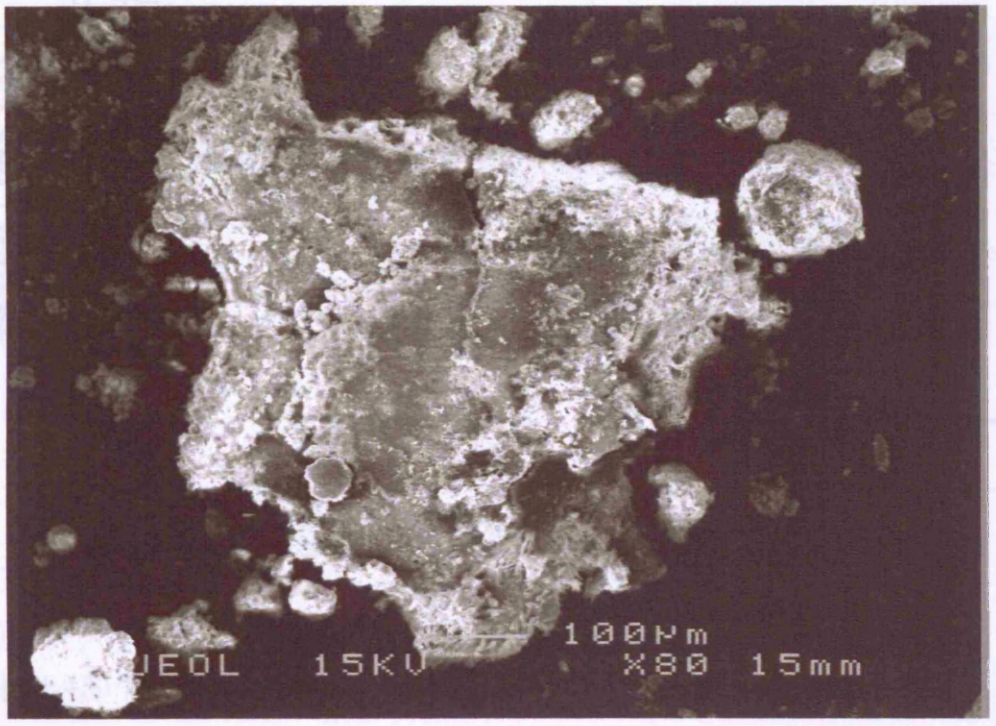

Figure 4.7: SEM image of layered material. The layers that can be seen in the material's unit cell are also clearly visible in the material's crystal morphology.

4.4.3 Thermo-Gravimetric Analysis

Thermo-gravimetric analysis (TGA) and differential thermal analysis (DTA) were performed on a PU 4K (Rigaku) equipped with a quadrupole mass

spectrometer (MS, Anelva M-QA200TS), under a mixture of argon (90%) and oxygen (10%) atmosphere with a heating rate of 5K / min between 22°C and 800°C. The thermogram revealed a weight loss of 51.8% up to 650°C (see Figure 4.8). This loss can be attributed to the loss of the organic anchors, holding the structure together.

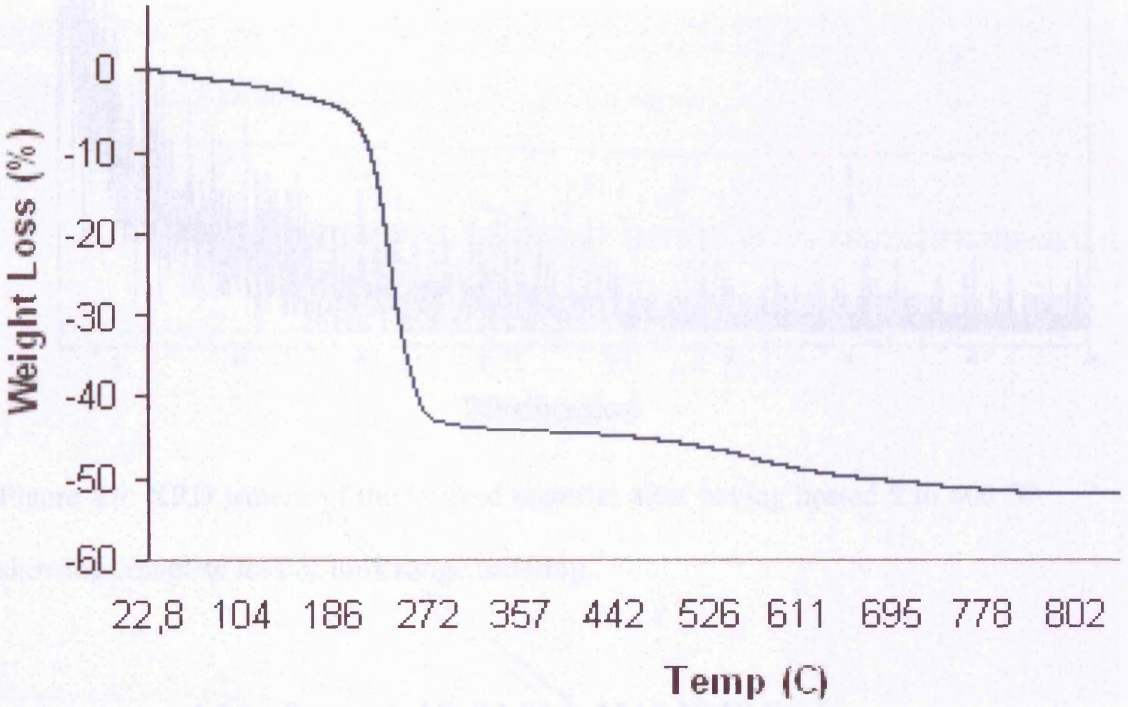

Figure 4.8: Thermo-gravimetric analysis of the layered material under a 90% argon and 10% oxygen atmosphere (heating rate 5°C / min).

The residue obtained after heating the material to 400°C was examined using X-ray diffraction employing a Siemens D4 (see Figure 4.9). The material had lost all long-range order and was completely amorphous after having been heated to 400°C, which can be explained by the material's crystallinity being lost due to the loss of the organic anchor, holding the inorganic planes together.

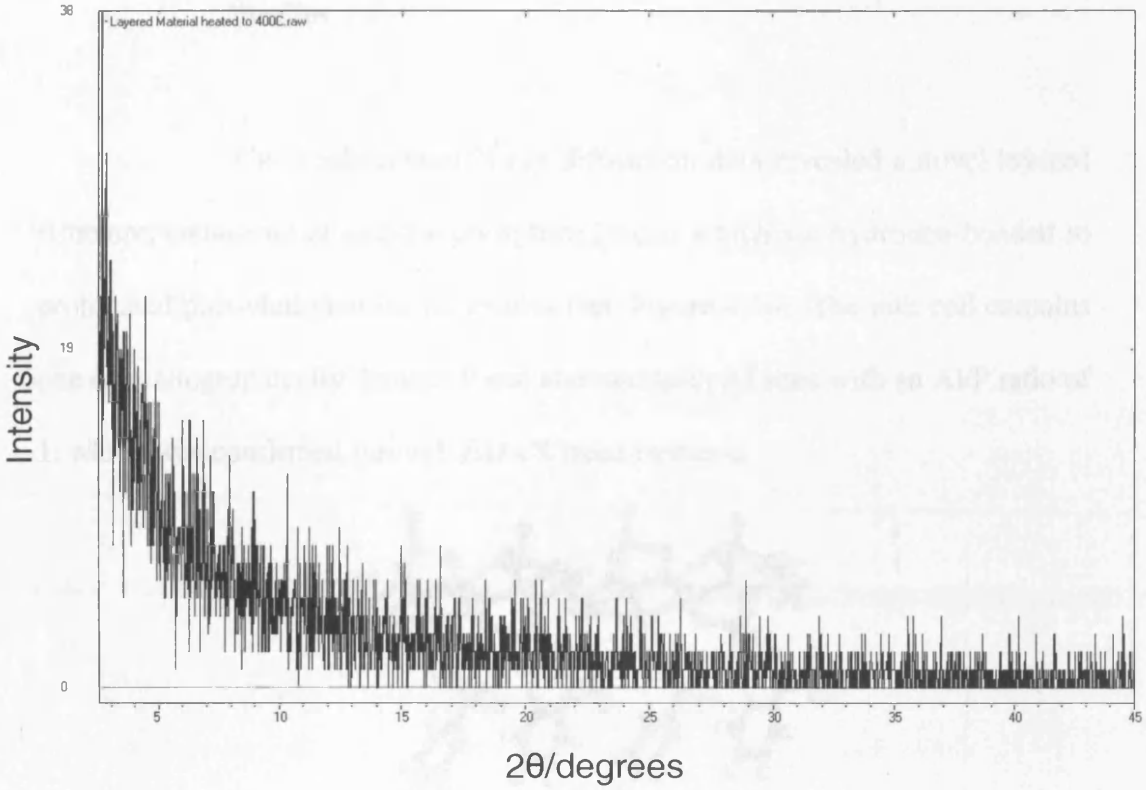

Figure 4.9: XRD pattern of the layered material after having heated it to 400 °C, showing complete loss of long range ordering.

4.4.4 Decoupled Solid-State MAS NMR Study

Decoupled solid-state Magic Angle Spinning (MAS) NMR was acquired for ^{27}Al to gain further insight into the co-ordination chemistry of the aluminium. ^{27}Al MAS NMR spectra were recorded on a Bruker MSL-300 spectrometer at 78.2 MHz. All measurements were carried out at room temperature, with $Al(H_2O)_6^{+3}$ being used as an external standard. The presence of octahedral aluminium was confirmed by decoupled ^{27}Al solid-state MAS NMR, giving rise to a peak at -7.93 ppm.

4.5 Structure Description from Single Crystal X-Ray Diffraction Studies

The single crystal X-ray diffraction data revealed a novel layered structure, consisting of aluminophosphate layers, which are hydrogen-bonded to protonated phenylethylamine molecules (see Figure 4.10). The unit cell contains one crystallographically distinct P site and two such Al sites with an Al/P ratio of 1, which was confirmed through EDAX measurements.

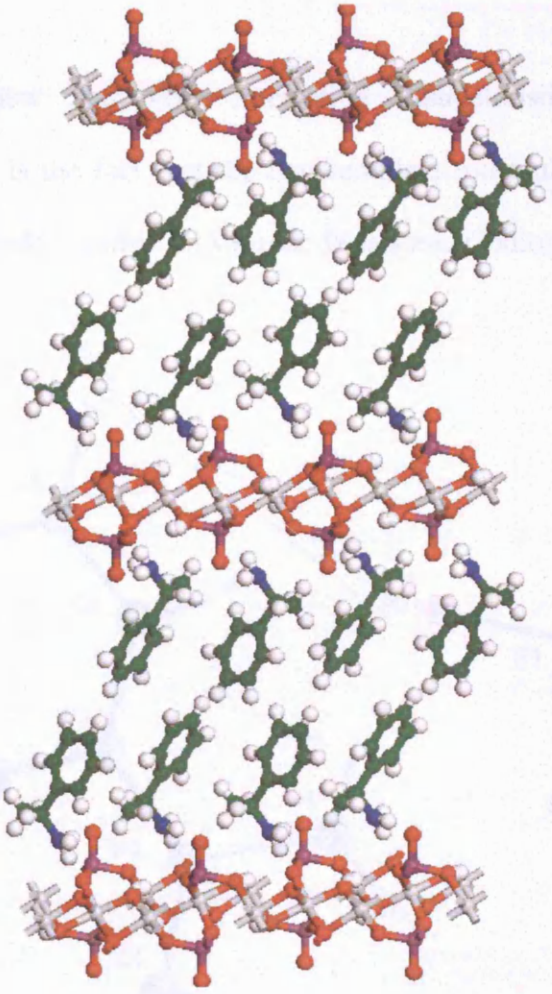

Figure 4.10: Structure of the layered aluminophosphate, showing two template molecules hydrogen-bonded to layers of the material.

Usually only one organic molecule can be found, connecting the sheets in layered aluminophosphates (9, 11, 13). However, in this structure two phenylethylamines can be found between the inorganic sheets leading to a very large d-spacing between the inorganic layers of approximately 14Å. The largest spacing between layers in other aluminophosphate materials found is approximately 11Å (6) arising from the template's (diaminooctane) relatively long alkane chain, rather than from two template molecules sitting in the void between the sheets.

Another new and very interesting characteristic of the layered aluminophosphate is the fact that the two template molecules between the two sheets are mainly held together by van-der-Waals and Coulombic forces.

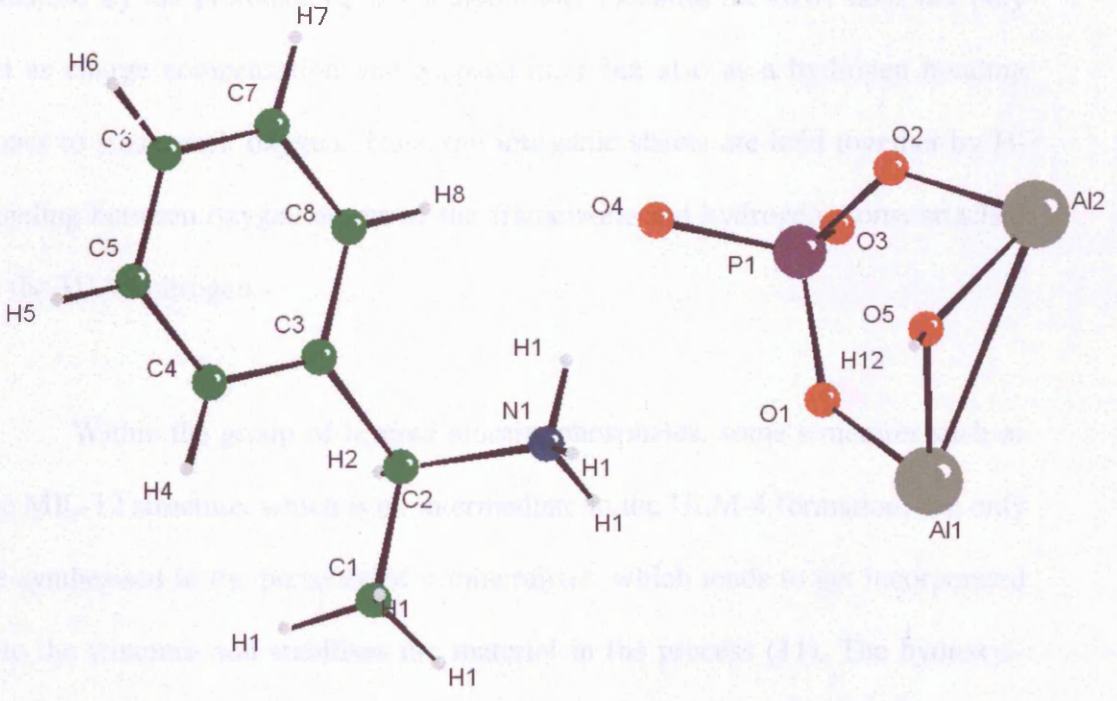

Figure 4.11: Asymmetric unit of the layered aluminophosphate.

The unit cell also includes one hydroxyl-group to partly charge compensate for the Al/P ratio of 1 (see Figure 4.11). The position of this hydrogen (on the O5 site) was confirmed by quantum mechanical (QM) calculations run by Dr. Corà (see Appendix A), showing that it is essential for the hydrogen to sit on this site as the structure tends to undergo deformation otherwise (O3 and O4). The QM code CRYSTAL was employed for these calculations, using the periodic hybrid DFT functional B3LYP code. Another possible position for the hydrogen is the O1 and O2 oxygen atom. The hydrogen however moves to the O5 site regardless during the calculations. Surprisingly however the Al-O bond length around the hydroxyl-group is unexpectedly short at ~1.85 Å.

The inorganic layer is however still negatively charged and is hence balanced by the protonated phenylethylamine, meaning the SDA does not only act as charge compensation and a space-filler but also as a hydrogen bonding donor to framework oxygen. Thus, the inorganic sheets are held together by H-bonding between oxygen atoms of the framework and hydrogen atoms attached to the SDA's nitrogen.

Within the group of layered aluminophosphates, some structures such as the MIL-12 structure, which is an intermediate in the ULM-4 formation, can only be synthesised in the presence of a mineraliser, which tends to get incorporated into the structure and stabilises the material in the process (11). The hydroxyl-group in this layered material might also be considered to act as a mineraliser as it is essential for the overall structure's stability.

The inorganic layer is made up of octahedral aluminium ions, which are connected to each other through bridging oxygen atoms forming *cis*-chains. All aluminium octahedra are interconnected through edge-sharing giving rise to a zig-zag arrangement lying along the (010) axis. Lowenstein's rule states that Al-O-Al bonds are forbidden. This rule, however, only applies to tetrahedrally coordinated aluminium. In contrast to 3D materials, where the aluminium usually is found in a tetrahedral arrangement, the aluminium in this layered material is in an octahedral arrangement and thus does not break Lowenstein's rule. Other layered materials have been reported before with this unusual Al-O-Al bonding (6, 9-12).

These Al-O-Al chains are interconnected to each other by tetrahedral phosphate groups above and below, which in turn are linked to three different aluminium octahedra. The fourth oxygen on the phosphate tetrahedron is hydrogen bonded to the protonated amine group of the SDA. The phosphate groups running along the *z*-axis are in alternating arrangements giving rise to a crisscross pattern. Unlike tancoite (as described in chapter 4.2), the phosphate groups lie exactly in the same position above and below the alumina chains along the *x*-axis, but in a staggered arrangement (see Figure 4.12).

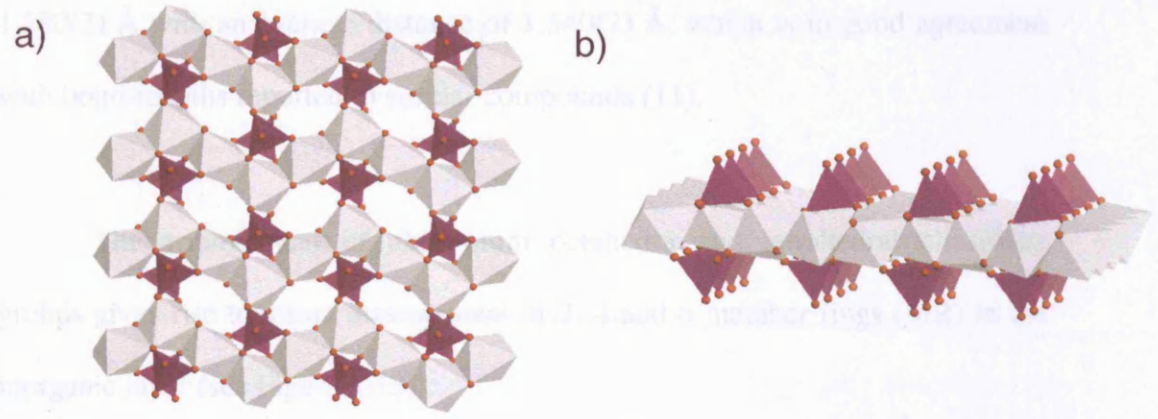

Figure 4.12: Layers of the aluminophosphate material (grey octahedral being aluminium and purple tetrahedra being phosphorus):

a) View along (100) axis showing octahedral aluminium chains interlinked by tetrahedral phosphate groups.
b) View along (010) axis showing the tetrahedral phosphate groups above and below the aluminium chains.

It can be assumed, that due to this arrangement of terminal phosphate groups with no terminal hydroxyl-groups present, lying exactly above each other in the different layers, it has not been possible to form 3-dimensional structures, as is the case with MIL-12, which is an intermediate in the formation of ULM-4 (11).

In the aluminium octahedron, distances range from 1.835(7) to 2.057(9) Å for Al (1) and from 1.826(3) to 1.958(2) Å for Al (2) (see Table 4.4). The mean values (1.914(9) and 1.902(6) Å for Al(1) and Al(2) respectively) are in good agreement to previous reported bond lengths for octahedral Al-O bonds (9). The O-Al-O linkage, showing a 180° angle is expected and has been reported before for similar compounds (10, 12). The P-O distances range from 1.502(0) to

1.580(3) Å with an average distance of 1.540(7) Å, which is in good agreement with bond-lengths reported in similar compounds (11).

The arrangement of aluminium octahedra and tetrahedral phosphate groups gives rise to a rare arrangement of 3, 4 and 6 member rings (MR) in the inorganic layer (see Figure 4.13).

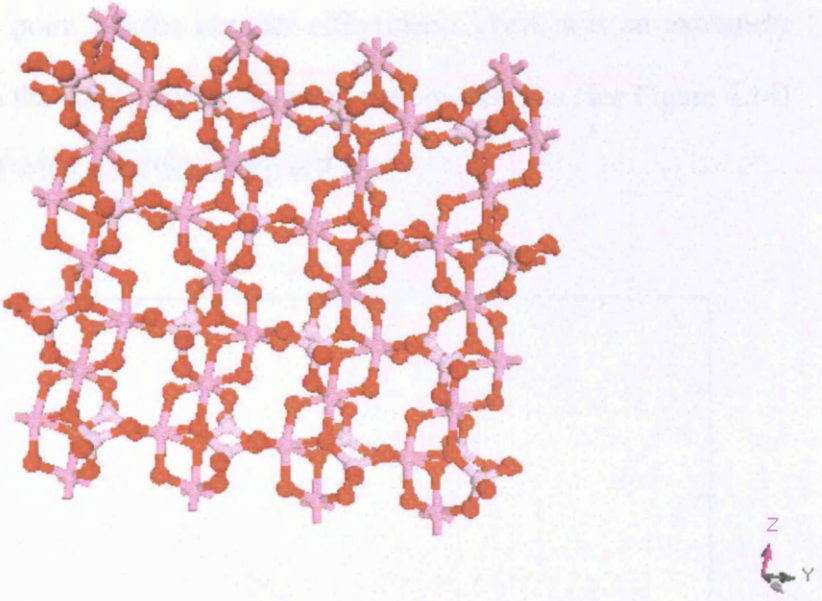

Figure 4.13: Structure of the aluminophosphate layer, made up of 3, 4 and 6 member rings.

The pseudo-2 MRs, present in the layers are made up of two aluminium octahedra linked together by two oxygen atoms, i.e. giving rise to edge sharing between the octahedra. Aluminium octahedra with a tetrahedral phosphate group located just above the 2 MRs then give rise to the 3 MRs. The 4 MRs are made up of 2 octahedral aluminium in two different chains connected *trans* to tetrahedral phosphate groups, which bind the aluminium chains together. Four

aluminium octahedra and two phosphate tetrahedra make up the 6 MRs, which lie along the *z*-axis.

The powder-XRD pattern of the sample collected on Station 2.3 at the SRS, was analysed using the GSAS EXPGUI Rietveld software (20, 21) to show that the crystal structure observed is the bulk material synthesised, rather than an impurity. The atom coordinates obtained from the single crystal refinement were used as the starting point for the powder refinement. There was an extremely good match between the single crystal data and the powder data (see Figure 4.14) with fitting values of wRp = 9.7% and Rp = 7.7%.

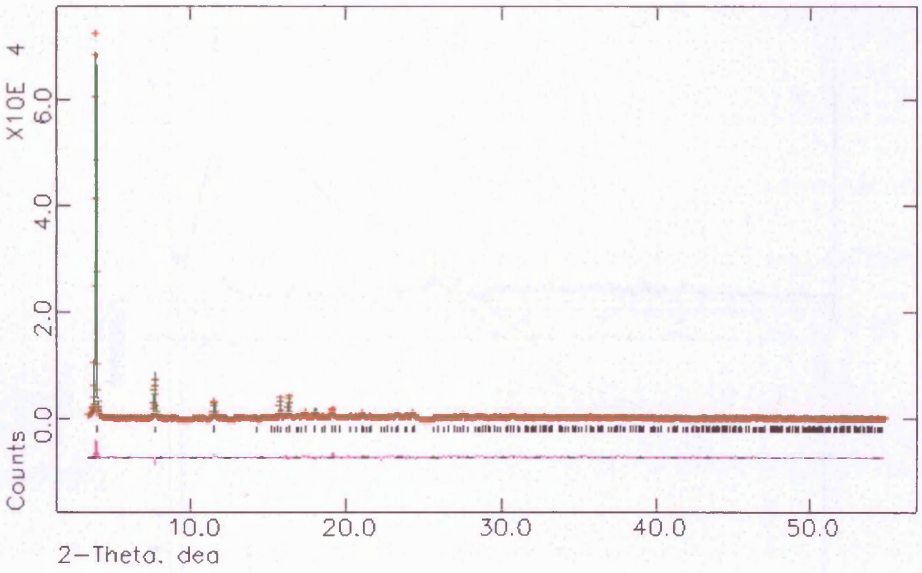

Figure 4.14: XRD pattern of the layered material solved by using the coordinates and space group obtained through the analysis of the single crystal X-ray diffraction data (giving rise to wRp = 9.7% and Rp = 7.7%).

4.6 Crystal Structures Obtained from Different Phenyl- and Benzyl-Based SDAs

Based on the principle of starting with aniline and reducing the SDAs pKb value through inductive groups, other phenyl- and benzyl-based SDAs (*N*-methylaniline, benzylamine and phenylpropylamine) were used. These templates did not yield single crystals of sufficient size to collect single crystal data on however. Only powder XRD patterns could be collected for these samples (see Figure 4.15).

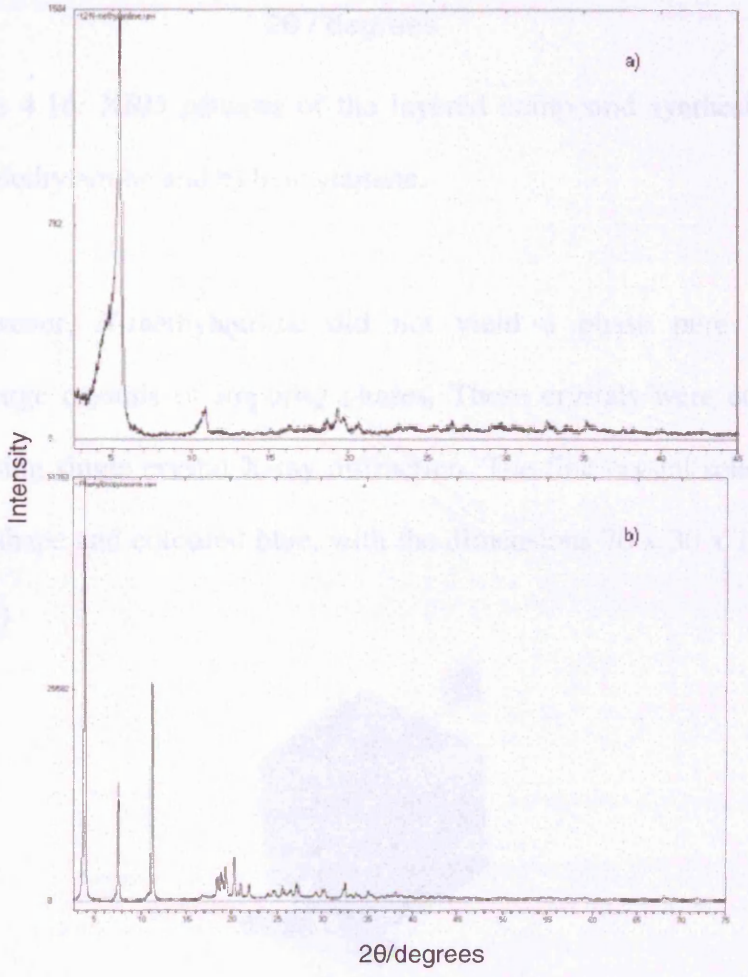

Figure 4.15: XRD pattern of the materials synthesised with a) *N*-methylaniline and b) phenylpropylamine.

The XRD pattern of the material synthesised with benzylamine shows that it is identical to the layered material formed by phenylethylamine (see Figure 4.16).

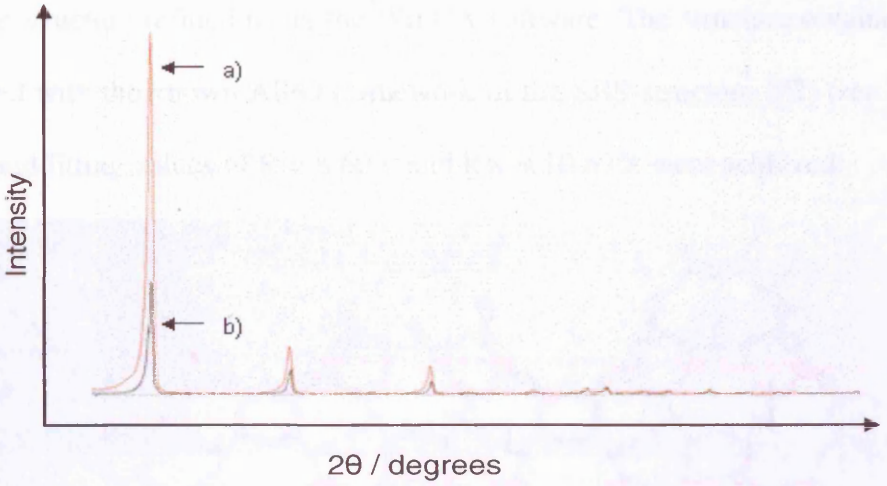

Figure 4.16: XRD patterns of the layered compound synthesised with a) phenylethylamine and b) benzylamine.

However, *N*-methylaniline did not yield a phase pure sample but produced large crystals of impurity phases. These crystals were collected and analysed using single crystal X-ray diffraction. The first crystal selected was of hexagonal shape and coloured blue, with the dimensions 70 x 30 x 17.5 μm (see Figure 4.17).

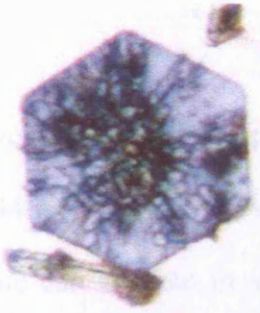

Figure 4.17: Crystal (70 x 30 x 17.5 μm) collected from the sample, using *N*-methylaniline as the SDA.

A whole hemisphere of data was again collected at a wavelength of 0.6869 Å at 120K. After obtaining the unit cell dimensions and space group on the basis of systematic absences and intensity statistics the data were analysed and the structure refined using the WinGX software. The structure obtained was matched with the known AlPO framework of the SBS-structure (22) (see Figure 4.18) and fitting values of R = 8.60% and Rw = 10.67% were achieved.

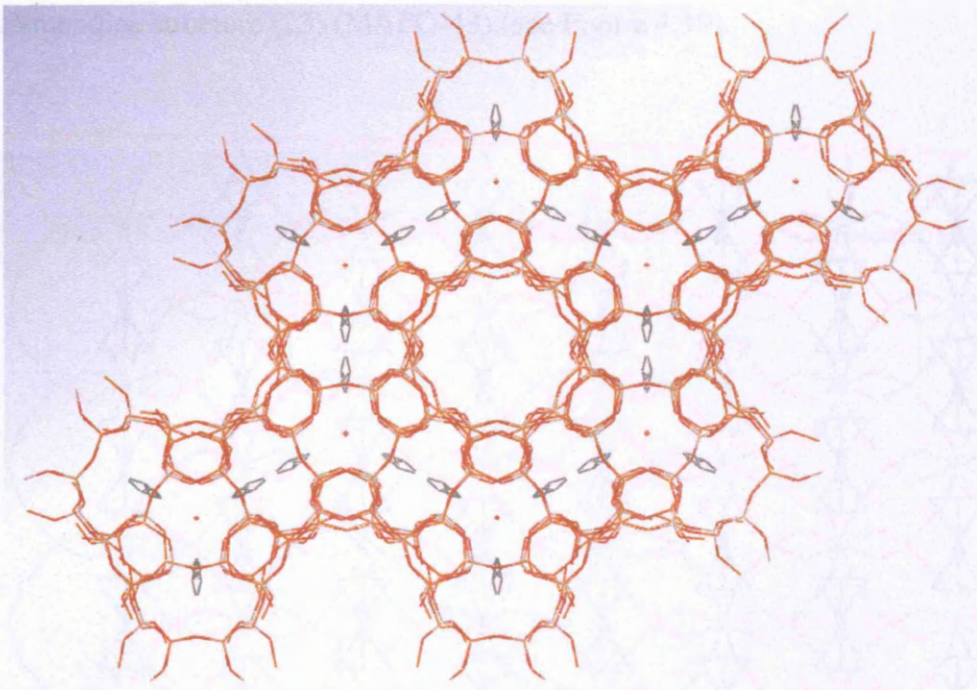

Figure 4.18: The SBS structure UCSB-6 (view along the (001) axis) obtained using *N*-methylaniline as SDA, which can be seen sitting within the framework structure.

The structure was solved in the trigonal space group *P -3 1 c* and had unit cell dimensions of a = 17.5694 Å; b = 17.5694 Å; c = 26.8772 Å; and $\alpha = 90°$; $\beta = 90°$; $\gamma = 120°$. The template can be seen in a disordered position within the framework. The XRD pattern obtained from the bulk material however did not show any signs of the peaks associated with the SBS structure. It can be hence assumed that the SBS structure was only formed as a minor component.

The synthesis furthermore yielded another type of blue crystal that showed optical extinction under the microscope and were hence also chosen to be investigated. A crystal of 50 x 75 x 40 μm was selected and mounted in the beam on station 9.8. Data were collected at 0.6869 Å and the space group and unit cell dimension were established. The structure was again solved using the WinGX software. The refinement established that the crystal was of the gismondine structure (23) (MAPO-43) (see Figure 4.19).

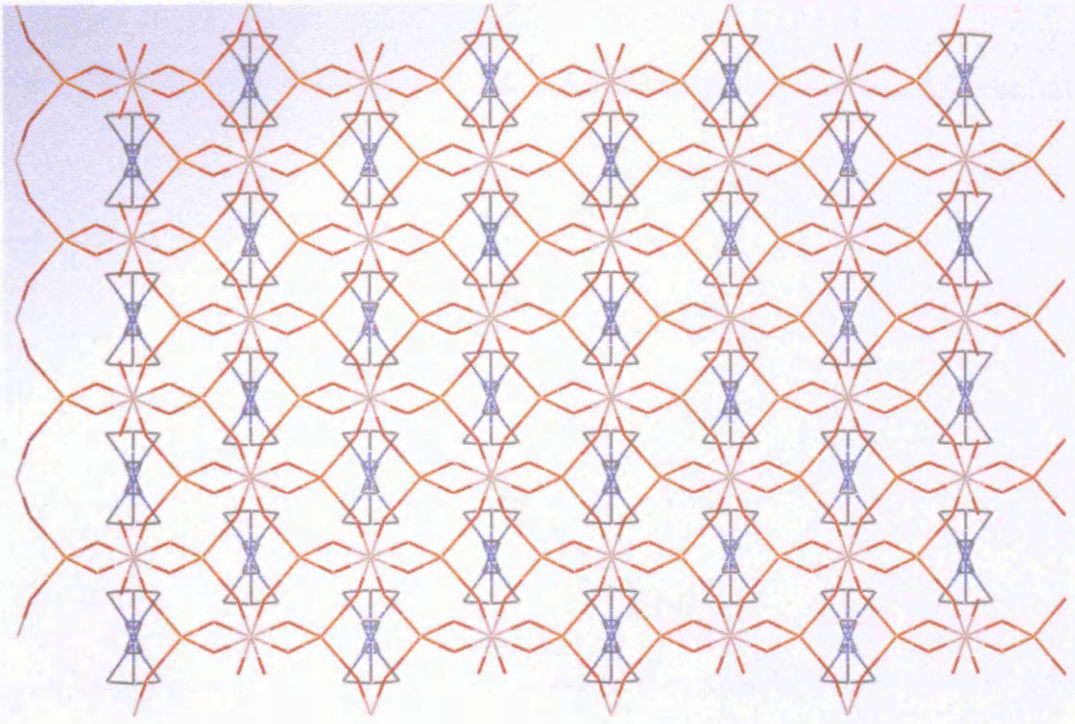

Figure 4.19: MAPO-43 structure synthesised using *N*-methylaniline as the SDA (view along the 010 axis). The template (grey and blue) can be seen sitting disordered within the framework.

Fitting values of R = 8.69% and Rw = 9.19% were obtained. The structure was solved in the orthorhombic space group *F d d d* and had unit cell

dimensions of a = 9.9712 Å; b = 14.1595 Å; c = 14.6406 Å; and α = 90°; β = 90°; γ = 90°. The template can be again seen as a disordered average within the framework. Comparison between the gismondine and the synthesised material's XRD pattern highlighted again that the structure obtained from the single crystal refinement was only a minor component and not representative of the bulk material. The template's ability to form several different phases will be touched on in chapter 4.8.

4.7 Synthesis Concept

In the past phenyl/benzyl-based compounds have not been paid much attention in the synthesis of aluminophosphates due to difficulties mixing the template with the gel composition. Aniline, the most readily available aromatic amine, forms $AlPO_4$-C. This material normally forms with water acting as a template and does not need an organic SDA to be synthesised. Aniline tends not to mix with the gel, but instead forms a layer on top of the gel and the pH of the solution tends to stay at +2.

Aniline is very hydrophobic due to the unavailability of the lone electron pair on the amine group attached to the phenyl-ring. The lone-pair on the aniline's nitrogen helps to stabilise the delocalised π-electrons of the phenyl-ring by being delocalised over the aromatic nucleus and hence is not available for hydration, which is manifested by aniline's extremely high pKb value of 9.7 (24).

The availability of the electron lone-pair for hydration, which makes the organic molecule more soluble in the gel during synthesis, depends on the introduction of inductive groups (e.g. alkane groups) to the phenyl-ring (24, 25), which can be achieved by changing the phenyl-group (C_6H_5) to a benzyl-group ($C_6H_5CH_2$). Compounds, such as phenylethylamine (pKb of 4.22) (25), *N*-methylaniline (pKb of 4.42), benzylamine (pKb of 4.26) and phenylpropylamine (pKb of 3.80) (26) with lower pKb values form a homogenous mixture after addition to the gel, as the lone-pair on the nitrogen is more available for

hydration. The importance of the amine group, and hence its effect on the gel's pH value can be seen very clearly by substituting the amine group on phenylethylamine with a hydroxyl-group. By substituting phenylethylamine with phenylethanol in the gel mixture, the dense material berlinite is formed instead of the layered material (see Figure 4.20), which proves that the pKb value of the amine as well as the solvation entropy plays an important role in the synthesis of porous materials.

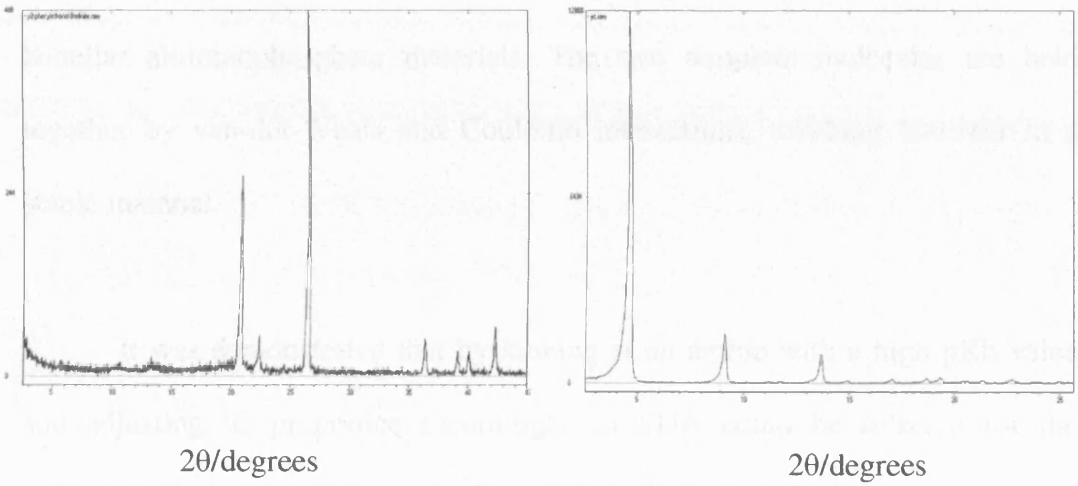

Figure 4.20: (a) XRD pattern of berlinite synthesised with phenylethylanol and (b) layered material synthesised with phenylethylamine.

Starting with aniline, the template's attributes were altered by the addition of inductive groups to the molecule, which leads to a change in the pKb value and hence makes the molecule more soluble in the gel composition. The results obtained from the work carried out on the template location within the AlPO-5 topology, emphasising the importance of the SDA's pKb value, were applied in this study to enable the synthesis of a new material. The goal of synthesising a new structure using new benzyl-based SDAs was achieved.

4.8 Conclusion

The utilisation of benzyl-based templates has led to the formation of a novel layered aluminophosphate. The structure, solved from single crystal X-ray diffraction data and confirmed through powder data, consists of octahedral aluminium chains, which are interlinked by phosphorus tetrahedra forming a 2D layered structure. Two template molecules separate neighbouring inorganic layers, leading to the largest known d-spacing observed between layers in lamellar aluminophosphate materials. The two template molecules are held together by van-der-Waals and Coulomb interactions, resulting however in a stable material.

It was demonstrated that by looking at an amine with a high pKb value and adjusting its properties accordingly an SDA could be selected for the synthesis of aluminophosphates. This finding has opened up a complete new family of possible SDAs for the synthesis of possible new aluminophosphate structures. Besides the novel layered material several different structures have been synthesised, but due to difficulties establishing even the appropriate space groups for the materials (most likely due to peaks present from impurities) it was not possible to solve these structures purely based on the material's powder X-ray diffraction pattern. Some of these materials however yielded minor components with crystals of sufficient size and crystallinity to be observed employing single crystal diffraction, highlighting some interesting side aspects.

N-methylaniline, the organic amine with the highest pKb value of all phenyl/benzyl-based templates used in the several different syntheses, yielded several different framework structures (SBS, GIS and unidentified bulk material), highlighting that with increasing pKb value of the SDA the selectivity to form a specific structure decreases.

Future work on the layered material could include testing it for its ability to store hydrogen. As the material uses phenyl-based organics as its anchors, linking the inorganic layers together it might show interesting hydrogen storage ability. Yaghi *et al.* have shown in the past that MOF-5 has good hydrogen storage ability (27). MOF-5's primary hydrogen absorption sites are the phenyl-ring based anchors with the metal cations the secondary binding site.

This layered material, when using transition metal salts in the synthesis, has got both those characteristics plus an aluminophosphate layer which can act as a hydrogen trap, as has been shown in microporous zeolites (28). Work on testing this material for hydrogen storage is a topic for future study.

4.9 References

1. S. T. Wilson, B. M. Lok, and E. M. Flaningen, *U.S. Patent No. 4,310,440* (1982).
2. S. T. Wilson, B. M. Lok, C. A. Messina, T. R. Cannon, and E. M. Flaningen, *J. Am. Chem. Soc.*, *104*, 1146 (1982).
3. R. Szostack, *Molecular Sieves*, Blackie Academic and Professional, London, 1992.
4. Q. S. Huo, R. R. Xu, S. G. Li, Z. G. Ma, J. M. Thomas, R. H. Jones, and A. M. Chippindale, *J. Chem. Soc. Chem. Comm.*, 875 (1992).
5. K. Maeda, A. Tuel, S. Caldarelli, and C. Baerlocher, *Microporous and Mesoporous Materials*, *39*, 465 (2000).
6. A. Tuel, V. Gramlich, and C. Baerlocher, *Microporous and Mesoporous Materials*, *47*, 217 (2001).
7. W. Yan, J. Yu, Y. Li, Z. Shi, and R. Xu, *Journal of Solid State Chemistry 167*, 282 (2002).
8. A. Tuel, V. Gramlich, and C. Baerlocher, *Microporous and Mesoporous Materials*, *41*, 217 (2000).
9. K. O. Kongshaug, H. Fjellvag, and K. P. Lillerud, *Microporous and Mesoporous Materials*, *38*, 311 (2000).
10. G. Mali, A. Meden, A. Ristic, N. N. Tusar, and V. Kaucic, *Journal of Physical Chemistry B*, *106*, 63 (2002).
11. N. Simon, N. Guillou, T. Loiseau, F. Taulelle, and G. Ferey, *Journal of Solid State Chemistry*, *147*, 92 (1999).
12. Q. Huang and S. J. Hwu, *Chemical Communications*, 2343 (1999).

13. A. Tuel, C. Lorentz, V. Gramlich, and C. Baerlocher, *Journal of Solid State Chemistry*, *178*, 2322 (2005).

14. W. Massa, O. V. Yakubovich, O. V. Karimova, and L. N. Dem'yanets, *Acta Crystallography Sect. C*, *51*, 1246 (1995).

15. R. A. Rämik, B. D. Sturman, P. J. Dunn, and A. S. Poverennykh, *Can. Mineral.*, *18*, 185 (1980).

16. L. Gomez-Hortiguela, F. Cora, C. R. A. Catlow, and J. Perez-Pariente, *Journal of the American Chemical Society*, *126*, 12097 (2004).

17. L. J. Farrugia, *Journal of Applied Crystallography*, *32*, 837 (1999).

18. D. J. Watkin, C. K. Prout, and P. M. Lilley, Chemical Crystallography Laboratory, University of Oxford, Oxford.

19. W. T. Robinson and G. M. Sheldrick, *Crystallographic Computing 4. Techniques and New Technologies.* , Oxford Univ. Press, Oxford, 1988.

20. A. C. Larson and R. B. Von Dreele, *Los Alamos National Laboratory Report LAUR 86-748* (2000).

21. B. H. Toby, *Journal of Applied Crystallography*, *34*, 210 (2001).

22. X. H. Bu, P. Y. Feng, and G. D. Stucky, *Science*, *278*, 2080 (1997).

23. C. Baerlocher and W. M. Meier, *Helvetica Chimica ACTA*, *53*, 1285 (1970).

24. J. J. Elliott and S. F. Mason, *Journal of the Chemical Society*, 2352 (1959).

25. M. M. Tuckerman, J. R. Mayer, and F. C. Nachod, *J. Am. Chem. Soc.*, *81*, 92 (1959).

26. H. J. Hall, *Journal of American Chemical Society 79*, 5697 (1957).

27. N. L. Rosi, J. Eckert, M. Eddaoudi, D. T. Vodak, J. Kim, M. O'Keeffe, and O. M. Yaghi, *Science*, *300*, 1127 (2003).

28. M. G. Nijkamp, J. Raaymakers, A. J. van Dillen, and K. P. de Jong, *Applied Physics a-Materials Science & Processing*, *72*, 619 (2001).

Chapter 5

One Dimensional Aluminophosphates as Hydrocarbon Traps in Cold Start Emission Control

5.1 Summary

Some carcinogenic compounds are found in car exhausts, with especially high concentrations emitted during the start-up phase of the car (*ca.* 2 minutes), as the catalytic converter has not yet reached its minimum working temperature. It would hence be of great use to develop a storage material, which binds these compounds for the time until the catalytic converter has reached its working temperature.

Several different types of microporous aluminophosphates were tested as storage devises for hydrocarbons found in exhaust fumes. Different approaches were taken to improve the material's ability to store toluene (used as probe molecule) in wet as well as in dry conditions. When mixing an H_2O filter in with our material it was possible to reproduce results obtained in a dry environment even though water was present. Water usually results in a poorer performance of the storage material.

Employing X-ray diffraction and computational studies, it was possible to gain a good insight into framework-toluene interactions. Thus, it was possible to determine the attributes, which lead to different absorption capacities of toluene in different materials.

5.2 Introduction

There has been an increasing concern regarding air pollution from car exhaust fumes as carcinogenic compounds are present in these fumes, which can have detrimental health effects on living organisms (1). Especially during the start-up phase of the car (*ca.* 2 minutes), high amounts of aromatic hydrocarbons are emitted, as the catalytic converter has not yet reached its minimum working temperature. As about 70% of all hydrocarbons are emitted during this cold start period (2), it has led to the failure of federal test procedures (FTP) (3-5). As a consequence, the focus has been to try and find a material having the ability to store hydrocarbons (HC) found in the exhaust during the cold start period and releases them again once the catalyst has reached its operating temperature (6).

The materials employed to date include active carbon and zeolites. Hydrocarbon absorbents must have the ability to store HC with chain lengths ranging from C1 to C11. Zeolites have shown great promise in the past to be able to store HC in the temperature range needed during the start-up phase (6-9) and also exhibiting good thermal stability.

Burke *et al.* have shown in the past that in the presence of water hydrophobic materials can work better. In dry conditions however hydrophilic materials outperform the equivalent hydrophobic ones considerably with the Si/Al ratio playing a crucial role in zeolites (10). Roughly 10% of water can be found in car exhausts, and it is hence important to maximise a material's storage capability in wet conditions.

The AlPO-5 (AFI) topology has been reported to show the greatest storage ability and the highest desorption temperature of all tested aluminophosphates to date (11). Large pore aluminophosphates have shown to be able to hold higher concentrations of toluene in comparison to the equivalent small and medium pore materials (11). The AFI topology also exhibits high hydrothermal stability, which is essential in any hydrocarbon trap to be investigated. Based on CoAPO-36's (ATS) pore size and acidity (12), it was also chosen as a material to be tested for its hydrocarbon storage ability. In addition, the effects of substituting different heteroatoms into the AlPO-5 topology, changing the pH for synthesis of SAPO-5, silylation of the sample (increasing the material's hydrophobicity) and insight into framework-toluene interactions are reported.

5.3 Experimental Details

5.3.1 Synthesis of One Dimensional Aluminophosphates

The different conditions of the AFI and ATS syntheses are given in Table 5.1. AFI and ATS were synthesised by adding aluminium hydroxide to an aqueous solution of phosphoric acid. Additionally, in the syntheses of the MeAPOs and SAPOs the appropriate metal-acetates and silicates were added. After rigorous stirring for *ca.* 10 minutes the gel attains homogeneity and the organic template, methyldicyclohexylamine (MCHA) in the case of AlPO-5 and ethyldicyclohexylamine (ECHA) or tripropylamine (TPA) for the ATS topologies, was added to form the final gel. After stirring the gel (*ca.* 50ml) for *ca.* 1 hour, it was transferred to a Teflon lined autoclave with a volume of 200 ml, which was heated in a pre-heated oven at 423K for *ca.* 16 hours. The solids, extracted by the conventional filtering and drying procedures were checked for phase purity by X-ray diffraction technique employing a Siemens D4 system (13).

Table 5.1: Synthesis condition of different aluminophosphate materials tested as hydrocarbon traps.

Sample	Gel Composition	Temp (°C)
AlPO-5	1.0 Al : 1.0 P : 0.8 MCHA : 25 H_2O	150
CoAlPO-5	0.9 Al : 0.1 Co : 1.0 P : 0.8 MCHA : 25 H_2O	150
SAPO-5 (pH 6)	0.9 Al : 0.1 Si : 1.0 P : 0.6 MCHA : 25 H_2O	150
SAPO-5 (pH 8.5)	0.9 Al : 0.1 Si : 1.0 P : 1.3 MCHA : 25 H_2O	150
MgAlPO-5	0.9 Al : 0.1 Mg : 1.0 P : 0.8 MCHA : 25 H_2O	150
ZnAlPO-5	0.9 Al : 0.1 Zn : 1.0 P : 0.8 MCHA : 25 H_2O	150
CoAlPO-36	0.9 Al : 0.1 Co : 1.0 P : 0.8 ECHA : 5 H_2O	150
MgAlPO-36	0.9 Al : 0.1 Co : 1.0 P : 0.8 TPA : 5 H_2O	150
ZnAlPO-36	0.9 Al : 0.1 Co : 1.0 P : 0.8 TPA : 5 H_2O	150

The samples were subsequently calcined by heating them up to 535°C in nitrogen, and then kept at this temperature for another 24 hours in air. The cobalt containing materials were subsequently heated up to 300°C in a stream of hydrogen to reduce the cobalt centres within the framework (14).

5.3.2 Experimental Set-Up

5.3.2.1 Silylation of CoAPO-5 Sample

The calcined SAPO-5 sample was placed in a round-bottom flask using hexane as a solvent and was attached to a Schlenk line (see Figure 5.1).

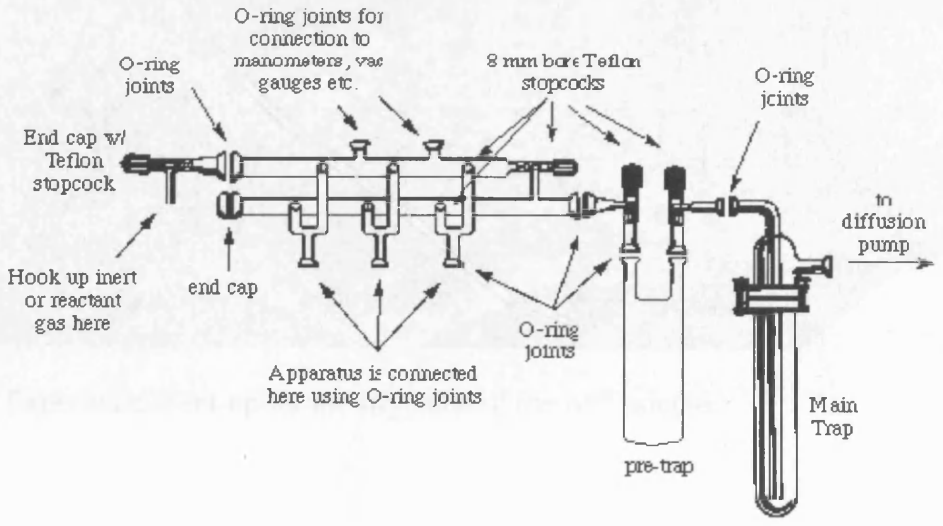

Figure 5.1: Schlenk line set-up.

The trimethylchlorosilane (TMCS) (empirical formula: $Si(CH_3)_3Cl$) is extremely sensitive to water and hence safety precautions had to be taken ensuring a secure experiment. When TMCS is exposed to water, it can lead to instant decomposition.

Argon was used to create an inert atmosphere within the system and hexane used as a solvent. The sample was heated to 75°C and the TMCS was added to the solution via a syringe ensuring no water could get in contact with the liquid added (15).

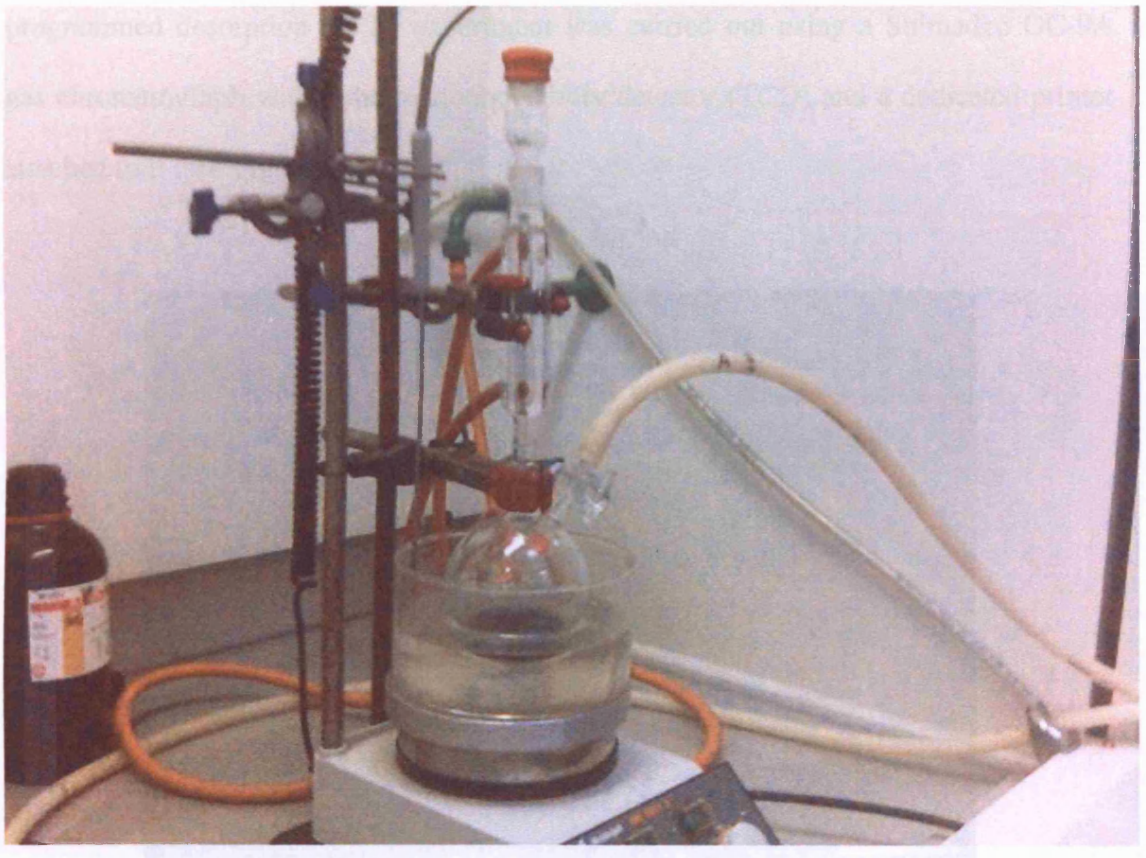

Figure 5.2: Experimental set-up for the silylation of the AFI sample.

5.3.2.2 Gas Chromatography TPD Set-Up

Toluene was used as sorbate in this study as it is less toxic than benzene and has been used as probe molecule in previous studies (6, 7, 11). The temperature-programmed desorption (TPD) experiment was carried out using a Shimadzu GC-9A gas chromatograph with a thermal conductivity detector (TCD) and a dedicated printer attached to it (see Figure 5.3).

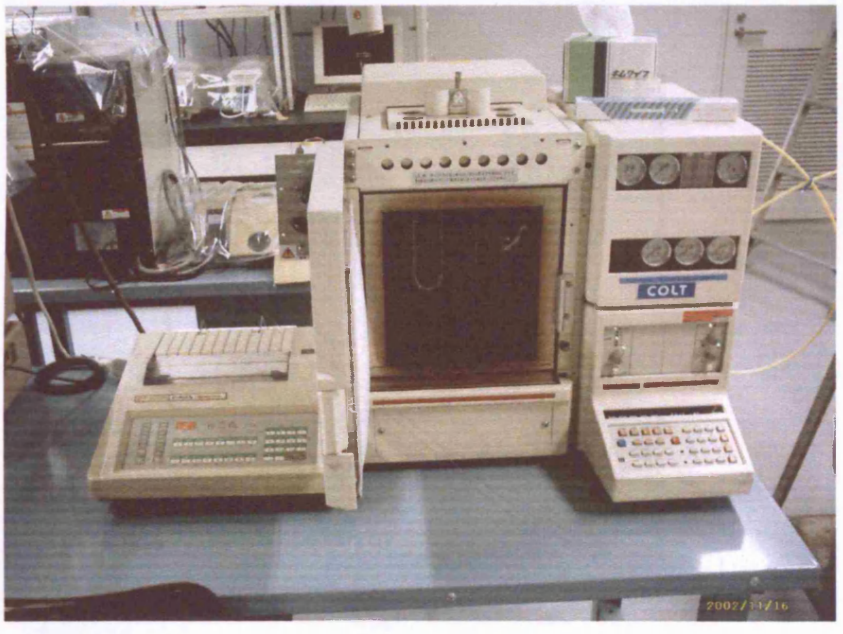

Figure 5.3: The Shimadzu GC-9A gas chromatograph employed for the TPD experiments.

A TC detector works on the basis of sensing a change in heat conductivity in the gas emerging from the column. It is not as sensitive as the flame ionisation detector (FID) but is capable of detecting water molecules, which the FID is not capable of and

was hence employed in this study. The sample was pre-treated before toluene was absorbed, by heating it up to 300°C at a rate of 2,5 K / min in helium (with a flow-rate of 50 ml / min) and subsequently kept at this temperature for 60 minutes to remove all water present in the sample. It is essential to keep the flow-rate constant for all of the experiments as this would adversely affect the comparability of the obtained experimental results. After the column had been cooled back down to 50°C, it got injected with toluene (pulse method) until saturation (11) and the injection profile was recorded. To mimic wet conditions, 10% of water was added to the toluene injection.

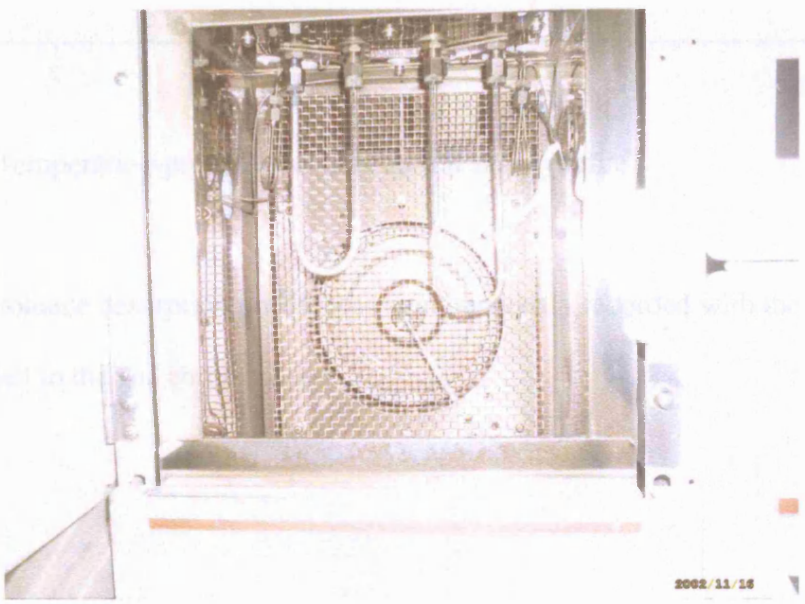

Figure 5.4: Glass capillary set in GC. The material (blue) can be seen in the top left arm of the glass tube. The material is packed between layers of glass wool and supported by glass beads, ensuring the catalyst does not move during the experiment.

The desorption was performed by first keeping the temperature of the column at 50°C for 5 minutes and then heating it to 390°C at a ramp rate of 20 K / min. After

reaching 390°C the column was then kept at this temperature for a further 10 minutes after which it was cooled back down to 50°C (see Figure 5.5).

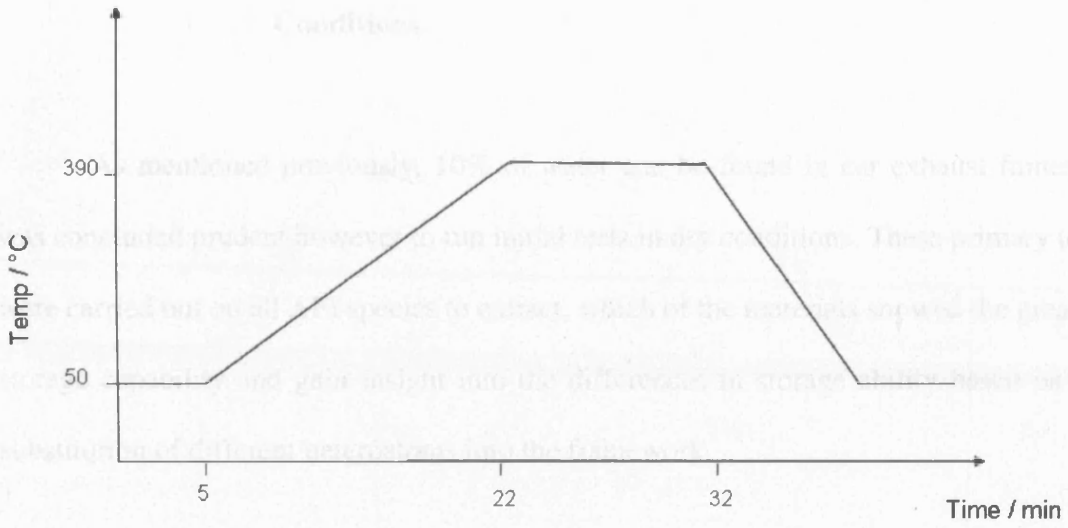

Figure 5.5: Temperature-programmed desorption study profile.

The toluene desorption profile was simultaneously recorded with the dedicated printer attached to the gas chromatograph.

5.4 Results

5.4.1 AFI topologies Tested for Hydrocarbon Storage in Dry Conditions

As mentioned previously, 10% of water can be found in car exhaust fumes. It was concluded prudent however to run initial tests in dry conditions. These primary tests were carried out on all AFI species to extract, which of the materials showed the greatest storage capability and gain insight into the differences in storage ability based on the substitution of different heteroatoms into the framework.

The materials investigated in this study were the pure AlPO-5, CoAPO-5, MAPO-5, ZnAPO-5, SAPO-5 synthesised at low and at high pH to establish if there were any differences in toluene storage ability. Using different synthesis conditions (for the SAPO-5 sample) and different heteroatoms (i.e. Si, Co, Mg and Zn), it was expected to create a range of materials with sites of different acid strengths (16). This consequently should lead to a difference in storage capacity (17), proving the importance of acidity in a material's ability to store toluene. TPD experiments, measuring the toluene absorption capacity of these different materials were measured for all samples (see Figure 5.6) employing the GC set-up described previously.

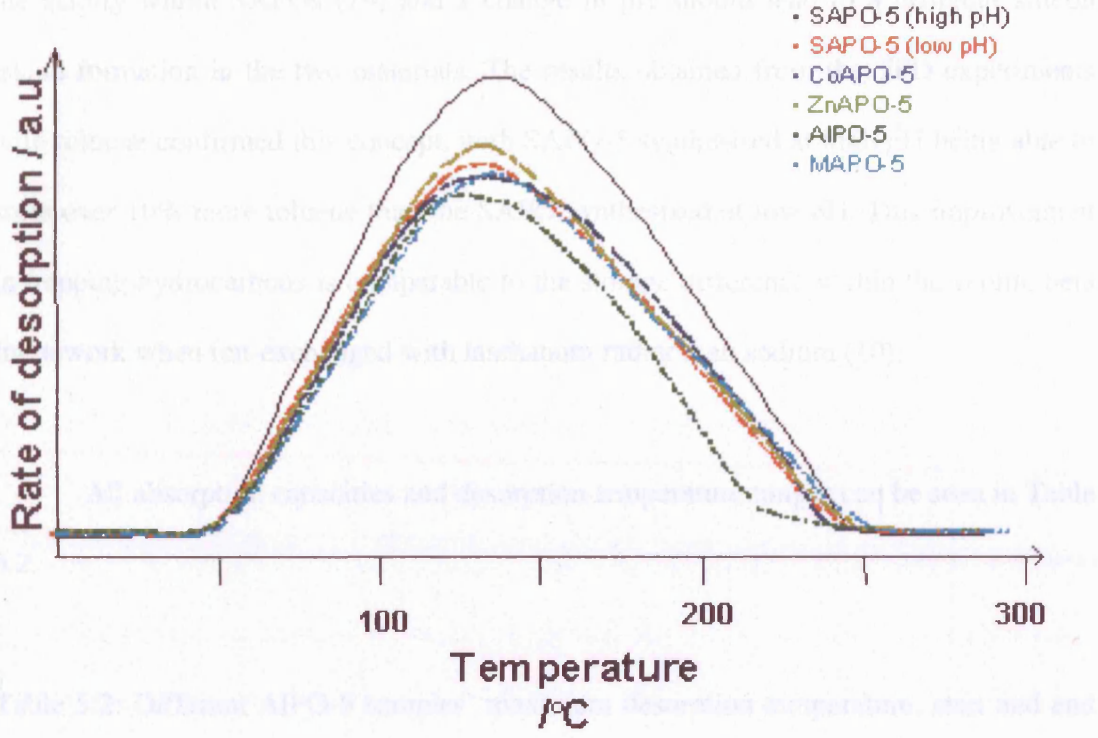

Figure 5.6: Toluene absorption ability (in molecules) of different AFI topologies in dry conditions.

As expected, AlPO-5 showed the lowest absorption capacity of all samples (10 – 20% less than the substituted AFI-structures). AlPO-5 shows the least acidity of all samples tested (18) as the framework is neutral and would only possess terminal OH-groups and OH-groups arising through defects. The best storage material tested was SAPO-5 synthesised at high pH. All SAPOs and MeAPOs tested had the same amount of heteroatom substitution and hence can be expected to have the same amount of hydroxyl-groups present, but all showed a different capacity to store toluene. However, in the case of the SAPO-5, changing the pH in the synthesis was expected to lead to a difference in the material's acidity. Formation of silicon islands plays a crucial role in

the acidity within SAPOs (19) and a change in pH should lead to a different silicon island formation in the two materials. The results obtained from the TPD experiments with toluene confirmed this concept, with SAPO-5 synthesised at high pH being able to store over 10% more toluene than the SAPO synthesized at low pH. This improvement in trapping hydrocarbons is comparable to the storage difference within the zeolite beta framework when ion-exchanged with lanthanum rather than sodium (10).

All absorption capacities and desorption temperature ranges can be seen in Table 5.2.

Table 5.2: Different AlPO-5 samples' maximum desorption temperature, start and end temperature of desorption and amount of toluene absorbed per gram of sample in dry conditions.

Sample	Desorption Temp Max (in °C)	Start Temp (in °C)	End Temp (in °C)	Absorption per gram of sample (in mg)
AlPO-5	120.38	52	225	47.88
CoAPO-5	122.24	52	230	52.45
SAPO-5 high pH	134	52	250	58.95
SAPO-5 low pH	126.5	52	250	52.49
MAPO-5	124	52	250	52.46
ZnAPO-5	129.96	52	250	54.08

5.4.2 AFI Topologies Tested for Hydrocarbon Storage in Wet Conditions

However, as mentioned previously, the conditions found in car exhausts include water, which tends to completely change a material's ability to store toluene (2).

Hydrophilic materials tend to show preference for absorbing water and hence their ability to store toluene is highly decreased as H_2O will show preferential behaviour towards adsorbing onto the Brønsted acid sites. This leaves the toluene with a limited number of binding sites within the material, resulting in a poorer performance of the material's toluene storage ability (10).

It can be thus concluded, that a material's storage capacity could be increased by changing the environment it is found in. Extracting water out of the exhaust stream will increase a material's storage capacity. The approach taken was to mix a highly hydrophilic material with the material to be tested. SAPO-5, synthesised at high pH was mixed with 10% zeolite A (Sigma Aldrich Linde Type A), which was employed as the water-trap, and then tested under wet conditions (10% water added to the toluene injection).

By introducing an H_2O filter, the material's acidity is not affected and it was hence expected that this approach would yield similar results as were obtained in dry conditions (6). Indeed, when mixing a filter in with our material it was possible to reproduce results obtained in a dry environment even though water was present (see Figure 5.7). The silylated SAPO-5 sample, however, performed very poorly. It was expected that due to a decrease in hydrophilicity, the material should be able to perform reasonably well in wet conditions. The material however showed almost no ability to store toluene (see Figure 5.7), which can almost certainly be attributed to the silylating agent causing pore blocking, and thus leading to a restriction in toluene diffusion into the microporous framework. Nitrogen adsorption measurements, to determine the

sample's surface area were however not possible as the silylating agent started to decompose during measurements, leading to the machine recording inadequate vacuum readings. It was hence not possible to record data to compare the surface areas of treated and untreated samples.

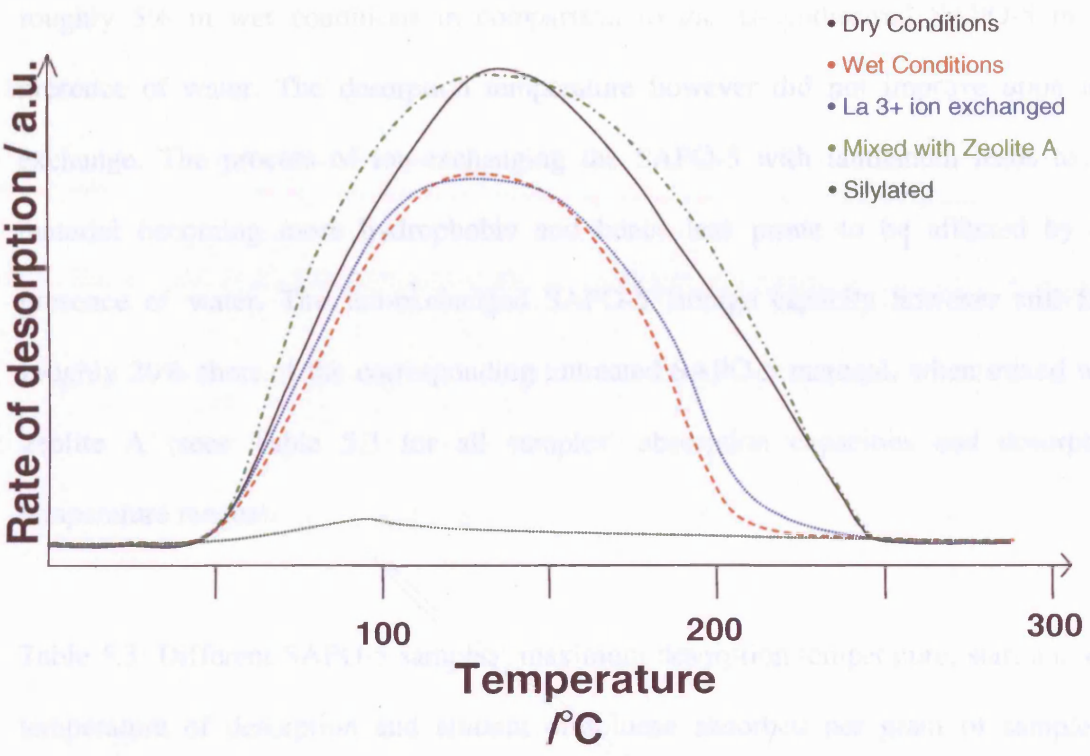

Figure 5.7: Toluene absorption ability of SAPO-5 (synthesised at high pH) under different conditions.

SAPO-5, when mixed with zeolite A in wet conditions seems to be able to absorb more toluene than SAPO-5 in dry conditions (see Figure 5.7 and Table 5.3). This difference, however, originates from the water absorbed by zeolite A. Zeolite A was also solely tested for its ability to absorb toluene but due to its small pore size, did not show the ability to hold any significant amounts of toluene. This exciting result indicates that

materials, which are good trapping materials for toluene in dry conditions, can also show good storage ability in the presence of water when mixed with zeolite A.

Lanthanum ion-exchanged SAPO-5 showed an increase in storage capacity by roughly 5% in wet conditions in comparison to the as-synthesised SAPO-5 in the presence of water. The desorption temperature however did not improve upon ion-exchange. The process of ion-exchanging the SAPO-5 with lanthanum leads to the material becoming more hydrophobic and hence less prone to be affected by the presence of water. The ion-exchanged SAPO-5 storage capacity however still falls roughly 20% short of the corresponding untreated SAPO-5 material, when mixed with zeolite A (sees Table 5.3 for all samples' absorption capacities and desorption temperature ranges).

Table 5.3: Different SAPO-5 samples' maximum desorption temperature, start and end temperature of desorption and amount of toluene absorbed per gram of sample in different conditions.

Condition	Desorption Temp Max (in °C)	Start Temp (in °C)	End Temp (in °C)	Absorption per gram of sample (in mg)
Dry	134	52	250	58,95
Wet	123,16	52	210	42,18
La3+ ion exchanged	117,94	52	220	43,96
Mixed with Zeolite A	124	52	246	68,55
Silylated SAPO5 - wet	95,14	52	152	0,13

5.4.3 Location of Toluene Within SAPO-5 by HRXRD

Toluene was located using HRXRD data to gain insight into how the AlPO material interacts with the toluene. HRXRD data was collected from Daresbury on Station 9.1 using a wavelength of 1.0002 Å and was analysed by Rietveld methodology using the GSAS EXPGUI software (20, 21). The pattern was analysed in space group *P 6 c c* as reported by Chao *et al.* (22) using the known framework atoms only. The data at high angle is least affected by the organic absorbent (23) and hence shows a good fit even before the toluene is fitted (see inset in Figure 5.8). The extra atoms of the absorbent were located through extra electron density peaks. Having added the toluene's atoms to the Rietveld refinement the fit between the calculated XRD-pattern and the experimentally obtained one increased drastically, leading to an improvement of wRp value from 17.4% to 6.3% (see Figure 5.10).

After fitting the framework atoms only, there was a bad fit for the whole data-set, resulting in a very high wRp value of 17.4%. It can clearly be seen, that at low angle the peak positions can all be matched (see Figure 5.8), but there is a strong mismatch between intensities of the different peaks, which can be allocated to the missing electron density arising from not having fitted the absorbed toluene molecules within the data-set.

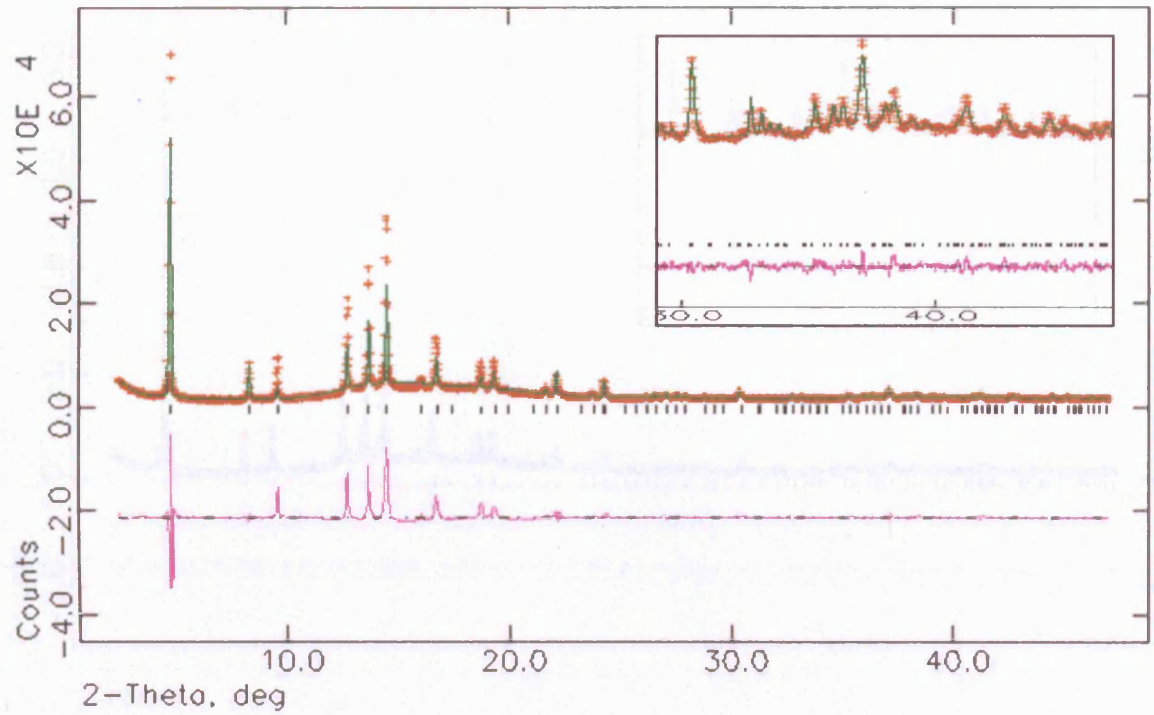

Figure 5.8: Experimental, simulated, and difference profiles for the powder XRD pattern of SAPO-5 with toluene absorbed before the organic was located (wRp = 17.4% and Rp = 12.2%) recorded at 1.0002 Å.

The next step was to locate the sorbed molecule through the difference electron density peaks. It was possible to locate extra electron density in the centre of the AFI channel system. Having fitted the obtained atom position of one carbon-atom to the XRD data, the fit improved and the refinement yielded a wRp value of 15.1%. Figure 5.9 shows an improvement in fit, but it can still be clearly seen that the refinement is not complete and there is still un-located electron density arising from un-located toluene atoms.

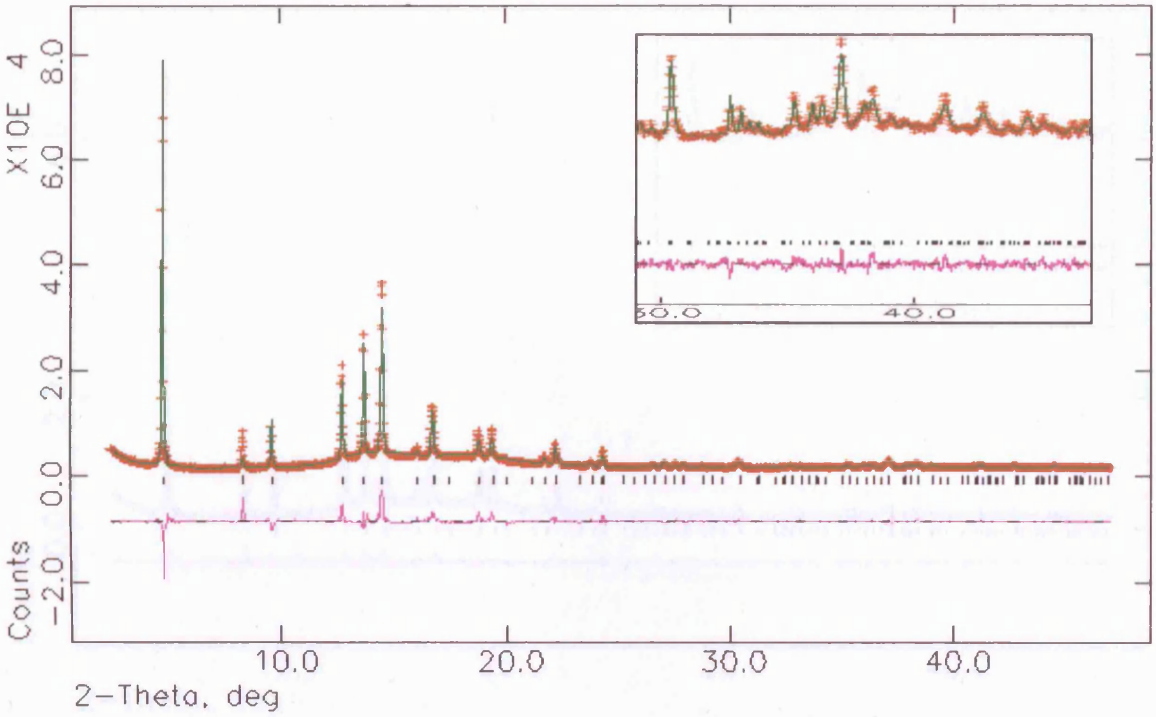

Figure 5.9: Rietveld refinement of SAPO-5 with toluene absorbed, having fitted one C-atom arising from toluene (wRp = 15.1% and Rp = 11.2%).

Having fitted just one carbon atom from the electron density map, it was clear from the refinement values and inspection of the data that the match between experimental and simulated pattern was not close enough, resulting in a too large difference profile. The electron density map was hence used again to locate a second carbon atom. Electron density much closer to the framework was also present in the system, from which the second carbon's co-ordinates were established. Having entered this atom into the refinement a much better fit between the experimentally obtained and simulated pattern could be observed, resulting in a wRp value of 6.3% (see Figure 5.10). This is a large improvement to the system where only one carbon atom has been fitted.

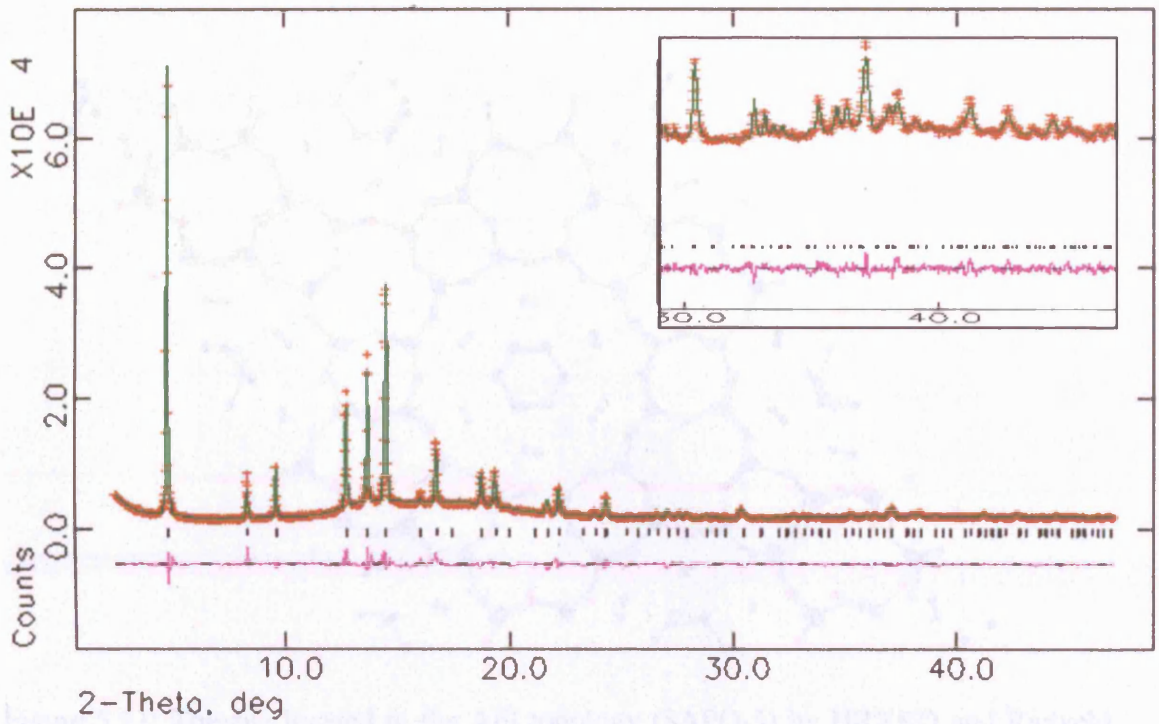

Figure 5.10: Experimental, simulated, and difference profiles for the powder XRD pattern of SAPO-5 with toluene absorbed after toluene location (wRp = 6.3% and Rp = 5.0%).

Once the fractional co-ordinates were deduced from the Rietveld analysis, the results were visualised using the PowderCell 2.4 software (24) (see Figure 5.11).

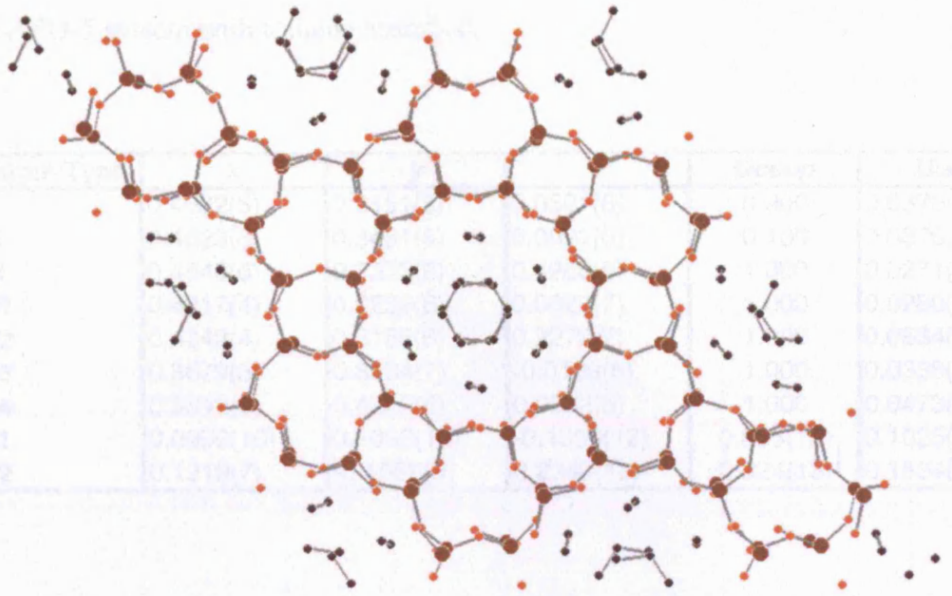

Figure 5.11: Toluene located in the AFI topology (SAPO-5) by HRXRD and Rietveld methodology.

The unit-cell parameters, symmetry and refined atom-positions are given in Table 5.4 and 5.5 and a list of selected bond lengths and angles in Table 5.6 and 5.7.

Table 5.4: Space group and unit cell dimensions obtained from the Rietveld refinement of the SAPO-5 system with toluene absorbed.

SAPO-5 with Toulene absorbed		
Spacegroup: *P 6 c c*		
a = 13.7903(2)	b = 13.7903(2)	c = 8.4106(2)
α = 90°	β = 90°	γ = 120°

Table 5.5: Atom co-ordinates and occupancy obtained from the Rietveld refinement of the SAPO-5 system with toluene absorbed.

Atom Type	*x*	*y*	*z*	*Occup*	Uiso
P	0.4622(5)	0.3451(5)	0.0591(6)	0.900	0.0376(6)
Si	0.4622(5)	0.3451(5)	0.0591(6)	0.100	0.0376(6)
Al	0.4540(6)	0.3332(6)	0.4266(6)	1.000	0.0271(4)
O1	0.4217(4)	0.2239(6)	0.0026(7)	1.000	0.0280(5)
O2	0.4342(4)	0.3185(6)	0.2272(7)	1.000	0.0534(5)
O3	0.3679(3)	0.3534(7)	-0.0109(6)	1.000	0.0338(5)
O4	0.5842(6)	0.4232(6)	0.0282(5)	1.000	0.0473(6)
C1	0.0999(10)	0.1098(13)	-0.1300(12)	0.835(12)	0.1025(18)
C2	0.1219(7)	-0.1586(9)	0.2349(12)	0.324(13)	0.1534(15)

Table 5.6: Selected bond lengths obtained from the Rietveld refinement of the SAPO-5 systems with toluene absorbed.

Vector	Length
P_O1	1.5480(4)
P_O2	1.4633(4)
P_O3	1.4835(4)
P_O4	1.4987(4)
Al_O1	1.8063(5)
Al_O2	1.6945(4)
Al_O3	1.7596(5)
Al_O4	1.7220(4)
C1_C1	1.4516(4)

Table 5.7: Selected bond angles obtained from the Rietveld refinement of the SAPO-5 systems with toluene absorbed.

Angle	Degrees
O1_P_O2	96.815(5)
O1_P_O3	95.969(5)
O1_P_O4	113.136(4)
O2_P_O3	105.740(6)
O2_P_O4	114.101(5)
O3_P_O4	126.001(5)
O1_Al_O2	106.565(6)
O1_Al_O3	110.778(6)
O1_Al_O4	99.276(6)
O2_Al_O3	103.070(7)
O2_Al_O4	128.062(5)
O3_Al_O4	108.664(6)
C1_C1_C1	120.000

The toluene cannot be located in its actual configuration within the channel pores of SAPO-5 but instead is only visible as electron density. This can be explained by the fact that the toluene molecules are highly disordered within the AFI framework and hence are only represented as an average of many differently positioned toluene molecules. This finding is underlined by the relatively large U_{iso} values for the carbons, obtained through the Rietveld refinement. The result from the analysis of the HRXRD data however shows that there seems to be two different types of toluene–framework interactions.

The first type of toluene seems to have little interaction with the framework and is randomly distributed in the channel system. The second type of toluene, however, is

much closer to the framework and hence has a much stronger interaction with the aluminophosphate, which seems to stem from an electrostatic interaction between the Brønsted acid sites of the framework with the delocalised π-system of the toluene, underlying the fact that acidity seems to play a pivotal role in a material's ability to store toluene. A two staged desorption process, showing the presence of two types of toluene-framework interactions has been observed in zeolites where the maximum desorption temperature lies at a higher temperature (7) (see Figure 5.12). In the AlPO materials tested, the two desorption peaks however overlap, giving rise to only one desorption profile.

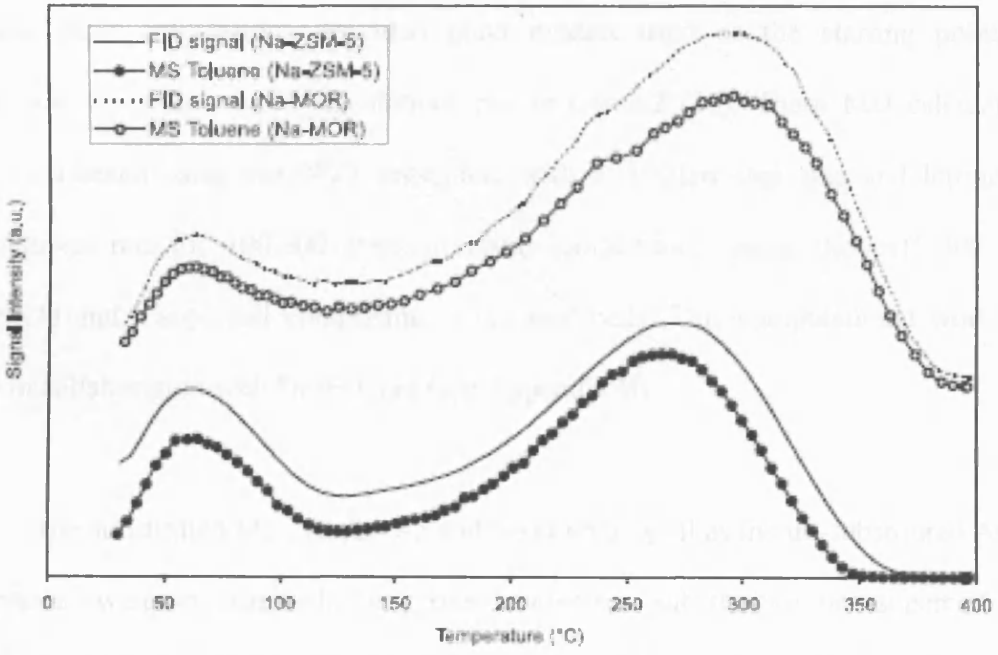

Figure 5.12: TPD profiles for Na–ZSM-5 and Na–MOR using toluene as probe molecule. In both cases there is a two stage desorption profile, underlying the fact that there are two types of framework – toluene interactions (7).

5.4.4 Computational Calculations on Toluene-AFI Interactions

Experimental results indicated a clear improvement in toluene storage ability based on the substitution of different heteroatoms into the AFI topology. The aim was to establish a link between different substituents and toluene storage-ability, as well as obtaining a clearer picture of the interactions occurring between the toluene and the framework. Complementary computational calculations were run to gain further insight into toluene-framework interactions.

The doped frameworks, including charge balancing hydrogen, were optimised in GULP (25), a lattice energy minimisation code. The charges and positions obtained through these calculations provided good models used as the starting point for Molecular Dynamics (MD) calculations run in Cerius2 (26). These MD calculations were performed using the NVT ensemble, with a 0.001ps step size and letting the calculations run for 100.000 steps at room temperature, using the cvff_300_1.01 forcefield and a supercell comprising 2x2x2 unit cells. This computational work was done in collaboration with Dr. F. Corà (see Appendix B).

The substituted Mg-, CoAPO-5 and SAPO-5 as well as the un-substituted AlPO-5 systems, were investigated. Only one heteroatom substitution per supercell was chosen, leading to the formation of one Brønsted acid site per unit cell. This model was selected to gain a more precise insight into the toluene–framework acid site interaction.

In the un-substituted AlPO-5 all configurations were on similar energy levels and no clear distinction could be drawn up between the different positions of the toluene within the framework (see Figure 5.13).

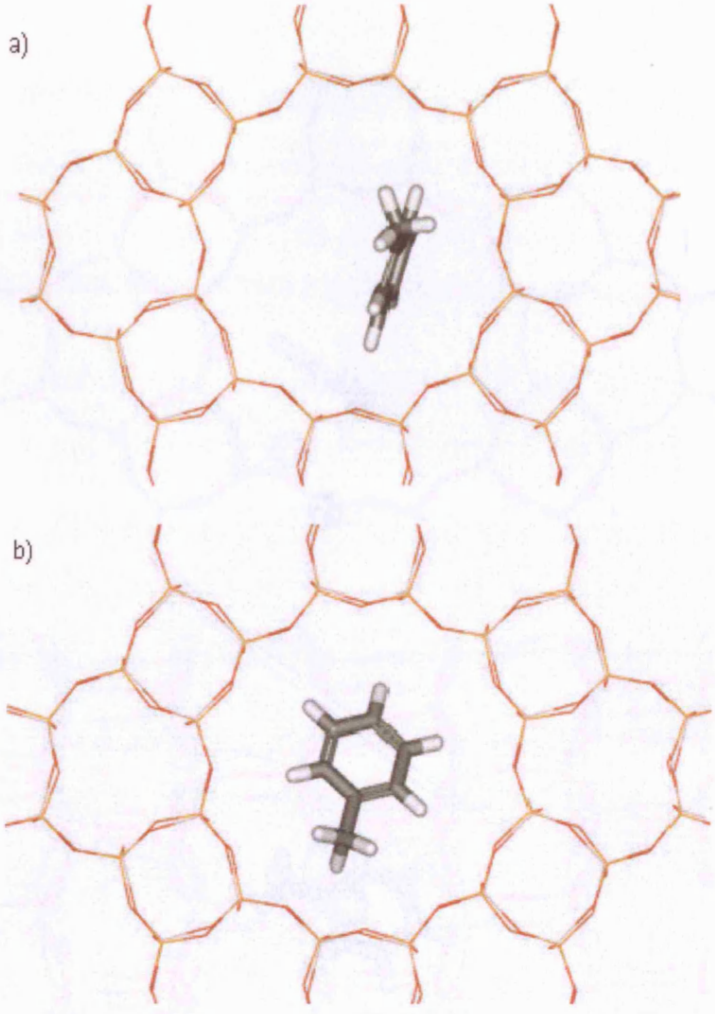

Figure 5.13: a) One of the possible toluene positions within the un-doped AlPO-5 structure obtained from MD calculations. b) Alternative toluene position within the un-doped AlPO-5 structure obtained from MD calculations.

In the substituted cases however, there was an energetically most favoured configuration, with the toluene's delocalized π-system exactly located above the framework's Brønsted acid site (see Figure 5.14). This energetically most favourable arrangement of the toluene was obtained for all of the other substituted AFI frameworks.

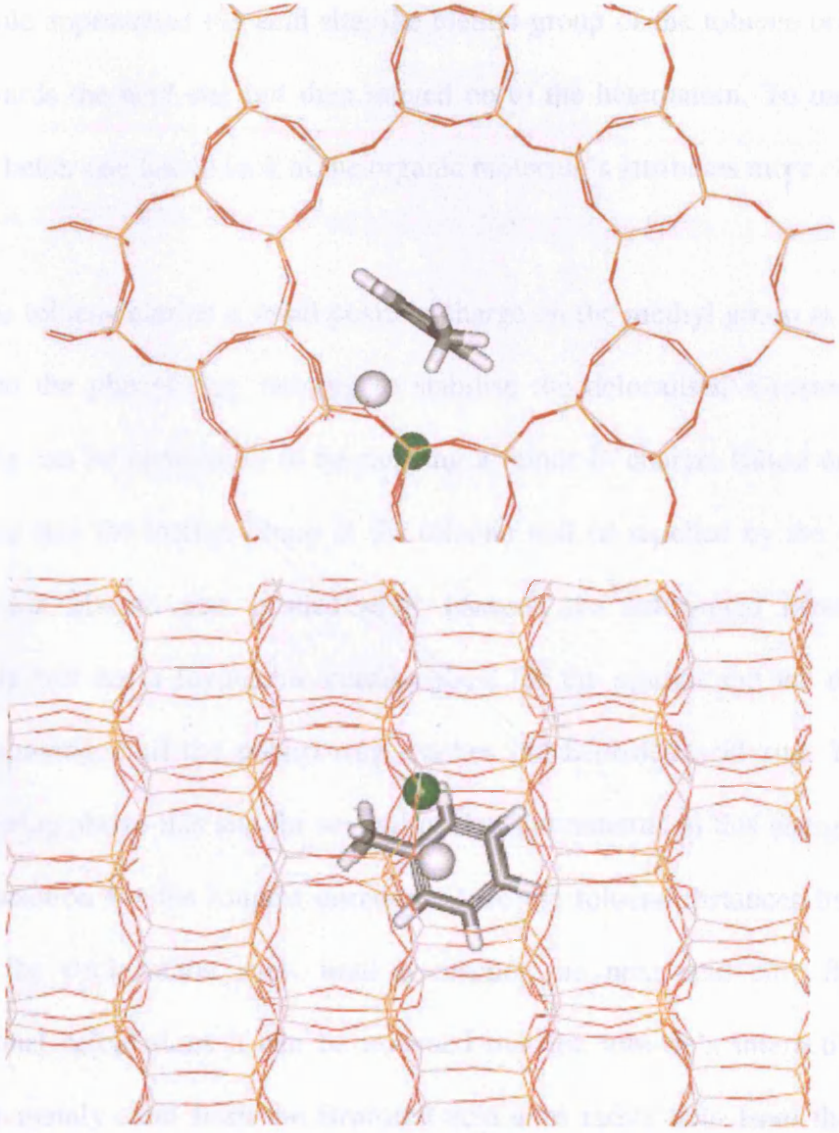

Figure 5.14: Energetically most favourable toluene position in doped AlPO-5, with the organic molecule's aromatic π-system over the acid site (view along the a- and c-axis) obtained from MD calculations (green = metal centre; white = proton).

The least stable configuration of these calculations was when the toluene molecule was located exactly in-between the two different Brønsted acid sites of two unit cells, showing a clear tendency for the toluene to be attracted by the framework's proton. The trajectory of the toluene was along the AlPO-5 channel. It moved freely along the section of the channel, which did not contain a substituted heteroatom. When the molecule approached the acid site, the methyl-group of the toluene orientates itself firstly towards the acid site but then moved on to the heteroatom. To understand this behaviour better one has to look at the organic molecule's attributes more closely.

The toluene carries a small positive charge on the methyl group as it is electron donating to the phenyl-ring, helping to stabilise the delocalised π-system, while the phenyl-ring can be considered to be carrying a minor δ- charge. Based on this model, one can see that the methyl-group of the toluene will be repelled by the proton of the acid site and instead gets pushed aside towards the substituted heteroatom. This however, is still not a favourable configuration for the system and the toluene hence keeps on moving until the phenyl-ring reaches the Brønsted acid site. The molecule keeps hovering above this site for several cycles and remains in this energetically most favoured position for the longest duration. Once the toluene distances itself from the acid site, the cycle starts anew until it reaches the next acid site. Based on the computational calculations it can be assumed that the toluene's interactions with the framework mainly stem from the Brønsted acid sites rather than from the Lewis acid sites, as the molecule shows no affinity for these sites but instead a clear preference towards the hydroxyl-group. See Figure 5.15 for selected frames taken from the MD calculation, representing the toluene's approach to the acid site.

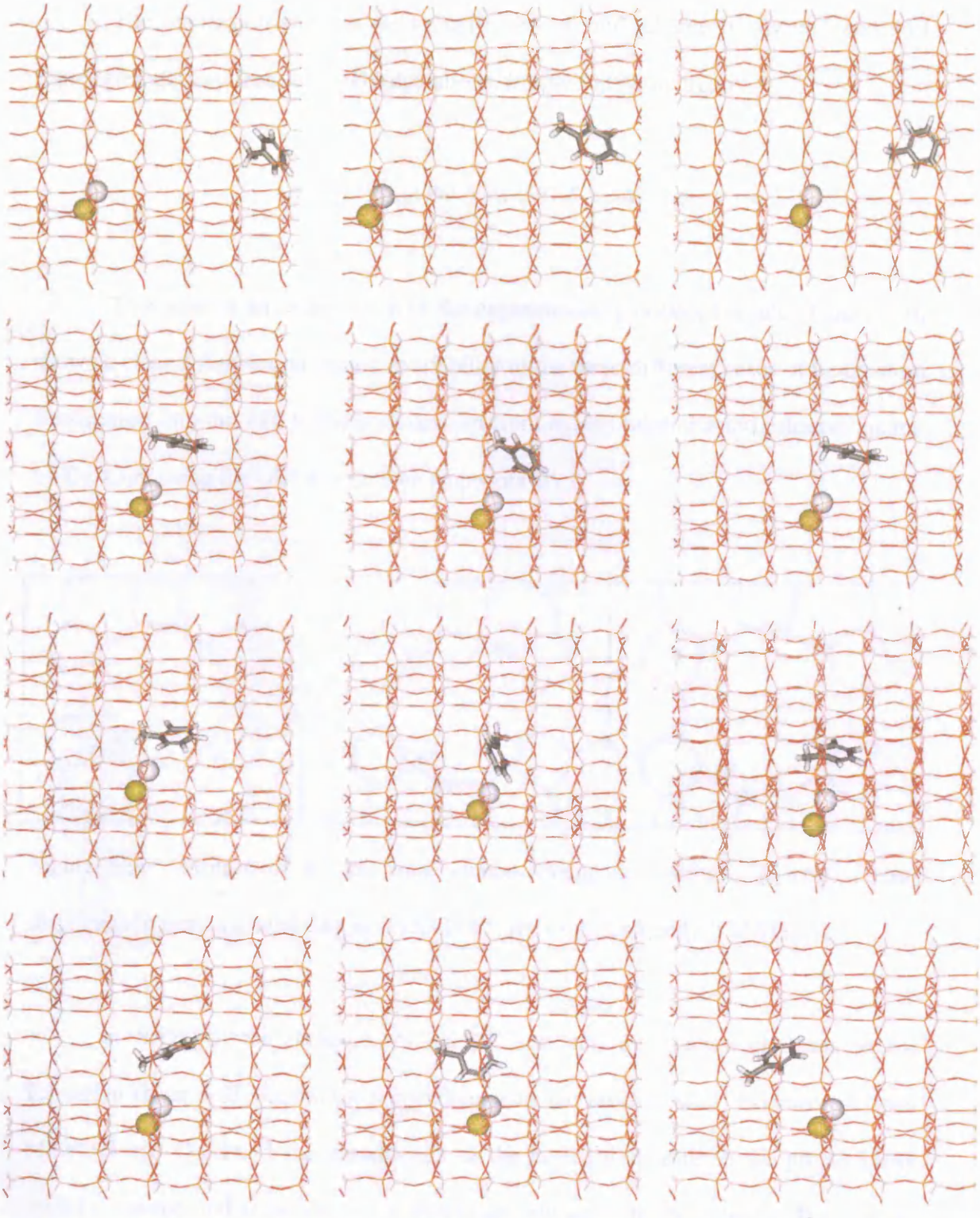

Figure 5.15: Images taken from MD calculations depicting the toluene approaching, physisorbing and then moving away again from the acid site within the SAPO-5.

The interaction energies between framework and toluene in the different AFI topologies, derived from the MD calculations, follow following trend:

AlPO-5 < CoAPO-5, MAPO-5 < SAPO-5

This trend is an exact match to the experimentally obtained results. Figure 5.16 shows a clear difference in proton availability in the three different cases of heteroatom substitution into the AFI framework derived from energy minimisation calculations run by Dr. Corà using the GULP code (see Appendix B).

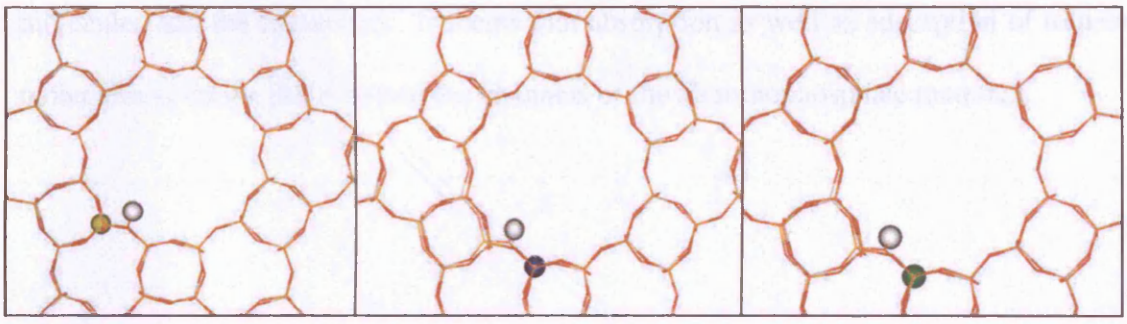

Figure 5.16: Position of H^+ ion from computational calculations, showing a clear difference in proton availability in (a) SAPO-5, (b) CoAPO-5 and (c) MAPO-5.

In SAPO-5, the inclusion of an Si^{4+} ion into the framework leads to the formation of an acid site almost perpendicular to the channel wall. However in both, MAPO-5 and CoAPO-5 the introduction of the heteroatom leads to the proton being slightly skewed and is hence less available to interact with the toluene. The proton-availability and acid strength seems to be the difference in the ability to store toluene in the different substituted topologies.

The toluene position obtained from the unsubstituted AlPO-5 system was superimposed with the picture obtained from the HRXRD data. There is a good match between the electron density located in the centre of the channel and the computationally obtained location of the toluene from the AlPO-5 system (see Figure 5.17a). Furthermore, the computationally derived location of the toluene molecule from the SAPO-5 system was also superimposed with the picture obtained from the HRXRD data. Again, a good match can be observed between the electron density located close to the framework and the computationally derived location of the toluene (see Figure 5.17b). The computational work reiterates the conclusions previously stated for the experimental work, i.e. two different types of interactions occur between the toluene molecules and the framework. It seems that absorption as well as adsorption of toluene molecules is taking place within the channels of the aluminophosphate materials.

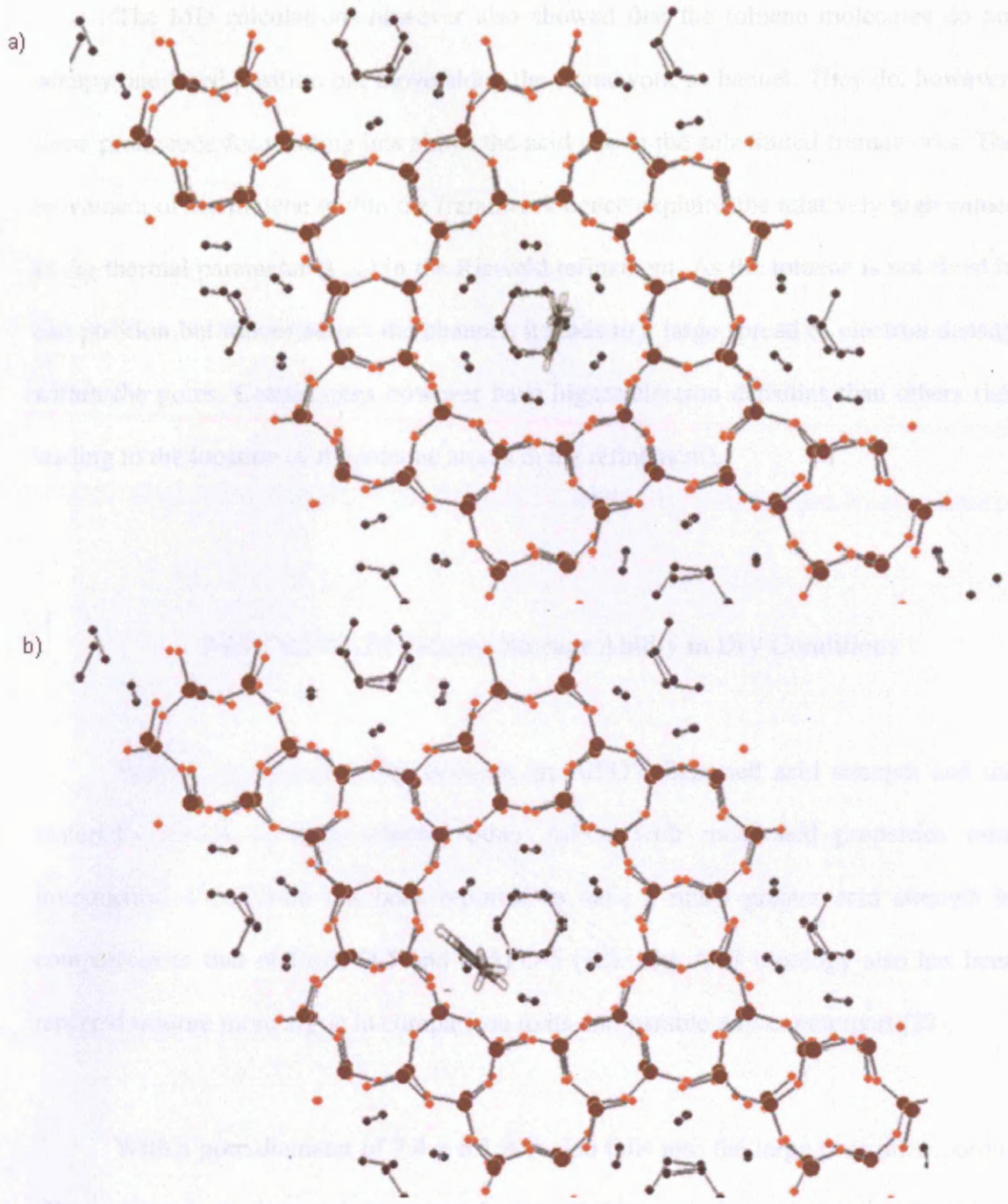

Figure 5.17: Superimposed images of computational (toluene positions obtained from (a) pure and (b) the substituted material) and experimental results, showing a good match of the toluene positions within the AFI topology.

The MD calculations however also showed that the toluene molecules do not occupy one fixed position but move along the framework's channel. They do, however, show preference for residing just above the acid site in the substituted frameworks. The movement of the toluene within the framework hence explains the relatively high values of the thermal parameter (U_{iso}) in the Rietveld refinement. As the toluene is not fixed in one position but moves across the channel, it leads to a large spread of electron density within the pores. Certain sites however have higher electron densities than others (i.e. leading to the location of the toluene atoms in the refinement).

5.4.5 CoAPO-36 Toluene Storage Ability in Dry Conditions

Having established a link between an AlPO's Brønsted acid strength and the material's ability to store toluene, other AlPOs with mentioned properties were investigated. CoAPO-36 has been reported to have a much greater acid strength in comparison to that of CoAPO-5 and MAPO-5 (12). The ATS topology also has been reported to store more argon in comparison to its comparable AFI counterpart (27).

With a pore diameter of 7.4 x 6.5 Å it also falls into the large pore microporous aluminophosphate class and the material also exhibits high thermal stability. Based on these findings, it was concluded that the ATS topology should be a better toluene storage material than its AFI equivalent. The ATS samples were tested in dry conditions (no presence of water), using the same approach as was taken with all AlPO-5 materials. It was found that the CoATS structure did indeed function much better than its

equivalent AFI topology. The results obtained with CoAPO-36 were almost 10% better than the results from the CoAPO-5 material. It almost was able to store the same amounts of toluene as the SAPO-5 (synthesised at high pH) sample.

Table 5.8 shows the storage ability of the different substituted ATS frameworks. The different materials showed a similar trend in ability to store toluene as was observed with the different AFI materials.

Table 5.8: Different ATS samples' maximum desorption temperature, start and end temperature of desorption and amount of toluene absorbed per gram of sample in dry conditions.

Sample	Desorption Temp Max (in °C)	Start Temp (in °C)	End Temp (in °C)	Absorption per gramm of sample (in mg)
CoATS (ECHA)	140	52	250	58,26
MgATS	145	52	250	58,32
ZnATS	150	52	250	59,51

As with the SAPO-5 (synthesised at high pH), the CoAPO-36 material was investigated by HRXRD to establish the position of the toluene within the framework. Unlike with the AFI structure however, the ATS topology did not yield a clear distinction between different toluene locations but showed only a large electron density area. However, there is a centralised arrangement of atoms present with further sets of atoms located closer to the framework (see Figure 5.18).

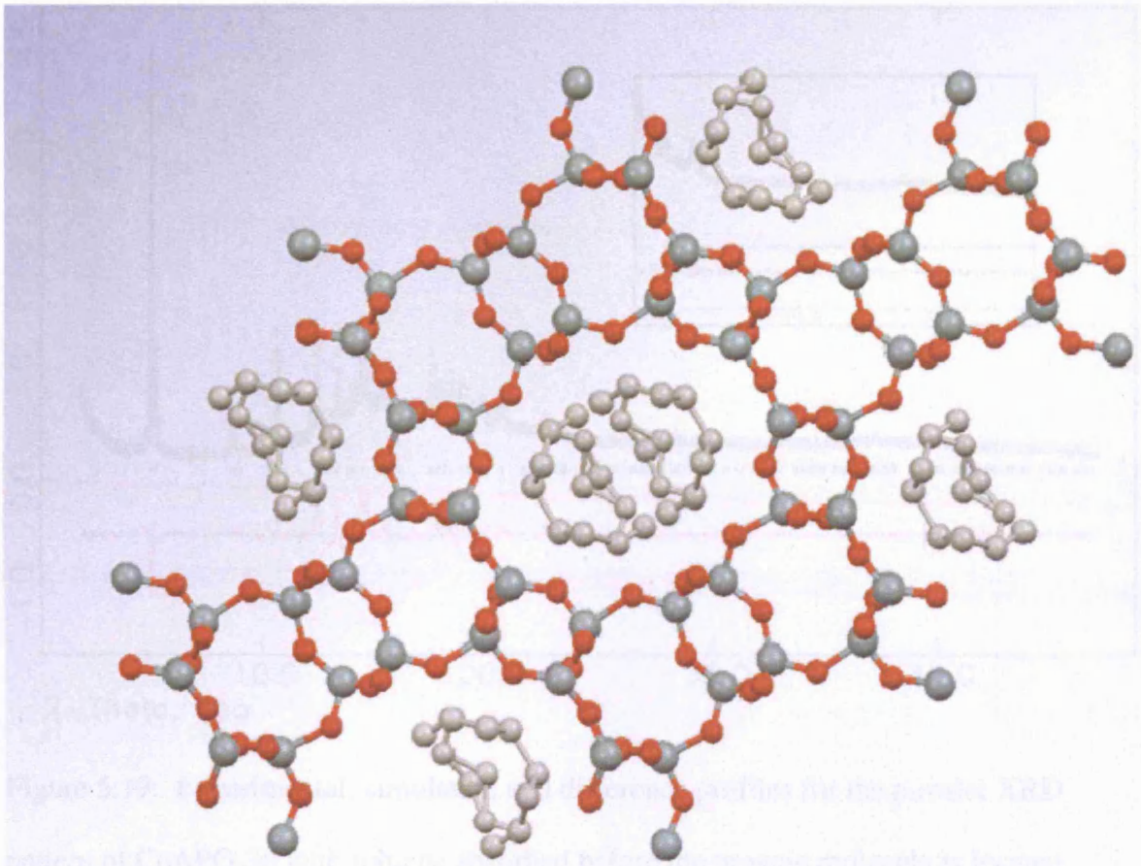

Figure 5.18: Toluene location within the ATS topology employing HRXRD powder data.

The data-sets were again collected at the SRS in Daresbury on station 9.1, employing a wavelength of 1.0002 Å. Firstly, only the framework atoms as reported by Smith *et al.* (12) were fitted to the high angle data. This yielded a very poor fit at low angle (see Figure 5.19) resulting in a wRp value of 19.6%.

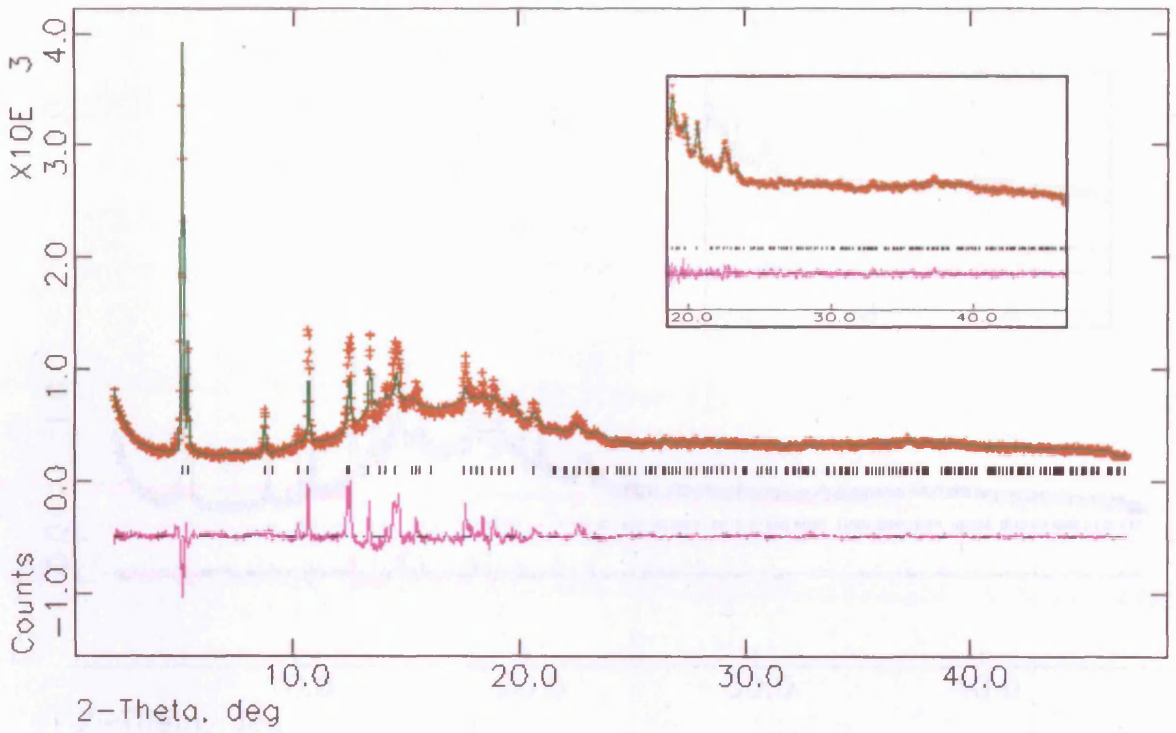

Figure 5.19: Experimental, simulated, and difference profiles for the powder XRD pattern of CoAPO-36 with toluene absorbed before the organic molecule is located (wRp = 19.6% and Rp = 12.9%).

The missing toluene atoms were again located using the same approach as was taken with the SAPO-5 material. The difference electron density peaks led to the location of the sorbent's missing carbon atoms. Figure 5.20 highlights the goodness of fit between experimental and simulated pattern with an improvement in wRp value from 19.6% to 6.3%.

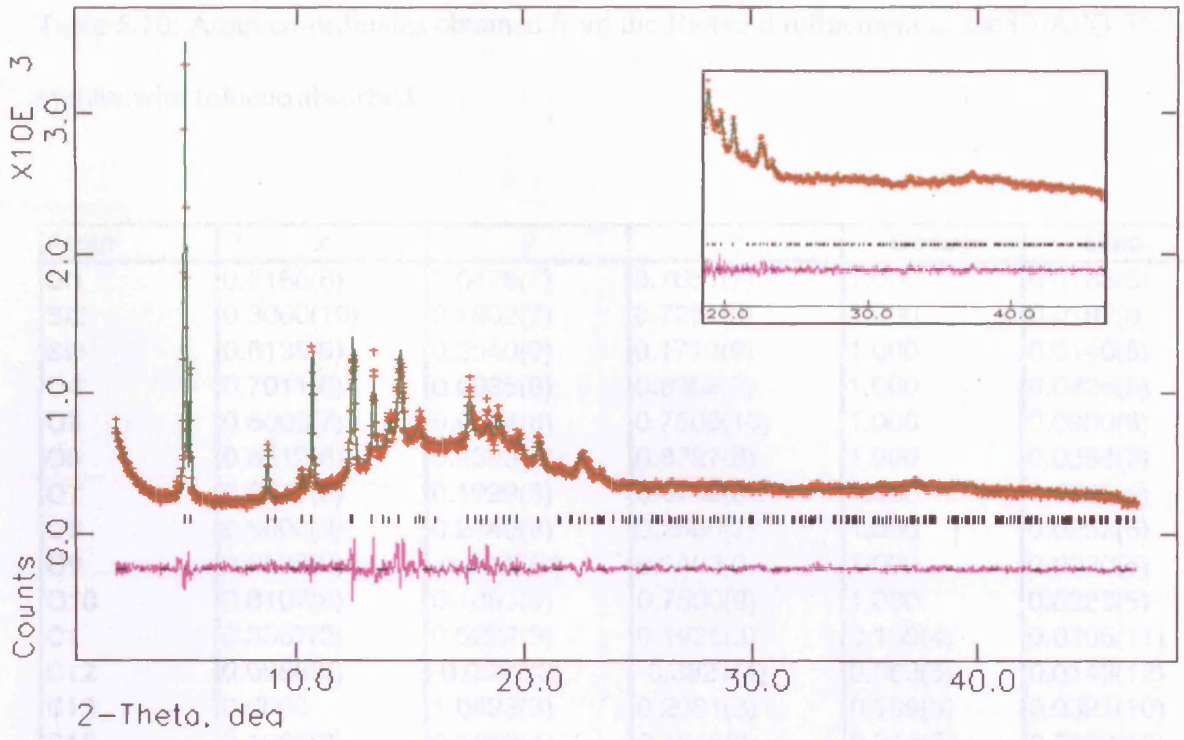

Figure 5.20: Experimental, simulated, and difference profiles for the powder XRD pattern of CoAPO-36 with toluene absorbed after the organic molecule is located (wRp = 6.3% and Rp = 4.6%).

The unit-cell parameters, symmetry and refined atom-positions can be seen in Table 5.9 and 5.10 and a list of selected bond lengths and angles in Table 5.11 and 5.12.

Table 5.9: Space group and unit cell dimensions obtained from the Rietveld refinement of the CoAPO-36 system with toluene absorbed.

CoAlPO-36 with Toulene absorbed		
Spacegroup: *C 2/c*		
a = 13.1300(2)	b = 21.4520(3)	c = 5.0901(2)
α = 90°	β = 89.94°(5)	γ = 90°

Table 5.10: Atom co-ordinates obtained from the Rietveld refinement of the CoAPO-36 system with toluene absorbed.

Atom	*x*	*y*	*z*	*Occup*	*Uiso*
Si1	0.6166(8)	0.0428(7)	0.7651(7)	1.000	0.0183(5)
Si2	0.3060(10)	0.1802(7)	0.7257(9)	1.000	0.0192(6)
Si3	0.6135(9)	0.2540(9)	0.1719(9)	1.000	0.0140(5)
O4	0.7011(8)	0.0935(8)	0.8359(8)	1.000	0.0426(5)
O5	0.5000(7)	0.0674(8)	0.7500(10)	1.000	0.0900(6)
O6	0.6212(8)	0.2303(7)	0.8727(8)	1.000	0.0394(7)
O7	0.3343(8)	0.1929(9)	0.0745(8)	1.000	0.0739(6)
O8	0.5000(9)	0.2440(8)	0.2500(7)	1.000	0.0252(6)
O9	0.6589(9)	-0.0097(9)	0.1603(9)	1.000	0.0220(5)
O10	0.8107(8)	0.1883(9)	0.7500(9)	1.000	0.0223(5)
C1	0.3367(2)	0.5222(3)	0.1925(3)	0.130(4)	0.0205(11)
C12	0.0988(3)	-0.0322(3)	-0.3821(4)	0.363(5)	0.0143(12)
C13	0.0000	1.0423(3)	0.2981(3)	0.169(3)	0.0321(10)
C15	0.1006(3)	0.1088(4)	0.7035(3)	0.713(2)	0.0552(13)
C16	0.0000	0.9298(2)	0.7171(3)	0.536(5)	0.0214(11)
C17	0.0657(4)	0.1379(3)	0.4200(4)	0.133(2)	0.0208(12)
C18	0.1640(2)	0.0707(4)	-0.5448(4)	0.107(5)	0.0563(13)

Table 5.11: Selected bond lengths obtained from the Rietveld refinement of the CoAPO-36 systems with toluene absorbed[1].

Vector	Length
SI1_O4	1.5949(13)
SI1_O5	1.6213(18)
SI1_O9	1.6040(24)
SI2_O4	1.8885(22)
SI2_O6	1.6219(12)
SI2_O7	1.8343(22)
SI2_O10	1.5463(18)
SI3_O6	1.6089(18)
SI3_O7	1.5605(14)
SI3_O8	1.5576(17)
SI3_O10	1.6371(13)
C1_C12	1.3020(11)
C1_C18	1.6948(15)
C12_C12	1.8288(16)
C12_C13	1.6033(14)
C12_C16	1.6134(14)
C12_C18	1.2478(10)
C15_C17	1.6374(16)
C15_C18	1.7200(13)
C16_C17	1.8280(15)
C17_C17	1.7308(22)

[1] Some bond lengths appear too short or too long in the framework as the T-atoms are just assigned as Si rather then Al and P. The toluene bond lengths appear too short or too long as they are not actual bonds between atoms but just an arrangement of electron density which arises from the toluene's motion within the framework's channel.

Table 5.12: Selected bond angles obtained from the Rietveld refinement of the CoAPO-36 systems with toluene absorbed[2].

Angle	Degrees
O4_SI1_O5	116.460(8)
O4_SI1_O9	102.039(8)
O5_SI1_O9	134.184(3)
O4_SI2_O6	121.939(6)
O4_SI2_O7	82.672(4)
O4_SI2_O10	92.078(2)
O6_SI2_O7	101.017(6)
O6_SI2_O10	118.281(5)
O7_SI2_O10	96.139(3)
O6_SI3_O7	112.916(7)
O6_SI3_O8	104.918(2)
O6_SI3_O10	115.527(2)
O7_SI3_O8	94.218(5)
O7_SI3_O10	97.645(7)
C12_C12_C18	107.343(2)
C12_C13_C16	93.484(2)
C12_C18_C15	101.673(7)
C13_C12_C1	121.462(8)
C16_C12_C1	111.985(7)
C16_C16_C17	112.442(3)
C18_C1_C1	125.813(5)
C18_C12_C16	110.054(8)
C18_C15_C15	137.306(4)

[2] As with the bond lengths, the same problem occurs with the bond angles giving rise to some unexpected values due to the same issues mentioned previously.

5.5 Conclusion

The aim of this study was to look at ways of improving a material's ability to store toluene in wet conditions, gain insight into the interactions between toluene and the framework as well as establishing a material's properties which make it a good toluene storage material.

It can be concluded, that the Brønsted acid sites of the material interact with the delocalised π–system of the toluene as was established through HRXRD and computational studies. It was hence possible to explain, why substituted aluminophosphates are capable of storing higher amounts of toluene in comparison to unsubstituted frameworks. Furthermore, it was possible to establish that there are two different types of framework–toluene interactions. The primary absorption mechanism, leading to the aluminophosphate storing the majority of the toluene molecules is through the organic just locating in the channel system of the material, and having very little interaction with the framework. Pure AlPO-5 can store only up to 20 – 30 % less toluene than the best AFI topology, SAPO-5 which was synthesised at a high pH. AlPO-5's ability to store a relatively high amount of hydrocarbons can be attributed to the material containing organic molecules located in the centre of the framework's channel.

The second type of framework–toluene interaction arises from the acid sites generated through heteroatom substitution into the framework structure, which lead to different AFI topologies absorbing different amounts of toluene based on the material's overall acidity. The availability of the acid sites, pore size and dimensionality also play

an important role in a material's storage ability. Small pore aluminophosphates, such as AlPO-18 have shown to be relatively poor hydrocarbon storage materials (11).

Finally, the introduction of an H_2O filter (zeolite A) led to the reproduction of results obtained in a dry environment even though water was present, which indicates that materials which are effective traps for toluene in dry conditions can also show good storage ability in the presence of water when mixed with zeolite A.

By combining computational with experimental techniques, it was possible to gain a very clear picture of the framework–toluene interactions in microporous materials, when employing them as hydrocarbon traps in cold start emission control. Not only was it possible to shed light onto different storage abilities within the same topology, but also to investigate the toluene's motional behaviour within the framework. Based on these findings a material's toluene storage ability can be predicted prior to experimental procedures being undertaken. However, the tested materials fall short in their ability to act as hydrocarbon traps in comparison to materials reported in previous studies (6, 10), but the experiments conducted have allowed gaining insight into materials' attributes, which make them effective hydrocarbon traps.

5.6 References

1. H. Rommelt, A. Pfaller, G. Fruhmann, and D. Nowak, *Science of the Total Environment, 241*, 197 (1999).
2. T. Kanazawa, *Catalysis Today, 96*, 171 (2004).
3. E. R. Becker and R. J. Watson, *SAE Paper, 980413* (1998).
4. B. J. Cooper, *Platinum Met. Rev., 38*, 2 (1994).
5. E. Otto, F. Albrecht, and J. Liebl, *SAE Paper, 980418* (1998).
6. D. S. Lafyatis, G. P. Ansell, S. C. Bennett, J. C. Frost, P. J. Millington, R. R. Rajaram, A. P. Walker, and T. H. Ballinger, *Applied Catalysis B-Environmental, 18*, 123 (1998).
7. K. F. Czaplewski, Reitz T. L., Kim Y. J., and Snurr R. Q., *Microporous and Mesoporous Materials, 56*, 55 (2002).
8. D. Caputo, P. Corbo, F. Iucolano, F. Migliardini, and C. Colella, *Separation Science and Technology, 39*, 1547 (2004).
9. S. P. Elangovan, M. Ogura, M. Davis, and T. Okubo, *J. Phys. Chem. B, 108*, 13059 (2004).
10. N. R. Burke, D. L. Trimm, and R. F. Howe, *Applied Catalysis B-Environmental, 46*, 97 (2003).
11. S. P. Elangovan, M. Ogura, Y. Zhang, N. Chino, and T. Okubo, *Applied Catalysis B-Environmental, 57*, 31 (2005).
12. J. Smith, J. Pluth, and K. Andries, *Zeolites, 13*, 166 (1993).
13. M. Sanchez-Sanchez, G. Sankar, A. Simperler, R. G. Bell, C. R. A. Catlow, and J. M. Thomas, *Catalysis Letters, 88*, 163 (2003).

14. P. A. Barrett, G. Sankar, C. R. A. Catlow, and J. M. Thomas, *Journal of Physical Chemistry*, *100*, 8977 (1996).

15. R. Van Grieken, J. L. Sotelo, C. Martos, J. L. G. Fierro, M. Lopez-Granados, and R. Mariscal, *Catalysis Today*, *61*, 49 (2000).

16. G. Lischke, B. Parlitz, U. Lohse, E. Schreier, and R. Fricke, *Applied Catalysis a-General*, *166*, 351 (1998).

17. S. P. Elangovan, V. Krishnasamy, and V. Murugesan, *Reaction Kinetics Catalasys Letters*, *55*, 153 (1995).

18. S. P. Elangovan, C. Kannan, B. Arabindoo, and V. Murugesan, *Applied Catalysis A General*, A (1998).

19. H. O. Pastore, S. Coluccia, and L. Marchese, *Annual Review of Materials Research*, *35*, 351 (2005).

20. B. H. Toby, *Journal of Applied Crystallography*, *34*, 210 (2001).

21. A. C. Larson and R. B. Von Dreele, *Los Alamos National Laboratory Report LAUR 86-748* (2000).

22. K.-J. Chao, S.-P. Sheu, and H.-S. Sheu, *Journal of the Chemical Society - Faraday Transactions*, *88*, 2949 (1992).

23. L. B. McCusker, R. B. Von Dreele, D. E. Cox, D. Louer, and P. Scardi, *Journal of Applied Crystallography*, *32*, 36 (1999).

24. W. Kraus and G. Nolze, BAM Berlin, *PowderCell 2.4*.

25. J. D. Gale, *Journal of the Chemical Society, Faraday Transactions*, *93*, 629 (1997).

26. Accelrys, *Cerius2*.

27. M. G. G. Wu, M. W. Deem, S. A. Elomari, R. C. Medrud, S. I. Zones, T. Maesen, C. Kibby, C. Y. Chen, and I. Y. Chan, *Journal of Physical Chemistry B*, *106*, 264 (2002).

Chapter 6

Summary

6.1 Hypothesis

The overall aim of this project was to shed light on the framework–organic molecule interactions within microporous aluminophosphate materials. The family of microporous aluminophosphates has been known for almost 30 years, but the role of the structure directing agent still holds many questions. Initially it was thought that the SDA purely acts as a space-filler, filling the pores of the material and hence defining which structure will be formed (1). However, this theory has more or less been ruled out as several SDAs of different sizes can, for example, form the AlPO-5 topology, while some amines such as cyclohexylamine can form more then one molecular sieve (2).

Other views of the SDA's role in the synthesis of aluminophosphates include them acting as pH adjusters, indicating that the pH is the underlying driving force in which a structure is formed. Experiments where certain pH levels were achieved by the addition of NaOH however undermine this theory.

It was hence decided to investigate the SDA's role by different experimental and computational techniques to try and understand the role the SDA plays in the synthesis of one-dimensional porous materials.

Experimental results indicated that the size of the template by itself did not seem to be the sole driving force behind the formation of a specific framework. The template TEA with the lower specificity for the formation of the AlPO-5 topology appeared to be filling the structure's channels better than the very specific SDA MCHA (3). Hence, rather than looking at the SDA's size only, it was decided to investigate the different attributes associated with the organic amines.

It has not been possible to synthesise microporous aluminophosphates using SDAs, which do not contain an amine or ammonium group. The reason behind this is the ability of the amine to be protonated, which is directly connected to the availability of the electron lone pair on the nitrogen giving rise to a pH around 7 in most syntheses. The pKb value of an amine is a direct measure of its ability to be protonated and hence was a good starting point to look at.

The pKb values of amines are governed by two factors: (a) the inductive effect of the side groups, which is directly related to the size of the groups and (b) the flexibility of the substitutents (4). Based on this, it is easy to determine that MCHA is more basic than TEA and as such, has a lower pKb value than TEA (see Figure 6.1).

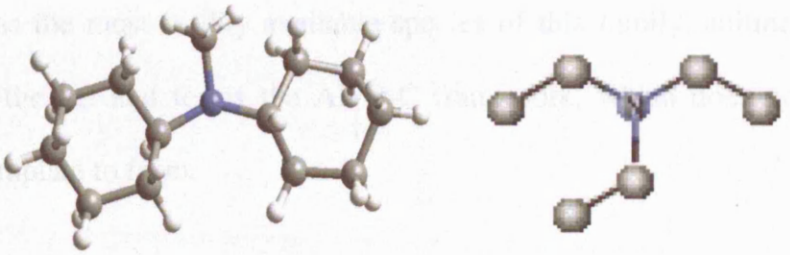

Figure 6.1: Molecular structures of MCHA and TEA. It is clearly visible that MCHA has larger and less flexible side-groups then TEA, which leads to it having a higher pKb value.

The lower pKb value is directly connected to a higher protonation and hence greater hydration of the MCHA molecule, which in turn leads to a shielding of the charge carried by the protonated nitrogen. The formation of water–SDA clusters was confirmed by TGA experiments, emphasising the correctness of the proposed model.

AlPO-5 is the most readily formed framework and as MCHA has very little interaction with the framework, due to the formation of SDA–water clusters, it can be concluded that MCHA's low pKb value is the underlying reason for it being so specific in the formation of the AFI topology. However, it can be established that the pKb value by itself does not seem to be the only driving force in the synthesis of microporous materials. The size-effect of SDAs seems to play a substantial role as well (5).

Having established that the pKb value of the amine plays an important role in the synthesis of aluminophosphate materials, benzyl- and phenyl-based

amines were investigated. Phenyl-based amines have been paid very little attention as the most readily available species of this family, aniline, does not mix with the gel and forms the AlPO-C framework, which does not need an organic template to form.

The pKb value of aniline was therefore examined to determine why it does not form a microporous material, even though it has an amine group. Aniline has a very high pKb value (6), which can be attributed to the fact that the electron lone-pair on the nitrogen stabilises the delocalised π–system of the phenyl-ring. It is hence not available for hydration and leads to the organic forming an insoluble layer above the gel-mixture. By replacing the phenyl- with a benzyl-group it is possible to decrease the pKb value of the organic compound considerably, which leads to it becoming soluble in the synthesis gel. The introduction of a methyl-group between the phenyl-ring and the amine group allows freeing-up the lone electron pair on the nitrogen for hydration and thus makes it much more hydrophilic.

The organic molecule phenylethylamine was hence used as an SDA and led to the formation of a novel layered aluminophosphate structure, which was possible due to the findings from the different AFI systems investigated in chapter 3, highlighting the importance of the SDA's pKb value.

Other templates that were found to also be able to act as SDAs are phenylpropylamine, *N*-methylaniline and benzylamine. Using benzylamine as the structure directing agent resulted in the same material being formed as was

synthesised by phenylamine. This was determined from the two materials' identical XRD patterns. The organic molecules' pKb values follow the trend below:

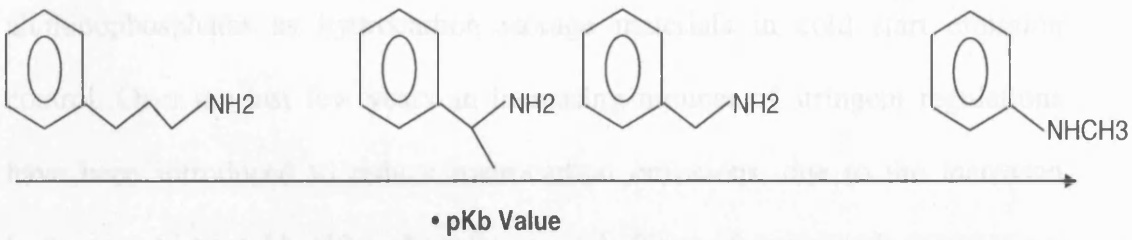

Figure 6.2: Phenyl-based SDAs used in the syntheses of layered aluminophosphate materials. The pKb value increases from left to right and hence the availability of the lone electron pair on the amine's nitrogen decreases accordingly.

It was however only possible to determine the structure of one bulk compound through single crystal X-ray diffraction experiments, as the other samples did not yield crystals of sufficient size. It was also not possible to determine unambiguously the space group of the other samples by powder XRD, as small impurities were present rendering structure solution from powder data almost impossible.

Another interesting fact established from this series of experiments was that *N*-methylaniline was able to produce two impurity phases (the GIS and SBS topologies) as was determined by single crystal diffraction. *N*-methylaniline has the highest pKb value of all the organics used in the syntheses. Based on all of the results from this project, it can be concluded that based on its high pKb value

it has the lowest specificity and hence has the ability to form several different structures.

The final part of this project was to look at microporous aluminophosphates as hydrocarbon storage materials in cold start emission control. Over the last few years an increasing number of stringent regulations have been introduced to reduce hydrocarbon emissions, due to the increased focus on detrimental health and environmental effects of compounds found in car exhaust fumes.

Previous work has shown the importance of a material's acidity in its ability to store organic molecules in cold start emission control (7). GC experiments did indeed show up differences in toluene storage ability based on different acidities of the framework. The same topology (AFI) could absorb different amounts of toluene when different heteroatoms were substituted into the framework, which is the origin of the difference in acidity in these materials.

It was again important to look at the organic molecule's attributes to get a better understanding of the reason behind certain trends found in these experiments. The methyl-group in the toluene is electron donating, which leads to the methyl-group carrying a $\delta+$ charge and the phenyl-ring consequently a $\delta-$ charge. This charge becomes concentrated at the ortho-para positions, as shown by the resonance structures below (see Figure 6.3).

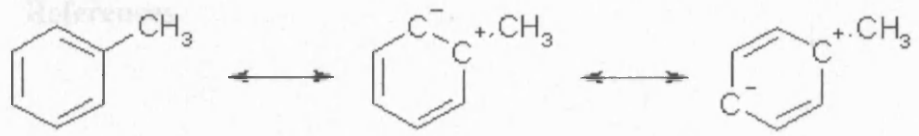

Figure 6.3: Charge delocalisation in a toluene molecule, leading to the phenyl-ring carrying a δ- charge and the methyl-group consequently a δ+ charge.

By combining computational with experimental techniques it was possible to create a very clear picture of the framework–toluene interactions in hydrocarbon traps.

It was not only possible to gain insight into the reasons underlying different storage abilities within the same topology, but also to investigate the motional behaviour of the toluene within the framework. This work highlighted the importance of a material's acid strength and proton accessibility to be able to act as a good hydrocarbon trap.

In all the different systems investigated during this project, the combination of experimental and computational techniques has led to an improved understanding of the systems. When looking at the host–guest interactions in microporous materials it is important to not only look at the framework's attributes (i.e. acidity, pore size etc.) but also to look at the organic molecule's attributes such as pKb value, protonation ability, hydration, charge distribution and size. We have shown that by including all these aspects a thorough picture of a system can be observed. It is important though to keep in mind that the electron density peaks found from the various Rietveld refinements represent disordered molecules, but they do not represent real atoms.

6.2 References

1. S. T. Wilson, B. M. Lok, C. A. Messina, T. R. Cannon, and E. M. Flaningen, *J. Am. Chem. Soc.*, *104*, 1146 (1982).
2. H. O. Pastore, S. Coluccia, and L. Marchese, *Annual Review of Materials Research*, *35*, 351 (2005).
3. M. Sanchez-Sanchez, G. Sankar, A. Simperler, R. G. Bell, C. R. A. Catlow, and J. M. Thomas, *Catalysis Letters*, *88*, 163 (2003).
4. B. Safi, K. Choho, F. De Proft, and P. Geerlings, *Chemical Physics Letters*, *300*, 85 (1999).
5. M. Sanchez-Sanchez and G. Sankar, *Studies in the Surface Science and Catalysis*, *154 Part A-C*, 1021 (2004).
6. J. J. Elliott and S. F. Mason, *Journal of the Chemical Society*, 2352 (1959).
7. N. R. Burke, D. L. Trimm, and R. F. Howe, *Applied Catalysis B-Environmental*, *46*, 97 (2003).

Appendices

Appendix A

Furio Corà

Davy Faraday Research Laboratory, The Royal Institution of Great Britain,

21 Albemarle Street, London W1S 4BS, United Kingdom

furio@ri.ac.uk, Fax: +44 (0)20 7670 2958; Tel: +44 (0)20 7409 2992

Computational work performed by Dr. Furio Corà on the layered material

In conjunction with the experimental work, we performed a computational study of the layered structure. Of interest to us was to examine the AlPO at an atomic level in order to determine the location of the protons in the layers, which is difficult to characterize via XRD techniques, and to investigate the structural stability of the layers. A two-step approach was adopted using quantum mechanical (QM) and interatomic potential (IP) techniques, selected as appropriate for the particular feature under examination.

The study of the AlPO layers is most suited to quantum mechanical techniques due to its unusual structure incorporating 6 coordinated Al, and 1, 2 and 3 coordinated O ions. To begin with, we exploited the layering of the structure and cleaved the solid along the (100) direction, forming a single layer model of composition $[AlPO_5H]^-$; the symmetry (*C 2/c*) and cell parameters were taken from the experimentally derived values (a = 39.06Å, b = 5.31Å, c = 9.67Å, $\alpha = 90.0^0, \beta = 94.6^0, \gamma = 90^0$). The experimentally derived coordinates for Al, P and O were used in this initial structure. Each primitive unit cell contains 5 symmetry unique O ions, and in principle each can act as a protonation site. We therefore generated 5 protonated single layer models each corresponding to the proton being bound to a different symmetry unique oxygen. The lattice parameters of these 2 dimensional computational models were not varied during our QM calculations; only internal optimisations of all the fractional coordinates were performed.

Quantum mechanical calculations have been performed within the Density Functional Theory (DFT). The QM code CRYSTAL was employed for these calculations, using the hybrid DFT functional B3LYP. The code CRYSTAL has been successfully used to model AlPOs in previous work. The Gaussian basis sets used to describe the electrons in the system were the same as those described in previous work and can be obtained from the online library of the code.

Ammonium ions (NH_4^+) were used in our single layer model to represent the protonated 1-phenylethylamine ions. Our rationale for using protonated SDA ions arises from the observed change in pH from 2 to 8 of the homogenous gel mixture, indicating that protons are removed from solution upon addition of the SDA. Each ammonium ion used here mimics the ammonium end of one organic template, which is the only part of the SDA close enough to the layer to have any significant chemical interaction with it. The remaining part of the organic template is likely to be involved in template-template interactions and / or is necessary for space filling. To examine the AlPO layer when no SDAs are present, we generated a neutral single layer system in which the ammonium ion and any charge inducing species in the layer are removed. A full optimisation including the lattice parameters was conducted on this neutral layer.

The stable protonated layer identified in the QM work was employed in the second stage of our computational study, performed using IP techniques. Energy minimisation and Molecular Dynamics (MD) calculations were carried out on the system with the experimentally derived composition, $[AlPO_4(OH)](NH_3C_2H_4C_6H_5)$. The goal of this approach was to study the organic templates residing in the interlayer region and in particular to examine the forces responsible for holding adjacent layers together. The cvff forcefield available in the Open Forcefield (OFF) suite of methods under Cerius2 was selected for this function because it yields good results for such organic – organic intermolecular interactions. The process adopted for this part of the computational study initially involved replacing the NH_4^+ ions

present in the QM model by an equal number of protonated 1-phenylethylamine ions. The structure of the AlPO-layers present in this system were fixed to that obtained in the QM work. The charges assigned to atoms in the layers are +1.4 to Al, +3.4 to P and -1.2 to O ions, as customary in AlPO calculations performed with cvff. The FF type and charge of the SDA atoms were obtained using the direct atom typing and the charge equilibration features available in Cerius2. The Ewald method was selected to describe the non-bonded dispersive and Coulombic interactions. The smart minimiser function and an N,V, T ensemble set at 423K with a time step of 0.001ps, for a total simulation time of 100ps were used for the energy minimisation and MD calculations. In order to examine the forces responsible for holding adjacent layers together, we calculated the energy of the system corresponding to different values of the a lattice parameter in the range of $35\text{Å} \leq a \leq 150\text{Å}$. The values selected allowed us to examine the system at small interlayer separation (i.e. compression of the bulk system) and large interlayer separation (i.e. expansion of the bulk system). For the experimentally derived value of the a lattice parameter, we performed a sequence of energy minimisation, molecular dynamics, energy minimisation steps. No disorder or reconstruction was observed after the MD calculations and in fact the internal energy calculated by energy minimisation of the structure before and after the MD step differed by only 1meV. Therefore, for all other values of the a lattice parameter, only energy minimisations of the organic molecules were performed, to calculate the system's energy, E_a, as a function of the interlayer separation. The interaction energy between the layers, E_{lay} , was then evaluated according to:

$$\Delta E_{lay} = \frac{E_a - E_\infty}{2}$$

Where ΔE_{lay} is the interaction energy per unit cell between two layers (these are separated by 4 SDA ions per unit cell); E_a is the total energy at lattice spacing a; E_∞ is the total energy at infinite layer separation (measured at a = 150Å).

After the experimental picture of the material was obtained, computational methods (QM calculations) were employed to establish the position of the proton within the layer and the stability of the overall material. Out of the 5 possible protonation sites available in the layer, i.e. the 5 symmetry unique O ions, only 2 are found to be local minima in the potential energy surface (PES). These are the O ions labelled as O1 and O5 and are the two oxygen atoms bridging the Al ions in the Al-Al edge-sharing units. The oxygen labelled 2, 3 and 4 are 1 and 2 coordinated and belong to Al-O-P units and the terminal P=O group, and are not involved in the Al-Al edge sharing linkage. A proton initially located on one of the latter oxygen types moves to O5 upon geometry optimisation, indicating that no energy barrier exists for these 'proton jumps'. Examination of the relative energies of the protonated layers after optimisation, reveals that protonation of sites O1 and O5 incurs a noticeable energetic difference, calculated as 1.52eV per proton in favour of O5. Although O1 is a local minimum in the PES, protonation of this oxygen is unlikely to occur due to its energetic instability. Only protonation of the oxygen labelled as O5 is therefore expected on the basis of the QM results. O5 is the two coordinated oxygen of the structure that bridges the two Al ions of the layer.

The geometry optimised structures of the AlPO layer obtained upon protonation of O1 and O5 show major differences. It is important to first notice that the P ions of the structure remained tetrahedrally coordinated to 4 oxygens throughout our computational study. This result is consistent with earlier work indicating the molecular-ionic nature of AlPO materials. All major differences observed in the optimised structures refer to the local environment around the Al ions.

The structure corresponds to the optimised layer when O1 is protonated. It bears no resemblance to the experimentally determined one. In fact a structural reconstruction of the AlPO layer occurs, with half of the Al ions being 4 coordinated in a tetrahedral geometry. Generally, this is the stable environment for Al in 3D AlPO frameworks, but not in the case of

this layered material. The other half of the Al ions in the system are 6 coordinated, forming AlO_6 octahedra with 2 long and 4 short Al-O bonds each.

The structure obtained when O5 is protonated yields a very good match with experimental results in both coordination numbers and bond distances. Upon closer examination of the structure, we find that protonation of O5 gives uniquely octahedrally coordinated Al where protonation of the O ions in each of the AlO_6 units occurs along vertices situated trans with respect to each other. The optimised values of all bond lengths in the layer are within 1% difference to the experimentally deduced values. As these differences are extremely small, we can be confident in the reliability of the experimental structural refinement, the calculated structure itself and in the suitability of the B3LYP functional to study AlPOs.

The combination of results discussed above, relative to the energetics and structural features of the AlPO layer, indicates clearly that only one protonation site is present in the layer, i.e. the oxygen-ion labelled O5. In practice, since this oxygen is always protonated, it should be described as part of a hydroxide ion. Anchoring of the hydroxide ion to the layer is necessary to charge balance the positive charge of the SDAs residing in the interlayer region and to yield the experimentally observed octahedral coordination of Al. The material can be considered to be an $AlPO_4$ – structure with a hydroxyl-group, which is acting as a mineraliser incorporated into the framework. In the past hydroxyl- and fluoride-groups have been shown to act as mineralisers in the synthesis of zeolitic materials. In some cases (i.e. the NON and STT structures) the fluoride-anions are directly bonded to one silicon T-atom and are thus integrated into the framework. Within the group of layered aluminophosphates, some structures such as MIL-12 can only be synthesised in the presence of a mineraliser, which tends to get incorporated into the structure and stabilises the material in the process. We therefore believe that in the case of this layered AlPO, the hydroxide groups anchored to the layers can be described as 'mineralisers' for the structure and therefore play a vital role in the construction of the layers.

The protonated SDA (1-phenylethylamine) does not only act as a space-filler within the structure but also as a hydrogen bonding donor to the framework oxygens. The inorganic sheets are being held together by H-bonding between oxygen atoms of the framework and hydrogen atoms attached to the nitrogen from the SDA and thus stabilising the structure. The presence of the hydroxyl group O5H is necessary to charge-balance the protonated SDA.

The second part of our computational work focused on the role that the SDA molecules play in holding the AlPO layers together. Our MD calculations, performed on the protonated layers at full loading of SDAs and at the experimental value of the interlayer separation, indicate that the templates are stable within the channels. No disorder and/or reconstruction of the SDA molecules is observed after 100ps of MD simulation at 423K. This result indicates that the SDAs are tightly packed within the interlayer region of the AlPO. It also suggests that the removal of the SDAs during calcination results in the creation of large voids, which may contribute to the structural collapse of the AlPO framework, as no species is present to bind the AlPO layers together.

We created a plot in order to examine the forces responsible for holding the SDAs and AlPO layers together, showing the relative energy as a function of the interlayer separation. Our results indicate that the optimal interaction energy between two layers in the bulk material amounts to 26.1 kcal/mol per unit cell (comprised of 2 layers), and corresponds to the lattice parameter a = 38.3Å, which is in reasonable agreement with the experimentally derived value of 39.06Å. The calculated interlayer binding corresponding to this value of a is -0.353J/m^2; a small, yet non-negligible value that suggests that the AlPO layers interact with each other, probably via dispersive interactions in the SDA region. For all values of a, the SDAs remain close to the layers. Specifically the ammonium end of each 1-phenylethylamine SDA is strongly bound to the negatively charged inorganic layers, even at large layer separations. A combination of non-bonded Coulombic and dispersive interactions is therefore responsible for holding the SDAs and AlPO-layers together.

Finally the effects of calcination on the structure were modelled computationally. One of the effects of calcination on the AlPO – SDA adduct is the removal of the SDA and other non-framework ions, except those needed for charge balance. The QM calculations designed to examine the effects of calcination focused on hypothetical systems, of one layer thickness; in our initial examination, the O_5H^- mineraliser group, and all extraframework ions were removed, leaving a slab of composition of $AlPO_4$. Full geometry optimisations were performed on the slab 1) retaining all symmetry operators of the original $AlPO_5H$ – SDA system and; 2) with all symmetry constraints removed.

In the calculated AlPO structures, of composition $AlPO_4$, we see that the 1 dimensional chains of AlO_6 octahedra present in the as-synthesised material are no longer present, and are replaced by a chess-board like arrangement of the Al ions in which the coordination polyhedra around Al are connected by corner-sharing only. The PO_4 tetrahedra locate above and below the plane but cover only half of the empty squares of the chess-board pattern. In practice, this geometry defines dense 1 dimensional chains in the structure, of composition $[AlP_2O_8]^{3-}$, bonded via AlO_x units (x = 4 or 6) in the interchain region. For both cases, the layer calculated when symmetry is and is not present, Al-O_2-P edge sharing is found, which is an unstable feature in AlPOs. For the case in which the geometry optimisation was performed with full symmetry, the 1 dimensional $[AlP_2O_4]^{3-}$ chains consist of 6 coordinated AlO_6 octahedra and 4 coordinated PO_4 tetrahedra. These chains are held together by 4 coordinated square planar AlO_4 units in the interchain region. The composition ratio of Al in 4 and in 6 coordination is 1. The presence of AlO_4 units in square planar coordination suggests that this structure is unstable, and that Al in this geometry can be easily solvated and possibly removed from the interchain region; therefore we do not expect this phase to be stable under harsh experimental conditions, such as those present during calcination.

Performing a full geometry optimisation on the layer with all symmetry constraints removed has instead predicted a more stable structure, in which the $[AlP_2O_8]^{3-}$ 1 dimensional chains

consist solely of AlO_4 and PO_4 tetrahedra, and are held together by AlO_6 octahedra in the interchain region. Akin to the previous calculation, the ratio of 4 coordinated and 6 coordinated Al ions is found to be 1, but now the Al ions linking the AlP_2O_8 chains are in stable 6 coordinated octahedral environment. The differences in the geometry of the Al ions in the structures examined explains the energetic difference, calculated as 0.1296 eV/unit cell in favour of the structure obtained in the absence of symmetry. This result confirms the instability of the square planar AlO_4 units in comparison to the tetrahedral AlO_4 geometry. The more energy favourable conformation of the charge neutral AlPO layer, predicted in the absence of any symmetry constraints, shows a major change in the bonding between ions of the framework. Specifically, we find that the Al-O-Al zig-zag linkage reconstructs and forms a linear chain of corner sharing AlO_4 and PO_4 tetrahedra that are held by AlO_6 octahedra in the interchain space. The latter $AlPO_4$ structure is very unstable; its energy difference with respect to the stable AlPO4 polymorph, i.e. Berlinite, is calculated as 2.07 eV per AlPO4 formula unit. This value should be compared with the relative energy with respect to Berlinite of other stable microporous modifications, which at B3LYP level is calculated in a range of 0.1-0.2 eV per formula unit. The energetic instability of the calcined layered structure, as well as the reconstruction of the atoms in the layers discussed above, explain why the novel layered AlPO collapses upon calcination; the 1 dimensional chains formed are unable to maintain the integrity of the layers.

These results indicate that the presence of charged species, the $O5H^-$ ions in the layer and the ammonium templates (i.e. the protonated 1-phenylethylammonium ions during synthesis) in the interlayer region are essential to the integrity and structural stability of the new layered AlPO described here.

Appendix B

Furio Corà

Davy Faraday Research Laboratory, The Royal Institution of Great Britain,

21 Albemarle Street, London W1S 4BS, United Kingdom

furio@ri.ac.uk, Fax: +44 (0)20 7670 2958; Tel: +44 (0)20 7409 2992

Computational work performed by Dr. Furio Corà on toluene-framework interactions

To complement the experimental work, a computational modelling of the toluene interactions within the AlPO-5 and substituted AlPO-5 systems (substituents = Si^{4+}, Mg^{2+}, Co^{2+}) was performed in the aim of: 1) examining the behaviour of the toluene molecule within the large 12 member ring channel and; 2) determining the strength of interaction between the toluene molecule and the inorganic solids. Using a combination of quantum mechanical (QM) and interatomic potential (IP) techniques, we have prepared frameworks that reproduce the characteristics of true AlPO frameworks, and subsequently examined their toluene trapping ability.

AlPO-5 cells of 2x2x3 unit dimensions, previously optimised via energy minimisation techniques with the General Utility Lattice Program (GULP) were used as templates to perform our calculations. The suitability of the GULP code to prepare microporous oxide frameworks has been proven in a variety of previous works. The substituted AlPO-5 systems, namely: SAPO-5, MAPO-5 and CoAPO-5 were created via a single Si^{4+}/P^{5+}, $Mg^{2+}/Al^{3+}$and Co^{2+}/Al^{3+} substitution in each of the 2x2x3 supercells. Protons were used for charge balancing in our study. The parameters used to describe the dopant ions and protons anchored to the framework have been derived making reference to periodic quantum mechanical calculations, performed with the hybrid-

DFT functional B3LYP using the CRYSTAL 03 code. The QM calculations were carried out at a higher loading of 1 dopant ion per unit cell of AlPO-5. All four proton docking sites corresponding to the 4 oxygen nearest neighbours of the dopant ion have been examined with the B3LYP calculations; only the stable site is employed in the pair potential study of toluene in the larger 2x2x3 supercells of the solid. For all of the substituted AlPO-5 systems investigated, this corresponds to an OH bond that points towards the centre of the main 12 member ring channel; therefore a single Brønsted acid site was created in each of the substituted AlPO-5 systems. Each of the inorganic solids was then optimized with the GULP code, in P 1 symmetry, using the interatomic potential parameters that have been developed by Gale and Henson. The pair potentials used in the IP geometry optimisations accurately reproduce the QM results concerning the equilibrium geometry of the dopant and Brønsted OH group.

Once the pure AlPO and the substituted systems (CoAPO-5, MAPO-5 and SAPO-5) were fully optimised, a series of energy minimisation and molecular dynamics (MD) calculations were performed using the open force field (OFF) suite of methods available under the Cerius^2 interface. In particular we employed the CVFF forcefield which incorporates the van Beest potential, assigning charges of +1.4, +3.4 and -1.2 to Al, P and O ions respectively. This choice of method is based on previous successful studies in which the CVFF forcefield was employed to yield good results.

Due to the molecular - ionic and insulating nature of the AlPO framework, only atoms directly bonded to the dopant ions are substantially affected by the framework replacement, and display different net charges at the QM level. Parameters have been obtained in the following way: 1) the Mulliken charges, Q_i (substituted AlPO-5

systems), of each atom around the dopant have been calculated at the QM (B3LYP) equilibrium geometry. These charges are compared with those calculated with the same B3LYP Hamiltonian and computational parameters, for undoped AlPO-5, Q_i (AlPO-5); 2) The difference between the two values, $\Delta Q_i = Q_i$ (substituted AlPO-5 systems) – Q_i (AlPO-5) describes, at least the difference in net charges between pure AlPO and substituted AlPO-5 systems calculated quantum mechanically and; 3) the difference in charges calculated above, ΔQ_i, has been added to the charges employed in CVFF to describe the AlPO framework, i.e. +1.4, +3.4 and -1.2 to Al, P and O atoms. This scheme for the net charges used in our investigation has the benefit of reproducing correctly (at least at 1st order) the electrostatic field created by the dopant ion in its neighbourhood; this is a most important feature when studying the diffusion of polar or polarisable molecules in the empty channels of the doped structures.

Dopant ion	Dopant charge (au)	Unprotonated O ions (au)	Protonated O ion (au)	Proton (au)
Si	2.55	-1.10	-1.00	0.35
Mg	0.90	-1.20	-1.05	0.35
Co	0.85	-1.20	-1.00	0.35

In order to study the interaction of toluene with the inorganic framework, a toluene molecule was created and inserted into the large 12 member ring channel of each of the substituted AlPO-5 systems at a position close to the dopant. In the case of the pure AlPO-5 system, the toluene was placed into the centre of the large 12 member ring channel, that is, the centre perpendicular to the channel direction. The use of large 2x2x3 unit cells of solid meant that toluene - toluene interactions were neglected and therefore our investigations were designed to focus exclusively on framework - toluene interactions. The FF type and charge, assigned to atoms constituting the

toluene molecule were obtained using the direct atom typing and the charge equilibration features available in Cerius[2]. For all MD calculations, the inorganic frameworks were held fixed. Ewald summation was utilised to describe the non-bonded dispersive and Coulombic interactions. The smart minimiser feature was initially used to minimise the toluene molecule into favourable starting configurations within the large channel. MD calculations were performed using an N,V,T ensemble set at 300 K with a time step of 0.001 ps for a total simulation time of 1 ns. Interaction energies were calculated by energy minimisation using the smart minimiser option and then subtracting the energy of a free toluene molecule in vacuo from this value. This energy was calculated in a similar manner to that described above using energy minimisation with the smart minimiser option.

The behaviour of the toluene molecule during the MD simulations is examined first. We find that irrespective of the inorganic system under investigation, the toluene molecule progressively diffuses along one direction of the channel. In the case of the substituted AlPO-5 systems, the position of the organic perpendicular to the channel direction, changes depending on its distance from any active site, with two geometries identified.

Upon far active site – toluene separation, the toluene molecule remains in the centre of the channel and adopts a geometry such that the aromatic benzene ring lies parallel to the channel direction. This leaves the methyl end of the toluene molecule also lying parallel to the channel direction, in fact we find that the methyl end 'leads' the toluene molecule in the direction it is moving in.

The second stable configuration of the toluene molecule is observed when the separation distance between the active site and the toluene molecule is small along the *c* direction. Here, we observe the toluene molecule to drift towards the active site in a direction perpendicular to the channel direction and therefore no longer remains approximately in the centre of the channel. Its displacement along the channel is also temporarily halted and in fact we find the toluene molecule to 'flip' in such a manner that the molecule temporarily lies perpendicular to the channel direction before recovering its orientation parallel to the channel. The fact that the displacement of the molecule is temporarily halted serves as an initial indication of the possible toluene trapping ability of the AFI systems. At close active site – toluene separation the second stable configuration observed involves the aromatic 6 membered ring of the organic laying approximately on top of the Brønsted proton. This favoured conformation of the toluene molecule is observed for all substituted AlPO-5 systems and therefore is non-specific. Our calculations have furthermore shown that the perpendicular orientation of the toluene is only a temporary transition state. Our calculations have therefore modeled two stable geometries of the toluene molecule in the substituted AlPO-5 systems corresponding to the benzene ring of the organic aligning itself parallel to the channel direction

The second aim of our computational investigation was to examine the trapping ability of the different substituted AlPO-5 systems in respect to the different dopant used. This is a complex problem due to the presence of many local minima of similar energy in the potential energy surface of the undoped and substituted AlPO-5 systems which therefore makes it difficult to identify the global minimum. We have attempted to overcome this problem by monitoring a range of parameters over the whole

trajectory of the toluene during the 1 ns of dynamic simulation time, which were the 10 points with the lowest potential, electrostatic and van der Waals energy. At each of the selected points, we have performed geometry optimisations. Such a strategy gave us greater confidence in finding the global minimum.

We will first point out that irrespective of the substituted AlPO-5 systems investigated, the toluene molecule minimises into a position, where the molecule resides close to an active site in such a way that it is orientated parallel to the channel direction The positions with the best overall electrostatic and van der Waals energies are obtained from configurations, which have the best Coulombic energy. This infers that the electrostatic energy is the key force in the AFI – toluene interaction. After isolating the global configuration according to our examination, we have used this to calculate the true interaction energy.

The calculated interaction energies in the observed systems follow the order: SAPO (-29.500 kcal/mol) > CoAPO (-29.337 kcal/mol) > MAPO (-29.099 kcal/mol) > AlPO (-28.858 kcal/mol). This trend in the interaction energy agrees with the experimental findings: 1) very little difference exists between the different AFI systems in their ability to trap toluene, as observed in the TPD experiments and; 2) SAPO is expected to act as the best toluene trap whilst un-doped AlPO-5, the worst.

Performing a computational modeling of the AFI - toluene interactions allowed us to examine the systems at an atomic level which was necessary to explain the trend in results reported above. We find that the orientation of the Brønsted proton with respect to the channel direction is key to understanding the trend in the interaction

energies. The proton anchored to the SAPO framework lies perpendicular to the channel direction by the greatest magnitude, i.e. the angle it makes with respect to the channel direction is greater than that found in the CoAPO and MAPO systems. The order of angle size in the substituted AlPO-5 systems investigated is of the order: SAPO (73.06^{o}) > CoAPO (46.26^{o}) > MAPO (44.05^{o}). This trend in results coincides with the order of relative interaction energy calculated above.

We conclude therefore that doping the aluminophosphate, AlPO-5, leads to an improvement in its ability to trap toluene. This is mainly due to the increased electrostatic interactions that results between the proton of the Brønsted OH active sites and the aromatic benzene ring of the toluene molecule. The strength of interaction between the substituted AlPO-5 systems and the toluene molecule is primarily based on the availability of the proton to interact with the π electron system of the benzene ring.